Type Synthesis, Kinematics Analysis and Dynamic Modelling of Metamorphic Parallel Mechanisms

Gan, Dongming

Awarding institution:
King's College London

TYPE SYNTHESIS, KINEMATICS ANALYSIS AND DYNAMIC MODELLING OF METAMORPHIC PARALLEL MECHANISMS

Dongming Gan / 1465968

A Thesis Submitted in Partial Fulfilment of the Requirements for the Degree of Doctor of Philosophy in Robotics

Department of Informatics

King's College London

April 2018

Abstract

Metamorphic parallel mechanisms (MPMs) are a class of mechanisms that possess adaptability and reconfigurability to change permanent finite mobility based on topological structure change. Metamorphic parallel mechanisms keep the advantages of traditional parallel mechanisms in terms of high load-carrying capacity, good positioning accuracy and low inertia but with reconfiguration. MPMs are a new class of reconfigurable parallel mechanisms and have not been studied much. Therefore, this thesis is devoted to explore the fundamentals of mechanism theory on MPMs by focusing on two parts:

(1) Systematic Methods of Synthesizing and Designing Metamorphic Parallel Mechanisms: A general strategy using reconfigurable joint to construct reconfigurable limbs has been proposed on synthesizing metamorphic parallel mechanisms and a general synthesis procedure has been provided based on screw theory. With two invented reconfigurable joints, many metamorphic parallel mechanisms have been obtained using the proposed method and their reconfiguration has been modelled in terms of geometric constraints. From the design point of view, the design parameters need to serve all phases of a metamorphic parallel mechanism. Thus a unified design performance representation is desired. Based on this, motion/force transmissibility is proposed to unifying the performance representation for optimal design of metamorphic parallel mechanisms considering all working phases and performance in each phase. Optimal design examples are demonstrated on some selected metamorphic parallel mechanisms.

(2) Unified Kinematics and Dynamics Modelling of Metamorphic Parallel Mechanisms: Since each of all reconfigured phases of a metamorphic parallel mechanism is equivalent to a traditional parallel mechanism and all phases with different mobility share the same mechanical structure, a unified strategy has been proposed by considering the reconfiguration of the joint and taking the reconfigured phases as special cases of the general configuration. Some selected metamorphic parallel mechanisms have been studied and their unified kinematics, workspace representation, and dynamics modelling are solved.

Thus this thesis provides basic synthesis, design, and modelling theory for metamorphic parallel mechanisms considering their reconfiguration and variable mobility.

Table of Contents

ABSTRACT 2

TABLE OF CONTENTS 3

TABLE OF FIGURES 8

TABLE OF TABLES 12

ACKNOWLEDGEMENTS 13

ABBREVIATIONS 14

CHAPTER 1 INTRODUCTION 19

1.1 Research Problem 19

1.2 Aims and Objectives 20

1.3 Research Outcomes 21

1.3.1 Research Outcomes 21

1.3.2 Publications 22

1.4 Outline of the Thesis 24

CHAPTER 2 LITERATURE REVIEW 26

2.1 Parallel Mechanisms 26

2.2 Motivation of Reconfigurable Parallel Mechanisms 29

2.3 Reconfiguration Principles 30

2.3.1 Singularity based Reconfiguration 32

2.3.2 Reconfigurable Platform based Reconfiguration 34

2.3.3 Metamorphic Parallel Mechanism Reconfiguration 35

2.3.4 Lockable Joint based Reconfiguration 37

2.4 Synthesis of Reconfigurable Parallel Mechanisms 38

2.5 Modelling of Reconfigurable Parallel Mechanisms 39

2.6 Applications of Reconfigurable Parallel Mechanisms 39

2.6.1 Reconfiguration in Manufacturing 39

2.6.2 Reconfiguration in Grasping 41

2.6.3 Reconfiguration in Mobile Robots 42
2.6.4 Reconfiguration in Automation Tasks 43
2.7 Conclusions 44
CHAPTER 3 GENERAL SYNTHESIS OF METAMORPHIC PARALLEL MECHANISMS 45
3.1 Synthesis Strategy of MPMs 45
3.2 Reconfigurable Joints 46
3.2.1 Reconfigurable Hooke (rT) Joint 46
3.2.2 Reconfigurable Revolute (rR) Joint 48
3.3 Reconfigurable Limbs 48
3.3.1 Reconfigurable Limbs with the rT Joint 49
3.3.2 A Reconfigurable Limb with the rR Joint 55
3.4 A General Synthesis Method for MPMs 57
3.4.1 A General Synthesis Method 57
3.4.2 Synthesis of a Family of Metamorphic Parallel Mechanisms With Mobility-Change Between 6-5-4-3 And with Spherical Motion at Mobility 3 60
3.5 Obtained Metamorphic Parallel Mechanisms and Comparison with Literature 65
3.6 Conclusions 67
CHAPTER 4 CONSTRAINT-PLANE-BASED SYNTHESIS AND TOPOLOGY VARIATION OF A CLASS OF MPMS 69
4.1 Two phases of the reconfigurable rT*PS* limb 69
4.2 MPMs with Two limbs 71
4.2.1 Two Intersecting Planes 72
4.2.2 Two Parallel Planes 73
4.2.3 Topology change of the 2-rTPS MPM 75
4.3 MPMs with Three Limbs 75
4.3.1 Three Parallel Planes 76
4.3.2 Two Parallel and One Intersecting Planes 80
4.3.3 Three Intersecting Planes 81
4.3.4 Topology Change of the 3-rTPS MPM 83

4.4 MPMs WITH FOUR LIMBS 85
4.4.1 Four Parallel Planes 85
4.4.2 Three Parallel Planes among the Four 85
4.4.3 Two Parallel Planes among the Four 86
4.4.4 Four Intersecting Planes 88
4.4.5 Topology Change of the 4-rTPS MPM 89
4.5 MPMs WITH FIVE LIMBS 90
4.6 MPMs WITH SIX LIMBS 92
4.7 SUMMARY OF OBTAINED NEW METAMORPHIC PARALLEL MECHANISMS 95
4.8 CONCLUSIONS 97
CHAPTER 5 SOME NOVEL MPMS AND THEIR RECONFIGURATION 98
5.1 THE 3-RTPS MPM WITH PERPENDICULAR CONSTRAINT SCREWS 98
5.1.1 Geometric Constraints of the 3-rTPS MPM 98
5.1.2 Topology Change of the 3-rTPS MPM 100
5.2 THE 4-RTPS MPM WITH BIFURCATED MOTION 102
5.2.1 Geometric Constraints of the 4-rTPS MPM 102
5.2.2 Topology Change based Reconfiguration of the 4-(rT)2PS MPM 104
5.3 THE 3-RTPRT MPM WITH PURE ROTATION AND PURE TRANSLATION 107
5.3.1 The 3-rTPrT MPM with Pure Rotation 107
5.3.2 Reconfiguration To a Pure Translational Configuration 110
5.3.3 Reconfiguration to Three Translations and One Rotation Mobility 112
5.4 THE 3-RRPS MPM WITH 3R MOTION AND 1T2R MOTION 114
5.5 CONCLUSIONS 118
CHAPTER 6 UNIFIED KINEMATICS MODELLING OF MPMS COVERING ALL PHASES 120
6.1 RELATED KINEMATICS OF PARALLEL MECHANISMS IN THE LITERATURE 120
6.2 THE PROPOSED STRATEGY AND METHOD 122
6.3 UNIFIED KINEMATICS MODELLING AND WORKSPACE ANALYSIS OF THE 3-RTPRT 122
6.3.1 Geometric Parameters and Inverse Kinematics 122
6.3.2 Forward Kinematics 125

6.3.3 Jacobian Matrix and 3D Singularity Loci 128

6.3.4 Limb actuation singularity 130

6.3.5 Forward Kinematics Solution Distribution for $\alpha'_a = \alpha'_b = Sin^{-1}(\sqrt{2/3})$ Case 131

6.3.6 Analytical Singularity-Free Workspace 133

6.4 Unified Kinematics Modelling of the 3-rTPS 136

6.4.1 Unified Geometric Constraints 136

6.4.2 Inverse and Forward Kinematics Analysis 138

6.4.3 Numerical Examples of the Kinematics Analysis 142

6.5 Unified Kinematics Modelling and Workspace Analysis of the 4-rTPS 146

6.5.1 Unified Limb Kinematics Modelling 146

6.5.2 Inverse and Forward Kinematics Analysis 148

6.5.3 Unified Singularity Modeling with Workspace Analysis 153

6.6 Unified Kinematics Modelling and Workspace Analysis of the 3-rRPS 163

6.6.1 Unified Kinematics Modelling 163

6.6.2 Singularity Loci 166

6.6.3 Singularity-Free Workspace 169

6.6.4 Parameter Effect on Maximum Singularity-Free Workspace 170

6.7 Conclusions 174

CHAPTER 7 UNIFIED KINEMATICS PERFORMANCE REPRESENTATION AND OPTIMAL DESIGN OF MPMS CONSIDERING VARIABLE WORKING PHASES 176

7.1 Optimal Design Methods of Parallel Mechanisms 176

7.2 Unified Kinematics Performance Representation 177

7.2.1 Motion/Force Transmissibility of the 3-rTPrT 178

7.2.2 Motion/Force Transmissibility of the 3-rRPS 190

7.3 Unified Optimal Design of the 3-rRPS Based on Motion/Force Transmissibility 196

7.3.1 Design Variables and Performance Indices 196

7.3.2 Optimal Design 197

7.3.3 An Optimal Design Example 199

7.4 Unified Optimal Design of the 3-rRPS Based on Jacobian Condition Number 200

7.4.1 Design Variables and Performance indices 201
7.4.2 Optimal Design 203
7.5 Prototype Design and Challenges 206
7.5.1 Prototyp Design of the 3-rTPrT 206
7.5.2 Prototyp Design of the 3-rRPS 208
7.6 Conclusions 211
CHAPTER 8 UNIFIED INVERSE DYNAMIC MODELLING OF MPMS COVERING ALL PHASES 213
8.1 Overview of the Strategy and Method 213
8.2 Unified Dynamic Modelling of the 3-rTPrT [183] 213
8.2.1 Two Phases and Coordinates of the 3-rTPrT 213
8.2.2 Velocity and Acceleration Analysis 215
8.2.3 Inverse Dynamic Analysis of the 3-(rT)*P*(rT) metamorphic parallel mechanism 217
8.2.4 Joint Force Decomposition for Decoupled Inverse Dynamics Analysis 219
8.2.5 Numerical Example and Analysis 222
8.3 Unified Dynamic Modelling of a 3-rTPS 226
8.3.1 The 3-rTPS and Its Reconfiguration 226
8.3.2 Unified Kinematics Analysis 230
8.3.3 Unified Inverse Dynamics Based Virtual Work Principle 234
8.3.4 Numerical Example 237
8.4 Applicability of the Dynamic Models 239
8.5 Conclusions 240
CHAPTER 9 CONCLUSIONS AND FUTURE WORK 242
9.1 Conclusions 242
9.2 Future Work 248
REFERENCES 251

Table of Figures

Figure 2-1 Stewart Gough Platforms 26
Figure 2-2 The 6-DOF Parallel mechanism applications 27
Figure 2-3 Commercial Delta Robots 27
Figure 2-4 The Tricept robot and a 3-RPS robot 28
Figure 2-5 Spherical parallel mechanism applications 29
Figure 2-6 Industrial need change 29
Figure 2-7 Reconfigurable Parallel Robots 30
Figure 2-8 Parallel Mechanism Reconfiguration Principles 31
Figure 2-9 Reconfiguration through reconfigurable platform 35
Figure 2-10 Link coincidence based reconfiguration 36
Figure 2-11 Reconfiguration in manufacturing 40
Figure 2-12 Reconfiguration for 3D printing [127] 41
Figure 2-13 The metamorphic anthropomorphic hand and its applications [128, 130] 41
Figure 2-14 A metamorphic rover [131] 42
Figure 2-15 The vA joint and its application in light-duty vehicle [108] 43
Figure 2-16 A hatch metamorphic mechanism [133] 43
Figure 2-17 A metamorphic repair robot for extra-high-voltage power transmission lines [134] 44
Figure 3-1 Synthesis strategy of MPMs 45
Figure 3-2 The Reconfigurable Hooke (rT) joint and its symbolic representation 47
Figure 3-3 Two phases of the rT joint 47
Figure 3-4 The reconfigurable revolute (rR) joint 48
Figure 3-5 Co-line order change 49
Figure 3-6 Co-spherical and co-planar order-change of the reconfigurable-limb twist system .. 51
Figure 3-7 A 2-stage mobility-change of a reconfigurable limb 54
Figure 3-8 The rR*PS* limb 56
Figure 3-9 The *R*(rT)*S* reconfigurable limb 62
Figure 3-10 Arrangement of constraint forces and corresponding 3*R*(rT)$_2$*S* parallel mechanism 64
Figure 3-11 The three more topological configurations of the 3*R*(rT)$_2$*S* parallel mechanism 64
Figure 4-1 Two phases of the rT*PS* limb 69

Figure 4-2 The 2(rT)$_2$*PS* parallel mechanism 71
Figure 4-3 The 2(rT)$_2$PS with parallel constraint planes 74
Figure 4-4 Two topology changes of the 2(rT)$_2$PS 75
Figure 4-5 The 3-(rT)$_2$PS with parallel constraint planes 76
Figure 4-6 Location condition of constraint plane $\sum 3$ 78
Figure 4-7 Two special topologies with parallel planes 79
Figure 4-8 The 3-(rT)$_2$PS with two parallel and one intersecting constraint planes 80
Figure 4-9 The 3-(rT)$_2$PS with three intersecting constraint planes 81
Figure 4-10 The 3(rT)$_2$PS with three parallel intersecting lines 82
Figure 4-11 The 2(rT)$_2$PS-1(rT)$_1$PS with two constraint planes 84
Figure 4-12 The 4-(rT)$_2$PS with three parallel planes 86
Figure 4-13 The 4-(rT)$_2$PS with two parallel planes 87
Figure 4-14 The 4(rT)$_2$PS with two-two parallel planes 87
Figure 4-15 The 4(rT)$_2$PS with intersecting planes 89
Figure 4-16 Topology and mobility variation map of the 4rT*PS* MPM 90
Figure 4-17 The 5-(rT)$_2$PS parallel mechanisms (1R or 1T) 91
Figure 4-18 The 6-(rT)$_2$PS structure 93
Figure 4-19 Topology change map of the 6-(rT)$_2$PS 94
Figure 5-1 The 3-(rT)$_2$*PS* with three perpendicular constraint screws 98
Figure 5-2 The 2(rT)$_2$*PS*-1(rT)$_1$*PS* with two perpendicular constraint screws 100
Figure 5-3 Two more topologies of the 3rT*PS* 101
Figure 5-4 Mobility change map 102
Figure 5-5 The 4-(rT)$_2$*PS* MPM with bifurcated motion 103
Figure 5-6 Variable topologies of the 4(rT)*PS* MPM 105
Figure 5-7 The 3-rT*P*rT with pure rotation 108
Figure 5-8 The 3-rT*P*rT with pure translation 110
Figure 5-9 The 3-rT*P*rT with 3T1R motion 112
Figure 5-10 The 3-rR*PS* Metamorphic Parallel Mechanism 114
Figure 5-11 Two topologies of the 3rR*PS* with 1T2R motion 118
Figure 6-1 The 3-rTPrT MPM with pure rotation 123
Figure 6-2 The controllable rotation center 124

Figure 6-3 Singularity Loci 129
Figure 6-4 Limb actuation singularity loci in the mechanism singularity loci (α'_a=2π/9)..... 131
Figure 6-5 Assembly zones of the 3-rTPrT with orthogonal base and platform 132
Figure 6-6 Workspace boundaries (α'_a=π/6) 135
Figure 6-7 Workspace boundaries with different rotation centers 136
Figure 6-8 Unified modelling of the rTPS limb 137
Figure 6-9 Unified kinematics modelling of the 3rT*PS* with perpendicular constraint screws .. 138
Figure 6-10 The platform coordinate system 139
Figure 6-11 Mechanism assemblies corresponding to the real solutions in Table 4-4..... 145
Figure 6-12 The 4-rT*PS* MPM..... 146
Figure 6-13 Unified limb modelling 147
Figure 6-14 Workspace and singular configurations of 4-$(rT)_2$*PS* 156
Figure 6-15 Workspace and singularity locus of the 3$(rT)_2$*PS*-1$(rT)_1$*PS*..... 157
Figure 6-16 Singularity 5 159
Figure 6-17 Singularity 6 in two different configurations..... 160
Figure 6-18 Unified kinematics modelling of the 3-rT*PS* with perpendicular constraint screws 164
Figure 6-19 Singularity loci and two singular configurations of the 1T2R case (θ_1= θ_2= θ_3=0) 168
Figure 6-20 Singularity loci of topologies with 3R motion 169
Figure 6-21 Workspace of different topologies 170
Figure 6-22 Maximum singularity-free workspace volume and the limb length range 172
Figure 6-23 Maximum singularity-free workspace volume and the base radius r_b 173
Figure 6-24 Maximum singularity-free workspace volume and the base radius r_a 174
Figure 7-1 Four different rotation centers 186
Figure 7-2 Variable transmission indices and singularity loci of the pure translation motion ... 188
Figure 7-3 Variable transmission indices and singularity loci of the pure rotation motion 190
Figure 7-4 Variable Transmission Indices and Singularity Loci 195
Figure 7-5 Optimal Design Results 199
Figure 7-6 An example with λ_a=0.4 (solid for workspace, dashed for transmission, green: 0, blue: π/6, red: π/3, purple: π/2) 200
Figure 7-7 Optimal design of the 3-rR*PS* MPM (blue for λ_a=0.3, green for λ_a=0.5, yellow for λ_a=0.8, red for λ_a=1) 204

Figure 7-8 Prototye design of the rT joint 207
Figure 7-9 Prototype of the 3-rTPrT 207
Figure 7-10 Prototype of the rR joint 208
Figure 7-11 Prototype of the 3-rRPS metamorphic parallel mechanism 209
Figure 7-12 Joint clearance and motion tracking setup 210
Figure 7-13 Platform motion error after locking all the three actuators 210
Figure 7-14 Bevel gear based synchronized rR joint solution 211
Figure 8-1 The pure rotation phase of the 3-rT*P*rT and its coordinate frames 213
Figure 8-2 The pure translation phase of the 3-rT*P*rT 214
Figure 8-3 Limb coordinate frame and parameters 215
Figure 8-4 A limb coordinate frame to simplify the joint force decomposition 221
Figure 8-5 Simulation results for the pure rotation phase 223
Figure 8-6 Simulation results for the pure translation phase 225
Figure 8-7 Two phases of the rT*PS* limb 227
Figure 8-8 The 3-$(rT)_2$*PS* metamorphic parallel mechanism 228
Figure 8-9 Variable topologies of the 3-(rT)*PS* 229
Figure 8-10 Simulation results 238

Table of Tables

Table 3-1 The 1-stage reconfigurable limbs 52

Table 3-2 The 2-stage reconfigurable limbs 55

Table 3-3 Reconfigurable limbs for the spherical motion 61

Table 3-4 Summary of Obtained Metamorphic Parallel Mechanisms 66

Table 4-1 Summary of Obtained Metamorphic Parallel Mechanisms 95

Table 5-1 Variable Topologies and mobility of the 4-rTPS 107

Table 6-1 References of Kinematics Analysis 121

Table 6-2 FK solutions and zones 133

Table 6-3 Inverse kinematics examples 142

Table 6-4 Forward kinematics solutions of 3-$(rT)_2PS$ 143

Table 6-5 Real solutions of forward kinematics 144

Table 6-6 Workspace and singularity loci of the 2$(rT)_2PS$-2$(rT)_1PS$ 161

Table 6-7 Workspace and singularity loci of the 1$(rT)_2PS$-3$(rT)_1PS$ 162

Table 6-8 Workspace and singularity loci of the 4$(rT)_1PS$ 162

Table 8-1 Numerical example parameters 222

Table 8-2 Parameters of the 3-(rT)PS 237

Acknowledgements

I would like to express my deepest gratitude to my supervisor and mentor, Prof. Jian Dai, for his invaluable guidance and support not only on my PhD study but also on my research and academic career. Without him, this PhD would not be completed in a so efficient way and I could not achieve those research outcomes.

I would also like to sincerely thank my co-supervisor, Prof. Lakmal Seneviratne, for his continuous support on my PhD study and academic work. The recommendation and support for this study from Prof. Qizheng Liao is also much appreciated.

I'm grateful to my colleagues and friends, Dr. Ketao Zhang, Dr. Guowu Wei, Dr. Xinsheng Zhang, Dr. Jie Sun, Dr. Chin-Hsing Kuo, Mr. Peng Cheng, and Mr. Yuanqing Yang for their valuable research discussions, kind friendship, and help during this PhD study.

At last, I'm deeply thankful to my wife, Shuiping Qi, for her encouragement and huge support on the life. I would like to thank my parents and all other family members for their continuous care and support.

Abbreviations

Abbreviation	Meaning
${}^1\boldsymbol{S}_1^r$	Reciprocal screw in the local frame 1
$\boldsymbol{a}_i'$	the position vector of spherical joint center A_i in the moving coordinate system *Quvw*
$\boldsymbol{m}_{12}'$	the unit vector of line A_1A_2 expressed in the moving coordinate system
$\dot{d}_i$	the input velocity of limb *i*
$\boldsymbol{S}_{i1}^r$	the reciprocal screws of geometric constraint to all motion screws in limb *i* in phase $(rT)_2PS$
$\boldsymbol{S}_{i2}^r$	the actuation screw reciprocal to all twists in the limb except the prismatic joint screw
$\boldsymbol{s}_{j1}^r$	the reciprocal screws of geometric constraint to all motion screws in limb *j* in phase $(rT)_2PS$
$\dot{\phi}_{ij}$	angular rates of the rR joint and spherical joint in limb *i*
λ_{Ci}	the constraint transmission power coefficient
γ_{OC}	the constraint transmission index
λ_{Ti}	the output transmission power coefficient
γ_O	The output transmission index
${}^i\boldsymbol{\omega}_i$	the *i*th limb angular velocity
$\dot{d}_i$	the *i*th limb linear velocity
${}^i\boldsymbol{s}_i$	the unit vector of the limb in its own coordinate frame
$\dot{\boldsymbol{v}}_{ai}$	the acceleration of the platform rT joint center A_i in the base frame
$\ddot{d}_i$	the *i*th limb linear acceleration
${}^i\dot{\boldsymbol{\omega}}_i$	the *i*th limb angular acceleration
${}^i\boldsymbol{n}_i^B$	the resultant moment exerted on the *i*th limb about the center B_i
${}^i\boldsymbol{h}_i^B$	the combined angular momentum of the *i*th limb about the center B_i
${}^i\boldsymbol{f}_{ai} = ({}^i f_{aix}, {}^i f_{aiy}, {}^i f_{aiz})^T$	the joint force at the platform rT joint center A_i
${}^i\boldsymbol{M}_{ai} = M_{ai}\,{}^i\boldsymbol{n}_{ai}$	the joint moment at the platform rT joint center A_i with magnitude M_{ai} and direction ${}^i\boldsymbol{n}_{ai}$
$\dot{\boldsymbol{v}}_p$	the platform linear acceleration
$\boldsymbol{\omega}_p$	the platform angular velocity
$\dot{\boldsymbol{\omega}}_p$	the platform angular acceleration
$\boldsymbol{S}_{aO} = [\dot{\boldsymbol{\omega}}_o \quad \dot{\boldsymbol{v}}_o - \boldsymbol{\omega}_o \times \boldsymbol{v}_o]$	the accelerator
$\dot{\boldsymbol{\omega}}_o$	the angular acceleration of the platform
$\dot{\boldsymbol{v}}_o$	the translational acceleration of the point on the moving platform and coincides with *O*
δW	The virtual work
$(\bullet)^T$	the transpose of vector/matrix
$(rT)_i$	The rT joint in phase *i*, *i*=1,2
(x, y, z)	The coordinate of a 3D point
${}^i\boldsymbol{v}_{1i}$, ${}^i\boldsymbol{v}_{2i}$	the velocities of the centers of mass of the cylinder and piston

${}^{i}\dot{\boldsymbol{v}}_{1i}$, ${}^{i}\dot{\boldsymbol{v}}_{2i}$	the accelerations of the centers of mass of the cylinder and piston
${}^{i}\mathbf{I}_{1i}$, ${}^{i}\mathbf{I}_{2i}$	the inertias of the cylinder and piston expressed in the limb coordinate frame
$\boldsymbol{S}'_{1\mathrm{rT}}$	the bracket axis twist of the second rT joint in the limb
$\boldsymbol{S}'_{2\mathrm{rT1}}$	the radial axis twist of the second rT joint in phase 1
$\boldsymbol{S}'_{2\mathrm{rT2}}$	the radial axis twist of the second rT joint in phase 2
[ ]	to list the options for the joints in a limb
[* *]	the Lie product
{$\boldsymbol{S}_i$}	the limb twist-system when the rT joint is in phases i, i=1 or 2
{$\boldsymbol{S}_{ij}$}	the limb twist system with the two rT joints in phase i and j, (i,j=1,2).
$\sum i$	plane i
$\angle A_2A_1A_3$	angle between lines A_2A_1 and A_1A_3
0	a 1×3 zero vector
${}^{1}o{}^{1}x{}^{1}y{}^{1}z$	limb coordinate system
${}^{1}\boldsymbol{S}_{ij}$	the first subscript i denotes the limb number, the second subscript j denotes the joint number within the limb and the leading superscript indicates the local frame
$2R_{xy}$	two rotations about x-axis and y-axis
$\boldsymbol{a}$	the position vector of the spherical joint centre
A	the spherical joint center
A_i	the center point of the spherical joint in limb i
$\boldsymbol{a}_{Pcm}$	the translational acceleration of the center of mass of the platform
a_y	y components of the unit vector for point A
B	the base joint center
$\boldsymbol{b}$	the vector of point B in the $oxyz$ coordinate system
B_i	the rT joint center in limb i
C	cylindrical joint
c_1, c_2 and c_3	the Rodriguez-Hamilton parameters
CTI	the constraint transmission index
d	the distance from the coordinate system center o to plane $\sum$
D	the Dixon matrix
d_i	the distance from coordinate center o to the plane $\sum i$
dim(·)	the order of a screw system
DOF	degree of freedom
$d_{Oi\max}$	the maximum distance between two screws
e_1	the distance between base rT joint center B_i and the center of mass of the ith limb cylinder
e_2	the distance between platform rT joint center A_i and the center of mass of the ith limb piston
$f(\cdot)$	a function of unknown power products in the bracket
$\boldsymbol{f}_P$, $\boldsymbol{\tau}_P$	the external force and torque applied to the center of mass of the platform
$\boldsymbol{g}=(0,0,-g)^{\mathrm{T}}$	the acceleration of gravity in the base coordinate system
h	housing ring
$\mathbf{I}_{li}$, $\mathbf{I}_{ui}$	the inertia matrices of the lower limb and upper limb in limb i
$\mathbf{I}_P$	the inertia matrix of the platform
$\mathbf{I}pc$	the inertia matrix of the platform expressed in its principal coordinate frame at the center of mass
${}^{i}\boldsymbol{v}_{ai}$	the velocity of the platform rT joint center A_i in the ith limb coordinate system
J	the Jacobian matrix

$\mathbf{J}_{a3R}$	the Jacobian matrix of the pure rotation phase of the 3-rRPS MPM
$\mathbf{J}_{\mathrm{D}}$	the 3×3 dimensional homogeneous Jacobian matrix with unified unit
$\boldsymbol{J}_i = (J_{i1}, J_{i2}, J_{i3})$	the ith row vector of the Jacobian matrix
$\boldsymbol{k}(kx, ky, kz)$	unit vector of an axis
$k_{3\mathrm{R}}$, $k_{1\mathrm{T2R}}$	the inverse averaged condition numbers in 3R and 1T2R phases
k_i	the number of i-stage reconfigurable limbs
k_i	the condition number of the Jacobian matrix
l	the length between the spherical joint and rT joint centres
l_{12}	the distance between points A_1 and A_2
$l_{i\max/\min}$	the maximum and minimum linear actuation input limit
link b	link bracket
link g	link groove
l_{iq}	the distance from point A_i to the moving coordinate center Q
m_1, m_2	the masses of the cylinder and piston
m_p	the mass of the platform
MPMs	metamorphic parallel mechanisms
$m\mathrm{T}n\mathrm{R}$	represents DOFs with m translations (T) and n rotations (R)
$\boldsymbol{n}$	the normal vector of a plane
$\boldsymbol{n}_0$	unit vector of a reference line
$\boldsymbol{n}_i$	the normal vector of plane i
N_{lim1}	limb mobility
N_m	the maximum mobility of the platform
$n\mathrm{T}_{xz}$, $n\mathrm{T}_{yz}$	indicate n translations along the corresponding axes in the subscripts
$o'x'y'z'$	a moving coordinate system attached at the platform center o'
OTI	the output transmission index
$oxyz$	a fixed coordinate system
P	prismatic joint
$\$_p(*)$, $\$_d(*)$	the primary part and dual part of the screw
$\boldsymbol{p} = (p_x, p_y, p_z)^{\mathrm{T}}$	the translation vector of platform coordinate system $Guvw$ with respect to the fixed coordinate system $Oxyz$
$\boldsymbol{q}$	vector of the moving coordinate center Q expressed in the fixed coordinate system $oxyz$
$Quvw$	moving coordinate system
R	revolute joint
$\mathbf{R}(k, g)$	a rotation matrix about axis k with angle g
$\mathbf{R}=[\boldsymbol{u}, \boldsymbol{v}, \boldsymbol{w}]$	the rotational matrix from the local coordinate system to the fixed coordinate system
$\mathbf{R}_0$	the input orientation matrix in the numerical example
r_{1i}	the position vector of the center of mass of the ith cylinder
r_{2i}	the position vector of the center of mass of the ith piston
r_a	radius of the base circle on which the limbs are arranged symmetrically
r_b	radius of the platform circle on which the limbs are arranged symmetrically
$\boldsymbol{r}_c$	the vector of the center of mass of the platform in the base coordinate frame
rR	reconfigurable revolute joint
$\acute{R}\acute{R}\acute{R}$	three revolute joints intersecting at one point
rT	reconfigurable Hook joint
S	spherical joint
$\boldsymbol{s}$	the unit vector along the limb
$\boldsymbol{S}_{1\mathrm{rT}}$	the twist of the bracket axis of the rT joint
$\boldsymbol{S}_{2\mathrm{rT1}}$	the twist of the radial axis of the rT joint in phase 1

$\boldsymbol{S}_{2rT2}$	the twist of the radial axis of the rT joint in phase 2
$\boldsymbol{S}_{Ci}$	the constraint wrench screw
$\boldsymbol{S}_{G}$	the infinitesimal twist of the moving platform
S_{ij}	the unit vector of the joint axis *j* in limb *i*
$\boldsymbol{S}_{Lie\text{-}i}$	the *Lie screw* in the *i*th limb
$\boldsymbol{S}_{Oi}$	the output twist screw
SPMs	spherical parallel mechanisms
$\boldsymbol{S}_{R1}$	the twist of the extra rotational joint
$\boldsymbol{S}_{Ti}$	the transmission wrench screw
$\boldsymbol{S}_{VO}$	the velocity twist of the moving platform
t	the total number of reconfigurable limbs
t_i	Tan(α_i/2)
U	universal joint
$\boldsymbol{u}$	unit vector of the revolute joint axis
$\boldsymbol{u}$, $\boldsymbol{v}$, $\boldsymbol{w}$ $u=(u_x, u_y, u_z)^T$, $v=(v_x, v_y, v_z)^T$, $w=(w_x, w_y, w_z)^T$	the unit vectors of the moving coordinate system axes expressed in the fixed coordinate system *oxyz*
u, w	x and z components of the unit vector of the revolute joint
$\boldsymbol{u}_i$	the rotation axis of the rR joint in limb *i*
V	maximum singularity-free workspace volume
V_{3R}, V_{1T2R}	normalized workspace volume in 3R and 1T2R phases
vA	variable axis joint
$\boldsymbol{v}_{ai}$	the velocity of the platform rT joint center A_i in the base coordinate system
v_i	the linear velocity along $\boldsymbol{n}$ at the selected point
$\boldsymbol{v}_o$	the linear velocity twist of the platform
$\boldsymbol{v}_p$	the platform linear velocity
$\boldsymbol{v}_p=[v_1, v_2, v_3]^T$	the linear velocity vector of selected points on the platform
W	total power performed by the mechanism system forces
w_1,w_2	the weights of the 3R topology and the 1T2R topology in the optimal design objective function
w_{i1}, w_{i2}	the weights for maximum singularity-free workspace and kinematics performance of each topology
$\underline{XXX}$	an equivalent planar joint formed by three 1-DOF joints, *X* represents an revolute joint or a prismatic joint
α	the angle between $\boldsymbol{S}_3$ and x_1,
α'_a	the angle between the radial axis of the platform rT joint and the *z*-axis after reconfiguration
α'_b	the angle between the radial axis of the base rT joint and the *z*-axis after reconfiguration
α_a	the initial angle between the radial axis of the platform rT joint and the *z*-axis
α_b	the initial angle between the radial axis of the base rT joint and the *z*-axis
β	the angle between two vectors
β_{12}	the angle between A_1A_2 and $\boldsymbol{n}_1$
Δh	the distance between *O* and *O*'
θ	the angle between revolute joints 1 and 2
λ_a	the ratio between the platform and base sizes
λ_{lmin}	the ratio of the minimum limb length over the base size
Σ	a plane
σ_{max}, σ_{min}	the maximum and minimum singular values of the Jacobian matrix

φ_1	the platform angle $A_2A_1A_3$
ϕ_1	radial axis angle of the rT joint
ϕ_2	bracket axis angle of the rT joint
$\phi_{i\max/\min}$	the maximum or minimum input angle limit
ψ_i	passive joint angles in optimal design process
$\boldsymbol{\omega}$	the platform orientation velocity
$\boldsymbol{\omega}_o$	the angular velocity twist of the platform

Chapter 1 Introduction

1.1 Research Problem

Parallel mechanisms have been successfully applied as tire test machine [1], industry assembly tools [2], manufacturing center [3], force transducer [4], rehabilitation platform [5] and robotics surgery instrument [6] based on their high load-carrying capacity, good positioning accuracy and low inertia [7] stemmed from their multi-loop geometric structures [8]. Due to fast task change with variable mobility requirements, like rapid customization and diverse environment changing [9], rehabilitation and surgery of different human joints, parallel mechanisms which are reconfigurable have attracted much interest from mechanism researchers. Based on this, metamorphic parallel mechanisms (MPMs) [10], which are a class of mechanisms that possess adaptability and reconfigurability to change permanent finite mobility based on topological structure change, were introduced.

Each phase of a metamorphic parallel mechanism is the same with a traditional parallel mechanism. Thus metamorphic parallel mechanisms can replace traditional ones in real applications with benefits of configuration change for workspace requirements and operation mobility change with energy saving. For example, in industrial machining, various parts from simple to complex shapes require cutting tools have mobility from 1 to 6. The metamorphic parallel mechanisms to be synthesized in this paper can adapt to these requirements by reconfiguring the mechanism to the corresponding mobility instead of using a 6-degree-of-freedom (DOF) one to cover all cases, helping ease the control, maintain high precision and save energy.

Thus, metamorphic parallel mechanisms have all the advantages of traditional parallel mechanisms but with ability of reconfiguring for mobility change. However, the research of metamorphic parallel mechanisms is still at the early stage which is lack of a systematic synthesis and design method and unified modelling theories to cover all configuration topologies. This study will focus on this topic to make progress on design and unified kinematics and dynamics modelling of metamorphic parallel mechanisms to provide foundations for their applications.

1.2 Aims and Objectives

This research aims at providing the fundamental theories of mechanisms and machines with focus on synthesis, design, kinematics, and dynamics of metamorphic parallel mechanisms which are a new class of reconfigurable parallel mechanisms. The research goal is to develop new mehtods in synthesizing metamorphic parallel mechanisms and modelling their variable topologies in a unified way for applying them in various applications. The detailed research aims and objectives cover the following two parts:

(1) Systematic Methods of Synthesizing and Designing Metamorphic Parallel Mechanisms

a) To propose a general strategy on synthesis of metamorphic parallel mechanisms. Case-by-case MPMs have been proposed and studied in the literature but a general strategy has not been presented. To develop this class of reconfigurable parallel mechanisms, a clear general strategy is expected to guide this topic;

b) To propose and formulate a systematic synthesis procedure for metamorphic parallel mechanisms. Based on the above strategy, a more detailed guideline is needed to implement it and to synthesize new metamorphic parallel mechaisms. This will be a key topic in the research since this is the step to conduct detailed synthesis by modelling the required geometric constraints and output motion requirements to obtain possible new mechanisms;

c) To synthesize some novel metamorphic parallel mechanisms and model their reconfiguration. Following the above synthesis method, many metamorphic parallel mechanisms are expected but novel ones with more potential use in applications need to be found and analysed in details of their reconfiguration and mobility change;

d) To propose unified performance representation for designing metamorphic parallel mechanisms considering all their working phases. For selected novel metamorphic parallel mechanisms, their kinematics performance representation is one of the important topics for real system design and applications. Since each phase of a metamorphic parallel mechanism is equivalent to a traditional parallel mechanism, the performance representation should cover all phases in a systematic way which is a challenge to be solved in this work;

e) To propose unified optimal design method for metamorphic parallel mechanisms covering all the working phases. The aim to develop new metamorphic parallel mechanisms is to satisfy variable applications for which a very necessary and important step is optimal design. Based on the performance representation, different optimal designs could be conducted for selected metamorphic parallel mechanisms targeting maximized performance;

(2) Unified Kinematics and Dynamics Modelling of Metamorphic Parallel Mechanisms

f) To propose a general strategy on unifying the kinematics modelling of the metamorphic parallel mechanisms by covering all their working phases with variable mobility. The kinematics analysis of metamorphic parallel mechanisms need to solve all phases with different mobility and motion types in a systematic way which is equivalent to solve a few parallel mechanisms at the same time. This is a challenge topic and the basis for futher mechanism analysis, design and applications;

g) To work out kinematics modelling in a unified way of some representative metamorphic parallel mechanisms. This is to find and model some novel and representative metamorphic parallel mechanisms with common used motion types, for example, pure rotation, pure translation, 2R1T motion, etc;

h) To solve dynamic modelling of the selected metamorphic parallel mechanisms to provide unified modelling reference for similar mechanisms. Following the kinematics analysis, unified dynamic modelling of all the phases is another fundamental step and also challenge in the development of mechanism control and application.

1.3 Research Outcomes

1.3.1 Research Outcomes

Following the research plan, this research has achieved the aims and objectives in Section 1.2 considering the two major parts:

(1) Systematic Methods of Synthesizing and Designing Metamorphic Parallel Mechanisms: A general strategy using reconfigurable joint has been proposed on synthesizing

metamorphic parallel mechanisms and a general synthesis procedure has been provided based on screw theory. Two reconfigurable joints are developed and some novel metamorphic parallel mechanisms have been obtained using the proposed method and their reconfiguration has been modelled. Motion/force transmissibility is proposed to unifying the performance representation for optimal design of metamorphic parallel mechanisms considering all working phases and performance in each phase.

(2) Unified Kinematics and Dynamics Modelling of Metamorphic Parallel Mechanisms: Unified strategies have been proposed by modelling the metamorphic parallel mechanisms from their limbs considering the reconfiguration of the joint and by taking the reconfigured phases as special cases of the general configuration. Since each reconfigured phase of a metamorphic parallel mechanism is equivalent to a traditional parallel mechanism, the proposed method can solve all the phases in the unified format. Some selected metamorphic parallel mechanisms have been studied and their unified kinematics and dynamics modelling are provided.

1.3.2 Publications

Since the start of this study, the above results have been achieved and presented by five journal and five international conference publications as below.

1. D. M. Gan, J. S. Dai, Jorge Dias, and L. D. Seneviratne, “Variable Motion/Force Transmissibility of a Metamorphic Parallel Mechanism with Reconfigurable 3T and 3R Motion”, ***Transactions of the ASME: Journal of Mechanisms and Robotics***, 8(5), 2016, 051001_1-9.
2. D. M. Gan, Jorge Dias, and L. D. Seneviratne, “Unified Kinematics and Optimal Design of a 3-rRPS Metamorphic Parallel Mechanism with a Reconfigurable Revolute Joint”, ***Mechanism and Machine Theory***, 2016, 96 (part 2), pp. 239-254.
3. D. M. Gan, J. S. Dai, Jorge Dias, and L. D. Seneviratne, “Joint force decomposition and variation in unified inverse dynamics analysis of a metamorphic parallel mechanism”, ***Meccanica***, 2016, 51(7), 1583-1593.
4. D. M. Gan, J. S. Dai, Jorge Dias, and L. D. Seneviratne, “Forward Kinematics Solution Distribution and Analytic Singularity-Free Workspace of Linear-Actuated Symmetrical Spherical Parallel Manipulators”, ***Transactions of the ASME: Journal of Mechanisms and Robotics***, 7(4), 2015, pp. 041007_1-8.

5. D. M. Gan, J. S. Dai, Jorge Dias, and L. D. Seneviratne, “Constraint-Plane-Based Synthesis and Topology Variation of A Class of Metamorphic Parallel Mechanisms”, ***Journal of Mechanical Science and Technology***, 28(10), 2014, pp. 4179-4191.
6. D. M. Gan, J. S. Dai, Jorge Dias, and L. D. Seneviratne, “Optimal Design of of a Metamorphic Parallel Mechanism with Reconfigurable 1T2R and 3R Motion Based on Unified Motion/Force Transmissibility”, *Proceedings of the ASME 2016 International Design Engineering Technical Conferences & Computers and Information in Engineering Conference*, Charlotte, North Carolina, USA, August 21-24, 2016.
7. D. M. Gan, J. S. Dai, Jorge Dias, and L. D. Seneviratne, “Variable Motion/Force Transmissibility of a Metamorphic Parallel Mechanism with Reconfigurable 3T and 3R Motion”, *Proceedings of the ASME 2015 International Design Engineering Technical Conferences & Computers and Information in Engineering Conference*, Boston, USA, August 2-5, 2015.
8. D. M. Gan, J. S. Dai, Jorge Dias, and L. D. Seneviratne, “Reconfiguration and Static Joint Force Variation of a 3rRPS Metamorphic Parallel Mechanism with 3R and 1T2R Motion”, *Proceedings of the IEEE/IFToMM International Conference on Reconfigurable Mechanisms and Robots*, Beijing, China, July 20-22, 2015.
9. D. M. Gan, J. S. Dai, Jorge Dias, and L. D. Seneviratne, “Unified Kinematics Analysis and Analytic Singularity-Free Workspace of a Metamorphic Parallel Mechanism with Controllable Rotation Center”, *Proceedings of the ASME 2014 International Design Engineering Technical Conferences & Computers and Information in Engineering Conference*, Buffalo, USA, August 17-20, 2014.
10. D. M. Gan, J. S. Dai, Jorge Dias, and L. D. Seneviratne, “Joint Force Decomposition and Variation in Unified Inverse Dynamics Analysis of a Metamorphic Parallel Mechanism”, *The 2014 Workshop on Fundamental Issues and Future Research Directions for Parallel Mechanisms and Manipulators*, Tianjin, China, July 7-8, 2014.

1.4 Outline of the Thesis

This thesis is organized in the following nine chapters.

Chapter 1 gives the general introduction of the research background, motivation, research problem, research aims and objectives, research outcomes, and the thesis structure of this study.

Chapter 2 introduces the detailed literature review on state-of-the-art of reconfigurable parallel mechanisms and their synthesis, design, kinematics and dynamics modelling. This provides the basis of the needs of a systematic study of the metamorphic parallel mechanisms as a class of new reconfigurable parallel mechanisms and the novelty of this work.

Chapter 3 presents the proposed general strategy on synthesis of metamorphic parallel mechanisms by using reconfigurable joints to construct reconfigurable limbs. Two developed reconfigurable joints are introduced and many reconfigurable limbs are numerated based on three reconfigurable units. A general synthesis method is proposed and formulated using screw theory with detailed procedures. Based on this a family of metamorphic parallel mechanisms with mobility-change between 6-5-4-3 and with spherical motion at mobility 3 is synthesized.

Chapter 4 investigates various topologies and mobility of a class of metamorphic parallel mechanisms synthesized with the reconfigurable rTPS limb. While in one phase the limb has no constraint to the platform, in the other it constrains the spherical joint center to lie on a plane which is used to demonstrate different topologies of the *n*-rTPS metamorphic parallel mechanisms. Geometric constraint equations of the platform rotation matrix and translation vector are set up based on the pointplane constraint, which reveals mobility and redundant geometric conditions of the mechanism topologies.

Chapter 5 follows the previous two chapters by selecting some novel metamorphic parallel mechanisms and investigating their mobility change and reconfiguration in details. This also provides the basis for further kinematics and dynamics analysis in the following chapters.

Chapter 6 shows the general strategy of unifying the kinematics modelling of metamorphic parallel mechanisms by considering the reconfigured phases of the mechanism with lower DOF as a special case of the phases with higher DOF. Unified kinematics modelling, singularity analysis and workspace representation are illustrated on some selected novel metamorphic parallel mechanisms.

Chapter 7 follows the unified kinematics analysis and proposes the unified kinematics performance representation using motion/force transmissibility to cover all phases of the metamorphic parallel mechanisms. Based on this, optimal design is conducted on a selected metamorphic parallel mechanism and a weighted method is also introduced to set weight on different design objectives and weight on different working phases of the metamorphic parallel mechanism.

Chapter 8 discusses the unified dynamic modelling of metamorphic parallel mechanisms considering all working phases. Since all phases share the same mechanical structure and physical properties, the major part of the dynamic models are the same for them but with different constraints and input-output relations. Unified dynamic modelling of selected metamorphic parallel mechanisms are explained and comparisons are made between different phases in terms of actuation input and joint force reaction.

Chapter 9 concludes the thesis by summarizing the main content and contribution of this study and suggests future research directions on the related topics.

Chapter 2 Literature Review

2.1 Parallel Mechanisms

Parallel mechanisms can date back to 1928 when James E. Gwinnett designed an entertainment platform used an actually spherical parallel mechanism [11, 12]. He then got the first parallel mechanism patent in 1931. Three years later in 1934, Pollard Jr. filed a patent on spray painting machine based on a two-limb parallel mechanism [13]. In 1947, Gough invented the famous octahedral hexapod parallel mechanism used for tire testing [1] and the platform started functional in 1954 as in Fig. 2-1(a) and was used until 2000. It was found Klaus Cappel built the first flight simulator using the octahedral arrangement of a parallel mechanism in the beginning of 1960s [14]. After that, the most famous paper on parallel mechanisms was published in 1965 by Stewart [15] who proposed to use the parallel mechanism for flight simulator as in Fig. 2-1(b). The successful industry use of Gough's hexapod and the huge academic impact of Stewart's paper led to the use of "Stewart-Gough platform" to represent parallel mechanisms.

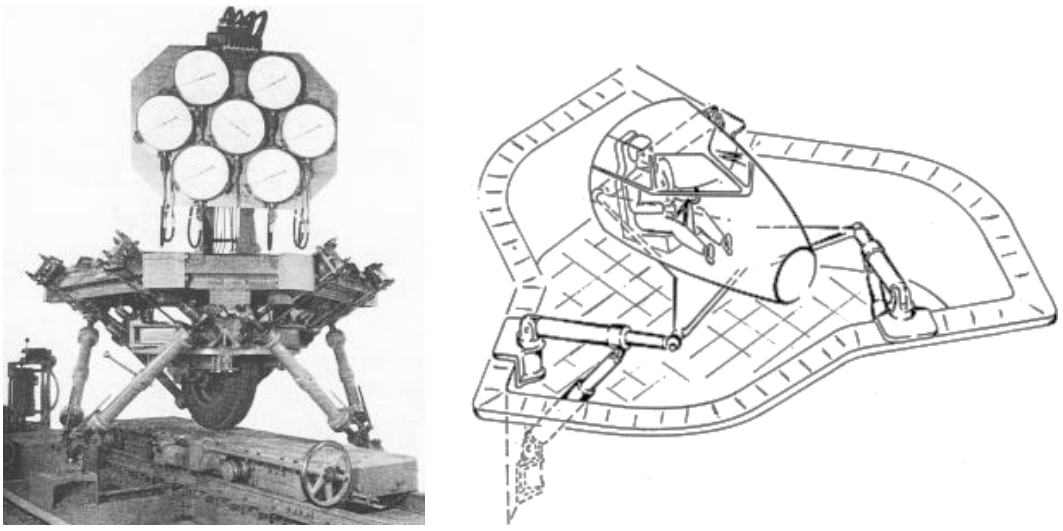

(a) Gough tire testing machine [11] (b) Stewart flight simulation concept [15]

Figure 2-1 Stewart Gough Platforms

Since then, parallel mechanisms have been widely studied in the past decades [16-24]. The general Stewart-Gough platform has six degrees of freedom and leads to many variants. Interest has been shown in their stiffness [25], workspace [26, 27], kinematics [28, 29], and dynamics [30, 31] in the early stage with applications on manufacturing [3], force sensing [4] in

Fig. 2-2(a), rehabilitation [5] and robotics surgery [6] as in Fig. 2-2(b). Later, because of the advantage of simpler forward position analysis, mechanical assembly, larger workspace, simpler singularity and control, and wider applications in industries, parallel mechanisms with less than six degrees of freedom attracted much interest [32-38].

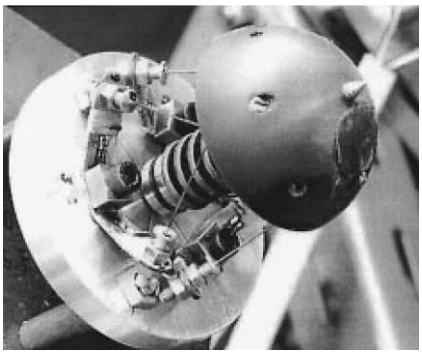

(a) Force transducer [4]

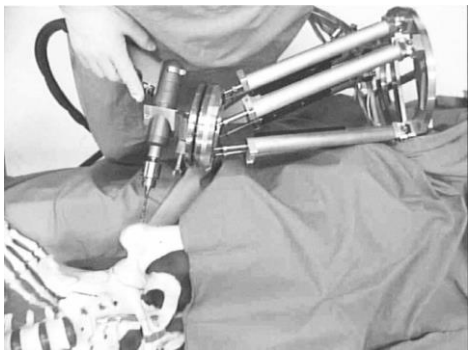

(b) Robotics surgery [6]

Figure 2-2 The 6-DOF Parallel mechanism applications

One of the most popularly used parallel mechanisms with less than six DOFs is the Delta mechanism [39] which has three translational DOFs with very simple limb structure. It was developed in the early 1980s and has been commercialized by some major robot companies, like ABB [40] and FANUC [41]. Its kinematics and dynamics performance has also been comprehensively investigated [42, 43], based on which some variants [44, 45] were developed looking at some specific performance improvement.

(a) ABB IRB 360 robot [40]

(b) FANUC delta robot [41]

Figure 2-3 Commercial Delta Robots

Another successfully applied parallel mechanism is the Tricept type [46, 47] mainly in manufacturing for high precision drilling and machining as in Fig. 2-4(a). This mechanism has two rotation and one translation DOFs which is one of the most studied motion types of parallel mechanisms as the tilting motion about lines on a plane and the translation perpendicular to the plan are commonly needed in the machining tasks. Another representative parallel mechanism having this motion type is the famous 3-RPS parallel mechanism proposed by Hunt [17] and has been researched a lot and applied in many applications [48-52] as in Fig. 2-4(b).

(a) The Tricept robot [53]

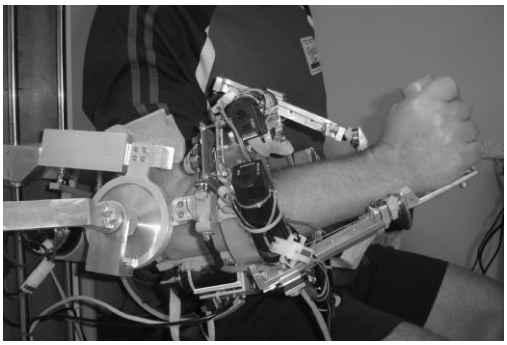

(b) MAHI Exo II [52]

Figure 2-4 The Tricept robot and a 3-RPS robot

Another popular motion type of parallel mechanisms is the pure-rotation motion represented by spherical parallel mechanisms, like the well designed and studied Agile eye [54]. Generally there are two types of SPMs [55]: (a) over-constrained (represented by 3-RRR [54]) and (b) non-over-constrained (represented by 3SPS-1S [56-58] and 3-UPU [59-61]). Spherical parallel mechanisms have attracted much interest in the mechanisms research community due to their usefulness in real applications and ability to provide decoupled rotations. Novel applications of SPMs include camera orienting devices [54], robotic wrists [62-64], shoulders [65] and hips [66], robotic palm [67, 68], robotic surgery [69, 70], and human joint rehabilitation [71].

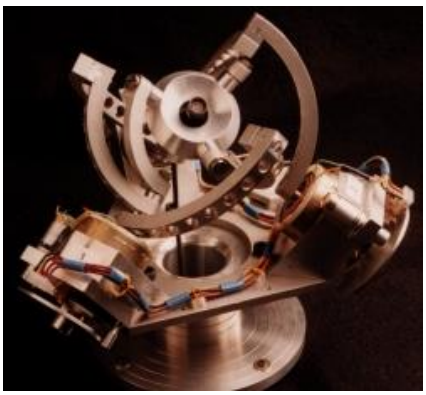

(a) The Agile eye [54]

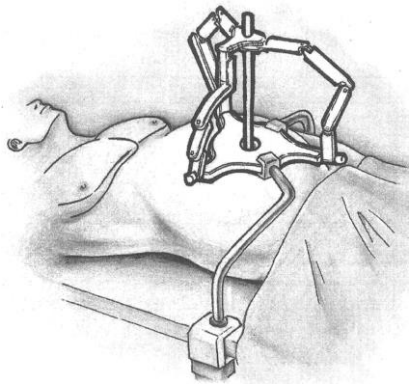

(b) A spherical manipulator for surgery [70]

Figure 2-5 Spherical parallel mechanism applications

Thus, parallel mechanisms with less than six DOFs are preferred due to their advantages stated above. However, they normally have fixed number of DOFs and motion types once designed. To meet the changing market requirements, there is a desired target to generate a parallel mechanism with changed mobility based on the same design. This results in the development of reconfigurable parallel mechanisms that can reconfigure their mobility and motion types.

2.2 Motivation of Reconfigurable Parallel Mechanisms

Based on the 2016 US Robotics Road Map of Robot in Manufacturing section [72]:

5/10/15 years goal: Achieve ability to set up, configure and program basic assembly line operations for new products with a specified industrial robot arm, tooling and auxiliary material handling devices in under **24/8/1** hours.

This reflects the current industry is moving from the traditional mass product case to one-off product system with rapid customized production change (Fig.2-6).

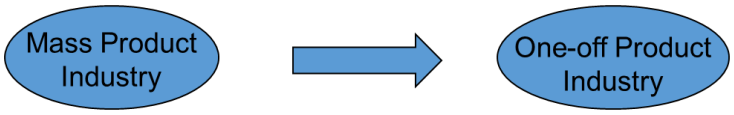

Figure 2-6 Industrial need change

For parallel robot systems, less than six DOFs are showing simpler design, modeling and control with better performance including large workspace, good accuracy and low energy

consumption. Since traditional parallel robots have fixed structure and mobility, they are normally designed for fixed application or for a class of applications with similar motion requirements. Based on this and the changing industry needs, parallel mechanisms that can reconfigure into different mobility and output motion with less than six DOFs are expected. For example in Fig. 2-7, there is the 3-DOF translational Delta robot and the Agileye pure rotation parallel robot which can work on two comlete different tasks with pure translation end-effector motion or pure orientation motion. But the two cannot swap in the tasks. For a reconfigurable parallel robot, it can reconfigure into either pure translation motion or pure rotation motion and each of them is equivalent with the traditional Delta or Agileye robot. Thus one design of the reconfigurable parallel robot can be placed into both of those two tasks to replace the Delta and Aigleye. This can show an immediate effect on function and saving by avoiding development of two compelet different robot systems.

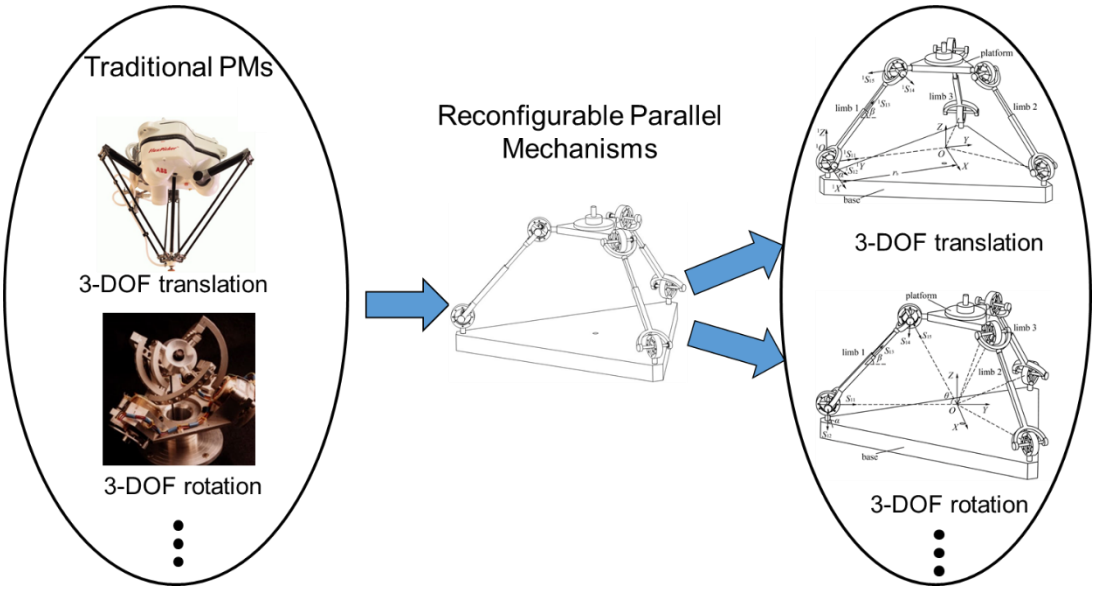

Figure 2-7 Reconfigurable Parallel Robots

In the literature, many different reconfigurable parallel mechanisms have been developed and will be classified in the following section.

2.3 Reconfiguration Principles

The mobility of a parallel mechanism is determined by the topology of the mechanism including limbs, joints, links and their arrangement in the assembly. The key outcome from the limb to the

platform is their geometric constraints which intrinsically determine the mobility and motion of the platform. Based on this, to make a parallel mechanism reconfigurable, the key is to make the geometric constraint change to the platform. In the literature, many methods have been developed and an early method focused on designs that the joints and links can be disassembled and reassembled into different parallel mechanisms for different mobility [73-75]. This shows one way to meet the application requirement of changing the platform for different motion types. However, this is not a desired way as the reassembling will cause extra effort on assembly, recalibration, and setup. Thus majority of the recent literature work follows the way that a parallel mechanism can reconfigure its mobility and motion type without disassembling the design, which is also the focus of this study. Based on the literature, it can be mainly divided into four different categories which represent four different methodologies in designing reconfigurable parallel mechanisms that can reconfigure but without disassembling as shown in Fig. 2-8.

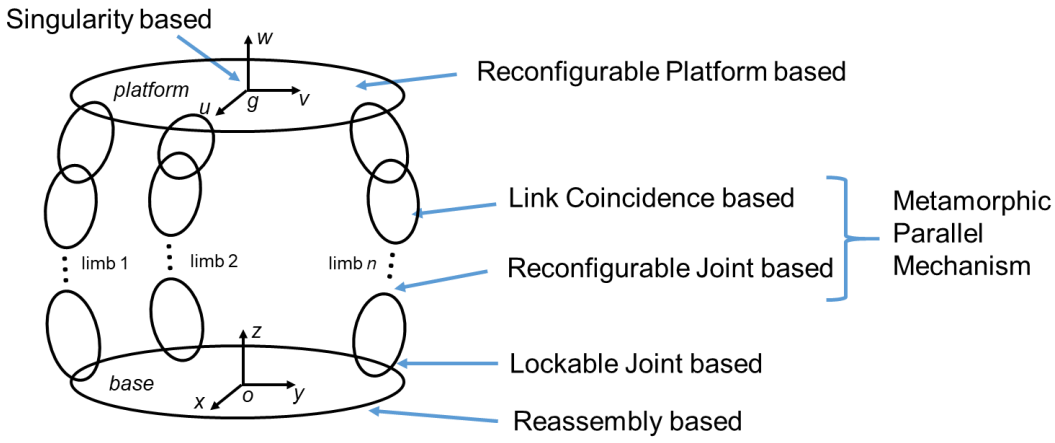

Figure 2-8 Parallel Mechanism Reconfiguration Principles

Based on singularity analysis, it was found that some parallel mechanisms could change their mobility and motion types after passing some singular configurations. This resulted in the method of reconfiguring parallel mechanisms based on singularity. This method is passive since it comes from the structure and the parallel mechanism will experience singularity in the transition which is not generally preferred in control. Other three methods are more active in term of their reconfiguration including reconfigurable platform based, lockable joint based and metamorphic parallel mechanisms that use link coincidence method and reconfigurable joint

method. In general, they all actively control the joint directions and their contribution in the limb to the platform geometric constraints. By reconfiguring the platform, the arrangement of the connecting joints between the platform and the lims will be reconfigured, resulting in the platform constraint change and mobility reconfiguration. This method needs a linkage platform which can be very complex for both design and application. Thus it has not been studied much. The lockable joint method changes the joint effectiveness by locking and unlocking its motion to make the limb and platform constraint reconfigurable. Theoretically, every parallel mechanism can be reconfigurable through this method by adding actuators to lock the joints. This freedom and wide possibility also makes the method not easily or systematically applicable. Moreover, the geometric constraint is also not reconfigured but due to effective number of joints change, which is not preferred in mechanism design and synthesis based on geometric constraints. Metamorphic parallel mechanisms show a promising way to develop reconfigurable parallel mechanisms by changing the joint directions and contribution to the limb geometric constraints through link coincidence or joint reconfiguration. This method theoretically is inline with geometric constraint based mechanism design and synthesis, and practically are flexible with local joint or link reconfiguration in the limb. This is also the focus of this work.

In the following, some literature work will be reviewed for each method to reveal more information and discussions.

2.3.1 Singularity based Reconfiguration

Another way of reconfiguration is through singularities. One of the cases is to have bifurcated configurations through constraint singularities [76]. Kinematotropic mechanisms were the earliest mechanisms that the permanent mobility could be changed after it passed through the singular positions [77]. Following the study of single-loop and multi-loop kinematotropic mechanisms, parallel mechanisms with bifurcated motion were also constructed [78]. Those early work paved one way of making reconfigurable parallel mechanisms through constraint singularities and has been followed in the literature. Based on the workspace property, this class of reconfigurable parallel mechanisms can be classified into two different types. One of them is that through constraint singularity, the two different operation modes can be switched and work effectively in the whole actuation range. For example, a family of parallel mechanisms

that have multiple operation modes were presented in [79, 80]. The parallel mechaisms can be either pure rotational or pure translational in the whole workspace after some limb tuning at the constraint singular configuration. Possible operation modes of the 3-UPU parallel mechanism were revealed based on the geometric constraint using Study parameters [81, 82]. A systematic synthesis was proposed in [83] on designing reconfigurable parallel mechanisms with bifurcated motion through constraint singularities and a number of those reconfigurable parallel mechanisms were illustrated.

The second type is that the two operation modes or bifurcated motion share the whole workspace of the mechanism which means the platform shows one motion in one side of the workspace but cannot reach the other side of the workspace which belongs to another motion branch. Most of the reconfigurable parallel mechanisms based on constraint singularity belong to this type. This type shows that the workspace of each of the operation modes is smaller than the whole workspace but in some cases can be still useful, for example, a parallel mechanism with changed motion on two different directions for machine tool applications was proposed [84]. A family of parallel mechanisms with bifurcated Schoenflies motion was found in [85] and two of them were further analyzed in [86]. Using linear transformations new 2T1R parallel mechanisms with a bifurcated rotation motion on two orthogonal directions [87] were synthesized and constraint singularity [88] and mechanism connectivity were also investigated. It was found that bifurcated motion occurs when the mechanism reaches mobility less than 3 in a metamorphic parallel mechanism [89] that covers a wide range of mobility change. At the same time, inspired from an origami fold, Zhang, Dai and Fang [90] proposed a metamorphic parallel mechanism with ability of performing orientation switch via the constraint singular configuration. Branch motions of a class of 3-*PUP* parallel mechanisms [91] were investigated and one of the bifurcated branch motion was a screw motion while the other one was a pure rotation. When the platform falls into one motion branch it can not move to another with shared workspace.

In addition to constraint singularities, through both Type 1 [92] and Type 2 [93] singularities, parallel mechanisms can be also reconfigured between different motion types. This is more obvious about the workspace sharing since the operation modes exist in different workspace zones separated by the singularity loci. For example, the 3-PRS parallel mechanism [94] had

different motion types within different workspace zones separated by singularity surfaces and reconfiguration can be realized through special trajectory planning [95] and variable actuation modes [96, 97] other than through the constraint singularity configurations.

In general, this class of reconfigurable parallel mechanisms show an interesting property of parallel mechanisms on mobility change and constraint change. But they are not practically preferrable by experiencing singularity and singularity-close configurations which can cause control disfunction and extra actuators are needed. Moreover, most of them work in separated workspace zones for different operation modes resulting in very small workspace since parallel mechanisms have already very small workspace due to their multi-loop structure.

2.3.2 Reconfigurable Platform based Reconfiguration

Traditionally, the platform of parallel mechanisms is a single rigid body and all the connecting joints between the platform and limbs have fixed arrangement between each other. A creative way of developing reconfigurable parallel mechanisms is to introduce linkage platforms which can change the connecting joint relative directions on the platform to change the combined limb constraints to the platform. In [98], the Bennett linkage, Bricard linkage, an 8-bar linkage and a 12-bar linkage were used as the platform of a parallel mechanism. The linkage configuration change will change the last limb joint configuration on the platform, thus changing the constraint to the platform without passing by the singularity configuration. A similar reconfigurable parallel mechanism using the Bricard linkage was also proposed and built [99] to have reconfigured motion between pure rotation, pure translation and planar motion [100]. So far only those few mechanisms have been proposed in the literature using reconfigurable platforms mainly through some symmetric linkages, like the Bricard linkage.

In summary, this type of reconfigurable parallel mechanisms has not been studied much and the method is generally complex to apply. A reconfigurable platform is also complex from the application, design, modelling and control point of view since the whole mechanism has more complex multi-loops than traditional parallel mechanisms with single-piece rigid platforms.

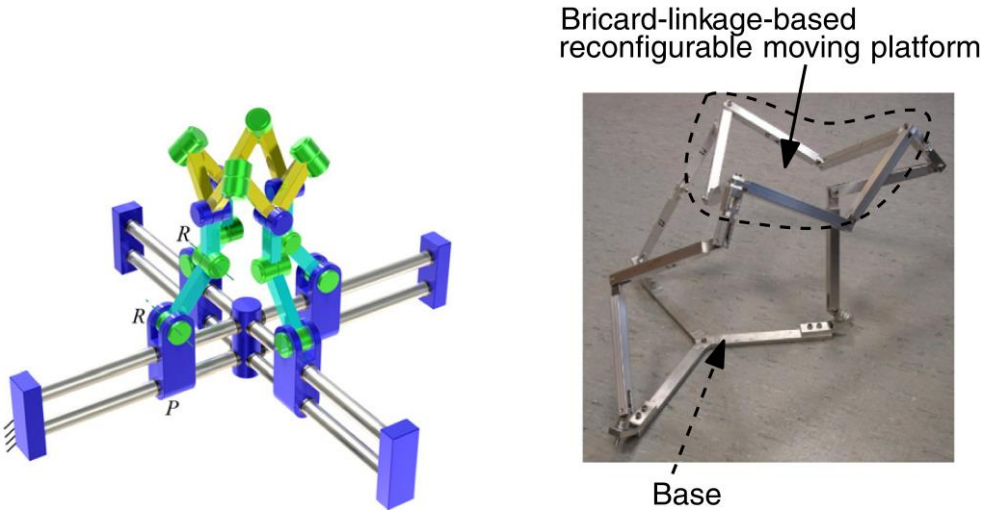

(a) hybrid-loop mechanism [98] (b) Bricard-linkage based reconfiguration [100]

Figure 2-9 Reconfiguration through reconfigurable platform

2.3.3 Metamorphic Parallel Mechanism Reconfiguration

Metamorphic parallel mechanisms are believed very promising considering their theoretical geometric constraint based model and practically flexible local reconfiguration tuning based on the following link and joint reconfiguration principles.

2.3.3.1 Link Coincidence based Reconfiguration

One method to design reconfigurable mechanisms is to change the number of links by link coincidence and self-locking as in [101-104]. It was used in proposing metamorphic mechanisms in the study of decorative carton folds and reconfigurable packaging [101]. Based on this concept, a metamorphic multi-fingered hand with an articulated palm by link coincidence of a spherical five bar linkage was invented [102]. A general approach for self-locking analysis was proposed in [103] while various joint types were explained and used in kinematic representations of metamorphic pop-up paper mechanisms in [104]. Based on the link coincidence of a four bar linkage, different motion branches were obtained and used in reconfiguring parallel mechanisms by varying the limb constraints between forces and wrenches [105].

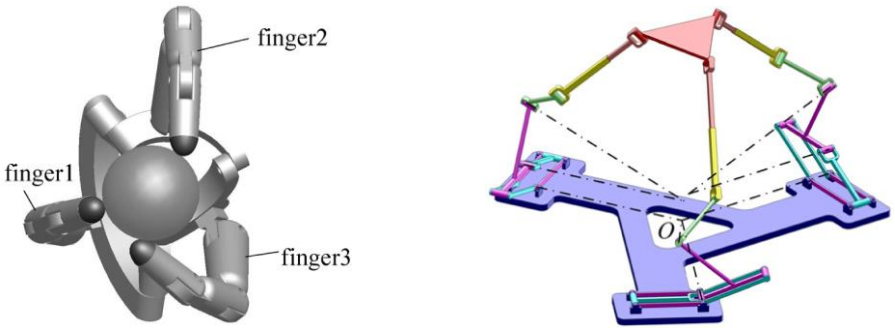

(a) Metamorphic hand [102] (b) Reconfigurable PM with diamond chain [105]

Figure 2-10 Link coincidence based reconfiguration

This method has the function of changing the joint contribution to the limb through link coincidence but existing work mainly focused on changing the effective number of links and joints. More work can be devoted to explore how the joint directions can be changed through link reconfiguration to eventually change the geometric contraints. The second method of reconfigurable joint based shows more flexibility and applicability in synthesizing metamorphic parallel mechanisms through direct joint property change as discussed below.

2.3.3.2 Reconfigurable Joint based Reconfiguration

By applying geometric constraints to joints to change the joint property, the mobility and motion types of parallel mechanisms will be also changed. This has been the active method recently in designing reconfigurable parallel mechanisms. Variable topologies of kinematic joints and their topological reconfiguration was presented in [106]. Based on a reconfigurable Hooke (rT) joint, various metamorphic parallel mechanisms [10, 89] have been designed and a construction method was introduced [107] using the rT joint. Similarly, a metamorphic parallel mechanism with ability of performing phase change and orientation switch was proposed by introducing a metamorphic kinematic pair [90] and a class of metamorphic parallel mechanisms was designed using a variable-axis (vA) joint [108] which can reconfigure among three different mobility. By designing a close-loop sub-chain joint with variable configurations, a class of reconfigurable parallel mechanisms was proposed [109] and their reconfiguration among 3-, 4- and 5-DOFs was demonstrated. A reconfigurable revolute joint was invented and a 3-rRPS metamorphic parallel mechanism was designed to have reconfigured motions between pure rotation and

1T2R motion (one translation and two rotation) [110], which is part of this study as detailed in following chapters.

This method touches the core of geometric constraints in the limbs and mechanisms by varing the joint relative direction in limbs. Comparing with reconfigurable platform method and reconfigurable link method in changing the joint contribution, this method directly goes to the joint property change. Its local joint reconfiguration also brings flexibility in parallel mechanism reconfiguration by avoiding affecting other links or joints or whole mechanism configuration change as needed in the singularity based methods. It also shows alinement with traditional synthesis methods based on joint modules for parallel mechanism. Thus it's easy to apply existing parallel mechanism theory for synthesize and design novel reconfigurable parallel mechanisms. This is the focused method of this thesis.

2.3.4 Lockable Joint based Reconfiguration

The last method is lockable joint based reconfiguration. This is not included in the metamorphic parallel mechanism method of reconfigurable joints since it does not reconfigure the joints to have changeable geometric constraints. Instead, it changes the effective number of joints in the limb system through which it changes the output motion and constraint of the limb to the platform. Thus this is a different method and theoretically, it can be applied for any mechanism by adding lockable actuators. Different reconfigurable parallel mechanisms can be obtained using geometric constraints based type thesis. For example, a 3-UPS parallel mechanism was presented in [111] with lockable revolute joint which enabled the parallel mechanism to reconfigurable between 3-DOFs to 6-DOFs by locking one of the revolute joint of the U joint. By rotating an extra revolute joint in the limb to tune the limb configuration, a 6-DOF parallel mechanism can reconfigure its kinematics performance [112]. This concept was then extended to develop a reconfigurable mobile parallel robots which can operate as equivalent rolling robot or quadruped robot [113]. Based on a lockable universal joint, a 3-URRRR parallel mechanism was proposed to reconfigure between five configurations including a 1-DOF translation configuration and a 3-DOF spherical motion configuration [114]. By designing a reconfigurable universal joint, a 3-CUP parallel mechanism was designed to be able to reconfigure into either pure rotation or pure translation motion [115]. Based on lockable joints, a class of 3-DOF

reconfigurable parallel mechanisms with both translational and spherical motion was synthesized [100]. Those novel reconfigurable parallel mechanisms were synthesized but the novel part of the method came from the geometric constraint based synthesis not from the joint locking method itself. So it has limited theoretical values from this point and is not preferred in the mechanism theory.

2.4 Synthesis of Reconfigurable Parallel Mechanisms

Many methods have been developed for type synthesis of parallel mechanisms, including displacement group theory [85, 116], vector approach [117], single-open chains [118, 119] and screw theory [79, 120-123]. Among those methods, displacement group theory and screw theory are widely used in parallel mechanism synthesis while the others are used for special classes. Displacement group theory focuses on motion generation while screw theory represents more on geometric constraints. Both can be used in reconfigurable parallel mechanism synthesis. For example, in [83], Lie group theory was applied in synthesizing general kinematotropic parallel mechanisms which can reconfigure their mobility through constraint singularities. But screw theory is used in this thesis considering the method is to change the geometric constraints from the reconfigurable joints and limbs.

The screw-synthesis method is based on the principle that the mobility of parallel mechanisms is determined by the intersection of structure constraints provided by the limbs. Mostly, the procedure of screw-synthesis for parallel mechanisms starts from a specified degree of freedom (DOF) [17] or motion pattern [123], or screw systems [124], followed by finding all the possible kinematic limbs that provide corresponding constraints for the mechanism, as an inverse of the synthesis procedure. In contrast, a forward-synthesis procedure is there with given limbs or joints to obtain all possible parallel mechanisms constructed by the limbs or joints. In [79] screw theory was used to model the constraints in two motion types of the platform and a general procedure was proposed to combine the constraints for designing a class of reconfigurable parallel mechanisms with pure rotation and pure translation motion. The method was also extended to synthesize a class of 3-DOF reconfigurable parallel mechanisms using lockable joints [100]. Based also on screw theory, new families of reconfigurable parallel mechanisms were presented using a reconfigurable chain joint [105] and a hybrid reconfigurable joint [109].

The above shows work on synthesis of reconfigurable parallel mechanisms through lockable joints, chain joints or constraint singularities. Although some novel metamorphic parallel mechanisms have been proposed, a systematic way of synthesis and design is still missing. This is one of the two main research topics of this study.

2.5 Modelling of Reconfigurable Parallel Mechanisms

Since the research on reconfigurable parallel mechanisms is still in the early stage, the focus has been mainly on new concepts and their reconfigurable mobility analysis. Thus there is not much work on kinematics and dynamics analysis on reconfigurable parallel mechanisms, especially considering their variable motion types and mobility. By using Study parameters, the detailed kinematics relation was revealed on the 3-PRS parallel mechanism [94] which has singularity based multi-operation modes. Motion/force transmissibility based kinematics performance comparison was made for its variable motion phases [125]. Kinematics and static force analysis was conducted for the two phases of a reconfigurable parallel mechanism with a reconfigurable universal joint [126]. Those are the few case-by-case work on kinematics modelling of reconfigurable parallel mechanisms but there was no systematic attempts of modelling all phases of a mechanism in a unified manner. This is the second big focus of this thesis and the methodology and some unified kinematics and dynamics modelling results will be detailed in chapters 6, 7 and 8.

2.6 Applications of Reconfigurable Parallel Mechanisms

Reconfigurable parallel mechanisms can replace traditional parallel mechanisms in applications, especially in the places that different mobility is required. Some existing novel applications can be summarized in the following.

2.6.1 Reconfiguration in Manufacturing

Based on the idea to use corresponding machining mobility to the required machining task, a family of reconfigurable parallel mechanisms was developed as machining tools with capability to reconfigure their rotation directions about two perpendicular axes while maintaining the translation axis [84] as Fig. 2-11(a). This is targeting machining tasks with single direction

trajectory at one time and the switch has to come back to the constraint singularity configuration.

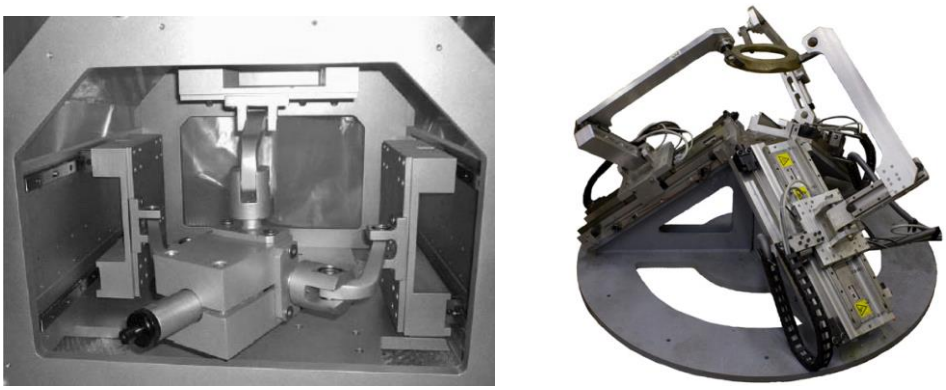

(a) reconfiguration in two directions [84] (b) reconfiguration between 3R and 3T [115]

Figure 2-11 Reconfiguration in manufacturing

Similarly, a new class of reconfigurable parallel kinematic machines was also proposed in [115] by using the two different motion types of the reconfigurable parallel mechanism for machining tasks using pure rotation or pure translation. That was based on a lockable universal joint that could change the effective joint motion directions and the geometric constraints to the platform from forces to moments. The challenge is the critical geometric constraint requirements and no successful reconfiguration has been shown in real platform. Similar challenges have also been faced in this work in the real design as will be discussed in chapter 3 and chapter 7.

Additive manufacturing has been widely used in fast prototyping. A novel reconfigurable parallel mechanism was invented in [127] to achieve four different motion types for 3D printing applications on different surfaces including planes, cylindrical surfaces, spherical surfaces and general surfaces as in Fig. 2-12. This is the link coincidence based method and taken as metamorphic parallel mechanisms. The local reconfiguration comes from the linkage subchain in each limb and initial prototype based tests have shown the effectiveness of the concept.

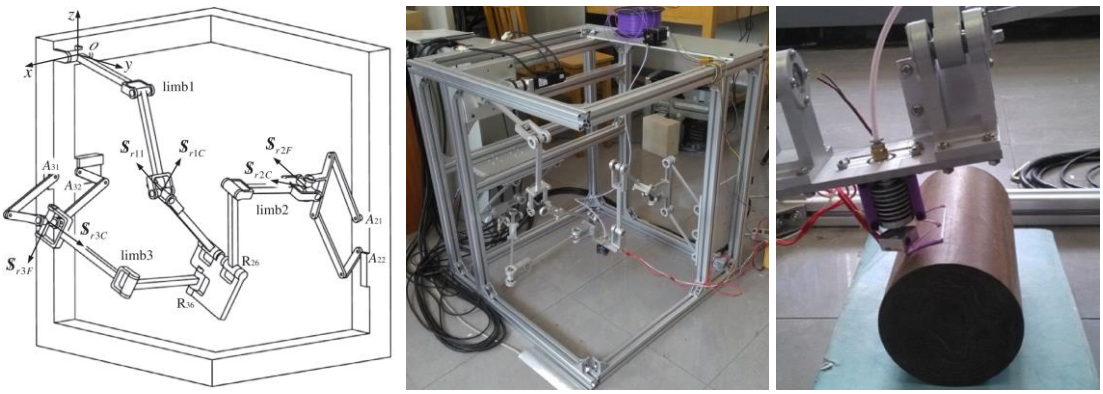

Figure 2-12 Reconfiguration for 3D printing [127]

2.6.2 Reconfiguration in Grasping

A metamorphic multi-finger hand was invented by using the link coincidence principle to change the configuration of the palm [101, 102]. The spherical mechanism in the palm can reconfigure its mobility from 2 to 1 and adjust the configuration to achieve reconfigurable dexterity and workspace. The reconfigurable motion of the palm can be also used to finely tune the hand pose to grasp an object [128]. A few versions of the MetaHand have been developed and have been successful applied in deboning and muscle extraction [129, 130]. The MetaHand is one of the most successful applications of metamorphic mechanisms.

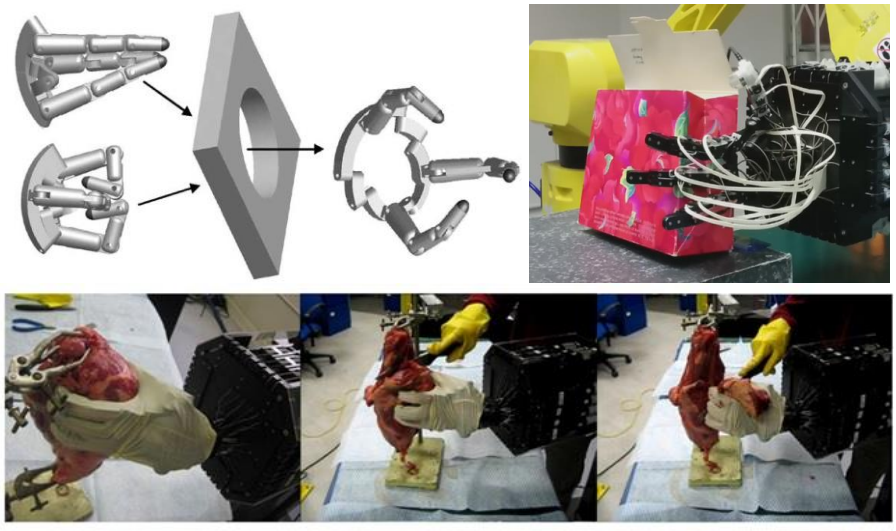

Figure 2-13 The metamorphic anthropomorphic hand and its applications [128, 130]

2.6.3 Reconfiguration in Mobile Robots

Mobile-legged robots can be taken as special parallel mechanisms considering their multi-loop mechanism constraint. Reconfiguration has been introduced into the design for variable walking phases and terrains.

A metamorphic rover mechanism was presented in [131] by using a six-bar spherical metamorphic mechanism. Following the principle of reconfigurable platform based reconfiguration, the platform using a six-bar mechanism can reconfigure to select two locomotion types including 4-leg walking and wheeled moving. This enables the rover to have high adaptability to different planet and exploration terrains.

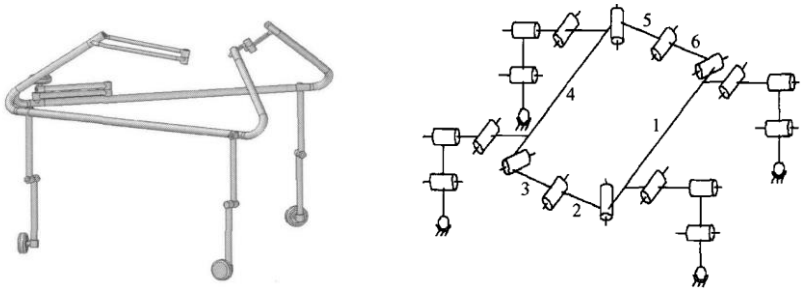

Figure 2-14 A metamorphic rover [131]

Similarly, a planar foldable mechanism based platform was used in the rover design which can also reconfigure into 4-leg walking and wheeled moving [132]. In addition to that, the width of the body can be changed based on the foldable mechanism, which allows the rover to adapt to the complex terrains and also narrow space. The above two have similar applications with novel reconfiguration but so far are still at the concept and theoretical level. More protoytpes and experiments are expected.

By introducing the variable-axis joint (vA joint) [108] into the carriage support of light-duty vehicles, the carriage becomes a special designed reconfigurable parallel mechanism which can reconfigure the carriage configuration and stiffness to achieve adaptable aerodynamic characteristics in different working conditions. This was still an early concept proposal and no even theoretical prove has been conducted.

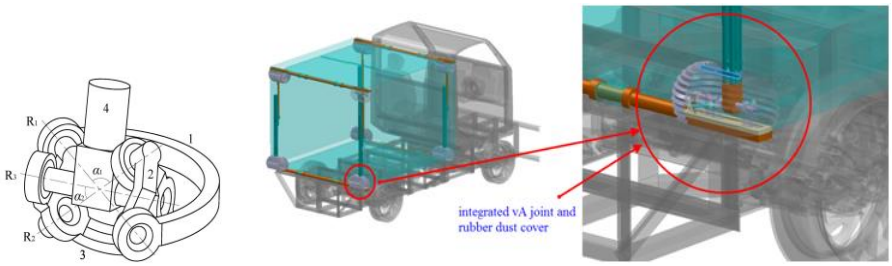

(a) vA joint (b) vA joint used in light-duty vehicle

Figure 2-15 The vA joint and its application in light-duty vehicle [108]

2.6.4 Reconfiguration in Automation Tasks

To automate the hatch process, a reconfigurable parallel mechanism was proposed in [133] considering its operating process and moving trajectory. The proposed mechanism can open, close and lock the hatch automatically through configuration transformation. This is joint reconfiguration based design by using the idea of joint coindence in special stages for variable function use.

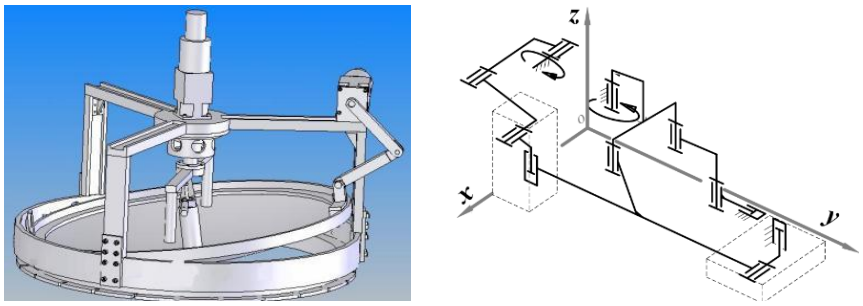

Figure 2-16 A hatch metamorphic mechanism [133]

To execute the locking and moving process in repairing the extra-high-voltage power transmission lines, a metamorphic two-limb parallel mechanism was developed and tested in real applications [134]. This is a link-coincidence based metamorphic parallel mechanism reconfiguration through link configuration locking in the limb linkage. This is a successful development close to real application and good demonstration of metamorphic parallel mechanism function.

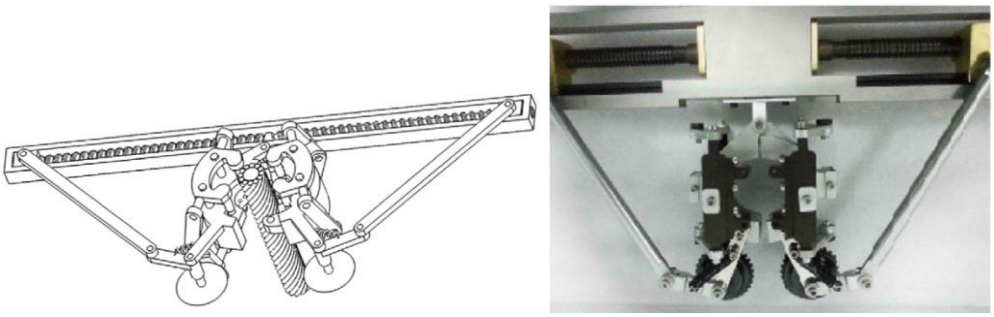

(a) Prototype (b) Simulation model

Figure 2-17 A metamorphic repair robot for extra-high-voltage power transmission lines [134]

2.7 Conclusions

In this chapter, the state-of-the-art of reconfigurable parallel mechanisms was presented based on the thorough literature review. A general background of parallel mechanism research was introduced from the original application oriented invention to the 6-DOF Stewart platforms and to recent effort on lower DOF parallel mechanisms. Based on this and the society change requirement, motivation of developing reconfigurable parallel mechanisms was revealed for the fact to fulluse the advantages of lower DOF parallel mechanisms for fast application change. The chapter creatively explored the core difference between existing reconfigurable parallel mechanism design principles, which is geometric constraint change to the platform through joint configuration change. This helped classify existing methods into five categories including reassembly based, singularity based, reconfigurable platform based, lockable joint based and metamorphic ways covering reconfigurable joint and link coincidence methods. The first four are not preferred methods due to their extra assembly effort, small workspace, complex model, and less theoretical value while the metamorphic parallel mechanisms show a promising way to develop reconfigurable parallel mechanisms. They have flexibility of local reconfiguration in the limb and possibility of applying existing synthesis/design methods for new development with the modular joint concept and direct joint geometric constraint change. Very few work on systematic synthesis and modelling of metamorphic parallel mechanisms has been done in the literature although some novel applications were proposed. This provides the basic background, justification and motivation of this work to propose a systematic synthesis method and unified modelling to cover variable configurations of metamorphic parallel mechanisms, an important branch of reconfigurable parallel mechaisms.

Chapter 3 General Synthesis of Metamorphic Parallel Mechanisms

3.1 Synthesis Strategy of MPMs

Generally, limbs in a parallel mechanism consist of several links and joints, such as revolute joints, prismatic joints, Hooke joints, cylindrical joints and spherical joints. However, these joints have fixed configurations after assembly and give fixed constraints to the platform, determining fixed mobility, fixed kinematics and dynamics performance of the mechanisms. Based on this, if the joints can change their configuration which can bring constraint change in the limb and to the platform, the mobility of the platform can be reconfigured and its kinematics and dynamics performance is also variable. This is the main synthesis strategy of metamorphic parallel mechanisms by designing reconfigurable joints and reconfigurable limbs to construct parallel mechanisms that are reconfigurable as illustrated in Figure 3-1.

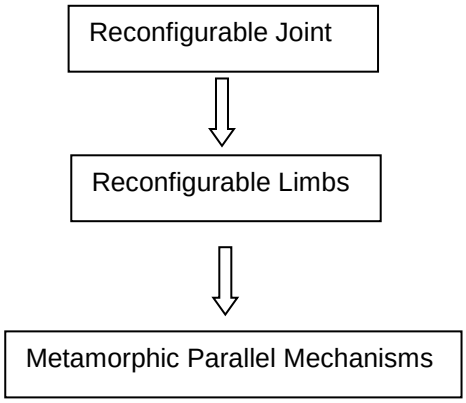

Figure 3-1 Synthesis strategy of MPMs

In the following subsections, two reconfigurable joints will be introduced and corresponding reconfigurable limbs will be enumerated. A general synthesis method is also formulated using screw theory and some examples are demonstrated. But before that, it should be stated that all the mechanism reconfiguration comes from the geometric constraint change which needs specific conditions that can be challenge in real system design and implementation. In the following, they are mainly based on ideal theoretical assumptions of all necessary geometric conditions are satisfied.

3.2 Reconfigurable Joints

3.2.1 Reconfigurable Hooke (rT) Joint

It is well known that Hooke's joint or Cardan's joint [135] consists of a pair of revolute joints with axes that intersect at right angles. The two axes intersect and generate a T shape connector resting on two pairs of bearing. This is usually named as T joint. The two links that are connected by this joint have two degrees of rotational freedom relative to each other about the axes of the connector T as in Fig. 3-2(a). Each link is perpendicular to its rotational axis. For example, link *g* is perpendicular to the rotational axis 1 and link *b* is perpendicular to its rotational axis 2. When a Hooke's joint is fixed, the axes of rotation are fixed with respect to a base or a limb. However, from the point of view of metamorphosis for reconfiguration, it is expected the direction of a rotation axis be altered. This leads to a new design that changes the rotation axis to realize the reconfiguration of the joint. This ability of changing the rotation axis is initiated by creating a groove along the housing ring to realize the reconfigurable Hooke joint as rT joint in Fig. 3-2(b), where T is commonly used for a Hooke joint and 'r' stands for reconfigurable or the added revolute joint. In the figure, the bracket is rigidly attached to link *b* and holds axis 2 as the bracket axis. The housing ring is rigidly attached to link *g* and holds axis 1 as a radial axis of the ring. Both axes 1 and 2 form a T-shaped connector. Inside the housing ring, there is a groove that the axis 1 of the radial axis can alter its direction by rotating freely along the groove. The symbolic representation is given in Fig. 3-2(c).

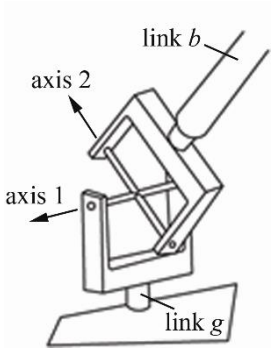

(a) The traditional Hooke Joint

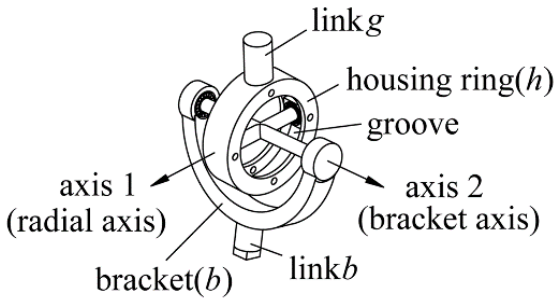

(b) The reconfigurable Hooke (rT) joint

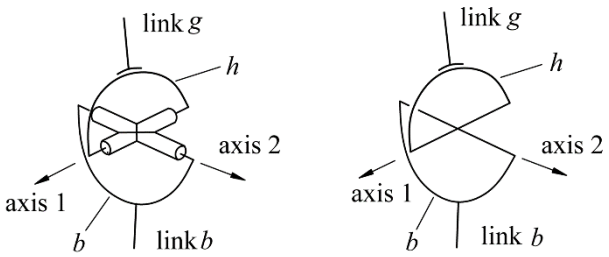

(c) Symbolic representations of the rT joint

Figure 3-2 The Reconfigurable Hooke (rT) joint and its symbolic representation

This changes the relative angle between link *g* and axis 1 in contrast to a conventional design with the angle between the link and its corresponding rotation axis being fixed. Thus along the groove, axis 1 can rotate by any angle about axis 2 and be fixed by bolting it to the groove. This allows link *g* to change its rotation axis with respect to link *b*. The new joint adds rotation mobility between the housing ring and the connector T to reconfigure the Hooke joint. In the symbolic representation, link *g* can slide along the housing ring *h* to change the relative angle between link *g* and axis 1.

The rT joint as a reconfigurable Hooke joint can have various configurations as one of the axes can have various configurations by rotating by any amount of angular displacement about the other axis, leading to special and useful configuration phases that have a subsequent effect on the limbs to achieve variable mobility.

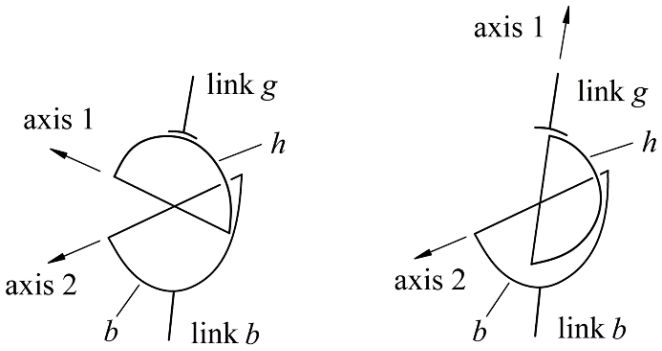

(a) Phase 1 (b) Phase 2

Figure 3-3 Two phases of the rT joint

Two typical phases of the rT joint are demonstrated in Fig. 3-3 and can be generated with respect to the radial axis of the grooved housing ring. When the radial axis 1 is fixed perpendicularly to link *g* as in Fig. 3-3(a), the configuration gives phase 1. When the radial axis

1 rotates about axis 2 to be in line with link *g*, it gives phase 2. Hereafter subscripts of notions $(rT)_1$ and $(rT)_2$ are used to denote that the rT joint is in an specific phase.

Using the rT joint, reconfigurable limbs can be produced to have variable topological phases. With this type of limbs, metamorphic parallel mechanisms can be generated with the ability to change their mobility with their topological configurations.

3.2.2 Reconfigurable Revolute (rR) Joint

As in Fig.3-4(a), the reconfigurable revolute joint, named rR joint, consists of a ring base, a rotation bar and a joint link. The joint link which is normally connected to a mechanism limb and perpendicular to the rotation bar rotates about the rotation bar with axis ***u***. The reconfiguration comes from that the rotation bar can be rotated along the groove of the ring base about the direction ***n*** which is the normal vector of the ring base plane Σ. This allows the revolute joint axis ***u*** to be alterable about ***n*** on the plane Σ and fixed along the groove. This changes the contribution of the rR joint in a parallel mechanism assembly and will make the mechanism reconfigurable.

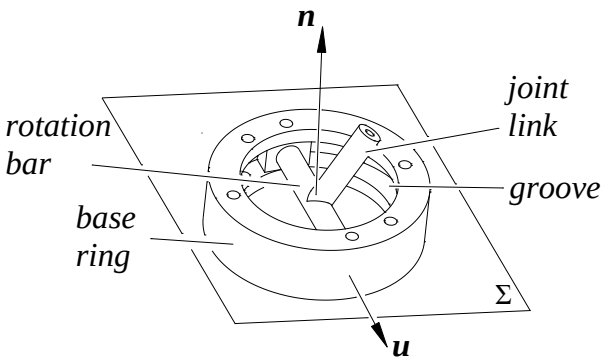

Figure 3-4 The reconfigurable revolute (rR) joint

3.3 Reconfigurable Limbs

Screws are used to represent motion of kinematic joints in a limb, which constitute the limb twist system of *n*th order, called an *n*-system. Generally, there are two kinds of change of the limb twist system. While one is order (*n*) change due to twist redundancy, resulting in mobility change of the limb, the other is twist-parameter change but with the same system order *n*, leading to motion pattern change of the limb. The former can be analysed by simple calculation

as illustrated in section 3.3.1 with the rT joint. The latter is much more complex as its results may only be found when coming to the mechanism wrench system as shown by the rR joint in section 3.3.2 and 3.6.4.

3.3.1 Reconfigurable Limbs with the rT Joint

Introducing the reconfigurable Hooke (rT) joint, order-change of the reconfigurable-limb twist-system is resulted from the phase change of the rT joint. Hence, twist dependency can be realized by two approaches. One is to make the radial-axis screw of the rT joint in the limb twist-system equal to another screw by making them co-linear. The order-change in this way can be denoted as *co-linear order-change*. The other approach is to let the radial-axis screw to be dependent with other three screws by making them co-spherical or co-planar, the corresponding order change can be denoted as *co-spherical order-change* and *co-planar order-change*. This combination of the rT joint with extra rotational joints capable of forming dependency can hence be defined as a *reconfigurable unit*. There will be four reconfigurable units in the first approach and eight in the second approach.

3.3.1.1 Reconfigurable Units

3.3.1.1.1 Co-Linear Order-Change of the Reconfigurable-Unit Twist-System

In order to make co-linear order-change of the reconfigurable-limb twist system, there should be a screw associated with another rotational joint to form the collinear dependency with the radial axis screw of the rT joint. Looking into the two phases of the rT joint including the radial axis of the rT joint being perpendicular to link *g* in phase 1 and being in line with link *g* in phase 2 as in Fig. 3-3, the extra rotational joint can be connected to link *g* collinearly as in Fig. 3-5.

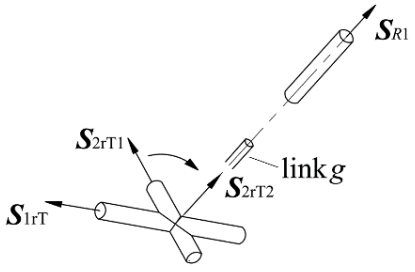

Figure 3-5 Co-line order change

In the figure, $\boldsymbol{S}_{1rT}$ stands for the twist of the bracket axis of the rT joint which is kept the same before and after the order-change. $\boldsymbol{S}_{2rT1}$ and $\boldsymbol{S}_{2rT2}$ denote the twists of the radial axis of the rT joint in phases 1 and 2 separately. $\boldsymbol{S}_{R1}$ denotes the twist of the extra rotational joint in the limb.

When the rT joint is in phase 1, the two rotation screws of the rT joint are independent with the extra rotation screw as they are in three orthogonal directions intersecting at the rT joint center. After altering the rT joint into phase 2, the radial axis of the rT joint is collinear to link *g* thus to the extra rotational axis, leading to two screws in the limb twist-system being collinear. The order change of the reconfigurable-limb twist-system can be expressed as,

$$\dim(\{\boldsymbol{S}_1\}) - \dim(\{\boldsymbol{S}_2\}) = 1 \tag{3.1}$$

where $\dim(\cdot)$ denotes the order of a screw system. $\{\boldsymbol{S}_1\}$ and $\{\boldsymbol{S}_2\}$ stand for the limb twist-systems when the rT joint is in phases 1 and 2 separately.

Based on the above analysis, the extra rotational joint in the reconfigurable limb can be picked up from a revolute (*R*) joint, a cylindrical (*C*) joint, a spherical (*S*) joint or another rT joint which can replace the general universal joint. Thus the possible reconfigurable units to give mobility change of the reconfigurable limbs are (rT)*R*, (rT)*C*, (rT)(rT) and (rT)*S*, where the *R*, *C* and *S* joint should be connected to link *g* of the corresponding rT joint with the rotational axis being in line with link *g* while two rT joints in the (rT)(rT) unit should be connected to each other by both of their link *g*. A prismatic joint can be located between the two joints in those four units with its direction collinear to link *g* of the rT joint.

3.3.1.1.2 Co-Spherical and Co-Planar Order-Change of the Reconfigurable-Unit Twist-System

In the second approach for the order-change of the reconfigurable-limb twist-system, the radial axis can be arranged to be dependent on other three screws by altering the rT joint between the two phases. This can be realized in two cases. One is the radial axis of the rT joint being co-spherical with other three rotational axes intersecting at a point as in Fig. 3-6(a). The unit is denoted as (rT)*ŔŔŔ*. In the other case the radial axis can be dependent by being co-planar with an equivalent planar joint formed by three 1-DOF joints, denoted as (rT)*XXX* (*X* represents an *R*

joint or a *P* joint). Case (rT)*RRR* is shown in Fig. 3-6(b), where the radial axis $\boldsymbol{S}_{2rT1}$ is parallel to other three *R* joints which are parallel to each other. For both cases, there is

$$\dim(\{\boldsymbol{S}_1\}) - \dim(\{\boldsymbol{S}_2\}) = -1 \tag{3.2}$$

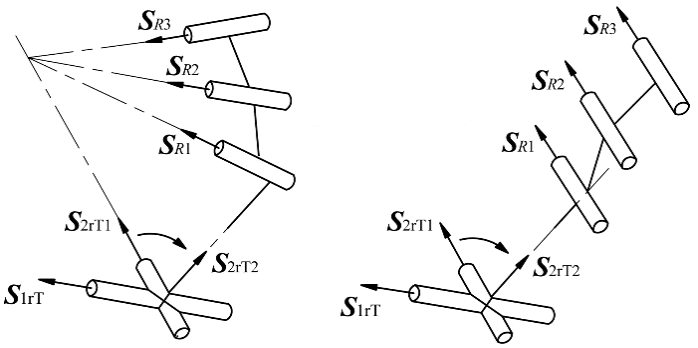

(a) Co-sphere (b) Co-plane

Figure 3-6 Co-spherical and co-planar order-change of the reconfigurable-limb twist system

Thus, with the co-spherical and co-planar order-change, the possible reconfigurable units are (rT)*ŔŔŔ* and (rT)*XXX*, where *XXX* can be *RRR*, *PRR*, *RPR*, *RRP*, *PPR*, *RPP* and *PRP*.

3.3.1.2 Reconfigurable Limbs and Their Enumeration

Based on the reconfigurable units, assembling them with other links and joints give various reconfigurable limbs. A reconfigurable limb can change its mobility once or twice by integrating one or two reconfigurable units and there cannot be more since joint redundancy needs to be avoided. Thus reconfigurable limbs can be classified by the stage of mobility change as the 1-stage reconfigurable limbs can change the mobility once, either increase by 1 or decrease by 1, and the 2-stage reconfigurable limbs can change the mobility twice by altering the rT joints one after the other.

3.3.1.2.1 1-Stage Reconfigurable Limbs by Introducing One Reconfigurable Unit

With four units from the collinear order-change units and eight from the co-spherical and co-planar order-change units, twelve reconfigurable units can have the ability to change the

mobility once. Thus there should be only one unit to be assembled in the 1-stage reconfigurable limbs. Use N_{lim1}-(N_{lim1}−1) to denote that the limbs can change their mobility between N_{lim1} and N_{lim1}−1. With the reconfigurable units, (rT)*R*, (rT)*C*, (rT)(rT), (rT)*S*, (rT)*ŔŔŔ* and (rT)*XXX*, by adding other links with basic joints (*R*, *P*, *C*, rT, *S*), 1-stage reconfigurable limbs can be enumerated in Table 3-1, where N_{lim1}=3,4,5,6. As the rT joint can give the same performance of a *U* joint, *U* joint is not accounted here. Since a limb containing more than six 1-DOF joints can be replaced by a limb with a lower number of joints, limb structures that contain more than six 1-DOF joints are excluded in the synthesis. Further, it is confined in this paper that all the twists within the same reconfigurable limb are linearly independent in a general configuration before the rT joint admits the redundancy.

Table 3-1 The 1-stage reconfigurable limbs

Type	*3-2*	*4-3*	*5-4*	*6-5*
1-link limbs	(rT)*R*	(rT)*C*’, (rT)(rT)’	(rT)*S*’	
2-link limbs		(rT)*P*’*R*’, (rT)*R*’*R*, *R*(rT)*R*’, *P*(rT)*R*’, (rT)*R*’*P*	[*P*,*R*](rT)[*C*’,(rT)’], [*C*,rT](rT)*R*’, (rT)*R*’[*C*,rT], (rT)*C*’[*P*,*R*], (rT)*P*’(rT)’,	[*C*,rT](rT)[*C*’,(rT)’], (rT)*C*’[*C*,rT], (rT)*P*’*S*’, (rT)*S*’[*P*,*R*], [*P*,*R*](rT)*S*’
3-link limbs			[*P*,*R*](rT)*R*’[*P*,*R*], [*P*,*R*][*P*,*R*][(rT)*R*’], [*P*,*R*][*P*,*R*][*R*’(rT)], (rT)*P*’*R*’[*P*,*R*], [*P*,*R*](rT)*P*’*R*’, (rT)*XXX*, (rT)*ŔŔŔ*	[*P*,*R*](rT)*R*’[*C*,rT] [*C*,rT](rT)*R*’[*P*,*R*], [*P*,*R*][*C*,rT][(rT)*R*’], [*P*,*R*][*C*,rT][*R*’(rT)], [*C*,rT][*P*,*R*][(rT)*R*’], [*C*,rT][*P*,*R*][*R*’(rT)], [*P*,*R*][*P*,*R*](rT)*C*’, [*P*,*R*][*P*,*R*](rT)(rT)’, (rT)*C*’[*P*,*R*][*P*,*R*], [*P*,*R*](rT)*C*’[*P*,*R*], [*P*,*R*](rT)(rT)’*P*,

	R(rT)(rT)'R, (rT)P'R'[C,rT], [C,rT](rT)P'R', (rT)P'(rT)'[P,R],
4-link limbs	[P,R][P,R][P,R](rT)R' (rT)R'[P,R][P,R][P,R] [P,R](rT)R'[P,R][P,R] [P,R][P,R](rT)R'[P,R] (rT)$\underline{XXX}$[P,R], (rT)P'$\underline{XXX}$, [P,R](rT)$\underline{XXX}$, (rT)$\acute{R}\acute{R}\acute{R}$[$P$,$R$], (rT)$P$'$\acute{R}\acute{R}\acute{R}$, [$P$,$R$](rT)$\acute{R}\acute{R}\acute{R}$

In Table 3-1, '[ ]' is used to list the options for the joints in a limb, take [*P*,*R*,*C*](rT)[*R*',*C*',*S*'] for example, there are three joints in the limb. The first joint has three choices of *P*, *R* and *C*, the second joint has a rT joint and the third joint has three choices of *R*', *C*' or *S*'. Thus [*P*,*R*,*C*](rT)[*R*',*C*',*S*'] represent nine assemblies, including *P*(rT)*R*', *P*(rT)*C*', *R*(rT)*R*' and so on, where *R*',*C*', *S*', (rT)' stand for *R*, *C*, *S* and (rT) joint that should be arranged in the limb and have the facility to be in line with the radial axis of the rT joints in one of its two phases. *P*' is a *P* joint that is arranged along link *g* of the rT joint.

In Table 3-1, joints are listed sequentially in the limb from one end to the other and each end of the limb can be chosen to connect to a base or a platform.

3.3.1.2.2 2-Stage Reconfigurable Limbs by Introducing Two Reconfigurable Units

In a 2-stage reconfigurable limb, the mobility of the limb can be changed twice. A simple way to construct this type of limbs based on the twelve reconfigurable units is to assemble two reconfigurable units in the limb structure. By altering the phases of the rT joints in the two units one by one, the mobility of the limb will change by 1 and 2 sequentially. Investigating the number of 1-DOF joints in the reconfigurable units shows that only rT*R* in Table 1 can be used

for the assembly as other units have either 4 or 5 1-DOF joints and any two will give redundant twist in the limb twist-system.

In addition, there is a compact way to form the two-stage mobility-change in the limb as in Fig. 5. A rotational joint is assembled between two rT joints and connected to both link *g* of the rT joints. With the axis of the rotational joint being collinear with both link *g*, it will be in line with the two radial axes of the rT joints in the rT phase 2 configuration, leading to three twists being the same in the limb twist system. In Fig. 5, $\boldsymbol{S}'_{1rT}$ is for the bracket axis twist of the second rT joint. $\boldsymbol{S}'_{2rT1}$ and $\boldsymbol{S}'_{2rT2}$ are the radial axis twists of the second rT joint in phase 1 and 2 separately.

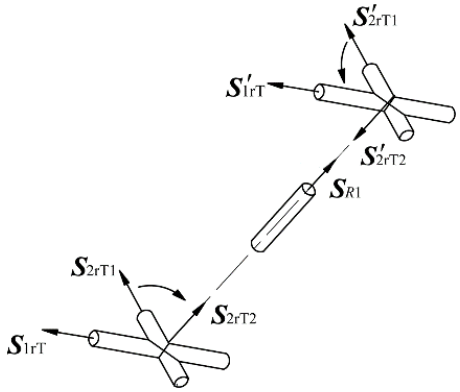

Figure 3-7 A 2-stage mobility-change of a reconfigurable limb

Then there can be two stages of mobility change of the limb by altering the two rT joints from phase 1 to 2 one by one as in Fig. 3-7, the corresponding order-change of the limb twist system can be described as:

$$\begin{cases} \dim(\{\boldsymbol{S}_{11}\}) - \dim(\{\boldsymbol{S}_{21}\} / \{\boldsymbol{S}_{12}\}) = 1 \\ \dim(\{\boldsymbol{S}_{11}\}) - \dim(\{\boldsymbol{S}_{22}\}) = 2 \end{cases} \tag{3.3}$$

where $\{\boldsymbol{S}_{ij}\}$ denotes the limb twist system with the two rT joints in phase *i* and *j*, (*i*,*j*=1,2). '/' means 'or'.

Generally, the rotational joint in the case in Fig. 3-7 can be selected from an *R* joint, a *C* joint, or an *S* joint. With two rT joints and one rotational joint in the limb of five twists, there can only be

at most one more 1-DOF joint. Hence, the rotational joint can be selected from an *R* joint or a *C* joint.

Using the above two methods, assembling two units in a limb in Fig.3-7, the 2-stage reconfigurable limbs can be enumerated in Table 3-2 in terms of the link numbers and mobility-change denoted as N_{lim2}-(N_{lim2}−1)-(N_{lim2}−2), (N_{lim2}=5,6).

Table 3-2 The 2-stage reconfigurable limbs

Type	*5-4-3*	*6-5-4*
2-link limbs	(rT)*R*”(rT)	(rT)*C*”(rT)
3-link limbs		(rT)*R*’(rT)*R*’, (rT)*R*’*R*’(rT), *R*’(rT)(rT)*R*’, [*P*,*R*](rT)*R*”(rT)

In Table 2, *R*” and *C*” are used to denote that the directions of the *R* and *C* joint in the reconfigurable limbs should be in line with link *g* of the two rT joints following the rule in Fig. 3-7.

Thus two types of reconfigurable limbs are enumerated. It is important to note that the limbs listed in Table 3-1 and Table 3-2 are serial combinations between the reconfigurable units and other joints, which do not constrain the joint directions in the limbs. Thus, the directions of the *P*, *R*, rT and *C* joints that are free to arrange and the bracket axes of the rT joints in the reconfigurable units can be assembled following the need of mobility-change.

3.3.2 A Reconfigurable Limb with the rR Joint

The rR*PS* limb consisting of an rR joint, a prismatic joint and a spherical joint, is shown in Fig. 3-8. The function of an rR*PS* limb in a parallel mechanism is equivalent to a general *RPS* limb but with an additional reconfigurable rotation axis of the revolute joint.

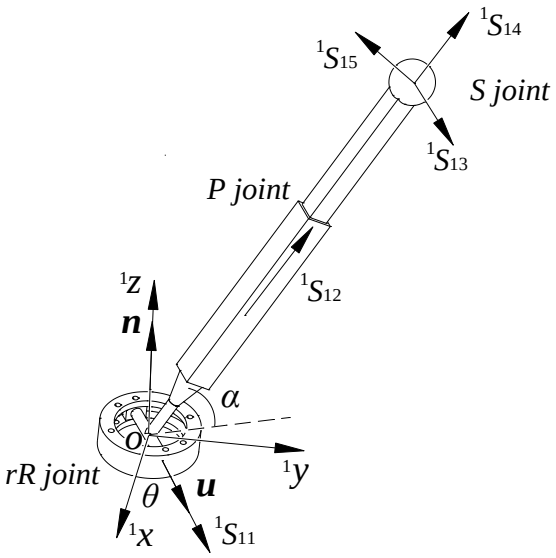

Figure 3-8 The rR*PS* limb

Set a limb coordinate system $^1o^1x^1y^1z$ at the intersecting point of the rotation bar and the joint link on the plane Σ, where ^1x axis and ^1y axis are on the plane Σ while ^1z axis is along $\boldsymbol{n}$. The twist system of the rR*PS* limb is given as:

$$\left\{{}^1\boldsymbol{S}_1\right\}=\left\{\begin{array}{l}{}^1\boldsymbol{S}_{11}=\left[\boldsymbol{u}^T \quad \boldsymbol{0}\times\boldsymbol{u}^T\right]\\ {}^1\boldsymbol{S}_{12}=\left[\boldsymbol{0} \quad \boldsymbol{s}^T\right]\\ {}^1\boldsymbol{S}_{13}=\left[\boldsymbol{u}^T \quad \boldsymbol{a}^T\times\boldsymbol{u}^T\right]\\ {}^1\boldsymbol{S}_{14}=\left[\boldsymbol{s}^T \quad \boldsymbol{a}^T\times\boldsymbol{s}^T\right]\\ {}^1\boldsymbol{S}_{15}=\left[\boldsymbol{u}^T\times\boldsymbol{s}^T \quad \boldsymbol{a}^T\times(\boldsymbol{u}^T\times\boldsymbol{s}^T)\right]\end{array}\right\} \tag{3.4}$$

where $(\bullet)^T$ is the transpose of vector/matrix $(\bullet)$, $\boldsymbol{u}=(\cos\theta,\ \sin\theta,\ 0)^T$, $\boldsymbol{s}=(-\cos\alpha\sin\theta,\ \cos\alpha\cos\theta,\ \sin\alpha)^T$ is the unit vector along the limb, $\boldsymbol{0}$ is a 1×3 zero vector and $\boldsymbol{a}$ is the position vector of the spherical centre. In (1), the first twist is for the rR joint, the second is generated from the prismatic joint, and the last three are generated from the spherical joint. θ is the angle between the rotation bar ($\boldsymbol{u}$) and the ^1x axis, α is the angle between the limb ($\boldsymbol{s}$) and its projection on plane $^1x^1o^1y$ (plane Σ). In the twist notation $^1\boldsymbol{S}_{ij}$, the first subscript i denotes the limb number, the second subscript j denotes the joint number within the limb and the leading superscript indicates the local frame.

The five twists in Eq. (3.4) form a five-system [136]. Thus, there is one reciprocal screw to Eq. (3.4) in the limb constraint system as

$$\left\{ {}^{1}\boldsymbol{S}_1^r \right\} = {}^{1}\boldsymbol{S}_1^r = \left[\boldsymbol{u} \quad \boldsymbol{a} \times \boldsymbol{u} \right] \tag{3.5}$$

This gives a constraint force acting along a line passing through the spherical joint center with a direction parallel to the rotation axis ($\boldsymbol{u}$) of the rR joint. By altering the revolute joint axis $\boldsymbol{u}=(\cos\theta, \sin\theta, 0)^{\mathrm{T}}$ with variable angle θ the constraint force in Eq. (3.5) is alterable and will change the constraint to the platform as analysed in the following 3-rR*PS* metamorphic parallel mechanism in section 3.6.4.

3.4 A General Synthesis Method for MPMs

3.4.1 A General Synthesis Method

Assembling the reconfigurable limbs into a parallel mechanism can submit it to having ability of mobility change. For a metamorphic parallel mechanism, the number and type of the essential reconfigurable limbs can be calculated following the mobility-change type of the parallel mechanism and the reconfigurable limbs can be arranged to satisfy the mobility-change conditions. Based on the above constraint-based limb synthesis, a general procedure can be presented to construct an expected metamorphic parallel mechanism using the reconfigurable limbs in Section 3.3.

3.4.1.1 Type Representation of Metamorphic Parallel Mechanisms and Essential Reconfigurable Limbs

Similar to the reconfigurable limbs, mobility change of the mechanism has several stages, such as one mobility-change from mobility 6 to 5, or sequential change from 6 to 5, then to 4, and 3. Hence the metamorphic parallel mechanisms can be classified into types represented by their stages of mobility change denoted as N_m-(N_m–1)-...-(N_m–t), where the subscript m stands for mechanism. Thus, the above two examples can be denoted as 6-5 and 6-5-4-3. It should be mentioned that the mechanisms can change their mobility between any two of N_m–t to N_m, e.g. from 6 to 3 or from 4 to 6 directly.

When constructing an expected type of a metamorphic parallel mechanism, the number of essential reconfigurable limbs can be calculated based on its type. Generally, for a N_m-(N_m–1)-...-(N_m–t) type mechanism, there are t stages of mobility change. Thus, there can be k_1 1-stage reconfigurable limbs and k_2 2-stage reconfigurable limbs, where the numbers follow:

$$k_1 + 2k_2 = t \tag{3.6}$$

After knowing the number of reconfigurable limbs, the next step is to choose the right reconfigurable limbs which can satisfy the mobility change of the mechanism. For a general N_m-(N_m–1)-...-(N_m–t) type metamorphic parallel mechanism, it can have at most N_m degrees of freedom. Firstly, the choice of the reconfigurable limbs can be limited to those which can support the parallel mechanism to have mobility N_m when the limbs are in the initial configuration before forming redundancy in the twist systems. Then there is $N_m \leq (N_{lim1}, N_{lim2}) \leq 6$, indicating that the mobility of the limbs cannot be less than the mobility of the mechanism. Secondly, the limbs should have the ability to be arranged to enable the mechanism to have the expected motion pattern, such as pure rotation, pure translation or planar motion.

With these conditions, some choice can be chosen from Tables 3-1 and 3-2. However, these limbs cannot be assembled freely in the parallel mechanisms and the arrangement should follow the following mobility-change condition. This section restricts the synthesis in a parallel mechanism with the same structure for all limbs.

3.4.1.2 The Mobility-Change Condition

Assuming that there is a 1-stage reconfigurable limb in the metamorphic parallel mechanism, the mechanism constraint system is $\{\boldsymbol{S}_1^r\}$ when the rT joint is in phase 1 and is $\{\boldsymbol{S}_2^r\}$ when the rT joint is in phase 2 assuming the same structure is used for every limb. Assuming that the mobility of the reconfigurable limb decreases by 1 after changing the rT joint from phase 1 to 2, then there will be one more constraint $\boldsymbol{S}_{+1}^r$ in the mechanism constraint-system when the rT joint is in phase 2 as

$$\left\{\boldsymbol{S}_2^r\right\} = \left\{\left\{\boldsymbol{S}_1^r\right\}, \boldsymbol{S}_{+1}^r\right\} \tag{3.7}$$

The condition that the mechanism changes its mobility with the extra constraint is that $\boldsymbol{S}_{+1}^r$ is independent of all other constraints in $\{\boldsymbol{S}_1^r\}$ [137]. Then the order of the mechanism constraint system will be increased by 1, leading to the mechanism mobility being decreased by 1. Similarly, the mobility of the mechanism will increase when the mobility of the reconfigurable limb increases assuming all limbs have the same structure.

Concluding these results, the mobility-change condition for assembling reconfigurable limbs in a parallel mechanism is that the increased or decreased constraint resulted from the phase change of the rT joint should be independent of all other constraints in the mechanism constraint system. This result can be extended to the case when there is more than one constraint change, each of which should be independent of all other constraints in the mechanism constraint system.

3.4.1.3 A General Procedure for Mobility-Change-Aimed Construction of Metamorphic Parallel Mechanisms

Various reconfigurable limbs and the mobility-change condition have been given for the mobility-change-aimed construction of the metamorphic parallel mechanisms. A general procedure for the construction can be presented as follows.

Step 1 Give the expected mobility-change type and motion which determine the number t of mobility-change stages and maximum mechanism mobility N_m, e.g., 6-5-4-3, then $t = 3$ and $N_m = 6$;

Step 2 Calculate essential numbers (k_1, k_2) of 1-stage and 2-stage reconfigurable limbs from $k_1 + 2k_2 = t$ based on the value of t in step 1;

Step 3 List all possible reconfigurable limbs from Table 3-1 and Table 3-2 by considering the maximum limb mobility (N_{lim1}, N_{lim2}) which satisfy the mobility-change request as $N_m \leq (N_{lim1}, N_{lim2}) \leq 6$. Perform type synthesis of limbs for each expected mobility-change stage of the parallel mechanism and find common structures of these limbs with the listed possible reconfigurable limbs. The reconfigurable limbs having common structures will be the choices for the mechanism construction.

In practical design, each expected mobility-change stage of the parallel mechanism has its own requirement, e.g. workspace. This can be dealt with by designing each stage separately and then taking the intersection of all specific design parameters to get an optimized system;

Step 4 Choose the limbs from the reconfigurable limbs obtained in step 3 and investigate all the constraints the limbs provide to the platform, including the constraints resulting from altering the phases of the rT joints, e.g. constraint forces or torques;

Step 5 Assemble the constraints generated by the limbs according to the expected mobility of the parallel mechanism and make the constraints resulted from the phase change of the rT joints to be independent of all other constraints in the mechanism-constraint-screw system. Construct the expected parallel mechanism by arranging the reconfigurable limbs corresponding to the constraint assembly.

3.4.2 Synthesis of a Family of Metamorphic Parallel Mechanisms With Mobility-Change Between 6-5-4-3 And with Spherical Motion at Mobility 3

Various metamorphic parallel mechanisms can be generated by taking the limbs in Tables 1 and 2 with different numbers and types. A family of metamorphic parallel mechanisms with expected type 6-5-4-3 and spherical motion is constructed in this section.

Step 1: The expected type of the metamorphic parallel mechanism is 6-5-4-3 which indicates that the mechanism has the ability to change its mobility from 6 to 3, then t=3 and N_m=6.

Step 2: With t=3, there is $k_1 + 2k_2 = 3$, leading to two choices: $k_1 = 3$, $k_2 = 0$, there are three 1-stage reconfigurable limbs, or $k_1 = 1$, $k_2 = 1$, there is one 1-stage reconfigurable limb and one 2-stage reconfigurable limb.

Step 3: As $N_m = 6$, thus $N_{lim1} = 6$ and $N_{lim2} = 6$ due to $N_m \leq (N_{lim1}, N_{lim2}) \leq 6$, indicating that the 1-stage reconfigurable limbs should be 6-5 type while the 2-stage limbs should be 6-5-4 type. Looking up the lists in Table 3-1 and Table 3-2, there are 121 1-stage reconfigurable limbs and 6 2-stage reconfigurable limbs satisfying the requests.

Further, the expected parallel mechanism has spherical motion when it reaches mobility 3, requesting that the reconfigurable limbs provide pure force constraints to the platform when changing the orders of the limb twist-systems from 6 to 5. Thus the limb structures should satisfy the conditions in [123], where the revolute joints in the limb are co-planar with the constraint force and prismatic joints are perpendicular to the force. By comparing between the structure types in [123] and the reconfigurable limbs in Tables 1 and 2, it is found that only some 6-5 1-stage reconfigurable limbs as in Table 3 have common structures and can be arranged to satisfy the spherical motion conditions. Then the expected metamorphic parallel mechanisms can be constructed by assembling three 1-stage limbs from Table 3-3 and there are 76 metamorphic parallel mechanisms when using the same structures in the three limbs and considering different ends to connected to the base.

Table 3-3 Reconfigurable limbs for the spherical motion

Type	*1-stage, 6-5*
2-link limbs	(rT)(rT)(rT)', 24, (rT)*S*'*R*, 24, *R*(rT)*S*', 23
	R[(rT)*R*'](rT) 24, (rT)(rT)*R*'*R*, 24, *R*(rT)(rT)*R*', 23
3-link limbs	*R*(rT)[*R*'(rT)], 24, (rT)*RR*'(rT), 24, (rT)*PR*'(rT), 50
	RR(rT)(rT)', 24, *R*(rT)(rT)'*R*, 23
	RRR(rT)*R*', 23, (rT)*R*'*RRR*, 23 or 24
	RR(rT)*R*'*R*, 23 or 24, *R*(rT)*R*'*RR*, 23 or 24
	(rT)*R*'*PRR*, 50, *R*(rT)*R*'*PR*, 47, *R*(rT)*R*'*RP*, 46
4-link limbs	(rT)*R*'*RPR*, 49, *RPPR*'(rT), 68, *PPR*'(rT)*R*, 65,
	(rT)*XXXR*, 21, 49-51, 68-70,
	R(rT)*XXX*, 20, 46-48, 65-67, (rT)*ŔŔŔR*, 24,
	R(rT)*ŔŔŔ*, 23, *P*(rT)*ŔŔŔ*, 26, (rT)*ŔŔŔP*, 27

In Table 3-3, the number following the type is the number corresponding to the structures in Tab. 2 in [123].

Step 4: Based on the analysis in step 3, a reconfigurable limb *R*(rT)*S*' can be chosen to demonstrate the construction and mobility change analysis. The structure is given as in Fig. 3-9 (a), where the *R* joint is connected to link *b* of the rT joint of which link *g* is connected to the *S*

joint. The bracket axis of the rT joint intersects the *R* joint axis at point *A* with angle θ and the limb can be represented by $R(rT)_1S$ in Fig. 3-9 (a), where rT joint is in phase 1 and *S*' is replaced by *S* as there is no confusion that the *S* joint forms the redundancy with the rT joint in this section.

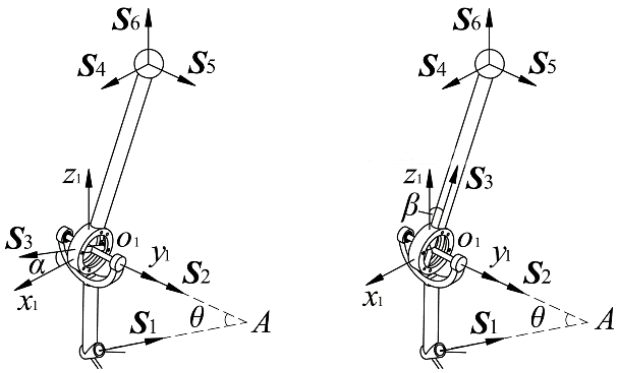

(a) $R(rT)_1S$ (b) $R(rT)_2S$

Figure 3-9 The *R*(rT)*S* reconfigurable limb

The constraint change of the limb can be analysed by locating a coordinate system $o_1x_1y_1z_1$ at the rT joint centre with axis y_1 being collinear with the bracket axis and axis x_1 being perpendicular to the plane formed by both bracket axis and the *R* joint axis. In an arbitrary configuration, the limb twist-system can be expressed as a set of finite twists [138],

$$\{\boldsymbol{S}\}=\begin{Bmatrix}\boldsymbol{S}_1=\begin{bmatrix}u & \cos\theta & w & a_y w & 0 & -a_y u\end{bmatrix}\\ \boldsymbol{S}_2=\begin{bmatrix}0 & 1 & 0 & 0 & 0 & 0\end{bmatrix}\\ \boldsymbol{S}_3=\begin{bmatrix}\cos\alpha & 0 & \sin\alpha & 0 & 0 & 0\end{bmatrix}\\ \boldsymbol{S}_4=\begin{bmatrix}1 & 0 & 0 & 0 & z & -y\end{bmatrix}\\ \boldsymbol{S}_5=\begin{bmatrix}0 & 1 & 0 & -z & 0 & x\end{bmatrix}\\ \boldsymbol{S}_6=\begin{bmatrix}0 & 0 & 1 & y & -x & 0\end{bmatrix}\end{Bmatrix} \tag{3.8}$$

where α is the angle between $\boldsymbol{S}_3$ and x_1, $(u, \cos\theta, w)^T$ is the direction of the *R* joint, the coordinate of *A* and the *S* joint centre are denoted as $(0, a_y, 0)^T$ and $(x, y, z)^T$ separately.

The six twists in Eq. (3.8) form a six-system and there is no constraint screw. Thus the reconfigurable limb $R(\mathrm{rT})_1S$ has mobility 6 and does not provide any constraint to the platform, satisfying the request of mobility six for the expected parallel mechanism.

The reconfigurable limb $R(\mathrm{rT})_1S$ can be altered into another configuration of $R(\mathrm{rT})_2S$ by changing the rT joint from phase 1 to 2 as in Fig. 2 and Fig. 3-9 (b).

The limb twist-system as a set of finite twists becomes

$$\{\boldsymbol{S}\} = \begin{Bmatrix} \boldsymbol{S}_1 = \begin{bmatrix} u & \cos\theta & w & a_y w & 0 & -a_y u \end{bmatrix} \\ \boldsymbol{S}_2 = \begin{bmatrix} 0 & 1 & 0 & 0 & 0 & 0 \end{bmatrix} \\ \boldsymbol{S}_3 = \begin{bmatrix} -\sin\beta & 0 & \cos\beta & 0 & 0 & 0 \end{bmatrix} \\ \boldsymbol{S}_4 = \begin{bmatrix} 1 & 0 & 0 & 0 & l\cos\beta & 0 \end{bmatrix} \\ \boldsymbol{S}_5 = \begin{bmatrix} 0 & 1 & 0 & -l\cos\beta & 0 & -l\sin\beta \end{bmatrix} \\ \boldsymbol{S}_6 = \begin{bmatrix} 0 & 0 & 1 & 0 & l\sin\beta & 0 \end{bmatrix} \end{Bmatrix} \tag{3.9}$$

where β is the angle between $\boldsymbol{S}_3$ and z_1, l is the length between the S and rT joint centres.

The limb constraint screw system can be obtained by calculating the reciprocal screws of Eq. (3.9) as:

$$\{\boldsymbol{S}^r\} = [l\sin\beta \quad a_y \quad -l\cos\beta \quad -la_y\cos\beta \quad 0 \quad -la_y\sin\beta] \tag{3.10}$$

This is a constraint force passing through the spherical joint centre and point A.

Thus this limb satisfies the condition that it provides one force constraint and can be used to construct the spherical motion.

Step 5: Arrange the limbs to construct the expected metamorphic parallel mechanism. When all three limbs are in configuration $R(\mathrm{rT})_2S$, there are three constraint forces, which should be

independent in the mechanism construction. This is also the condition for the mechanism to have spherical motion and further, the three constraint forces should intersect at the spherical motion centre, indicating that they cannot be in the same plane. By assembling the three $R(\mathrm{rT})_2S$ limbs symmetrically with their point A at one point and the three lines passing through S joint centres and A in the limbs are not in a plane as in Fig. 3-10, the three constraint forces will intersect at point A with three independent directions, leading to the three constraint forces being independent and the three translations of the mechanism being constrained. Thus, the expected metamorphic parallel mechanism with pure spherical motion around point A is obtained in Fig. 3-10.

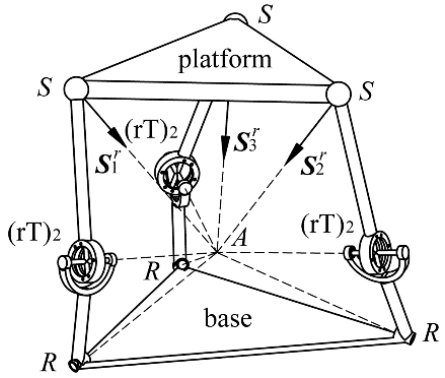

Figure 3-10 Arrangement of constraint forces and corresponding $3R(\mathrm{rT})_2S$ parallel mechanism

By altering the rT joints in the three limbs from phase 2 to 1 one by one, the $3R(\mathrm{rT})_2S$ parallel mechanism can have another three topological configurations, denoted as $1R(\mathrm{rT})_1S$-$2R(\mathrm{rT})_2S$, $2R(\mathrm{rT})_1S$-$1R(\mathrm{rT})_2S$ and $3R(\mathrm{rT})_1S$ in Fig. 3-11.

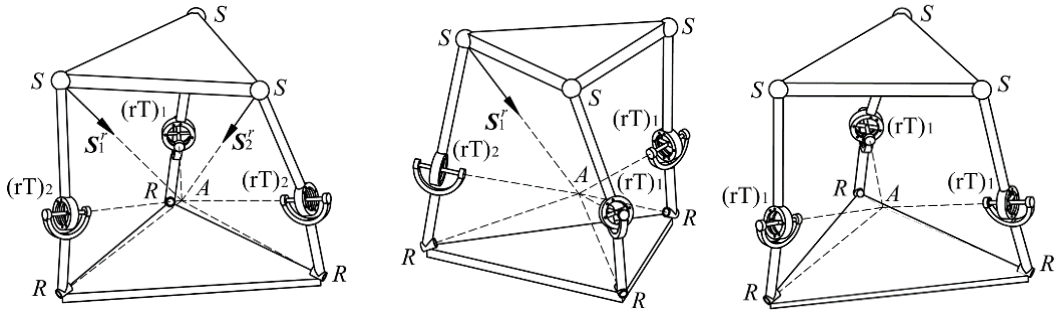

(a) $1R(\mathrm{rT})_1S$-$2R(\mathrm{rT})_2S$ (b) $2R(\mathrm{rT})_1S$-$1R(\mathrm{rT})_2S$ (c)$3R(\mathrm{rT})_1S$

Figure 3-11 The three more topological configurations of the $3R(\mathrm{rT})_2S$ parallel mechanism

From the analysis in step 4, the $R(rT)_1S$ limb does not constrain the platform, thus the force screws in the mechanism constraint system will decrease when the number of $R(rT)_1S$ limb increases. Then there are two constraint forces acting on the platform of the configuration of $1R(rT)_1S$-$2R(rT)_2S$, making the mobility be 4 in this case with three rotations and one translation along the line perpendicular to both $\boldsymbol{s}_1^r$ and $\boldsymbol{s}_2^r$. In the constraint system of the topological configuration of $2R(rT)_1S$-$1R(rT)_2S$, only one constraint force is left and the mechanism has mobility 5 with three rotations and two translations along the lines perpendicular to $\boldsymbol{s}_1^r$. For the $3R(rT)_1S$, there is no constraint on the platform and the mechanism has mobility 6.

Thus the expected metamorphic parallel mechanism, having ability of mobility change from 6 to 3 and with spherical motion mobility reaches 3, has been constructed based on a reconfigurable limb $R(rT)S$. More metamorphic parallel mechanisms of this family can be constructed by using different limbs in Table 3-3.

3.5 Obtained Metamorphic Parallel Mechanisms and Comparison with Literature

The above sections show a systematic synthesis method of metamorphic parallel mechanisms based on the invented new reconfigurable joints and reconfigurable units. Theoretically, this could lead to a big number of new mechanisms following the proposed method and only some of them are studied in details in this work as presented in the following chapters. To summarize and also show the motivation of the value to do further detailed analysis, this section lists the obtained metamorphic parallel mechanisms and comparison with existing related reconfigurable parallel mechanisms in the literature. Since this work applies the reconfigurable joint method of developing reconfigurable parallel mechanisms, all obtained mechanisms are different with existing ones in the literature in term of the structure. Thus the following comparison is mainly from the mobility reconfiguration point of view.

Table 3-4 Summary of Obtained Metamorphic Parallel Mechanisms

Metamorphic Parallel Mechanisms	Mobility Reconfiguration	Related ones in literature
3-RrTS and other 75 metamorphic parallel mechanisms based on Table 3-3	3-DOF: 3R at a single point 4-DOF: 3R1T$_x$, 5-DOF: 3R2T$_{xy}$, 6-DOF: 3R3T	Similar mobility change reconfigurable mechanisms are not found, the pure rotation mechanism phase at mobility 3 is similar to those in [123] that are not reconfigurable
3-rTPS with perpendicular structure	3-DOF: 3R without intersecting point 4-DOF: 3R1T$_x$, 3R1T$_y$, 3R1T$_z$ 5-DOF: 3R2T$_{xy}$, 3R2T$_{yz}$, 3R2T$_{xz}$ 6-DOF: 3R3T	No similar ones found. The 3R phase without intersecting rotation center is similar to the pyramid 3-RPS parallel mechanism [139].
3-rTPS with symmetrical limb arrangement	3-DOF: 2R1T 4-DOF: 3R1T 5-DOF: 3R2T 6-DOF: 3R3T	The closely related one can be the reconfigurable parallel mechanisms [98] based on the reconfigurable platform principle but with different mobility change of 1R3T, 3R1T, 1T and 3R3T.
4-rTPS	2-DOF: 1R$_{x/y}$1T$_z$ with bifurcated rotation 3-DOF: 2R$_{xy}$1T$_z$ 4-DOF: 2R$_{xy}$2T$_{xz}$, 2R$_{xy}$2T$_{yz}$, 3R1T$_z$ 5-DOF: 3R2T$_{xz}$, 3R2T$_{yz}$ 6-DOF: 3R3T	No similar mobility change of reconfigurable parallel mechanisms is found.
3-rTPrT	3-DOF: 3R, 3T 4-DOF: 1R3T	Related one is the 3-SvPSv metamorphic parallel mechanism [108] which can also realize 3R, 3T motion. But it's based on a variable-axis (vA) joint which is different with this work using rT and rR joints. The Diamon chain based metamorphic parallel mechanism [105] has similar 3R and 3T mobility based on a linkage limb. The Bricard-linkage based reconfigurable parallel mechanism [100] has 3R and 3T

		using reconfigurable platform principle. But they all do not have the 1R3T mobility.
3-rRPS	3-DOF: 3R, 2R1T	The Diamon chain based metamorphic parallel mechanism [105] can also realize the 3R and 2R1T mobility based on a linkage limb but the 3R has intersecting rotaton point and cannot be reconfigured as our 3-rRPS which will be detailed in section 5.4.

The obtained metamorphic parallel mechanisms show very wide range of mobility in Table 3-4 with variable motion directions. There are not exactly the same kind of reconfigurable parallel mechanisms found in the literature but some of them have partially similar mobility change types based on different reconfiguration principles.

3.6 Conclusions

Metamorphic parallel mechanisms are a class of new reconfigurable parallel mechanisms with case-by-case designs exist in the literature. To progress on their development, this chapter prposed a systematic synthesis strategy for metamorphic parallel mechanisms through designing reconfigurable joints and reconfigurable limbs. From design side, two reconfigurable joints, rT joint and rR joint, have been invented as the reconfiguration source to build twelve reconfigurable units. Following this, possible reconfigurable limbs were obtained by numerating all joint and link combinations classified based on their mobility change. From the synthesis side, the basic condition of mobility change was formulated in screw theory representing their geometric constraint change through the screw rank change before and after the reconfiguration in the limb. This is the same condition when constructing metamorphic parallel mechanisms using the reconfigurable limbs. Based on those two foundations, a general procedure for mobility-change-aimed metamorphic parallel mechanism construction was created and systematically described by introducing the mobility number representation, limb type selection and number calculation.

Using the proposed model and procedure, a family of metamorphic parallel mechanisms, facilitating a range of mobility change between 3 and 6 and a spherical motion when the mobility reaches 3, was synthesized. This was not only a demonstration and validation of the proposed method but also obtained 76 metamorphic parallel mechanisms which are new in the literature. The presented method can be extended to synthsize more metamorphic parallel mechanisms based on the strategy of using reconfigurable joints and limbs. Some obtained ones were summarized as examples and also worth exploring more on their reconfiguration and modelling since they are new in the literature.

Chapter 4 Constraint-Plane-Based Synthesis and Topology Variation of a Class of MPMs

This chapter investigates various topologies and mobility of a class of metamorphic parallel mechanisms synthesized with reconfigurable rTPS limbs. Based on the reconfigurable Hooke (rT) joint, the rTPS limb has two phases which result in parallel mechanisms having ability of mobility change. While in one phase the limb has no constraint to the platform, in the other it constrains the spherical joint center to lie on a plane which is used to demonstrate different topologies of the *n*-rTPS metamorphic parallel mechanisms by investigating various relations (parallel or intersecting) among the *n* constraint planes (n=2,3,..,6) [140]. Geometric constraint equations of the platform rotation matrix and translation vector are set up based on the pointplane constraint, which reveals mobility and redundant geometric conditions of the mechanism topologies. By altering the limbs into the non-constraint phase, new mechanism phases are deduced with mobility change based on each mechanism topology.

4.1 Two phases of the reconfigurable rT*PS* limb

The reconfigurable rT*PS* limb consists of a reconfigurable Hooke (rT) joint, a prismatic joint and a spherical joint. The reconfiguration of this limb stems from the configuration change of the rT joint, the two phases in Fig. 3-3. While in Fig. 4-1(a), the radial axis is perpendicular to the limb (prismatic joint) which is denoted as $(rT)_1PS$, it is collinear with the limb passing through the spherical joint center in Fig. 4-1(b) and the limb phase is symbolized as $(rT)_2PS$.

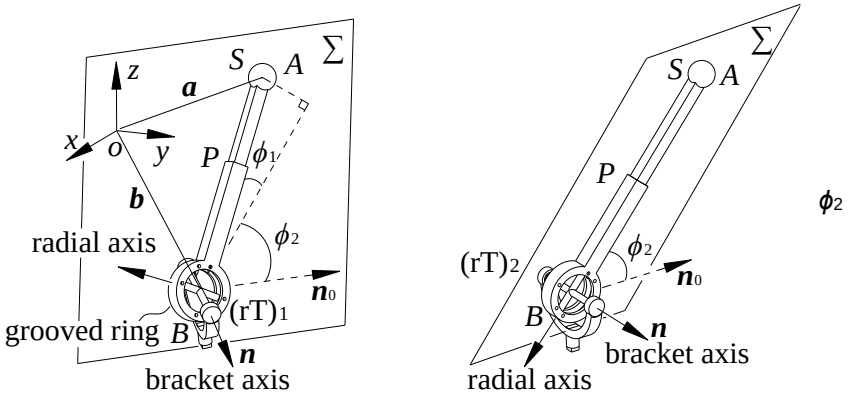

(a) $(rT)_1PS$ (b) $(rT)_2PS$

Figure 4-1 Two phases of the rT*PS* limb

Set an arbitrary coordinate system *oxyz* as in Fig. 4-1(a). Let points *A* and *B* denote the spherical joint center and the rT joint center respectively, $\boldsymbol{a}$ and $\boldsymbol{b}$ denote the vectors of points *A* and *B* in the *oxyz* coordinate system. Let the distance between *A* and *B* is *h*, then the geometric constraint of the $(rT)_1PS$ limb is given as:

$$\begin{cases} (\boldsymbol{a}-\boldsymbol{b})^2 = h^2 \\ (\boldsymbol{a}-\boldsymbol{b}).\boldsymbol{n} = h\cos(\phi_1 + \pi/2) \\ \dfrac{((\boldsymbol{a}-\boldsymbol{b})-((\boldsymbol{a}-\boldsymbol{b}).\boldsymbol{n})\boldsymbol{n}).\boldsymbol{n}_0}{\left\|(\boldsymbol{a}-\boldsymbol{b})-((\boldsymbol{a}-\boldsymbol{b}).\boldsymbol{n})\boldsymbol{n}\right\|} = \cos\phi_2 \end{cases} \tag{4.1}$$

which shows that position of the spherical joint center *A* is determined by stroke (*h*) of the prismatic joint and rotational angles (radial axis angle ϕ_1 and bracket axis angle ϕ_2) of the rT joint as in Fig. 4-1, where ϕ_1 is between the limb and its projection on plane ∑ passing through *AB* and perpendicular to the bracket axis ($\boldsymbol{n}$) of the rT joint, $\boldsymbol{n}_0$ is a reference line passing through rT joint center *B* and perpendicular to $\boldsymbol{n}$.

For the $(rT)_2PS$ limb as in Fig. 4-1(b), radial axis of the rT joint is collinear with the prismatic joint passing through the spherical joint center *A*. Thus, point *A* can only lie on the plane ∑. Geometric constraint of the $(rT)_2PS$ limb is given as:

$$\begin{cases} (\boldsymbol{a}-\boldsymbol{b})^2 = h^2 \\ (\boldsymbol{a}-\boldsymbol{b}).\boldsymbol{n} = \boldsymbol{a}.\boldsymbol{n} - d = 0 \\ (\boldsymbol{a}-\boldsymbol{b}).\boldsymbol{n}_0 = h\cos\phi_2 \end{cases} \tag{4.2}$$

which shows that position of the spherical joint center *A* is determined by stroke (*h*) of the prismatic joint and bracket axis angle (ϕ_2) of the rT joint. *d* is the distance from the coordinate system center *o* to plane ∑.

From Eqs. (4.1)-(4.2) it can be seen that the $(rT)_2PS$ limb has one degree of freedom less than the $(rT)_1PS$ limb as it has one more constraint. In fact, the $(rT)_1PS$ limb has six DOFs and the $(rT)_2PS$ limb has five [10]. When constructing parallel mechanisms with the rT*PS* limbs, the

mechanisms will have ability of mobility change by altering the rT*PS* limbs into these two phases. In this section, the rT*PS* limb will be used by connecting the rT joint to the base and the spherical joint with the moving platform. The obtained new mechanisms will demonstrate different topologies by considering the numbers (2 to 6) of the rT*PS* limbs and the limb arrangement. The method is to use the constraint plane of the $(rT)_2PS$ limb to represent the limb configuration to investigate all possible assemblies. Then altering the limbs into the $(rT)_1PS$ phase will generate new mechanism phases with mobility change.

4.2 MPMs with Two limbs

A parallel mechanism consisting of two $(rT)_2PS$ limbs is shown in Fig. 4-2(a), in which the platform connects to limb 1 and limb 2 with their spherical joints centered at point A_1 and A_2 respectively. By fixing the two rT joints on the base with their centers at points B_1 and B_2, the two limbs are constrained in plane ∑1 and ∑2 with normal vectors $\boldsymbol{n}_1$ and $\boldsymbol{n}_2$ respectively as in Fig. 4-2(a). A fixed coordinate system *oxyz* is located on the base and a moving coordinate system *Quvw* is attached on the moving platform.

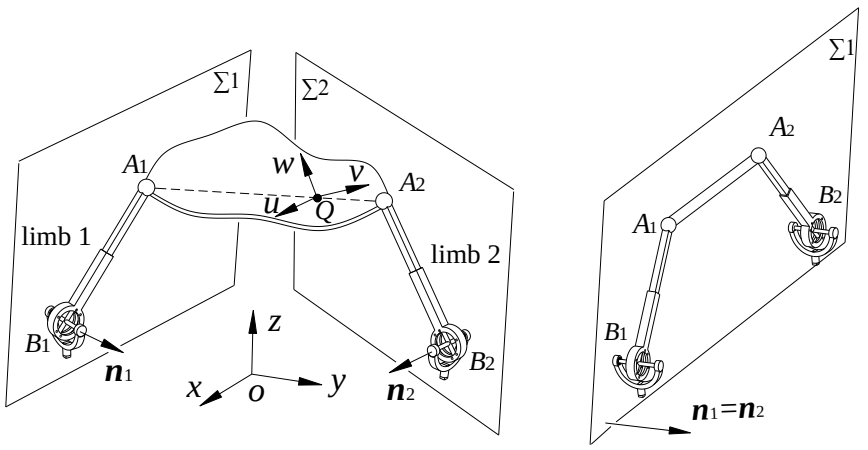

(a) general case (b) coincident plane

Figure 4-2 The $2(rT)_2PS$ parallel mechanism

Based on the constraint equations in Eq. (4.2) for the $(rT)_2PS$ limb, the geometric constraint of the $2(rT)_2PS$ parallel mechanism can be given as:

$$\begin{cases} (\mathbf{R}\,\boldsymbol{a}_1' + \boldsymbol{q}).\boldsymbol{n}_1 = d_1 \\ (\mathbf{R}\,\boldsymbol{a}_2' + \boldsymbol{q}).\boldsymbol{n}_2 = d_2 \end{cases} \tag{4.3}$$

where **R=[*u*, *v*, *w*]** is the rotational matrix from the local coordinate system to the fixed coordinate system *oxyz*, ***u***, ***v***, ***w*** and ***q*** are the unit vectors of the moving coordinate system axes and vector of the coordinate center *Q* expressed in the fixed coordinate system *oxyz* respectively. $\boldsymbol{a}_i'$ is the position vector of spherical joint centers A_i in the moving coordinate system *Quvw*. d_i is the distance from coordinate center *o* to the plane $\sum i$. These symbols are used for the same meaning in the following sections.

The two equations in Eq. (4.3) indicate that translations of the moving platform along normal $\boldsymbol{n}_1$ and $\boldsymbol{n}_2$ relate to the platform rotations. In mechanism motions, independent translations will not result in rotations but rotations can have dependent translations. Thus, it can be interpreted that two translations are constrained and the mechanism has three rotational DOFs and one translational DOF perpendicular to both $\boldsymbol{n}_1$ and $\boldsymbol{n}_2$. Obviously, the platform can rotate about line A_1A_2 freely due to the local degree of freedom between two spherical joints. An additional constraint between the spherical joints can be added to control this mobility as analyzed in the analysis of parallel mechanisms with line platforms [141, 142].

By using normal vectors to represent planes, different topologies of the metamorphic parallel mechanism consisting of two reconfigurable $(rT)_2PS$ limbs can be demonstrated in the following sections.

4.2.1 Two Intersecting Planes

When the two constraint planes intersect with each other as in Fig. 4-2(a), there is

$$\boldsymbol{n}_1.\boldsymbol{n}_2 = \cos\alpha \tag{4.4}$$

where $\alpha \in [0, \pi]$ is the angle between normal $\boldsymbol{n}_1$ and $\boldsymbol{n}_2$.

When $\alpha = 0$ or π, $\boldsymbol{n}_1 = \pm \boldsymbol{n}_2$, the two planes are parallel to each other. A special topology exists when the two planes are coincident as in Fig. 4-2(b) in which the platform can be simplified by a line segment A_1A_2, from Eq. (4.3) there is:

$$\mathbf{R}(\boldsymbol{a}_1' - \boldsymbol{a}_2').\boldsymbol{n}_1 = 0 \tag{4.5}$$

Thus, line A_1A_2 is perpendicular to normal $\boldsymbol{n}_1$ and located in the constraint plane $\sum 1$ as in Fig. 4-2(b). The platform has a plane motion and a local rotation about A_1A_2. Another special topology of the mechanism is with angle $\alpha = \pi/2$ in which the two limbs work in two perpendicular planes.

4.2.2 Two Parallel Planes

When two constraint planes are parallel to each other, there is $\boldsymbol{n}_1=\boldsymbol{n}_2$ as in Fig. 4-3(a). Set the unit vector of line A_1A_2 as $\boldsymbol{m}'_{12}$ expressed in the moving coordinate system and locate the moving coordinate center Q on the line between A_1 and A_2. There is:

$$\begin{cases} (\mathbf{R}\,\boldsymbol{a}'_1 + \boldsymbol{q}).\boldsymbol{n}_1 = (\mathbf{R}\,\boldsymbol{m}'_{12} l_{1q} + \boldsymbol{q}).\boldsymbol{n}_1 = d_1 \\ (\mathbf{R}\,\boldsymbol{a}'_2 + \boldsymbol{q}).\boldsymbol{n}_1 = (\mathbf{R}\,\boldsymbol{m}'_{12} l_{2q} + \boldsymbol{q}).\boldsymbol{n}_1 = d_2 \end{cases} \tag{4.6}$$

where l_{1q} and l_{2q} are the distances from points A_1 and A_2 to the moving coordinate center Q.

Respectively, subtracting the second equation from the first one in Eq. (4.6) and subtracting the second equation multiplied by l_{1q} from the first one multiplied by l_{2q} in Eq. (4.6), there is

$$\begin{cases} (l_{1q} - l_{2q})\,\mathbf{R}\,\boldsymbol{m}'_{12}.\boldsymbol{n}_1 = l_{12}\cos\beta = d_1 - d_2 \\ \boldsymbol{q}.\boldsymbol{n}_1 = (l_{2q} d_1 - l_{1q} d_2) / (-l_{12}) \end{cases} \tag{4.7}$$

where β is the angle between line A_1A_2 and $\boldsymbol{n}_1$. l_{12} is the distance between points A_1 and A_2.
It can be seen that line A_1A_2 has fixed angle with normal $\boldsymbol{n}_1$ and the coordinate center Q of the platform is constrained on plane $\sum q$ parallel to the two limb constraint planes and between them as in Fig. 4-3(a). Furthermore, from the first equation in Eq. (4.7), there is

$$\left\| d_1 - d_2 \right\| = \left\| l_{12}\cos\beta \right\| \le l_{12} \tag{4.8}$$

This gives a physical constraint that distance between the two parallel constraint planes should be shorter than the distance between the two spherical joints in the platform when constructing the parallel mechanisms.

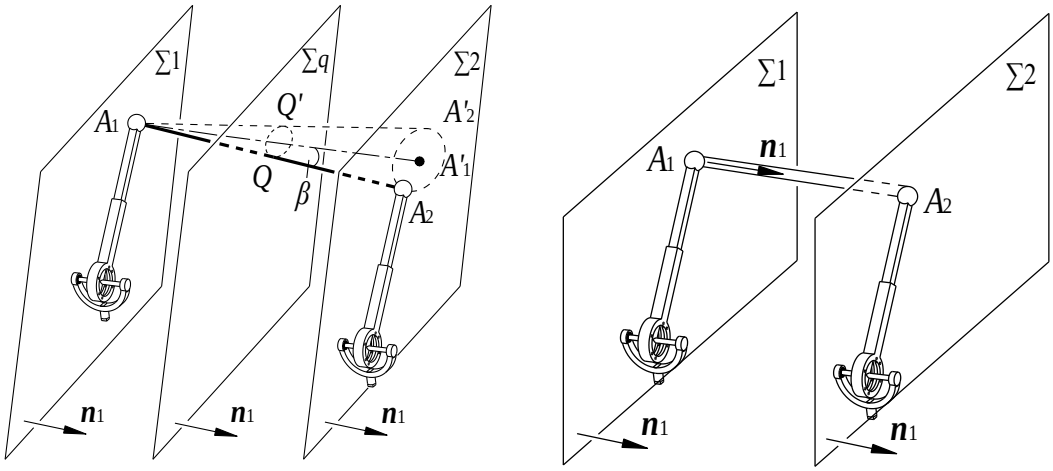

(a) general case (b) $||d_1-d_2||=l_{12}$

Figure 4-3 The $2(rT)_2PS$ with parallel constraint planes

Distance between the two parallel planes determines the motion behavior of the moving platform (A_1A_2) and its workspace. Generally, when $||d_1-d_2||<l$, line A_1A_2 has constant angle β with normal $\boldsymbol{n}_1$ and the coordinate center Q lies on the fixed plane $\sum q$. When fixing point A_1, point A_2 can only move along a circle with radius $l\sin\beta$ and centered at the projection point A'_1 of A_1 as in Fig. 4-3(a). When point A_1 moves, the circle moves. It follows the same rule when considering point A_2 with respect to point A_1. This describes the rotation motion rule of the platform A_1A_2.

Two special cases occur when d_1 and d_2 are set particularly. When the distance between the two planes $d_1-d_2=0$, the two planes are coincident to each other, which gives the same topology in Fig. 4-2(b). When the distance between the two planes $|| d_1-d_2||= l_{12}$, then $\cos\beta =1$ from (4.7) and A_1A_2 is perpendicular to the constraint planes as in Fig. 4-3(b) with geometric constraints:

$$\begin{cases} \mathbf{R}\,\boldsymbol{m}'_{12} = \boldsymbol{n}_1 \\ \boldsymbol{q}.\boldsymbol{n}_1 = d_1 - l_{1q} = d_2 - l_{2q} \end{cases} \tag{4.9}$$

Thus, the platform line A_1A_2 has fixed orientation and the moving coordinate center Q is determined by point A_1 or A_2 only. A_1 and A_2 are mutual projection points to each other along $\boldsymbol{n}_1$ on each other's plane. The mechanism has two translational degrees of freedom along the constraint plane and one local rotation about line A_1A_2. There are two constraints, but the mechanism has three DOFs instead of four, indicating that the mechanism is in structure singularity.

4.2.3 Topology change of the 2-rTPS MPM

Above sections illustrate various topologies of the 2(rT)$_2$*PS* parallel mechanism using the constraint planes. Based on this, altering the rT*PS* limb from phase (rT)$_2$*PS* to phase (rT)$_1$*PS* one by one in the mechanism will show all the other work phases of the mechanisms. When changing one limb phase, all the topologies in the above sections become the same topology 1(rT)$_1$*PS*-1(rT)$_2$*PS* as in Fig. 4-4(a) which has a translation constraint along normal $\boldsymbol{n}_1$ and is a five-DOF mechanism including the local rotation DOF about line A_1A_2. When further altering the other limb into (rT)$_1$*PS* phase, the mechanism changes to another topology 2(rT)$_1$*PS* as in Fig. 4-4(b). Since no geometric constraint exists, the 2(rT)$_1$*PS* parallel mechanism has six DOFs.

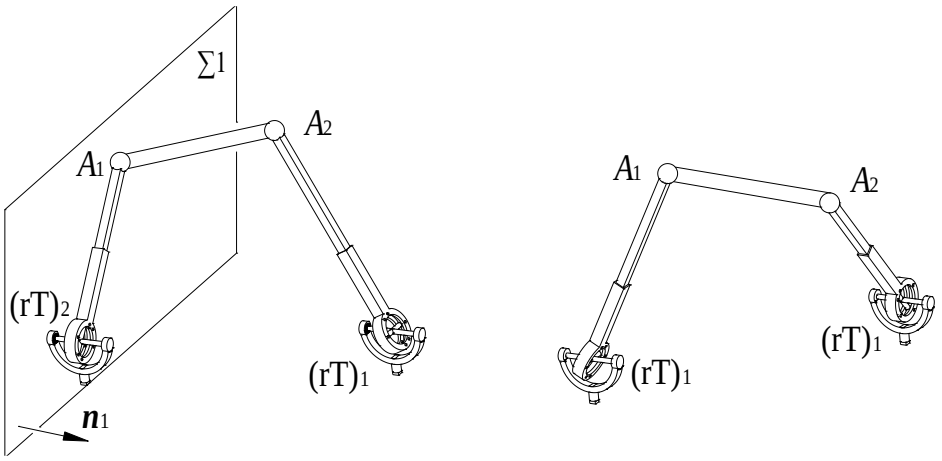

(a) 1(rT)$_1$*PS*-1(rT)$_2$*PS* (b) 2(rT)$_1$*PS*

Figure 4-4 Two topology changes of the 2(rT)$_2$PS

4.3 MPMs with Three Limbs

When constructing a metamorphic parallel mechanism with three rT*PS* limbs, there will be three constraint planes of which the normal relationships describe the topologies of the mechanisms. Generally, there are three categories: all three planes are parallel, two of them are parallel and

intersect with the third one, and all three planes intersect. Comparing with the two-limb mechanisms in section 4.2, a main difference is that the local degree of freedom on the platform vanishes if the three spherical joint centers are not in-line.

4.3.1 Three Parallel Planes

When three constraint planes are parallel to each other, there is $\boldsymbol{n}_1=\boldsymbol{n}_2=\boldsymbol{n}_3$ as in Fig. 4-5. Any line segment of the three, A_1A_2, A_2A_3 and A_1A_3, follows the rule in Section 4.2.1 with two parallel constraint planes.

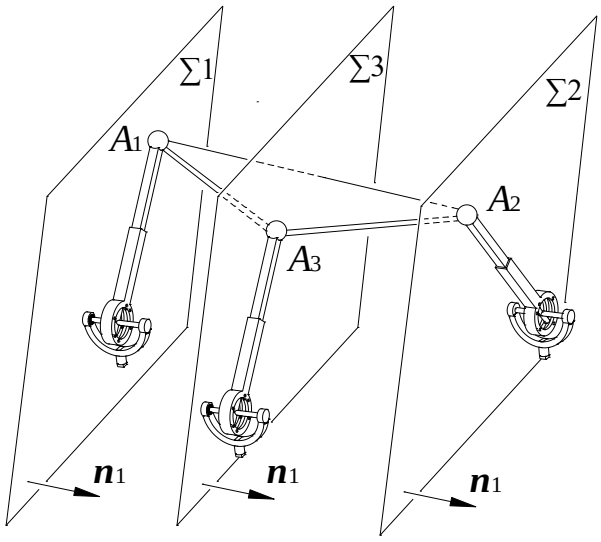

Figure 4-5 The 3-(rT)$_2$PS with parallel constraint planes

Based on Fig. 4-5 and Eq. (4.3), constraint equations of the 3-(rT)$_2$*PS* with parallel constraint planes can be obtained as:

$$(\mathbf{R}\,\boldsymbol{a}_i' + \boldsymbol{q}).\boldsymbol{n}_1 = d_i \quad (i = 1, 2, 3) \tag{4.10}$$

which can be rewritten in the matrix form as:

$$\begin{pmatrix} (\boldsymbol{a}_1')^{\mathrm{T}} & 1 \\ (\boldsymbol{a}_2')^{\mathrm{T}} & 1 \\ (\boldsymbol{a}_3')^{\mathrm{T}} & 1 \end{pmatrix} \begin{pmatrix} \boldsymbol{u}.\boldsymbol{n}_1 \\ \boldsymbol{v}.\boldsymbol{n}_1 \\ \boldsymbol{w}.\boldsymbol{n}_1 \\ \boldsymbol{q}.\boldsymbol{n}_1 \end{pmatrix} = \begin{pmatrix} d_1 \\ d_2 \\ d_3 \end{pmatrix} \tag{4.11}$$

where $\boldsymbol{w}.\boldsymbol{n}_1=\boldsymbol{u}\times\boldsymbol{v}.\boldsymbol{n}_1$ is dependent on $\boldsymbol{u}.\boldsymbol{n}_1$ and $\boldsymbol{v}.\boldsymbol{n}_1$.

Thus, $\boldsymbol{u}.\boldsymbol{n}_1$, $\boldsymbol{v}.\boldsymbol{n}_1$ and $\boldsymbol{q}.\boldsymbol{n}_1$ can be taken as independent parameters and solved directly from Eq. (4.11), which shows they are constant values in the mechanism kinematics. The constant $\boldsymbol{q}.\boldsymbol{n}_1$ shows that the moving coordinate center Q is constrained on a plane perpendicular to $\boldsymbol{n}_1$, leaving the platform two translational DOFs on the plane. Here the coordinate center Q can be anywhere on the platform. The constant $\boldsymbol{u}.\boldsymbol{n}_1$ and $\boldsymbol{v}.\boldsymbol{n}_1$ indicate that there is one independent parameter left in the rotation matrix **R** and the platform has one rotational DOF about axis $\boldsymbol{n}_1$. Thus, the 3-(rT)$_2$*PS* parallel mechanism with parallel constraint planes has three DOFs with two translations and one rotation.

A special case is that the three spherical joint centers are in line which gives a local rotational DOF about line A_1A_2 and the constraints from Eq. (4.10) can be written as:

$$\begin{cases} (\mathbf{R}\,\boldsymbol{a}_1'+\boldsymbol{q}).\boldsymbol{n}_1=d_1 \\ (\mathbf{R}(\boldsymbol{a}_1'-\boldsymbol{a}_2').\boldsymbol{n}_1=l_{12}\,\mathbf{R}\,\boldsymbol{m}_{12}'.\boldsymbol{n}_1=d_1-d_2 \\ (\mathbf{R}(\boldsymbol{a}_1'-\boldsymbol{a}_3').\boldsymbol{n}_1=l_{13}\,\mathbf{R}\,\boldsymbol{m}_{12}'.\boldsymbol{n}_1=d_1-d_3 \end{cases} \tag{4.12}$$

where l_{1i} is the distance between points A_1 and A_i (i=2,3) which are on the same line. Then (d_1-d_i)/l_{1i} is the same when i=2,3. Thus the last two equations in Eq. (4.12) constrain the same rotation between line A_1A_2 and normal $\boldsymbol{n}_1$. One of limb 2 and limb 3 becomes redundant.

In order to assemble the 3(rT)$_2$*PS* parallel mechanism in Fig. 4-5, the three parallel constraint planes cannot be located arbitrarily. The intrinsic constraint for this can be investigated by fixing constraint planes for limb 1 and limb 2 first and then identifying the conditions for limb 3. When giving spherical joint centers A_1 and A_2, the geometric constraints for the third spherical joint center A_3 can be obtained by intersecting constraint plane $\sum 3$ with a circle centered at point A_{30} with radius A_3A_{30} as in Fig. 4-6. The circle is the intersecting of two spheres centered at point A_1 and A_2 with radii A_1A_3 and A_2A_3 respectively. A_{30} is the projection point of A_3 on line A_1A_2.

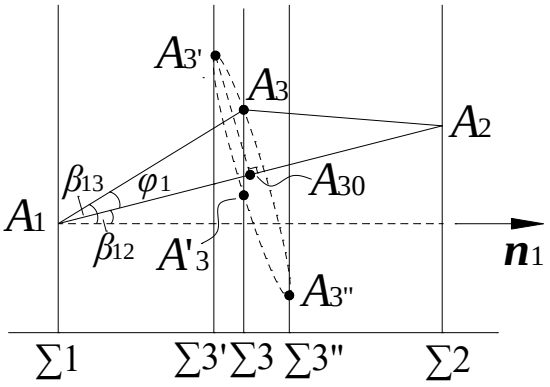

Figure 4-6 Location condition of constraint plane ∑3

From Eq. (4.10), there is

$$d_3 - d_1 = \mathbf{R}\left(\boldsymbol{a}_3' - \boldsymbol{a}_1'\right).\boldsymbol{n}_1 = l_{13}\,\mathbf{R}\,\boldsymbol{m}_{13}'.\boldsymbol{n}_1 = l_{13}\cos\beta_{13} \tag{4.13}$$

where β_{13} is the angle between A_1A_3 and $\boldsymbol{n}_1$. It is dependent on the location of plane ∑3 as in Fig. 4-6. When plane ∑3 is tangible with the constraint circle as in location ∑3' or ∑3", angle β_{13} has maximum and minimum values $\beta_{13\max}$ and $\beta_{13\min}$ respectively. Then there is:

$$\begin{cases} l_{13}\cos\beta_{13\max} \le d_3 - d_1 = l_{13}\cos\beta_{13} \le l_{13}\cos\beta_{13\min} \\ \beta_{13\max} = \varphi_1 + \beta_{12} \\ \beta_{13\min} = \varphi_1 - \beta_{12} \end{cases} \tag{4.14}$$

where φ_1 is the platform angle $A_2A_1A_3$ and β_{12} is the angle between A_1A_2 and $\boldsymbol{n}_1$.

Thus, constraint plane ∑3 should be located at ∑3' or ∑3" or between them as in Fig. 4-6. When it is at ∑3' or ∑3", there is one intersecting point ($A_{3'}$ or $A_{3''}$) and there are two intersecting points (A_3 and A'_3) when plane ∑3 is between the two extreme locations. From Fig. 4-6, it can be also seen that location (d_3) of plane ∑3 determines the orientation of the platform about line A_1A_2.

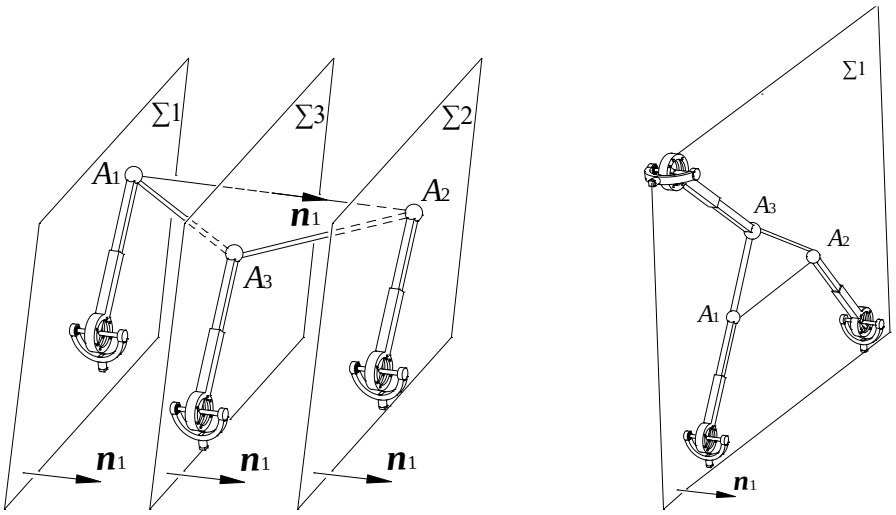

(a) d_1-d_2 =l_{12} (b) Three limbs in one constraint plane

Figure 4-7 Two special topologies with parallel planes

Two special topologies of the 3-(rT)$_2$*PS* with parallel constraint planes are shown in Fig. 4-7. In Fig. 4-7(a), the constraint of limb 1 and limb 2 follows that in Eq. (4.9) and line A_1A_2 is constantly parallel to normal $\boldsymbol{n}_1$. In this case, equation Eq. (4.12) becomes

$$d_3 - d_1 = \mathbf{R}\left(\boldsymbol{a}_3' - \boldsymbol{a}_1'\right).\boldsymbol{n}_1 = \mathbf{R}\left(\boldsymbol{a}_3' - \boldsymbol{a}_1'\right).\left(\boldsymbol{a}_2' - \boldsymbol{a}_1'\right) = l_{13}\cos\varphi_1 \tag{4.15}$$

As φ_1 is a constant angle of the platform, Eq. (4.15) is an identical equation, indicating that limb 3 is redundant. In Fig. 4-7(a), limb 1 and limb 2 can be used to define the place of line A_1A_2 and limb 3 will determine the rotation of the platform about line A_1A_2. This shows difference with the 2(rT)$_2$*PS* mechanism in Fig. 4-4(b) in which the local rotational DOF exists. Thus, the mechanism in Fig. 4-7(a) has three DOFs with two translations parallel to the constraint plane and one rotation about normal $\boldsymbol{n}_1$.

A further special topology can be obtained by setting the distance between the three constraint planes to zero as in Fig. 4-7(b) in which all three limbs are constrained in the same plane. The geometric constraint follows that in Eq. (4.10) with d_1=d_2=d_3 and the platform formed by $A_1A_2A_3$ is constrained on plane ∑1, making the platform have a planar motion with two translations on the plane and one rotation perpendicular to the plane.

4.3.2 Two Parallel and One Intersecting Planes

When the three constraint planes in the 3(rT)$_2$*PS* parallel mechanism have two parallel ones, there is $\boldsymbol{n}_1 = \boldsymbol{n}_2 \neq \boldsymbol{n}_3$ as in Fig. 4-8. Line A_1A_2 follows the rule in Section 4.2.1 with two parallel constraint planes.

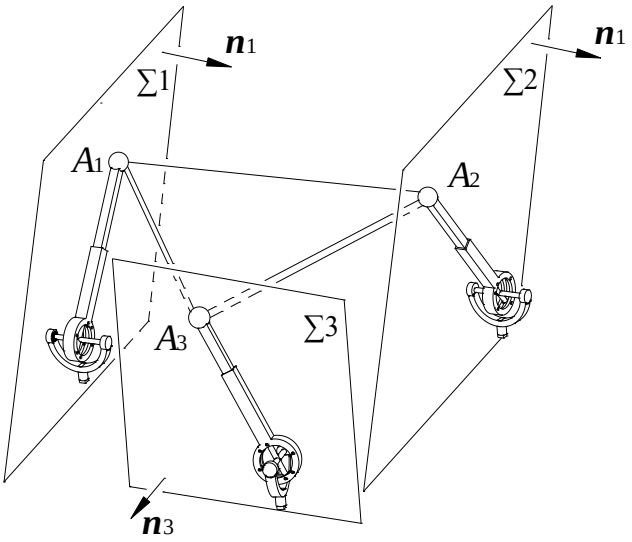

Figure 4-8 The 3-(rT)$_2$PS with two parallel and one intersecting constraint planes

Based on Fig. 4-8 and Eq. (4.11), geometric constraint can be given as:

$$\begin{cases} (\mathbf{R}\,\boldsymbol{a}_1' + \boldsymbol{q}).\boldsymbol{n}_1 = d_1 \\ \mathbf{R}(\boldsymbol{a}_1' - \boldsymbol{a}_2').\boldsymbol{n}_1 = (\boldsymbol{a}_1' - \boldsymbol{a}_2').(\mathbf{R}^{\mathrm{T}}\,\boldsymbol{n}_1) = d_1 - d_2 \\ (\mathbf{R}\,\boldsymbol{a}_3' + \boldsymbol{q}).\boldsymbol{n}_3 = d_3 \end{cases} \tag{4.16}$$

The second equation in Eq. (4.16) shows that line A_1A_2 has constant angle with normal $\boldsymbol{n}_1$, which gives a constraint of the platform rotation (**R**) and the platform can only rotate about line A_1A_2 and direction $\boldsymbol{n}_1$. The first and third equations indicate that translations of the moving platform along normal $\boldsymbol{n}_1$ and $\boldsymbol{n}_3$ depend on the platform rotations. Thus, there are two independent parameters in rotation matrix **R** and one in translation $\boldsymbol{q}$ based on Eq. (4.16). Hence, this mechanism has two rotational DOFs and one translational DOF with direction perpendicular to both $\boldsymbol{n}_1$ and $\boldsymbol{n}_3$. When the three spherical joint centers are in line, the mobility is the same but includes a local rotation. This is different with the case with all three planes parallel in Fig. 4-5 in which the third limb is used to constrain one more rotation and it is redundant when the three spherical joint centers are in line. In the mechanism in Fig. 4-8, the

third limb gives one more constraint on the translation which is not redundant when the points are in line. In fact, except the case in Fig. 4-5, the third limb is not redundant in the following sections under the in-line condition.

4.3.3 Three Intersecting Planes

When the constraint planes of the three limbs have different normals with $\boldsymbol{n}_1 \neq \boldsymbol{n}_2 \neq \boldsymbol{n}_3$ as in Fig. 4-9(a), a general configuration of the 3-(rT)$_2$*PS* parallel mechanism is illustrated. This gives three intersecting lines and considering relations among these lines will show different topologies of the mechanism. There are basically two different relations including three intersecting at one point and three parallel to each other. In the general configuration in Fig. 4-9(a), the three lines intersect at one point.

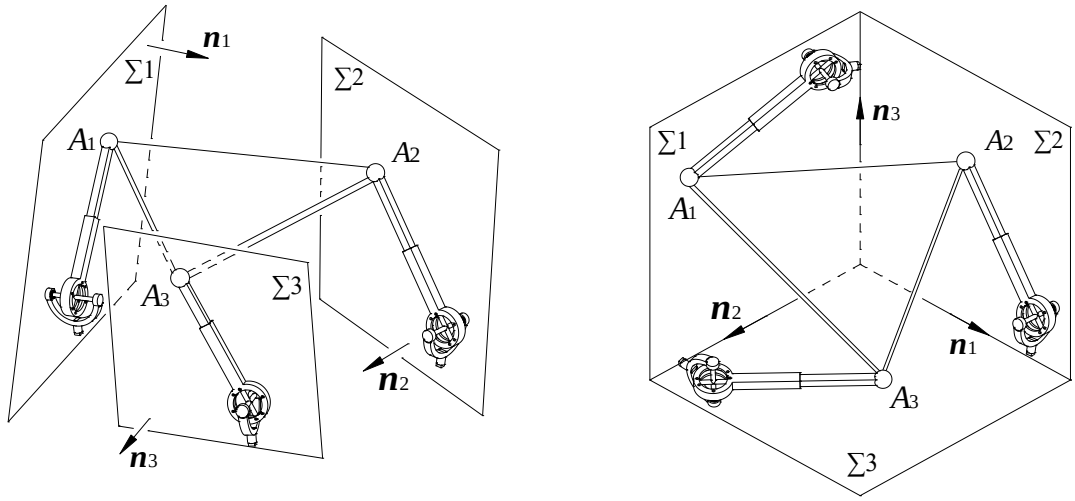

(a) general case (b) perpendicular planes

Figure 4-9 The 3-(rT)$_2$PS with three intersecting constraint planes

Based on Fig. 4-9 and Eq. (4.10), the geometric constraint can be given as:

$$\mathbf{R}\,\boldsymbol{a}_i'.\boldsymbol{n}_i + \boldsymbol{q}.\boldsymbol{n}_i = d_i \quad (i = 1, 2, 3) \tag{4.17}$$

which shows that translations of the moving platform along three independent directions $\boldsymbol{n}_1$, $\boldsymbol{n}_2$ and $\boldsymbol{n}_3$ relate to the platform rotations. Thus, this mechanism has three rotational DOFs with dependent translations.

A special topology of this kind of parallel mechanisms is that the three intersecting lines are perpendicular to each other as in Fig. 4-9(b). This is similar to the pyramid parallel mechanism [139] consisting of three *RPS* limbs in three perpendicular constraint planes and having pure rotational mobility.

When the three intersecting lines are parallel to each other, another topology of the 3(rT)$_2$*PS* parallel mechanism with intersecting planes can be obtained as in Fig. 4-10(a).

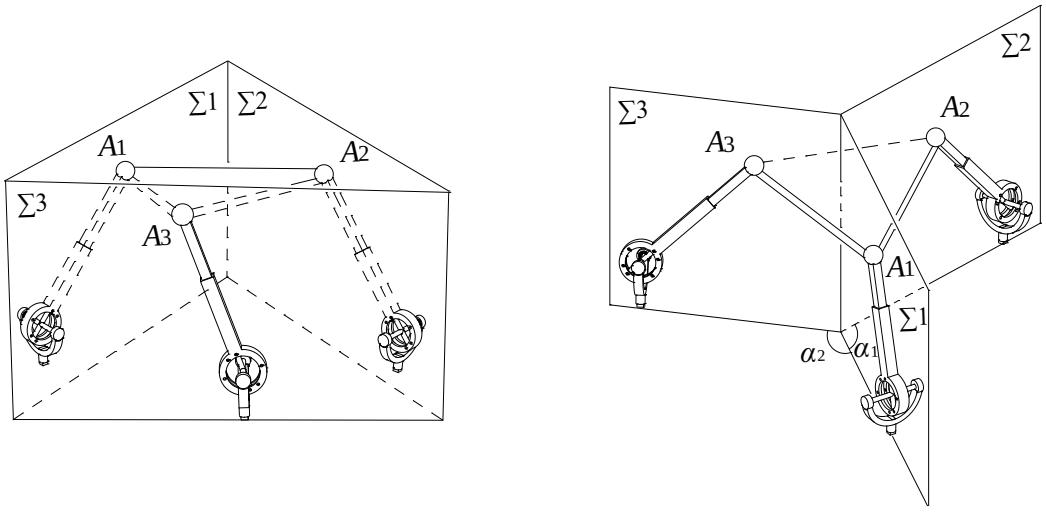

(a) three parallel lines (b) coincident at one line

Figure 4-10 The 3(rT)$_2$PS with three parallel intersecting lines

In this case, normal $\boldsymbol{n}_1$, $\boldsymbol{n}_2$ and $\boldsymbol{n}_3$ are all perpendicular to the intersecting lines and are not independent. Thus, the geometric constraint of this mechanism can be given as:

$$\begin{cases} (\mathbf{R}\,\boldsymbol{a}_1' + \boldsymbol{q}).\boldsymbol{n}_1 = d_1 \\ (\mathbf{R}\,\boldsymbol{a}_2' + \boldsymbol{q}).\boldsymbol{n}_2 = d_2 \\ (\mathbf{R}\,\boldsymbol{a}_3' + \boldsymbol{q}).(k_1\boldsymbol{n}_1 + k_2\boldsymbol{n}_2) = d_3 \end{cases} \tag{4.18}$$

where k_1 and k_2 are coefficients to describe the dependency among the three normal vectors.

Subtracting the summary of the first equation multiplied with k_1 and the second equation multiplied with k_2 from the third equation in Eq. (4.18) gives:

$$k_1 \mathbf{R}(\boldsymbol{a}_1' - \boldsymbol{a}_3').\boldsymbol{n}_1 + k_2 \mathbf{R}(\boldsymbol{a}_2' - \boldsymbol{a}_3').\boldsymbol{n}_2 = k_1 d_1 + k_2 d_2 - d_3 \quad (4.19)$$

which gives a constraint of the platform rotation. Thus, Eq. (4.18) equivalently describes two translational and one rotational constraints. The mechanism in Fig. 4-10(a) has three DOFs with two rotations and one translation perpendicular to both $\boldsymbol{n}_1$ and $\boldsymbol{n}_2$. It can be seen from Eq. (4.19) that when the three spherical joint centers are in line, $(\boldsymbol{a}_1' - \boldsymbol{a}_3')$ and $(\boldsymbol{a}_2' - \boldsymbol{a}_3')$ has the same direction about which the local rotational DOF exists as Eq. (4.19) becomes identical.

When the three intersecting lines are coincident, the three constraint planes intersect at one line as in Fig. 4-10(b), in which α_1 and α_2 are the angles between plane ∑1 and plane ∑2, plane ∑1 and plane ∑3 respectively. The geometric constraints follow the same in Eq. (4.18) and Eq. (4.19) constraining the mechanism to have the same mobility. When $\alpha_1=\alpha_2=2\pi/3$, the mechanism has symmetric limb arrangement with a similar topology of the well-known 3-*RPS* parallel mechanism proposed by Hunt [17].

4.3.4 Topology Change of the 3-rTPS MPM

Altering the $(rT)_2PS$ limbs in the previous 3-$(rT)_2PS$ parallel mechanisms into phase $(rT)_1PS$ will result in various new mechanism topologies with increased mobility. After changing the phase of one limb, all 3-$(rT)_2PS$ parallel mechanisms become one of two topologies in Fig. 4-11 as 2$(rT)_2PS$-1$(rT)_1PS$ that has two constraint planes. The geometric constraints follow those in Eq. (4.3) with one less. This makes the 2$(rT)_2PS$-1$(rT)_1PS$ have four DOFs with one translation and three rotations for the case in Fig. 4-11(a) having two intersecting constraint planes and two translations and two rotations for the topology in Fig. 4-11(b) having two parallel constraint planes.

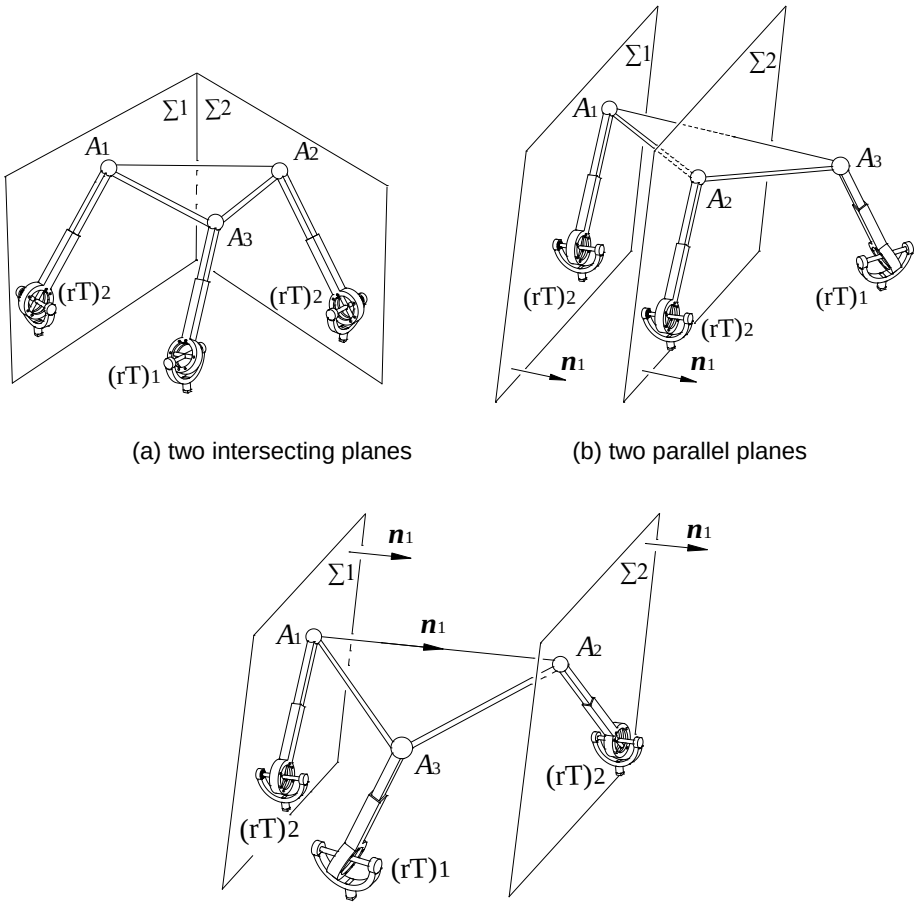

(a) two intersecting planes (b) two parallel planes

(c) A special case

Figure 4-11 The 2(rT)$_2$PS-1(rT)$_1$PS with two constraint planes

When changing the phase of limb 1 or limb 2 in Fig. 3-18(a) the mechanisms change to the case in Fig. 4-11(b). But when changing the phase of limb 3, it becomes topology in Fig. 4-11(c) which has mobility three with two translations and one rotation. Thus, the mechanism in Fig. 4-7(a) does not change mobility after changing the phase of limb 3.

When further changing one more limb phase, all topologies in Fig. 4-11 change to the same mechanism 1(rT)$_2$*PS*-2(rT)$_1$*PS* which has one constraint plane that limited one translation perpendicular to the plane. Thus, this mechanism has five DOFs. When changing all limbs to phase (rT)$_1$*PS*, the mechanism becomes 3-(rT)$_1$*PS* that does not have any constraint and has full mobility 6.

It is worth mentioning that the topology in Fig. 4-7(b) has all three limbs in a plane and it is a planar parallel mechanism. By changing the limb phases one by one, the topology becomes 3-

DOF in Fig. 4-11(a) and then to 6 DOFs. Thus, a planar parallel mechanism becomes a spatial one while the mobility changes from 3 to 6.

4.4 MPMs with Four Limbs

The method in the previous sections can now be extended to analysis of constructing metamorphic parallel mechanisms with four $(rT)_2PS$ limbs. Number of parallel planes can be used to categorize different topologies which include four, three or two parallel ones among the four constraint planes.

4.4.1 Four Parallel Planes

From Eq. (4.11), the constraint equations can be directly solved leading to constant $\boldsymbol{u}.\boldsymbol{n}_1$, $\boldsymbol{v}.\boldsymbol{n}_1$ and $\boldsymbol{q}.\boldsymbol{n}_1$ when there are three parallel constraint planes. Thus, when adding one more parallel constraint plane to assemble the $4(rT)_2PS$ parallel mechanism, the new constraint equation will be redundant with those in Eq. (4.11). Hence, the $4(rT)_2PS$ with four parallel constraint planes has the same mobility with the $3(rT)_2PS$ case with two translational and one rotational DOFs. It can be concluded that when more than three constraint planes of $(rT)_2PS$ limbs are parallel, they are dependent. This gives reference when constructing parallel mechanisms with five and six $(rT)_2PS$ limbs in Sections 4.5 and Section 4.6.

4.4.2 Three Parallel Planes among the Four

$4(rT)_2PS$ parallel mechanisms with three parallel constraint planes can be synthesized by adding one $(rT)_2PS$ limb to the topologies of $3(rT)_2PS$ with three parallel constraint planes in Section 4.3.1 with one more constraint equation as below in addition to those three in Eq. (4.10).

$$\mathbf{R}\,\boldsymbol{a}_4'.\boldsymbol{n}_4 + \boldsymbol{q}.\boldsymbol{n}_4 = d_4 \tag{4.20}$$

A general topology is demonstrated in Fig. 4-12. Based on the previous analysis in section 4.1, Eq. (4.20) gives one more constraint on the platform translation on normal $\boldsymbol{n}_4$ which is different with $\boldsymbol{n}_1=\boldsymbol{n}_2=\boldsymbol{n}_3$. Thus, the mechanism in Fig. 4-12 has the mobility with one rotation about $\boldsymbol{n}_1$

and one translation perpendicular to both $\boldsymbol{n}_1$ and $\boldsymbol{n}_4$. Specially, if the four spherical joint centers are in line, the mobility does not change.

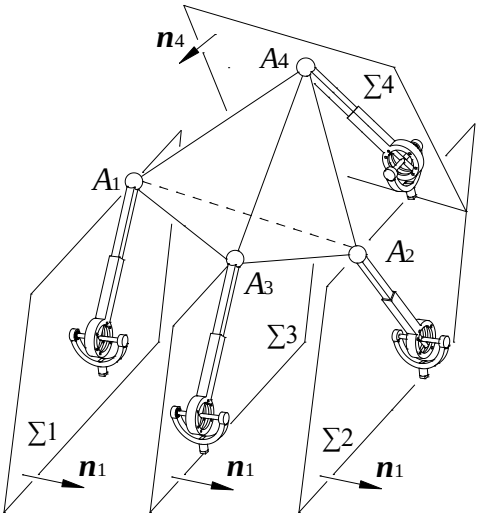

Figure 4-12 The 4-(rT)$_2$PS with three parallel planes

4.4.3 Two Parallel Planes among the Four

When there are only two parallel constraint planes among the four, a general topology is in Fig. 4-13(a) while a special case in Fig. 4-13(b) with line A_1A_2 perpendicular to the constraint plane. The geometric constraint follows the four equations in Eq. (4.10) and Eq. (4.20). Two of them constrain one rotation and one translation while the other two constrain two translations. Thus, the general case has two rotational DOFs about line A_1A_2 and normal $\boldsymbol{n}_1$ while the one in Fig. 4-13(b) has only one rotation DOF about A_1A_2 parallel with $\boldsymbol{n}_1$.

Differently, if normal $\boldsymbol{n}_4$ is in a parallel plane formed by $\boldsymbol{n}_1$ and $\boldsymbol{n}_3$, they are dependent and the geometric constraint becomes:

$$\begin{cases} (\mathbf{R}\,\boldsymbol{a}_1' + \boldsymbol{q}).\boldsymbol{n}_1 = d_1 \\ \mathbf{R}(\boldsymbol{a}_1' - \boldsymbol{a}_2').\boldsymbol{n}_1 = d_1 - d_2 \\ (\mathbf{R}\,\boldsymbol{a}_3' + \boldsymbol{q}).\boldsymbol{n}_3 = d_3 \\ \mathbf{R}(\boldsymbol{a}_1' - \boldsymbol{a}_4').k_1\boldsymbol{n}_1 + \mathbf{R}(\boldsymbol{a}_3' - \boldsymbol{a}_4').k_3\boldsymbol{n}_3 = k_1d_1 + k_3d_3 - d_4 \end{cases} \tag{4.21}$$

where $\boldsymbol{n}_4$ is represented by $k_1\boldsymbol{n}_1 + k_3\boldsymbol{n}_3$ since they are in parallel planes.

Eq. (4.21) gives two translational and two rotational constraints, leading to that the mechanisms have one rotational DOF and one translational DOF perpendicular to both $\boldsymbol{n}_1$ and $\boldsymbol{n}_3$. However, when coming to the special one in Fig. 4-13(b) it has only the translational DOF.

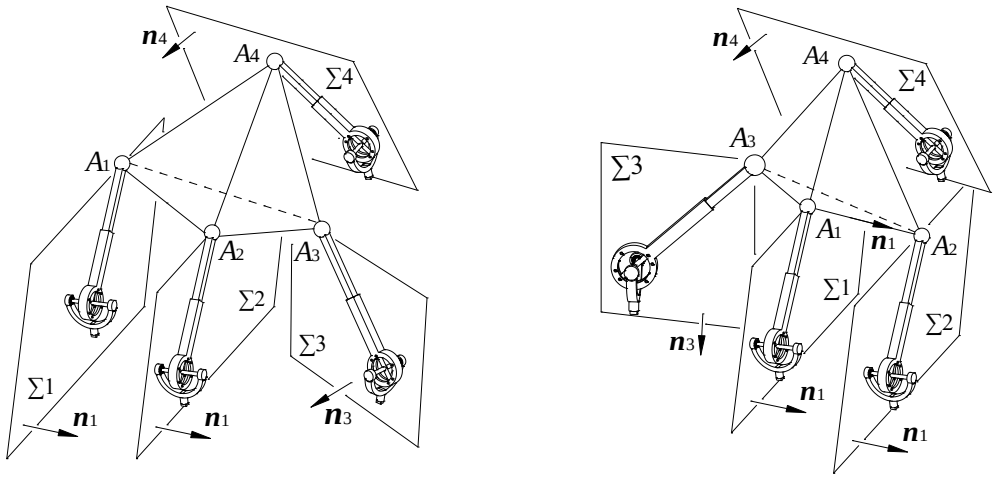

(a) general case (b)d_1-d_2 =l_{12}

Figure 4-13 The 4-(rT)$_2$PS with two parallel planes

Considering two planes are parallel among the four, a special case can be categorized into this section that while two planes are parallel, the other two are also parallel to each other as in Fig. 4-14(a). The geometric constraint is similar with Eq. (4.21) but giving k_1=0, k_3=1 which shows two translation and two rotation constraints and the mechanism has two DOFs with one rotation and one translation perpendicular to both $\boldsymbol{n}_1$ and $\boldsymbol{n}_3$.

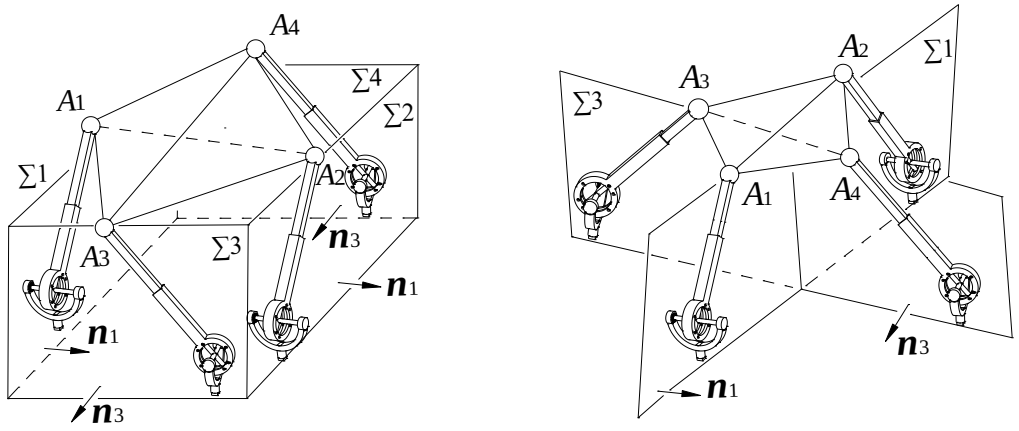

(a) intersecting (b) two-two coincident

Figure 4-14 The 4(rT)$_2$PS with two-two parallel planes

Another case with two pairs of parallel constraint planes is shown in Fig. 4-14(b) with both pairs of parallel planes coincident (d_1=d_2 and d_3=d_4) and its mobility is one rotation and one translation. When further considering that the two constraint planes are perpendicular to each other in Fig. 4-14(b), line A_1A_2 will be perpendicular to A_3A_4. At the configuration that A_1A_2 is perpendicular to constraint plane ∑3 (A_3A_4 is perpendicular to constraint plane ∑1 at the same time), the rotational constraints can be written as:

$$\begin{cases} \mathbf{R}(\boldsymbol{a}_1' - \boldsymbol{a}_2').\boldsymbol{n}_1 = l_{12}\boldsymbol{n}_3.\boldsymbol{n}_1 = 0 \\ \mathbf{R}(\boldsymbol{a}_3' - \boldsymbol{a}_4').\boldsymbol{n}_3 = l_{34}\boldsymbol{n}_1.\boldsymbol{n}_3 = 0 \end{cases} \tag{4.22}$$

Thus, the two constraints are dependent and the mechanism at this configuration has one translational and two rotational DOFs about normal $\boldsymbol{n}_1$ and $\boldsymbol{n}_3$. However, when the mechanism rotates about any direction of the two, Eq. (4.22) does not exist. There will be two rotational constraints and the mechanism has one rotational DOF only. This indicates that the mechanism has bifurcated rotation at the configuration described by Eq. (4.22) with two branch rotations about two orthogonal directions.

4.4.4 Four Intersecting Planes

When none of any two of the four constraint planes are parallel to each other, it comes to a new topology of the mechanism in Fig. 4-15(a) which follows the geometric constraint:

$$\begin{cases} (\mathbf{R}\,\boldsymbol{a}_1' + \boldsymbol{q}).\boldsymbol{n}_1 = d_1 \\ (\mathbf{R}\,\boldsymbol{a}_2' + \boldsymbol{q}).\boldsymbol{n}_2 = d_2 \\ (\mathbf{R}\,\boldsymbol{a}_3' + \boldsymbol{q}).\boldsymbol{n}_3 = d_3 \\ \boldsymbol{n}_4 = k_1\boldsymbol{n}_1 + k_2\boldsymbol{n}_2 + k_3\boldsymbol{n}_3 \\ \mathbf{R}(\boldsymbol{a}_1' - \boldsymbol{a}_4').k_1\boldsymbol{n}_1 + \mathbf{R}(\boldsymbol{a}_2' - \boldsymbol{a}_4').k_2\boldsymbol{n}_2 + \mathbf{R}(\boldsymbol{a}_3' - \boldsymbol{a}_4').k_3\boldsymbol{n}_3 = k_1d_1 + k_2d_2 + k_3d_3 - d_4 \end{cases} \tag{4.23}$$

As there are no parallel planes, generally three of them are independent and the forth normal $\boldsymbol{n}_4$ can be represented by the first three $\boldsymbol{n}_i$ with coefficient k_i (i=1,2,3) as in Eq. (4.23). Thus, Eq.

(4.23) gives three translational and one rotational constraints, leading to that the mechanism has two rotational DOFs.

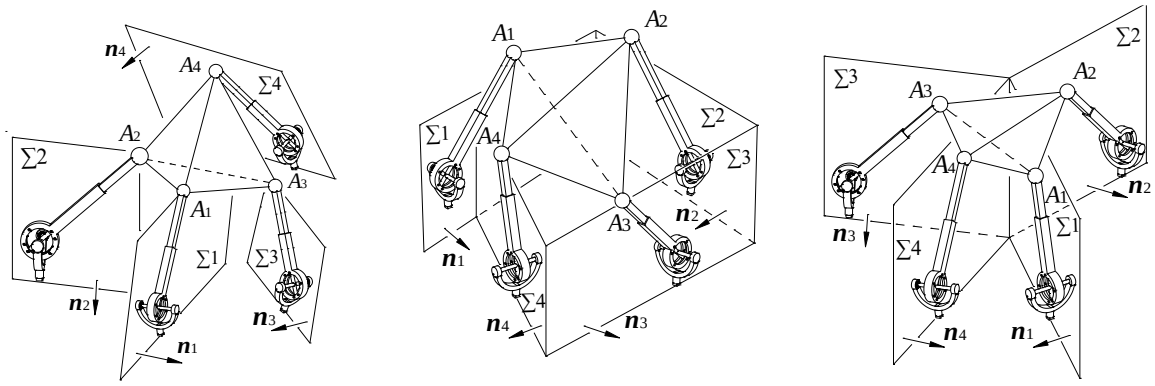

(a) general case (b) four parallel intersecting lines (c) intersecting at one line

Figure 4-15 The 4(rT)$_2$PS with intersecting planes

One special case of the topology in Eq. (4.23) is that there are only two independent normals among the four, indicating that the four normals are in parallel planes as in Fig. 4-15(b) and (c). In this case, the geometric constraint becomes:

$$\begin{cases} (\mathbf{R}\,\boldsymbol{a}_1' + \boldsymbol{q}).\boldsymbol{n}_1 = d_1 \\ (\mathbf{R}\,\boldsymbol{a}_2' + \boldsymbol{q}).\boldsymbol{n}_2 = d_2 \\ \mathbf{R}(\boldsymbol{a}_1' - \boldsymbol{a}_3').k_1\boldsymbol{n}_1 + \mathbf{R}(\boldsymbol{a}_2' - \boldsymbol{a}_3').k_2\boldsymbol{n}_2 = k_1d_1 + k_2d_2 - d_3 \\ \mathbf{R}(\boldsymbol{a}_1' - \boldsymbol{a}_4').k_3\boldsymbol{n}_1 + \mathbf{R}(\boldsymbol{a}_2' - \boldsymbol{a}_4').k_4\boldsymbol{n}_2 = k_3d_1 + k_4d_2 - d_4 \end{cases} \tag{4.24}$$

which give two translational and two rotational constraints. Thus, the mechanisms in Fig. 4-15 (b) and (c) have one rotational DOF and one translational DOF perpendicular to both $\boldsymbol{n}_1$ and $\boldsymbol{n}_2$.

4.4.5 Topology Change of the 4-rTPS MPM

When altering one limb from phase (rT)$_2$*PS* to (rT)$_1$*PS*, the 4-(rT)$_2$*PS* parallel mechanisms in the previous sections become 3(rT)$_2$*PS*-1(rT)$_1$*PS* which can be also obtianed by adding one (rT)$_1$*PS* limb to those 3(rT)$_2$*PS* parallel mechanisms in Section 4.3. Thus, mobility of 3(rT)$_2$*PS*-

1(rT)$_1$*PS* parallel mechanisms is the same with corresponding 3-(rT)$_2$*PS* parallel mechanisms in Section 4.3 and the mobility change map is shown in Fig. 4-16, where *m*T*n*R represents DOFs with *m* translations (T) and *n* rotations (R). Based on the above analysis, the 4(rT)$_2$*PS* can have two rotations (2R) or one translation and one rotation (1T1R). By changing one limb phase, both the two can change to 1T2R while 2R can go to 3R and 1T1R can become 2T1R respectively. By further changing one more limb phase, 3R will be 1T3R and 2T1R will become 2T2R. 1T2R can be both 1T3R and 2T2R. After then, all mechanism will have 5DOFs with 2T3R and all 6DOFs by altering the left two limb phases one by one. In fact, from one topology the mechanism can be changed to any other by changing one or more limbs at the same time, e.g. from mobility 2 directly to 6 by changing all the four limbs at once.

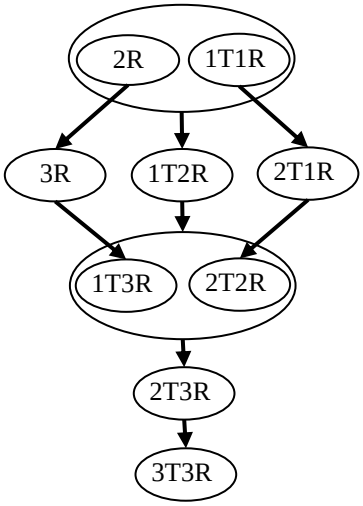

Figure 4-16 Topology and mobility variation map of the 4rT*PS* MPM

4.5 MPMs with Five Limbs

When constructing metamorphic parallel mechanisms with five (rT)$_2$*PS* limbs as in Fig. 4-17, five constraint planes will be considered and their relationship can be classified into four types: (1) Five or four parallel planes; (2) three parallel with the other two parallel or intersecting; (3) two parallel with another two parallel and one intersecting, or with the other three intersecting; (4) five intersecting planes.

Based on the analysis in Section 4.4.1, when the four constraint planes are parallel the fourth limb is redundant. Thus, the first type with five or four parallel planes is redundant case and the

mechanisms have the mobility of two translations and one rotation. The other three types can be simply synthesized by adding one limb to the 4-(rT)$_2$*PS* ones and are not illustrated one by one in this section. Basically these three types fall into two cases in terms of mobility with one rotation or one translation.

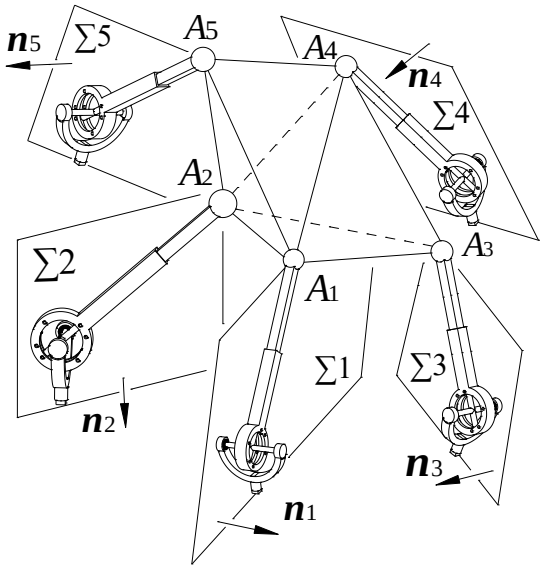

Figure 4-17 The 5-(rT)$_2$PS parallel mechanisms (1R or 1T)

Generally, when there are three normals among the five are independent, the 5(rT)$_2$*PS* parallel mechanism has one rotational DOF as the three independent planes constrain three translations and the other two further constrain two rotations. When the five normals are in parallel planes, two of them are independent and the mechanism has one translational DOF that is perpendicular to all the normals.

Specially, when the five spherical joint centers are in line for the case with one translational DOF, one limb is redundant. This can be analysed from the geometric constraint as:

$$\begin{cases} (\mathbf{R}\,\boldsymbol{a}_1' + \boldsymbol{q}).\boldsymbol{n}_1 = d_1 \\ (\mathbf{R}(\boldsymbol{a}_1' + l_{12}\boldsymbol{m}_1') + \boldsymbol{q}).\boldsymbol{n}_2 = d_2 \\ (\mathbf{R}(\boldsymbol{a}_1' + l_{13}\boldsymbol{m}_1') + \boldsymbol{q}).(k_1\boldsymbol{n}_1 + k_2\boldsymbol{n}_2) = d_3 \\ (\mathbf{R}(\boldsymbol{a}_1' + l_{14}\boldsymbol{m}_1') + \boldsymbol{q}).(k_3\boldsymbol{n}_1 + k_4\boldsymbol{n}_2) = d_4 \\ (\mathbf{R}(\boldsymbol{a}_1' + l_{15}\boldsymbol{m}_1') + \boldsymbol{q}).(k_5\boldsymbol{n}_1 + k_6\boldsymbol{n}_2) = d_5 \end{cases} \tag{4.25}$$

where four spherical joint centers are described by the fifth one $\boldsymbol{a}'$ with distances l_{1i} along a public platform line $\boldsymbol{m}_1'$. Three plane normals of the five are represented by two independent ones by introducing coefficients k_i (i=1,2,…,6).

The last three equations in Eq. (4.25) can be clarified using the first two as:

$$\begin{bmatrix} -k_1 l_{13} & k_2(l_{12}-l_{13}) \\ -k_3 l_{14} & k_4(l_{12}-l_{14}) \\ -k_5 l_{13} & k_6(l_{12}-l_{15}) \end{bmatrix} \begin{bmatrix} \mathbf{R}\,\boldsymbol{m}_1'.\boldsymbol{n}_1 \\ \mathbf{R}\,\boldsymbol{m}_1'.\boldsymbol{n}_2 \end{bmatrix} = \begin{bmatrix} k_1 d_1 + k_2 d_2 - d_3 \\ k_3 d_1 + k_4 d_2 - d_4 \\ k_5 d_1 + k_6 d_2 - d_5 \end{bmatrix} \tag{4.26}$$

which give three rotational constraints of the platform. Thus, it is obvious that one of the three constraints is redundant as two can determine the direction of the platform line $\mathbf{R}\,\boldsymbol{m}_1'$ from Eq. (4.26).

Topology change of the 5(rT)$_2$*PS* parallel mechanisms can be investigated based on the 4(rT)$_2$*PS* ones. By changing the limb phases one by one, topologies can be correspondingly obtained by adding one (rT)$_1$*PS* limb to those in Section 4.4. Meanwhile, the mobility changes from 1 through to 6.

4.6 MPMs with Six Limbs

Generally, when constructing metamorphic parallel mechanisms with six (rT)$_2$*PS* limbs, the assemblies are not mechanisms but structures with no mobility. When any redundant limb exists, the mechanism falls into one of the cases in the previous sections. To separate with previous topologies, those structures can be obtained by assembling the limbs by avoiding the redundant cases including:

1) three constraint planes are parallel and the three spherical joint centers are in line;
2) four constraint planes are parallel;
3) five constraint plane normals are in parallel planes and the five spherical joint centers are in line;
4) six constraint plane normals are in parallel planes;
5) six spherical joint centers are in line.

The last two cases are extended based on Eq. (4.24) and Eq. (4.25). In six-limb assemblies, there are six constraint equations with three for the translations and three for the rotations. When the six plane normals are in parallel planes, one translation DOF exists along the normal of the parallel planes showing one redundant limb. This gives point (4) above. When the six spherical joint centers are in line, the three rotational constraints are dependent as two can determine the direction of the line leading to redundant case (5).

Based on these rules, structures can be obtained by adding one $(rT)_2PS$ limb to the 5-$(rT)_2PS$ topologies which are not illustrated one by one here. Interestingly, these structures can be changed to mechanisms by altering the limb phases from $(rT)_2PS$ to $(rT)_1PS$, which can be demonstrated by a 6-$(rT)_2PS$ as in Fig. 4-18. The 6-$(rT)_2PS$ has a cubic structure formed by three pairs of parallel constraint planes with three independent normals. The spherical joint centers (A_1 and A_2) of limb 1 and limb 2 are constrained in parallel planes with the same normal $\boldsymbol{n}_1=\boldsymbol{n}_2$. This is the same for limb 3 and limb 4 with $\boldsymbol{n}_3=\boldsymbol{n}_4$, limb 5 and limb 6 with $\boldsymbol{n}_5=\boldsymbol{n}_6$. This structure avoids those redundant cases as concluded upon. However, the structure singularity for two parallel constraint planes should also be avoided as in Fig. 4-3(b), where the line connecting the two spherical joint centers is constantly perpendicular to the parallel planes, leading to extra mobility losing.

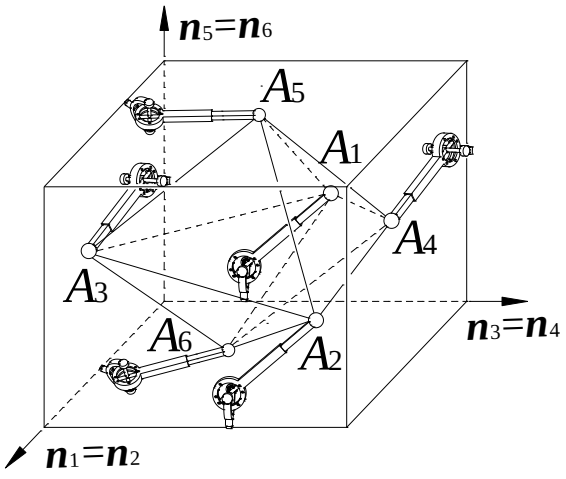

Figure 4-18 The 6-$(rT)_2PS$ structure

The geometric constraint of this 6-$(rT)_2PS$ structure can be given as:

$$\begin{cases} (\mathbf{R}\,\boldsymbol{a}_i' + \boldsymbol{q}).\boldsymbol{n}_i = d_i \\ \mathbf{R}(\boldsymbol{a}_i' - \boldsymbol{a}_{i+1}').\boldsymbol{n}_i = d_i - d_{i+1} \end{cases} \quad (i = 1, 3, 5) \tag{4.27}$$

which shows that each pair of parallel constraint planes give one translational and one rotational constraints.

When change one limb phase from $(rT)_2PS$ to $(rT)_1PS$, one constraint plane vanishes with one constraint equation less, leading to the mechanism mobility increases one. Based on Eq. (4.27), the topology change rule is that when one of each pair of parallel constraint planes vanishes, the rotational constraint is reduced first. Then the translational constraint will be reduced by altering the other limb in the parallel pair. Based on this, there are different topology change routes which are mapped in Fig. 4-19.

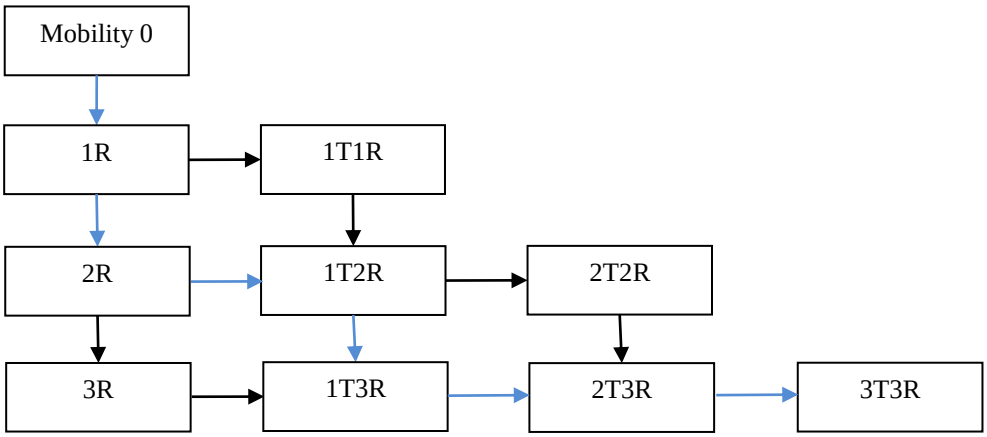

Figure 4-19 Topology change map of the 6-$(rT)_2PS$

In Fig. 4-19, it can be seen that after altering any limb from phase $(rT)_2PS$ to $(rT)_1PS$, the 6-$(rT)_2PS$ structure becomes the 5$(rT)_2PS$-1$(rT)_1PS$ parallel mechanism with 1 rotational DOF (for example, limb 4 is changed). Then, if changing the phase of limb 3 which is in the parallel pair of limb 4, the mechanism will obtain one translational DOF. However, when changing any other limb, the mechanism becomes topology 4$(rT)_2PS$-2$(rT)_1PS$ with two rotational DOFs (2R) (limb 2 is changed). From the 2R case, when changing limb 5 or limb 6, the mechanism will have three rotational DOFs (3R). When changing one of limb 1 and limb 3, it becomes topology 3$(rT)_2PS$-3$(rT)_1PS$ with one translational and two rotational DOFs (1T2R) (limb 3 is changed).

Based on the 1T2R case, when further changing limb 1, the mechanism becomes 2(rT)$_2$*PS*-4(rT)$_1$*PS* with two translational and two rotational DOFs (2T2R). When changing limb 5 or limb 6, the mechanism will have one translational and three rotational DOFs (1T3R) (limb 5 is changed). When changing any limb from the 3R case, it becomes this 1T3R topology as in the map in Fig. 4-19. There are two constraint planes left in both 1T3R and 2T2R topologies. When further changing one of the two corresponding limbs, the mechanism becomes the 1(rT)$_2$*PS*-5(rT)$_1$*PS* with two translational and three rotational DOFs (2T3R) (limb 1 is changed). After changing the last limb, the mechanism obtains one more translational DOF becoming a full mobility topology 6(rT)$_1$*PS*. The topology change route follows the blue arrows in Fig. 4-19, which shows the change map when altering one limb phase each time. In fact, from one topology the mechanism can be changed to any other by changing one or more limbs at the same time, e.g. from mobility zero directly to six DOF by changing all the six limbs at once.

4.7 Summary of Obtained New Metamorphic Parallel Mechanisms

To better show the achieved synthesis results of this class of new metamorphic parallel mechanisms, this section tries to summarize the obtained novel mechanisms in the above five sections and also to compare with existing related reconfigurable parallel mechanisms to show their difference. This will help stress the novelty of this work and also provides justification for further investigating those obtained new mehcanisms. Similar with chapter 3, those new mechanisms are based on the reconfigurable rT joint which is unique from this work, all obtained mechanisms are different with existing ones in the literature in term of the structure. Thus the following comparison is also to discuss the mobility change similarities with other reconfigurable parallel mechanisms.

Table 4-1 Summary of Obtained Metamorphic Parallel Mechanisms

Metamorphic Parallel Mechanisms	Mobility Reconfiguration	Related ones in literature
2-rTPS	4-DOF: 3R1T 5-DOF: 3R2T	No similar ones with two-limb reconfigurable parallel mechanisms found.

	6-DOF: 3R3T	
3-rTPS	3-DOF: 3R, 2R1T, 1R2T 4-DOF: 3R1T 5-DOF: 3R2T 6-DOF: 3R3T	The closely related one can be the reconfigurable parallel mechanisms [98] based on reconfigurable platform principle with mobility change of 1R3T, 3R1T, 1T and 3R3T.
4-rTPS	2-DOF: 2R, 1R1T 3-DOF: 3R, 2R1T, 1R2T 4-DOF: 3R1T, 2R2T 5-DOF: 3R2T 6-DOF: 3R3T	The Diamon chain based metamorphic parallel mechanism [105] can also realize the 3R and 2R1T mobility based on a reconfigurable linkage limb.
5-rTPS	1-DOF: 1R, 1T 2-DOF: 2R, 1R1T 3-DOF: 3R, 2R1T, 1R2T 4-DOF: 3R1T, 2R2T 5-DOF: 3R2T 6-DOF: 3R3T	Related ones can be the reconfigurable platform based parallel mechanisms [98] and the Diamon chain based metamorphic parallel mechanism [105] but they are all based on different reconfiguration principles.
6-rTPS	0-DOF: structure 1-DOF: 1R, 1T 2-DOF: 2R, 1R1T, 2T 3-DOF: 3R, 2R1T, 1R2T 4-DOF: 3R1T, 2R2T 5-DOF: 3R2T 6-DOF: 3R3T	Not found so wide range of mobility change.

Similar to those in chapter 3, the obtained metamorphic parallel mechanisms show very wide range of mobility change. The 6-rTPS metamorphic parallel mechanism covers almost all the possible 3D motion types. There are not exactly the same kind of reconfigurable parallel mechanisms found in the literature but some of them have partially similar mobility change types. It should be noticed that here only the mobility is compared, which does not show the under each mobility how the kinematics and dynamics performance can be. This needs further investigation and comparison.

4.8 Conclusions

Following the general synthesis procedure presented in Chapter 3, this chapter proposed a new synthesis method for a specific class of metamorphic parallel mechanisms using the reconfigurable rTPS limb. The reconfiguration capability of the rTPS limb was modelled and explained using the basic geometric constraint equations representing the motion of the spherical joint center in the limb. It was found in one phase, the spherical joint center could move freely in the space, in another phase it was constrained on a plane. This finding was then used to set up the new synthesis method by considering all possible dependency and 3D arrangement of the constraint planes to construct new parallel mechanism structures. All possible cases have been considered from using two to six rTPS limbs to assemble *n*-$(rT)_2PS$ (n=2,3,..,6) parallel mechanisms.

Another important contribution of this chapter is the geometric constraint equation based mechanism mobility analysis. The platform rotation matrix and translation vector were used to reveal the independent relation among their parameters which clealy represented the independent translation and rotation freedom of the platform. This relation also provided the way to explain all the redundant geometric conditions for the *n*-$(rT)_2PS$ assemblies. By altering the limbs from $(rT)_2PS$ to $(rT)_1PS$, new mechanism phases are obtained with mobility change based on each topology. Generally, an *n*-$(rT)_2PS$ (n=2,3,..,6) parallel mechanism has *n*+1 phases with mobility change varied from 6-*n* to 6.

In addition to the new synthesis and modelling method, the main achievement of this chapter are the obtained new metamorphic parallel mechanisms which have shown very wide range of mobility change capabilities. For example, the 6-rTPS metamorphic parallel mechanism covers almost all the possible 3D space motion types from a structure with mobility 0 to the full mobility 6. Some novel symmetrical mechanisms have also been found and have potential good performance for real applications, like the 3-rTPS and 4-rTPS metamorphic parallel mechanisms which are going to be studied more on their reconfiguration in Chapter 5 and kinematics modelling in Chapter 6.

Chapter 5 Some Novel MPMs and Their Reconfiguration

Based on the synthesis results from the previous two chapters, some novel metamorphic parallel mechanisms are slected and their mobility change and reconfiguration are investigated in this chapter. This also provides the basis for further kinematics and dynamics analysis in the following chapters.

5.1 The 3-rTPS MPM with Perpendicular Constraint Screws

5.1.1 Geometric Constraints of the 3-rTPS MPM

The 3rT*PS* metamorphic parallel mechanism is shown in Fig. 5-1 with all limbs in phase $(rT)_2PS$. The three limbs are arranged symmetrically on three perpendicular planes with the bracket axes perpendicular to the planes [143] as in Fig. 5-1.

Let points A_i and B_i denote the spherical joint center and the rT joint center in limb i (i=1,2,3) respectively. Locate a global coordinate system *oxyz* at point *o* with *x* axis passing through rT joint center B_2 in limb 2 and *y* axis passing through rT joint center B_3 in limb 3 as in Fig. 5-1. Then, *z* axis passes through rT joint center B_1 in limb 1. Let a_i and b_i denote the vectors of points A_i and B_i in the coordinate system *oxyz*, l_i be the limb length between the spherical joint center A_i and the rT joint center B_i.

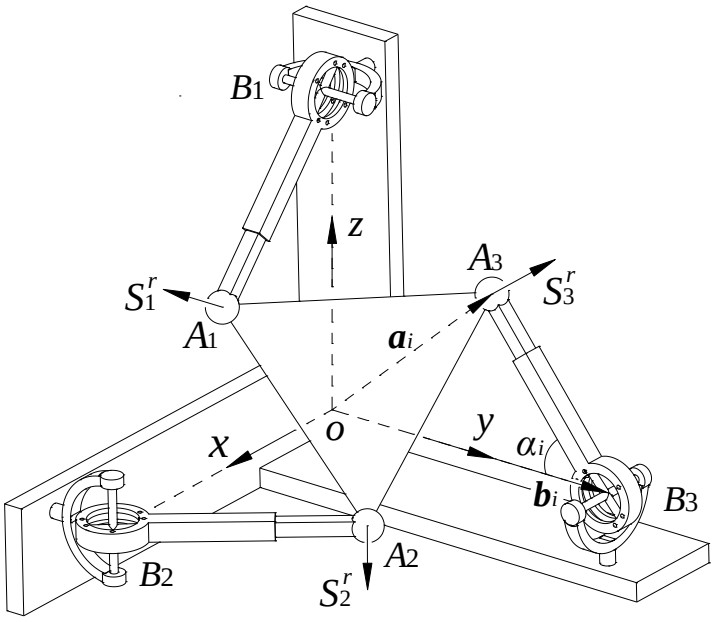

Figure 5-1 The 3-$(rT)_2PS$ with three perpendicular constraint screws

Based on the description in Fig. 5-1, the parameters expressed in the coordinate system *oxyz* can be given as

$$\begin{cases} \boldsymbol{b}_1 = (0,0,r_b),\ \boldsymbol{a}_1 = \boldsymbol{b}_1 + l_1(\sin\alpha_1, 0, -\cos\alpha_1) \\ \boldsymbol{b}_2 = (r_b,0,0),\ \boldsymbol{a}_2 = \boldsymbol{b}_2 + l_2(-\cos\alpha_2, \sin\alpha_2, 0) \\ \boldsymbol{b}_3 = (0,r_b,0),\ \boldsymbol{a}_3 = \boldsymbol{b}_3 + l_3(0, -\cos\alpha_3, \sin\alpha_3) \end{cases} \tag{5.1}$$

where α_i is the angle between limb *i* and the line oB_i passing through the rT joint center B_i and the coordinate system origin *o*.

From Eq. (4.2), it can be seen that (rT)$_2$*PS* limb supplies one constraint force to the platform with the direction parallel to its bracket axis. Thus, the constraint system of the 3-(rT)$_2$*PS* parallel mechanism in Fig. 5-1 can be given as:

$$\left\{\boldsymbol{S}^r\right\} = \begin{Bmatrix} \boldsymbol{S}_1^r = \left[(0,1,0) \quad \boldsymbol{a}_1 \times (0,1,0)\right] \\ \boldsymbol{S}_2^r = \left[(0,0,1) \quad \boldsymbol{a}_2 \times (0,0,1)\right] \\ \boldsymbol{S}_3^r = \left[(1,0,0) \quad \boldsymbol{a}_3 \times (1,0,0)\right] \end{Bmatrix} = \begin{Bmatrix} [0 \quad 1 \quad 0 \quad l_1\mathrm{c}\alpha_1 - r_b \quad 0 \quad l_1\mathrm{s}\alpha_1], \\ [0 \quad 0 \quad 1 \quad l_2\mathrm{s}\alpha_2 \quad l_2\mathrm{c}\alpha_2 - r_b \quad 0], \\ [1 \quad 0 \quad 0 \quad 0 \quad l_3\mathrm{s}\alpha_3 \quad l_3\mathrm{c}\alpha_3 - r_b] \end{Bmatrix} \tag{5.2}$$

which are three constraint forces perpendicular to each other.

By taking reciprocal screws to Eq. (5.2), motion screws of the mechanism can be obtained as:

$$\left\{\boldsymbol{S}_m\right\} = \begin{Bmatrix} [1 \quad 0 \quad 0 \quad 0 \quad r_b - l_1\mathrm{c}\alpha_1 \quad -l_2\mathrm{s}\alpha_2], \\ [0 \quad 1 \quad 0 \quad -l_3\mathrm{s}\alpha_3 \quad 0 \quad r_b - l_2\mathrm{c}\alpha_2], \\ [0 \quad 0 \quad 1 \quad r_b - l_3\mathrm{c}\alpha_3 \quad -l_1\mathrm{s}\alpha_1 \quad 0]. \end{Bmatrix} \tag{5.3}$$

which represent three rotational DOFs with directions parallel to the axes of the coordinate system *oxyz*.

Thus, the 3-(rT)$_2$*PS* parallel mechanism with perpendicular constraint screws has mobility three with pure rotations, which is similar to the pyramid parallel mechanism [139] consisting of three *RPS* limbs in three perpendicular constraint planes.

5.1.2 Topology Change of the 3-rTPS MPM

Altering the (rT)$_2$*PS* limbs in the previous 3-(rT)$_2$*PS* parallel mechanism into the phase (rT)$_1$*PS* will result in various new mechanism topologies with increased mobility. After changing the phase of limb 1, the 3-(rT)$_2$*PS* parallel mechanism becomes the topology in Fig. 5-2 with name of 2(rT)$_2$*PS*-1(rT)$_1$*PS*.

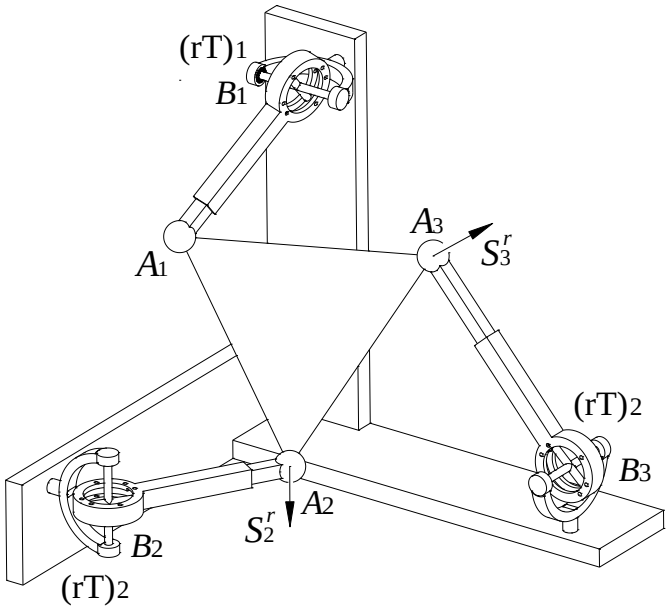

Figure 5-2 The 2(rT)$_2$*PS*-1(rT)$_1$*PS* with two perpendicular constraint screws

Since the (rT)$_1$*PS* limb does not supply any constraint on the platform, the first constraint screw in Eq. (5.2) vanishes and the other two constraint forces in Eq. (5.2) are left on the platform as in Fig. 3. The reciprocity of this two-screw system gives one more motion screw than those three in Eq. (5.3) as:

$$\boldsymbol{S}_{m1} = \begin{bmatrix} 0 & 0 & 0 & 0 & 1 & 0 \end{bmatrix} \tag{5.4}$$

which is a translation along *y* axis.

Thus, the 2(rT)$_2$*PS*-1(rT)$_1$*PS* parallel mechanism has four DOFs with one translation and three rotations, which is one more DOF than the 3-(rT)$_2$*PS* in Fig. 5-1. Hence, with the topology change from 3(rT)$_2$*PS* to 2(rT)$_2$*PS*-1(rT)$_1$*PS*, the mobility of the mechanism increases one.

When further changing the phase of limb 2 to (rT)$_1$*PS*, the 2(rT)$_2$*PS*-1(rT)$_1$*PS* topology in Fig. 5-2 changes to the 1(rT)$_2$*PS*-2(rT)$_1$*PS* in Fig. 5-3(a). Based on the platform constraint system in Eq. (5.2), only the third constraint screw is left and platform motion screw system has one more translation screw along *z*-axis than those in Eq. (5.3) and Eq. (5.4). Thus, the 1(rT)$_2$*PS*-2(rT)$_1$*PS* parallel mechanism has five DOFs with two translations and three rotations, indicating that one more mobility gained after changing the topology from 2(rT)$_2$*PS*-1(rT)$_1$*PS* to 1(rT)$_2$*PS*-2(rT)$_1$*PS*.

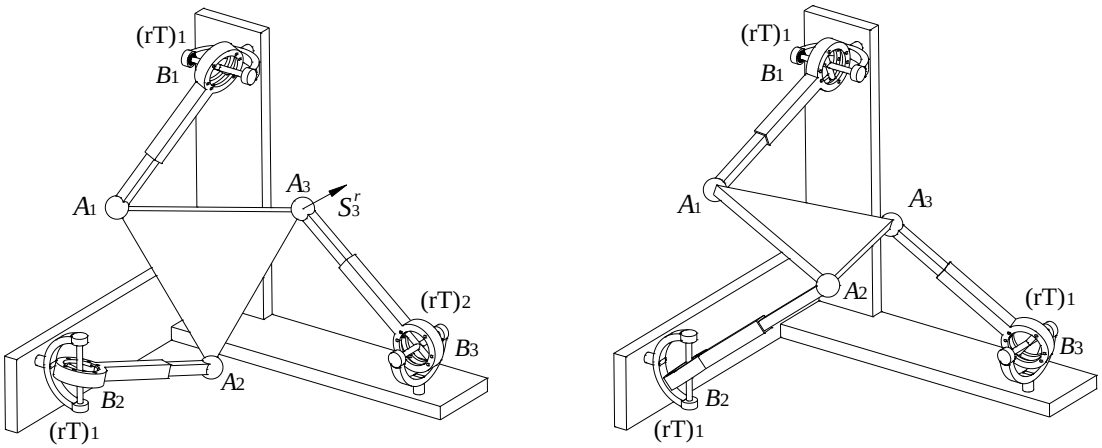

(a) 1(rT)$_2$*PS*-2(rT)$_1$*PS* (b) 3(rT)$_1$*PS*

Figure 5-3 Two more topologies of the 3rT*PS*

Finally, when changing the third limb to phase (rT)$_1$*PS*, the mechanism becomes another topology 3-(rT)$_1$*PS* as in Fig. 5-3(b) with no constraint on the platform. Thus, the mechanism changes to the topology with mobility 6.

The foregoing analysis shows that when changing phases of limb 1, limb 2 and limb 3 one after another, the 3-(rT)$_2$*PS* parallel mechanism changes to three other topologies with mobility change from 3 to 4, to 5 and then to 6. However, this only shows one procedure of topology change of the 3rT*PS* parallel mechanism. When changing the limb phases in different orders and with different numbers at the same time, the four topologies can be altered into any other. The rule is that there is the translation along *y* axis when limb 1 is in phase (rT)$_1$*PS* and it is

constrained when limb 1 is in phase $(rT)_2PS$. Similarly, limb 2 and limb 3 correspond to the translation along *z* and *x* axes respectively. The combination of the phases of the three limbs contributes to different mechanism topologies with variable mobility.

Based on this, a mobility change map can be illustrated in Fig. 5-4, in which $3R1T_k$ means three rotations with 1 translation along *k* axis, $3R2T_{ki}$ means three rotations with 2 translations along *k* and *i* axes, 3R3T represent full mobility 6. The double-arrow lines between any two mobility types indicate that any two of them can be changed into each other. For example, change from 3R to $3R2T_{xy}$ can be realized by altering phases of limb 1 and limb 3 from $(rT)_2PS$ to $(rT)_1PS$ at the same time based on the topology 3-$(rT)_2PS$ in Fig. 5-1. The obtained 1$(rT)_2PS$-2$(rT)_1PS$ topology has three rotations and two translations along *x* and *y* axes.

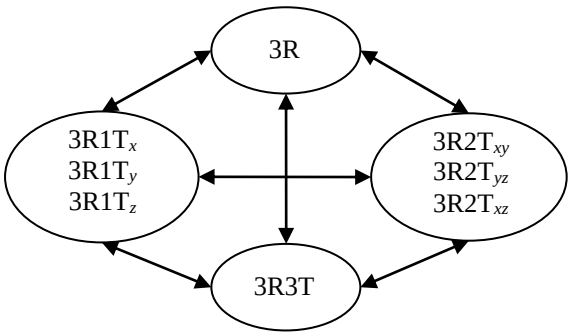

Figure 5-4 Mobility change map

5.2 The 4-rTPS MPM with Bifurcated Motion

5.2.1 Geometric Constraints of the 4-rTPS MPM

The 4-$(rT)_2PS$ metamorphic parallel mechanism consisting of four $(rT)_2PS$ limbs is shown in Fig. 5-5, in which the four limbs are arranged symmetrically on a circle with radius r_a on the platform and a circle with radius r_b on the base [144]. Let A_i be the center point of the spherical joint and B_i be the rT joint center in limb *i* as Fig. 5-5. Locate a fixed coordinate system *Oxyz* at the geometric center *O* of the square $B_1B_2B_3B_4$ with *x*-axis passing through B_1 and *y*-axis passing through B_2. Similarly, attach a platform coordinate system *Guvw* at the geometric center *G* of square $A_1A_2A_3A_4$ with *u*-axis passing through A_1 and *v*-axis passing through A_2. Based on the geometric constraint in Eq. (4.2), the spherical joint centers A_i are constrained in their own planes:

$$\begin{cases} \boldsymbol{a}_i.(0,1,0)^{\mathrm{T}} = (\mathbf{R}\,\boldsymbol{a}_i' + \boldsymbol{p}).(0,1,0)^{\mathrm{T}} = 0 \quad (i = 1,3) \\ \boldsymbol{a}_j.(1,0,0)^{\mathrm{T}} = (\mathbf{R}\,\boldsymbol{a}_j' + \boldsymbol{p}).(1,0,0)^{\mathrm{T}} = 0 \quad (j = 2,4) \end{cases} \tag{5.5}$$

where $\boldsymbol{a}_i'$ is the vector of A_i expressed in the platform coordinate system *Guvw* and can be given as $\boldsymbol{a}_1' = -\boldsymbol{a}_3' = r_a(1,0,0)^{\mathrm{T}}$, $\boldsymbol{a}_2' = -\boldsymbol{a}_4' = r_a(0,1,0)^{\mathrm{T}}$, **R**= (*u*, *v*, *w*) and $\boldsymbol{p} = (p_x, p_y, p_z)^{\mathrm{T}}$ are the transformation matrix and the translation vector of platform coordinate system *Guvw* with respect to the fixed coordinate system *Oxyz*, *u*, *v*, *w* are unit vectors of the axes of platform coordinate system *Guvw* expressed in the fixed coordinate system *Oxyz* with $u=(u_x, u_y, u_z)^{\mathrm{T}}$, $v=(v_x, v_y, v_z)^{\mathrm{T}}$, $w=(w_x, w_y, w_z)^{\mathrm{T}}$.

From Eq. (5.5) and the above assumption, there is

$$\begin{cases} (\boldsymbol{a}_1 - \boldsymbol{a}_3) = \mathbf{R}(\boldsymbol{a}_1' - \boldsymbol{a}_3').(0,1,0)^{\mathrm{T}} = r_a\boldsymbol{u}.(0,1,0)^{\mathrm{T}} = r_a u_y = 0 \\ (\boldsymbol{a}_2 - \boldsymbol{a}_4) = \mathbf{R}(\boldsymbol{a}_2' - \boldsymbol{a}_4').(1,0,0)^{\mathrm{T}} = r_a\boldsymbol{v}.(1,0,0)^{\mathrm{T}} = r_a v_x = 0 \end{cases} \tag{5.6}$$

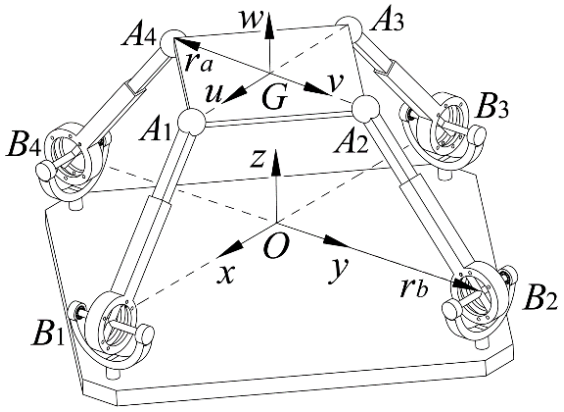

Figure 5-5 The 4-(rT)$_2$*PS* MPM with bifurcated motion

Thus, there is $v_x = 0$ and $u_y = 0$, substituting these into the orthogonal property of matrix R leads to the following

$$u_x v_x + u_y v_y + u_z v_z = u_z v_z = 0 \tag{5.7}$$

The above equation presents two possible rotations but cannot be simultaneously executed. This leads to two bifurcated rotations and a home position based on three motion possibilities. They are home position when $u_z = v_z = 0$ with rotation matrix R becoming the identity matrix I, branch 1 motion as $u_z = 0$, $v_z \neq 0$ with R as a pure rotation about *x*-axis and branch 2 motion as $u_z \neq 0$, $v_z = 0$ with R as a pure rotation about *y*-axis. This indicates whenever if the platform tilts to one direction from the constraint singularity, it falls into that directional rotation. Vice vase, when the platform tilts to another direction, it falls into another directional rotation. These two motions cannot be executed simultaneously.

Expanding Eq. (5.5) when *i*=1 and *j*=2, there is

$$\begin{cases} (\mathbf{R}\boldsymbol{a}_1' + \boldsymbol{p}).(0,1,0)^{\mathrm{T}} = r_a u_y + p_y = p_y = 0 \\ (\mathbf{R}\boldsymbol{a}_2' + \boldsymbol{p}).(1,0,0)^{\mathrm{T}} = r_a v_x + p_x = p_x = 0 \end{cases} \tag{5.8}$$

which determines the property of the translation vector *p* with elements on *x*-axis and *y*-axis being zeros.

From the above analysis, it can be concluded that the four geometric constraints in Eq. (5.5) lead to two rotational constraints in Eq. (5.6) and two translational constraints in Eq. (5.8). Thus, the mechanism has one translation along *z*-axis and one rotation, a pure rotation either about *x*-axis or *y*-axis, bifurcated based on Eq. (5.7).

5.2.2 Topology Change based Reconfiguration of the 4-(rT)2PS MPM

When altering the limb phases from $(rT)_2PS$ to $(rT)_1PS$, the $4(rT)_2PS$ parallel mechanism will change to different topologies with variable mobility. First, changing the phase of limb 1, the mechanism becomes the topology $3(rT)_2PS$-$1(rT)_1PS$ as in Fig. 5-6(a). Based on the geometric constraint, there will be one geometric constraint less in the mechanism in Eq. (5.5) by reducing *i*=1 for limb 1. Then, the relation can be given as:

$$\begin{cases} r_a u_y + p_y = 0 \\ r_a v_x + p_x = p_x = 0 \\ v_x = 0 \end{cases} \tag{5.9}$$

which shows that the there is one constraint for the rotation with v_x=0 and two constraints for the translation with p_x=0 and p_y depending on the rotation. Thus, the 3(rT)$_2$*PS*-1(rT)$_1$*PS* parallel mechanism has mobility three with two rotations and one translation.

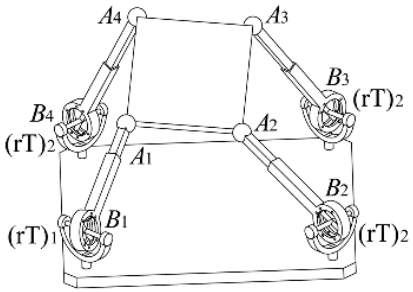

(a) 3(rT)$_2$*PS*-1(rT)$_1$*PS* (1T2R)

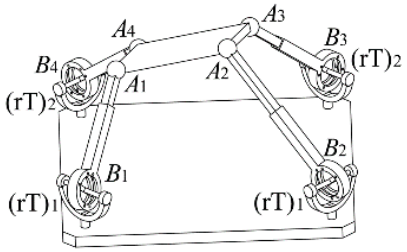

(b) 2(rT)$_2$*PS*-2(rT)$_1$*PS* (2T2R)

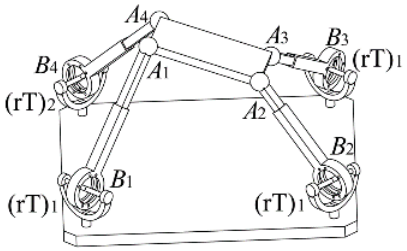

(c) 1(rT)$_2$*PS*-3(rT)$_1$*PS* (2T3R)

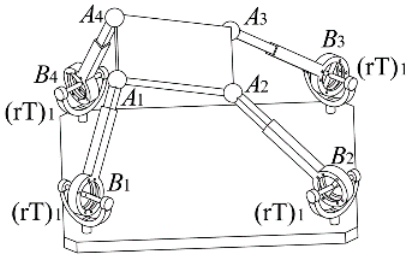

(d) 4(rT)$_1$*PS* (3T3R)

Figure 5-6 Variable topologies of the 4(rT)*PS* MPM

When further changing the phase of limb 2, the mechanism becomes the topology 2(rT)$_2$*PS*-2(rT)$_1$*PS* as in Fig. 5-6(b). Hence, one more constraint vanishes in Eq. (5.5) and the geometric constraints become:

$$\begin{cases} r_a u_y + p_y = 0 \\ r_a v_x + p_x = 0 \end{cases} \tag{5.10}$$

which presents that the translation elements p_x and p_y depend on the platform rotation and there is no constraint on the rotation matrix. Thus, the $2(rT)_2PS$-$2(rT)_1PS$ parallel mechanism has mobility four with three rotations and one independent translation along *z*-axis.

Following the above, a new topology $1(rT)_2PS$-$3(rT)_1PS$ will be obtained by changing the phase of limb 3 as in Fig. 5-6(c). In this case, only the second constraint in Eq. (5.10) is left, indicating that translation elements p_x can be determined by the platform rotation. Thus, the new mechanism has five degrees of freedom with one translation along *x*-axis constrained.

Finally, after further changing the forth limb into phase $(rT)_1PS$, the mechanism becomes the topology $4(rT)_1PS$ as in Fig. 5-6(d) with full mobility 6 as there is no geometric constraints for the platform by the limbs.

From this, it can be seen that the limb phases determine the topology and mobility of the mechanism. It's worth noticing that when changing the limb phases in different orders, the mechanism can have different topologies with those in Fig. 5-6. For example, in the reconfiguration from topology $3(rT)_2PS$-$1(rT)_1PS$ in Fig. 5-6(a) to $2(rT)_2PS$-$2(rT)_1PS$ in Fig. 5-6(b), when altering the phase of limb 3 instead of limb 2, the mechanism becomes a new topology $2(rT)_2PS$-$2(rT_{13})_1PS$ with mobility four of two translations and two rotations. Here, rT_{13} is used to indicate that the $(rT)_1PS$ phases are from limb 1 and limb 3. Based on this, all the topologies with variable mobility are concluded in Table I, in which $1R_{x/y}$ represents the bifurcated rotation about *x*-axis or *y*-axis, $2R_{xy}$ means two rotations about *x*-axis and *y*-axis, $1T_z$, $2T_{xz}$ and $2T_{yz}$ indicate 1 or 2 translations along the corresponding axes in the subscripts. In Table I, any two mobility types can be changed into each other directly by changing corresponding limb phases. For example, when changing the phases of limb 2 and limb 4 from $(rT)_2PS$ to $(rT)_1PS$ in $4(rT)_2PS$, the topology can be directly change into $2(rT)_2PS$-$2(rT_{24})_1PS$ with mobility $2T_{yz}2R_{xy}$. When further altering the other two limb phases to $(rT)_1PS$, the mechanism becomes directly to $4(rT)_1PS$ with full mobility 3T3R. The inverse phase change also works.

Table 5-1 Variable Topologies and mobility of the 4-rTPS

Mobility	DOFs	Topologies
2	$1T_z1R_{x/y}$	$4(rT)_2PS$
3	$1T_z2R_{xy}$	$3(rT)_2PS$-$1(rT_i)_1PS$ (i=1,2,3,4)
4	$2T_{xz}2R_{xy}$	$2(rT)_2PS$-$2(rT_{13})_1PS$
	$2T_{yz}2R_{xy}$	$2(rT)_2PS$-$2(rT_{24})_1PS$
	$1T_z3R$	$2(rT)_2PS$-$2(rT_{ij})_1PS$ (i=1,3, j=2,4)
5	$2T_{xz}3R$	$1(rT_i)_2PS$-$3(rT)_1PS$ (i=2,4)
	$2T_{yz}3R$	$1(rT_i)_2PS$-$3(rT)_1PS$ (i=1,3)
6	3T3R	$4(rT)_1PS$

5.3 The 3-rTPrT MPM with Pure Rotation and Pure Translation

5.3.1 The 3-rTPrT MPM with Pure Rotation

Two kinds of 3-*UPU* parallel mechanisms have been studied widely by scholars [60, 61]. They are pure translational 3-*UPU* parallel mechanisms and pure rotational 3-*UPU* parallel mechanisms. The 3-*UPU* parallel mechanism can also have four degrees of freedom and the instantaneous fifth degree of freedom. By replacing the *U* joints with the six rT joints in the assembly configuration, the 3-rT*P*rT parallel mechanism is generated and has the ability of mobility change from pure rotations to pure translations and further having mobility four.

In each leg, installing an rT joint at the lower end connecting base and an rT joint at the top end connecting the platform together with a prismatic joint in the middle, each leg becomes a rT*P*rT leg. The 3-rT*P*rT parallel mechanism is shown in Fig. 5-7. The limbs support the platform symmetrically around a reference circle of radius r_p and connect to the base around a circle of radius r_b. All the axes of the rings of the rT joints intersect at one point as in Fig. 5-7. Together with the structure of the limb, these satisfy the geometric conditions needed for the pure rotational 3-rT*P*rT parallel mechanism. This requires one of the two axes of the rT joint at each end of the limb be intersecting at a single point while the remaining axis of the rT joint be parallel to other remaining axis of the rT joint at the other end of the limb. These two axes are perpendicular to the limb.

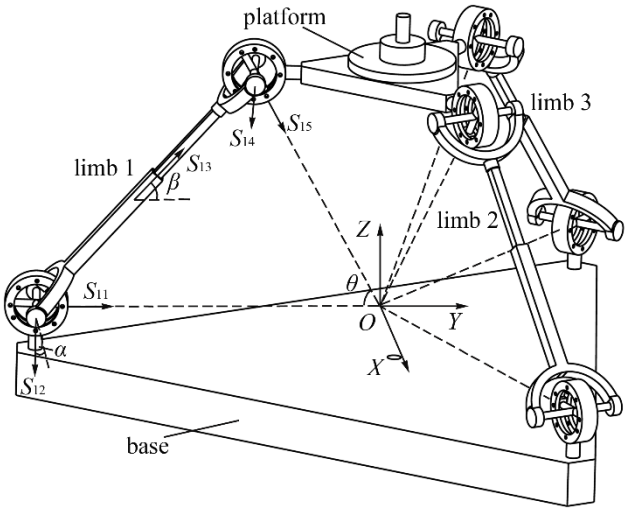

Figure 5-7 The 3-rT*P*rT with pure rotation

As all the limbs have the same structure, analysing one of them in a general configuration and expanding the result to others, the constraints to the moving platform can then be obtained and the mobility of the whole mechanism is known. Set a coordinate system *OXYZ* at the intersecting point with its *Y* axis align with the first rotation axis S_{11} of the rT joint in limb 1, the limb twist system can be obtained as

$$\left\{\boldsymbol{S}_1\right\}=\left\{\begin{array}{l}\boldsymbol{S}_{11}=[0\quad 1\quad 0\quad 0\quad 0\quad 0]\\ \boldsymbol{S}_{12}=[\mathrm{c}\alpha\quad 0\quad \mathrm{s}\alpha\quad -r\mathrm{s}\alpha\quad 0\quad r\mathrm{c}\alpha]\\ \boldsymbol{S}_{13}=[0\quad 0\quad 0\quad -\mathrm{s}\beta\mathrm{s}\alpha\quad \mathrm{c}\beta\quad \mathrm{s}\beta\mathrm{c}\alpha]\\ \boldsymbol{S}_{14}=[\mathrm{c}\alpha\quad 0\quad \mathrm{s}\alpha\quad \mathrm{s}\alpha(l\mathrm{c}\beta-r)\quad l\mathrm{s}\beta\quad \mathrm{c}\alpha(r\text{-}l\mathrm{c}\beta)]\\ \boldsymbol{S}_{15}=[-\mathrm{s}\theta\mathrm{s}\alpha\quad \mathrm{c}\theta\quad \mathrm{s}\theta\mathrm{c}\alpha\quad 0\quad 0\quad 0]\end{array}\right\} \tag{5.11}$$

where α is the angle between S_{12} and axis *X*, β is the angle between S_{13} and its projection on the *XO Y* plane. S_{11} and S_{15} intersect at *O* forming angle θ.

Calculating the reciprocal screws to the 5-system in Eq. (5.11), the limb constraint system is

$$\left\{\boldsymbol{S}_1^r\right\}=\boldsymbol{S}_1^r=\left[\mathrm{c}\alpha\quad 0\quad \mathrm{s}\alpha\quad 0\quad 0\quad 0\right] \tag{5.12}$$

This gives a constraint force vector parallel with S_{12} and passing through origin O and there is no local mobility. The remaining two limb constraint systems can be obtained by rotating $\boldsymbol{S}_1^r$ about Z axis by φ= ±2π/3 as described by the following matrices

$$\mathbf{T}(\varphi)(\boldsymbol{S}_1^r)^{\mathrm{T}} = \begin{bmatrix} \mathbf{R}(\varphi) & 0 \\ 0 & \mathbf{R}(\varphi) \end{bmatrix} (\boldsymbol{S}_1^r)^{\mathrm{T}},\ \mathbf{R}(\varphi) = \begin{bmatrix} \mathrm{c}\varphi & \mathrm{s}\varphi & 0 \\ \text{-}\mathrm{s}\varphi & \mathrm{c}\varphi & 0 \\ 0 & 0 & 1 \end{bmatrix} \tag{5.13}$$

Thus the remaining two limb constraint forces are

$$\begin{aligned} \boldsymbol{S}_2^r &= \left[-\frac{1}{2}\mathrm{c}\alpha \quad \frac{\sqrt{3}}{2}\mathrm{c}\alpha \quad \mathrm{s}\alpha \quad 0 \quad 0 \quad 0 \right], \\ \boldsymbol{S}_3^r &= \left[-\frac{1}{2}\mathrm{c}\alpha \quad -\frac{\sqrt{3}}{2}\mathrm{c}\alpha \quad \mathrm{s}\alpha \quad 0 \quad 0 \quad 0 \right] \end{aligned} \tag{5.14}$$

In the mechanism, there are no common constraint and redundant constraint. The local mobility of each limb is also equal to zero. Thus the constraint system base of the mechanism is given as

$$\left\{ \boldsymbol{S}^r \right\} = \begin{Bmatrix} \begin{bmatrix} 1 & 0 & 0 & 0 & 0 & 0 \end{bmatrix}, \\ \begin{bmatrix} 0 & 1 & 0 & 0 & 0 & 0 \end{bmatrix}, \\ \begin{bmatrix} 0 & 0 & 1 & 0 & 0 & 0 \end{bmatrix} \end{Bmatrix} \tag{5.15}$$

The three translational DOFs of the moving platform are constrained and the 3-rT*P*rT parallel mechanism has pure rotational DOFs.

Here, a special feature of the pure rotational 3-rT*P*rT parallel mechanism with the new rT joints can be found. As the ring of the rT joint can be turned about an axis of the rT joint by any angle in the range of 360°, directions of S_{11} and S_{15} at limb 1, of S_{21} and S_{25} at limb 2 and of S_{31} and S_{35} at limb 3 can be altered freely that the intersecting point can be moved along the Z axis. Thus the platform can rotate about any point on the Z axis after altering the rT joints into

different configurations. Consequently the workspace and other properties of this mechanism may be changed.

5.3.2 Reconfiguration To a Pure Translational Configuration

The above 3-rT*P*rT metamorphic parallel mechanism can be evolved into a pure translational configuration by altering the rotation axes of the ring part of the rT joints in all the three limbs to be parallel as in Fig. 5-8.

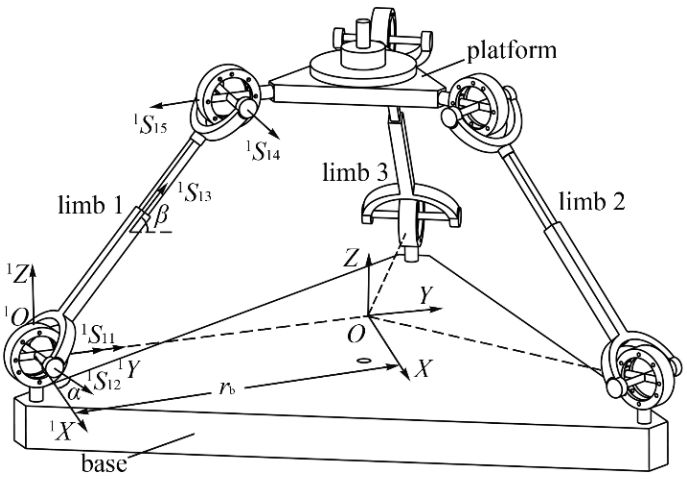

Figure 5-8 The 3-rT*P*rT with pure translation

Attach a local coordinate system ${}^1O{}^1X{}^1Y{}^1Z$ in Fig. 5-8 to the lower rT joint of limb 1 with its ${}^1Y$ axis aligned with the rotation axis of the grooved ring of the rT joint and ${}^1Z$ axis normal to the base, and after the platform experiences an arbitrary motion, the twist system in limb 1 is given as

$$\left\{{}^1\boldsymbol{S}_1\right\}=\left\{\begin{array}{l}{}^1\boldsymbol{S}_{11}=[0\quad 1\quad 0\quad 0\quad 0\quad 0]\\ {}^1\boldsymbol{S}_{12}=[\mathrm{c}\alpha\quad 0\quad \mathrm{s}\alpha\quad 0\quad 0\quad 0]\\ {}^1\boldsymbol{S}_{13}=[0\quad 0\quad 0\quad -\mathrm{s}\beta\mathrm{s}\alpha\quad \mathrm{c}\beta\quad \mathrm{s}\beta\mathrm{c}\alpha]\\ {}^1\boldsymbol{S}_{14}=[\mathrm{c}\alpha\quad 0\quad \mathrm{s}\alpha\quad l\mathrm{c}\beta\mathrm{s}\alpha\quad l\mathrm{s}\beta\quad -l\mathrm{c}\beta\mathrm{c}\alpha]\\ {}^1\boldsymbol{S}_{15}=[0\quad 1\quad 0\quad -l\mathrm{s}\beta\mathrm{c}\alpha\quad 0\quad -l\mathrm{s}\beta\mathrm{s}\alpha]\end{array}\right\} \tag{5.16}$$

where the first two twists are for the lower rT joint, the third is for the prismatic joint, and the last two are for the upper rT joint in the limb; and α is the angle between ${}^1S_{12}$ and axis ${}^1X$, β is the angle between ${}^1S_{13}$ and its projection on the ${}^1X{}^1O{}^1Y$ plane, l is the distance between the two rT joint centers along the limb. This forms a 5-system and the limb constraint system is given as

$$\left\{{}^1\boldsymbol{S}_1^r\right\} = {}^1\boldsymbol{S}_1^r = \begin{bmatrix} 0 & 0 & 0 & -\mathrm{s}\alpha & 0 & \mathrm{c}\alpha \end{bmatrix} \tag{5.17}$$

This gives a constraint couple normal to the axes of the universal joints and there is no local degree of freedom with this arrangement of the limb.

The limb constraint can be transformed to the global reference frame fixed at the centre of the base by translating a distance of r_b along the *Y* axis [124, 145] by using the following equation

$$\boldsymbol{S}_1^r = ({}_1^0\mathbf{T})({}^1\boldsymbol{S}_1^r)^{\mathrm{T}} \tag{5.18}$$

Where,

$${}_1^0\mathbf{T} = \begin{bmatrix} \mathbf{I} & 0 \\ \mathbf{A} & \mathbf{I} \end{bmatrix},\ \mathbf{A} = \begin{bmatrix} 0 & 0 & -r_b \\ 0 & 0 & 0 \\ r_b & 0 & 0 \end{bmatrix}$$

As the symmetric structure of the three-leg parallel mechanism, the other two branches constraint couples can be obtained by rotating $\boldsymbol{S}_1^r$ about the *Z* axis by φ = ±2π/3 using Eq. (5.13).

Thus the remaining two limb constraint couples are

$$\begin{aligned} \boldsymbol{S}_2^r &= \begin{bmatrix} 0 & 0 & 0 & \frac{1}{2}\mathrm{s}\alpha & \frac{\sqrt{3}}{2}\mathrm{s}\alpha & \mathrm{c}\alpha \end{bmatrix}, \\ \boldsymbol{S}_3^r &= \begin{bmatrix} 0 & 0 & 0 & \frac{1}{2}\mathrm{s}\alpha & -\frac{\sqrt{3}}{2}\mathrm{s}\alpha & \mathrm{c}\alpha \end{bmatrix} \end{aligned} \tag{5.19}$$

In the mechanism, there is no common constraint and no redundant constraint. The local mobility of each limb is zero. The constraint system base is thus given as

$$\left\{\boldsymbol{S}^r\right\} = \begin{Bmatrix} \begin{bmatrix} 0 & 0 & 0 & 1 & 0 & 0 \end{bmatrix}, \\ \begin{bmatrix} 0 & 0 & 0 & 0 & 1 & 0 \end{bmatrix}, \\ \begin{bmatrix} 0 & 0 & 0 & 0 & 0 & 1 \end{bmatrix} \end{Bmatrix} \tag{5.20}$$

Hence three rotational mobility of the moving platform are constrained and the 3-rT*P*rT parallel mechanism has pure translational mobility.

5.3.3 Reconfiguration to Three Translations and One Rotation Mobility

Reconfiguring the rotation axes of the ring part of the rT joint in each limb to be perpendicular to the base plane results in a new 3-rT*P*rT parallel mechanism as in Fig. 5-9. During the motion, each joint has one vertical axis and one horizontal axis and keeps the platform and the base constantly parallel.

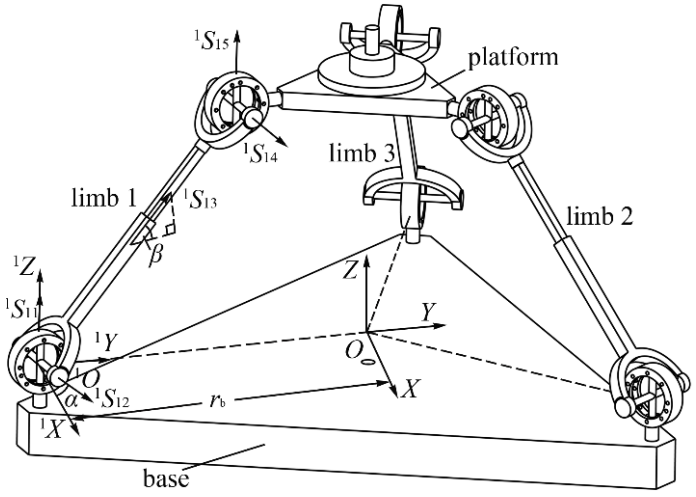

Figure 5-9 The 3-rT*P*rT with 3T1R motion

Set a local coordinate system $^1O^1X^1Y^1Z$ to the lower rT joint of limb 1 with its ^1Y axis aligned with the first rotation axis of the rT joint and ^1Z axis normal to the base as in Fig. 5-9, the limb twists can be obtained

$$\left\{{}^1\boldsymbol{S}_1\right\}=\left\{\begin{array}{l}{}^1\boldsymbol{S}_{11}=[0\quad 0\quad 1\quad 0\quad 0\quad 0]\\ {}^1\boldsymbol{S}_{12}=[\mathrm{c}\alpha\quad \mathrm{s}\alpha\quad 0\quad 0\quad 0\quad 0]\\ {}^1\boldsymbol{S}_{13}=[0\quad 0\quad 0\quad -\mathrm{c}\beta\mathrm{s}\alpha\quad \mathrm{c}\beta\mathrm{c}\alpha\quad \mathrm{s}\beta]\\ {}^1\boldsymbol{S}_{14}=[\mathrm{c}\alpha\quad \mathrm{s}\alpha\quad 0\quad -l\mathrm{s}\beta\mathrm{s}\alpha\quad l\mathrm{s}\beta\mathrm{c}\alpha\quad -l\mathrm{c}\beta]\\ {}^1\boldsymbol{S}_{15}=[0\quad 0\quad 1\quad l\mathrm{c}\beta\mathrm{c}\alpha\quad l\mathrm{c}\beta\mathrm{s}\alpha\quad 0]\end{array}\right\} \tag{5.21}$$

where α is the angle between ${}^1S_{12}$ and axis ${}^1X$ within ${}^1X{}^1O{}^1Y$ plane, β is the angle between ${}^1S_{13}$ and its projection on the ${}^1X{}^1O{}^1Y$ plane.

Calculate the reciprocal screws to Eq. (5.21), the limb constraint system can be obtained as

$$\left\{ {}^1\boldsymbol{S}_1^r \right\} = {}^1\boldsymbol{S}_1^r = \begin{bmatrix} 0 & 0 & 0 & \mathrm{s}\alpha & -\mathrm{c}\alpha & 0 \end{bmatrix} \tag{5.22}$$

This gives a constraint couple normal to the axes of the universal joint. Further there is no local degree of freedom with this arrangement of the limb.

As the translation does not affect ${}^1\boldsymbol{S}_1^r$, where ${}^1\boldsymbol{S}_1^r = \boldsymbol{S}_1^r$. To generate the other two constraints, $\boldsymbol{S}_1^r$ is rotated about the Z axis by φ= ±2π/3 at the global reference frame at the centre of the base using Eq. (5.13). Thus three limb constraint couples in the global reference frame can be obtained as

$$\begin{aligned}
\boldsymbol{S}_1^r &= \begin{bmatrix} 0 & 0 & 0 & \mathrm{s}\alpha & -\mathrm{c}\alpha & 0 \end{bmatrix}, \\
\boldsymbol{S}_2^r &= \begin{bmatrix} 0 & 0 & 0 & -\frac{1}{2}\mathrm{s}\alpha - \frac{\sqrt{3}}{2}\mathrm{c}\alpha & -\frac{\sqrt{3}}{2}\mathrm{s}\alpha + \frac{1}{2}\mathrm{c}\alpha & 0 \end{bmatrix}, \\
\boldsymbol{S}_3^r &= \begin{bmatrix} 0 & 0 & 0 & -\frac{1}{2}\mathrm{s}\alpha + \frac{\sqrt{3}}{2}\mathrm{c}\alpha & \frac{\sqrt{3}}{2}\mathrm{s}\alpha + \frac{1}{2}\mathrm{c}\alpha & 0 \end{bmatrix}
\end{aligned} \tag{5.23}$$

In contrast to the previous two configurations, this configuration results in a redundant constraint $\boldsymbol{S}_3^r$. The canonical constraint system is hence given

$$\left\{ \boldsymbol{S}^r \right\} = \begin{Bmatrix} \begin{bmatrix} 0 & 0 & 0 & 1 & 0 & 0 \end{bmatrix}, \\ \begin{bmatrix} 0 & 0 & 0 & 0 & 1 & 0 \end{bmatrix} \end{Bmatrix} \tag{5.24}$$

Thus two rotational DOFs about X and Y axis of the moving platform are constrained and the 3-rT*P*rT parallel mechanism has three translations and one rotation about Z axis. Here three limbs provide three constraints with one virtual constraint. This is equivalent to a standard 4-*UPU*

parallel mechanism [124] with the same mobility. Theoretically, n (n >= 3) rTPrT limbs can be assembled to form an n-rTPrT parallel mechanism which has the same mobility with the 3-rTPrT parallel mechanism and will have n-2 virtual constraints as all the constraints are coplanar.

5.4 The 3-rRPS MPM with 3R Motion and 1T2R Motion

The 3-rRPS metamorphic parallel mechanism as in Fig. 5-10 has three rRPS limbs symmetrically located on the base circle with radius r_b through the rR joints and on the platform circle with radius r_a through spherical joints. Let points A_i and B_i denote the spherical joint center and the rR joint center in limb i (i=1,2,3) respectively. $\boldsymbol{u}_i$ is the rotation axis of the rR joint in limb i. Locate a global coordinate system $oxyz$ at the geometric center o of the base with the negative part of y axis passing through rR joint center B_1 and z axis perpendicular to the base plane formed by $B_1B_2B_3$. Then, x axis is parallel to B_2B_3 as in Fig. 5-10. Based on symmetry, all the ring base plane Σ_i of the rR joint in limb i intersects the z axis with angle ϕ which is named rR joint base location angle. Let $\boldsymbol{a}_i$ and $\boldsymbol{b}_i$ denote the vectors of points A_i and B_i in the coordinate system $oxyz$, l_i be the limb length between the spherical joint center A_i and the rT joint center B_i. Similarly, a moving coordinate system $o'x'y'z'$ is attached at the platform center o' with the negative part of y' axis passing through spherical joint center A_1 and z' axis perpendicular to the platform plane formed by $A_1A_2A_3$.

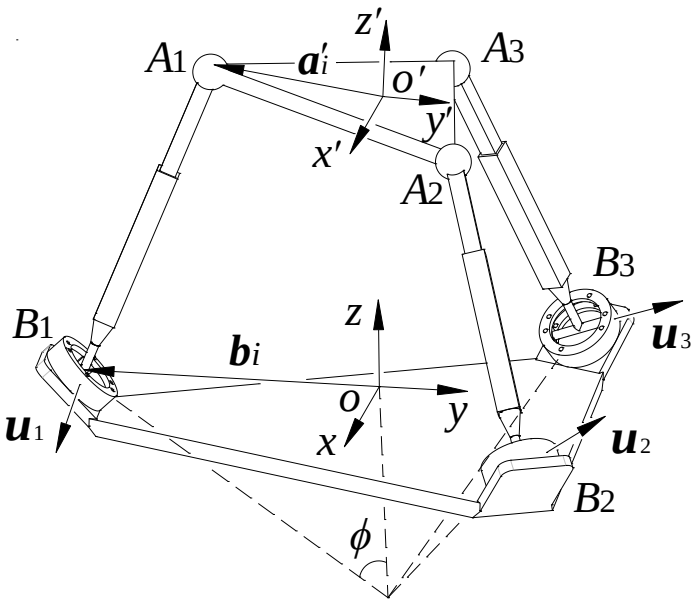

Figure 5-10 The 3-rRPS Metamorphic Parallel Mechanism

Based on the above description, the geometric constraint of the 3-rR*PS* is described in two parts. The first part expresses the length of the limbs

$$(\mathbf{R}\,\boldsymbol{a}_i' + \boldsymbol{p} - \boldsymbol{b}_i)^2 = l_i^2 \quad (i = 1, 2, 3) \tag{5.25}$$

and the second part describes the constraint that each limb is perpendicular to the rotation axis $\boldsymbol{u}_i$ of the rR joint:

$$(\mathbf{R}\,\boldsymbol{a}_i' + \boldsymbol{p} - \boldsymbol{b}_i)^T . \boldsymbol{u}_i = 0 \quad (i = 1, 2, 3) \tag{5.26}$$

where **R** is the rotational matrix from the moving coordinate system to the global coordinate system *oxyz*, $\boldsymbol{p}=(p_x, p_y, p_z)^{\mathrm{T}}$ is the vector of the moving coordinate center *o′* expressed in the global coordinate system. $\boldsymbol{a}_i'$ is the position vector of spherical joint center A_i expressed in the moving coordinate system *o′x′y′z′*.

Based on the six constraint Eqs. (5.25) and (5.26), the three independent rotation parameters in **R** and the three translation parameters in $\boldsymbol{p}=(p_x, p_y, p_z)^{\mathrm{T}}$ can be fully determined when l_i is given as actuation input of each prismatic joint. Thus, equations in Eq. (5.25) are related to the actuation and equations in Eq. (5.26) determine the mobility of the 3-rR*PS* MPM. Based on the reconfiguration of the rR joint with variable $\boldsymbol{u}_i$ by rotating the ring base, the 3rR*PS* MPM is reconfigurable and can have the following different topologies with two different motion types.

Case 1: the three rR joint axis $\boldsymbol{u}_i$ are independent

This is the general case as in Fig. 5-10, the position vector $\boldsymbol{p}=(p_x, p_y, p_z)^{\mathrm{T}}$ can be solved from the three equations in Eq. (5.26) as

$$\boldsymbol{p}^T = \begin{bmatrix} (\boldsymbol{b}_1 - \mathbf{R}\,\boldsymbol{a}_1')^T . \boldsymbol{u}_1 \\ (\boldsymbol{b}_2 - \mathbf{R}\,\boldsymbol{a}_2')^T . \boldsymbol{u}_2 \\ (\boldsymbol{b}_3 - \mathbf{R}\,\boldsymbol{a}_3')^T . \boldsymbol{u}_3 \end{bmatrix}^T . \begin{bmatrix} \boldsymbol{u}_1 & \boldsymbol{u}_2 & \boldsymbol{u}_3 \end{bmatrix}^{-1} \tag{5.27}$$

Thus, the translation parameters can be linearly solved for a given rotation matrix **R** but not inversely. Thus, considering kinematics simplicity, this topology is taken as pure rotation (3R) motion with parasitic translation motion that can be obtained from Eq. (5.27).

Before going to case 2, the following *Cayley* formula [146] is introduced and will be used to describe the rotation between the moving coordinate system and the global coordinate system as matrix **R**:

$$\mathbf{R} = \Delta^{-1}\begin{bmatrix} 1+c_1^2-c_2^2-c_3^2 & 2(c_1c_2-c_3) & 2(c_1c_3+c_2) \\ 2(c_1c_2+c_3) & 1-c_1^2+c_2^2-c_3^2 & 2(c_2c_3-c_1) \\ 2(c_1c_3-c_2) & 2(c_2c_3+c_1) & 1-c_1^2-c_2^2+c_3^2 \end{bmatrix} \tag{5.28}$$

where $\Delta = 1+c_1^2+c_2^2+c_3^2$, c_1, c_2 and c_3 are the Rodriguez-Hamilton parameters and $c_1 = k_x\tan(\gamma/2), c_2 = k_y\tan(\gamma/2), c_3 = k_z\tan(\gamma/2)$, which describes a 3D rotation about an axis ***k***(*kx*, *ky*, *kz*) with angle *γ*.

Cayley formula uses the three independent Rodriguez-Hamilton parameters to represent 3D rotation motion and shows a big advantage in simplifying the following geometric constraint equations for mobility analysis and also on singularity and workspace representation.

Case 2: the three rR joint axis $\boldsymbol{u}_i$ are dependent

Based on the symmetrical property, there are two dependent cases.

(1) Two $\boldsymbol{u}_i$ are dependent

This is the case when two $\boldsymbol{u}_i$ are parallel to each other and there are three cases ($\boldsymbol{u}_1 = \boldsymbol{u}_2$, $\boldsymbol{u}_1 = \boldsymbol{u}_3$, or $\boldsymbol{u}_2 = \boldsymbol{u}_3$). An example of $\boldsymbol{u}_1 = \boldsymbol{u}_3$ is in Fig. 5-11(a) and due to the symmetry $\boldsymbol{u}_1$, $\boldsymbol{u}_3$ should be parallel to the common line of the two base ring planes of the rR joints in limb 1 and limb 3.

Then from Eq. (5.26) there is:

$$\begin{cases} \boldsymbol{p}^T.\boldsymbol{u}_1 = (\boldsymbol{b}_1 - \mathbf{R}\,\boldsymbol{a}_1')^T.\boldsymbol{u}_1 \\ \boldsymbol{p}^T.\boldsymbol{u}_3 = (\boldsymbol{b}_3 - \mathbf{R}\,\boldsymbol{a}_3')^T.\boldsymbol{u}_3 \\ 0 = (\boldsymbol{b}_1 - \boldsymbol{b}_2 - \mathbf{R}\,\boldsymbol{a}_1' + \mathbf{R}\,\boldsymbol{a}_2')^T.\boldsymbol{u}_1 \end{cases} \tag{5.29}$$

From Eq. (5.29) two of the three translation parameters (p_x, p_y, p_z) in $\boldsymbol{p}$ can be linearly solved from the first two equations while the third equation only relates to the rotation parameters in **R**. By substituting *Cayley* formula from Eq. (5.28) into the third equation in Eq. (5.29), there is

$$c_3 = f(1, c_1, c_2, c_1^2, c_2^2) \tag{5.30}$$

where $f(\cdot)$ is a function of unknown power products in the bracket, with real constant coefficients depending on the input and mechanism dimensional parameters only. This further shows that the rotation about *z* axis can be linearly solved by the rotations about the other two axes. For simplicity, the mechanism is considered to have two main rotations about *x* axis and *y* axis. Thus, the mechanism has one translation and two rotation (1T2R) motion in this case.

(2) Three $\boldsymbol{u}_i$ are dependent

This is the case only when all the three $\boldsymbol{u}_i$ are on the base plane as in Fig. 5-11(b) where $\boldsymbol{u}_1$=(1, 0, 0)^T, $\boldsymbol{u}_2$=(–1/2, $\sqrt{3}$/2, 0)^T, $\boldsymbol{u}_3$=(–1/2, –$\sqrt{3}$/2, 0)^T, then $\boldsymbol{u}_1 + \boldsymbol{u}_2 + \boldsymbol{u}_3$=0, and there is

$$\begin{cases} \boldsymbol{p}^T.\boldsymbol{u}_1 = (\boldsymbol{b}_1 - \mathbf{R}\,\boldsymbol{a}_1')^T.\boldsymbol{u}_1 \\ \boldsymbol{p}^T.\boldsymbol{u}_2 = (\boldsymbol{b}_2 - \mathbf{R}\,\boldsymbol{a}_2')^T.\boldsymbol{u}_2 \\ 0 = (\boldsymbol{b}_1 - \mathbf{R}\,\boldsymbol{a}_1')^T.\boldsymbol{u}_1 + (\boldsymbol{b}_2 - \mathbf{R}\,\boldsymbol{a}_2')^T.\boldsymbol{u}_2 + (\boldsymbol{b}_3 - \mathbf{R}\,\boldsymbol{a}_3')^T.\boldsymbol{u}_3 \end{cases} \tag{5.31}$$

Similar with Eq. (5.29), two of the three translation parameters (p_x, p_y, p_z) in $\boldsymbol{p}$ can be linearly solved from the first two equations while the third equation provides a constraint among the rotation parameters in **R**. This can be further detailed as:

$$\begin{cases} p_x = (\boldsymbol{b}_1 - \mathbf{R}\,\boldsymbol{a}_1')^T.\boldsymbol{u}_1 \\ p_y = (\boldsymbol{b}_1 - \mathbf{R}\,\boldsymbol{a}_1')^T.\boldsymbol{u}_1 + 2(\boldsymbol{b}_2 - \mathbf{R}\,\boldsymbol{a}_2')^T.\boldsymbol{u}_2 / \sqrt{3} \\ c_3 = 0 \end{cases} \tag{5.32}$$

Thus translations along *x* axis and *y* axis can be linearly solved from the rotation motion while there is no rotation about *z* axis. The parallel mechanism in this case is considered to have one translation along the *z* axis and two rotations about *x* axis and *y* axis.

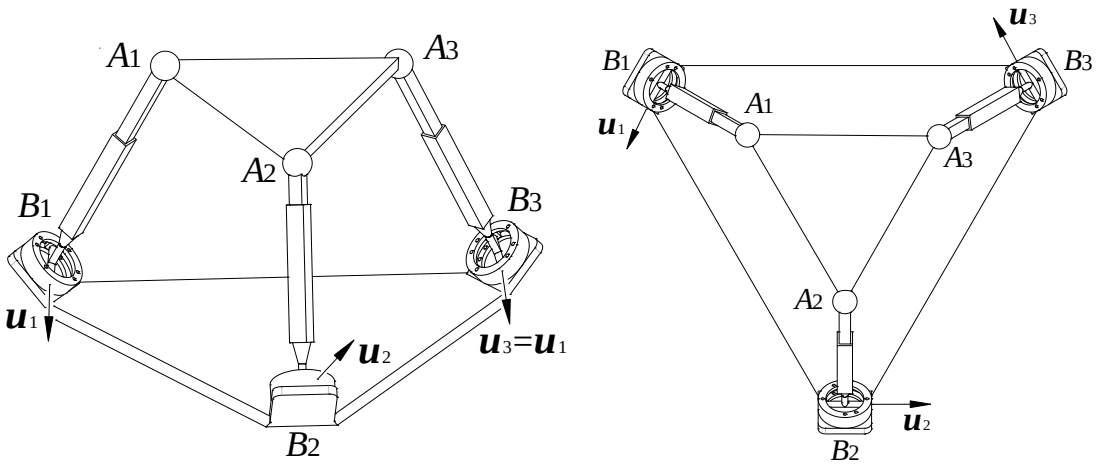

(a) $\boldsymbol{u}_1 = \boldsymbol{u}_3$ (b) $\boldsymbol{u}_1 + \boldsymbol{u}_2 + \boldsymbol{u}_3 = 0$

Figure 5-11 Two topologies of the 3rR*PS* with 1T2R motion

To summarize the above analysis, the 3rR*PS* MPM can have either pure rotation (3R) motion with parasitic translations or one translation and two rotation (1T2R) motion by reconfiguring the rotation axis of the rR joint into different directions. It should be noticed that there are infinite numbers of configurations with pure rotation motion by altering the rR joint in each limb as far as the three rotation axis vectors are not dependent. There are only four cases with 1T2R motion as stated in case 2.

5.5 Conclusions

This chapter contributed to modelling the geometric constraint change of four novel metamorphic parallel mechanisms, finding their reconfiguration rules and demonstrating their reconfigurable mobilities. As mentioned in the synthesis chapters, the core of metamorphic parallel mechanism reconfiguration is the geometric constraint change from the reconfigurable joints. This is very well described by screws and their dependency is represented by the screw rank change. By associating the motion screws to all joints including the reconfigurable rT joint, their geometric relation is modelled and the corresponding reciprocal screws illustrate their

constraint to the platform, which then tells the platform output mobility. This method was applied for the 3-rTPS with perpendicular constraint and it was found to be able to reconfigure into six different phases with mobility change from 3 to 6. Similarly, the constraint screw system also clearly demonstrated the pure rotation phase, pure translation phase and the 4-DOF 1R3T phase of the 4-rTPS metamorphic parallel mechanism.

Similar to the screw method, this chapter also introduced the basic geometric loop-close equation based constraint modelling and analysis method. Different with the screw method by associating a screw to each joint axis, this method considers the limb structure as a whole and focuses on the output motion capability of the limb end connecting to the platform. By revealing the dependency among all the limb equations, the relation of the translation and rotation parameters is found and that indicates the mobility of the platform. Based on this method, the 4-rTPS metamorphic parallel mechanism shows mobility change between 2 and 6. A special property is also found that it has bifurcated rotation motion at mobility 2 about two perpendicular directions. Similarly, the pure rotation and 1T2R phases of the reconfigurable revolute joint based 3-rRPS MPM was also demonstrated.

Chapter 6 Unified Kinematics Modelling of MPMs Covering All Phases

6.1 Related Kinematics of Parallel Mechanisms in the Literature

Kinematics modelling is one of the initial steps in parallel mechanism design and analysis. It provides basis for further dynamics analysis, design, control and motion planning of the mecanisms for applications. While inverse kinematics is generally easy, forward kinematics of a parallel mechanism is considered as a very complex problem due to the fact that it normally leads to high order polynomial equations with multi-solutions [24, 147]. Analytically solving the forward kinematics by obtaining the univariant equation with one unknown is the idea result as it gives straightforward solutions and the inter-relations for variable geometry parameters. Kinematics analysis of parallel mechanisms have been studied a lot in the literature and even the most complex one of the general Stewart platform has been solved and proved to have 40 solutions [24, 148]. Since a metamorphic parallel mechanism has several topologies with different mobility, each of them is a traditional parallel mechanism. Thus, the existing work in the literature of forward kinematics analysis of parallel mechanisms can be referred to and applied to solve one topology after another of a metamorphic parallel mechanism. However, it is preferred to solve all the topologies in a unified manner to ease further modelling and control in applications since all the topologies share the same mechanical structure and parameters. This has not been explored in the literature for reconfigurable parallel mechanisms and this chapter will contribute to this unified modelling method for metamorphic parallel mechanisms based on existing kinematics solving models for single parallel mechanism topologies.

Before going to the proposed unified modelling method and detailed modelling of the selected metamorphic parallel mechanisms, related parallel mechanisms in the literature are listed in the following table considering their forward kinematics solving is the direct reference for the work in this chapter.

Table 6-1 References of Kinematics Analysis

Metamorphic Parallel Mechanisms	Mobility Reconfiguration	Reference Parallel Mechanisms in the Literature
3-rTPrT	3-DOF: pure rotation with intersecting rotation center	Spherical parallel mechanisms [149, 150]
	3-DOF: pure translation	Solution is traight forward.
3-rTPS	3-DOF: pure rotation without intersecting rotation center	Related to the Pyramid 3-RPS with 3R motion [139].
	4-DOF: 3R1T 5-DOF: 3R2T 6-DOF: 3R3T	Can be related to the 3-CCC with 6-DOF decoupled rotation and translation [8].
4-rTPS	2-DOF: $1R_{x/y}1T_z$ with bifurcated rotation 3-DOF: $2R_{xy}1T_z$ 4-DOF: $2R_{xy}2T_{xz}$, $2R_{xy}2T_{yz}$, $3R1T_z$ 5-DOF: $3R2T_{xz}$, $3R2T_{yz}$ 6-DOF: 3R3T	Related to the 6-4 type 6-SPS Stewart mechanism [151], the 4-DOF 2SPS-2SPR [152], and the 4-RRPS reconfigurable parallel mechanism [111].
3-rRPS	3-DOF: 3R	Pyramid 3-RPS with 3R motion [139]
	3-DOF: 2R1T	Symmetric 3-RPS with 2R1T motion [17, 153].

In Table 6-1, those related parallel mechanisms provide reference to the kinematics analysis of the metamorphic parallel mechanisms in this chapter. In general, they are related to one of the possible reconfigurable topologies. Thus, one metamorphic parallel mechanism will refer to different traditional parallel mechanisms due to its

multi-topology from reconfiguration. In this case, the challenge comes from how to combine all those topologies in a unified way. This question is going to be solved by the following general strategy in section 6.2 with detailed demonstration of four selected metamorphic parallel mechanisms in sections following it.

6.2 The Proposed Strategy and Method

In the metamorphic parallel mechanisms in this work, only the reconfigurable joints change their configurations to reconfigure the mechanism mobility and motion types. In this case, the main limb geometric constraints have the same mathematic model before and after the reconfiguration while the moving platform of the mechanism has different output motion. Considering this, the general strategy is to model the MPMs from their limb geometric constraints. Moreover, in the model of the reconfigurable limbs, the reconfigurable joint configuration can be generalized by taking some reconfigured phases as special cases of the generalized model. Those will help unify the kinematics modelling as shown in the following sections.

6.3 Unified Kinematics Modelling and Workspace Analysis of the 3-rTPrT

The 3-rTPrT MPM can reconfigure into pure rotation and pure translation phases. The following shows the unified kinematics analysis covering both phases.

6.3.1 Geometric Parameters and Inverse Kinematics

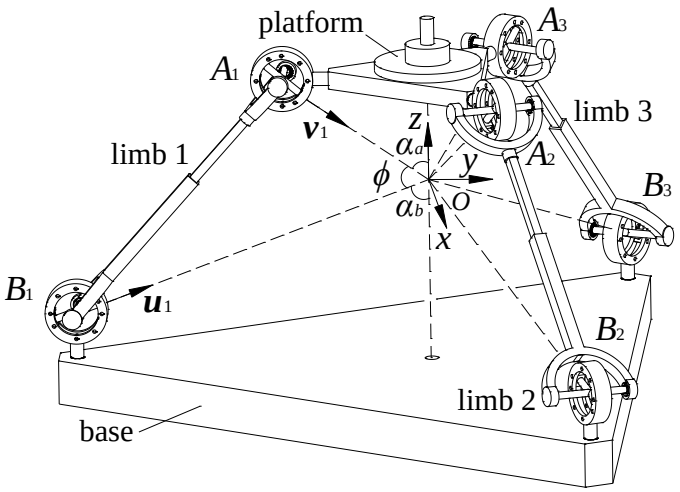

Figure 6-1 The 3-rTPrT MPM with pure rotation

In each limb of the 3-rTPrT as in Fig.6-1, the radial axis of the base rT joint forms an angle α_b with z-axis and hence called base-rT-joint angle, the radial axis of the platform-rT-joint forms an angle α_a with z'-axis and hence called platform-rT-joint angle. Thus the base radius r_b and base-rT-joint angle α_b describe the geometric structure of the base while the platform radius r_a and platform-rT-joint angle α_a show the geometric structure of the platform. As the radial axis of the rT joint can be rotated about the bracket axis by any angle, directions of the radial axes $\boldsymbol{v}_i$ and $\boldsymbol{u}_i$ in each limb can be altered freely, hence the intersecting point O can be moved along z-axis as in Fig. 6-2.

Assuming that the platform is at the initial configuration, the intersecting point O is changed from O to O' by rotating the radial axes of the rT joints, base-rT-joint angle α_b and platform-rT-joint angle α_a are changed to α'_b and α'_a respectively, the constraint equation among these parameters can be obtained as:

$$\pm\Delta h = r_b\cot\alpha_b - r_b\cot\alpha'_b \ = r_a\cot\alpha_a - r_a\cot\alpha'_a \tag{6.1}$$

where Δh is the distance between O and O'. When the change from O to O' is to the positive direction of z-axis, the sign before Δh is '+', otherwise it is '–'.

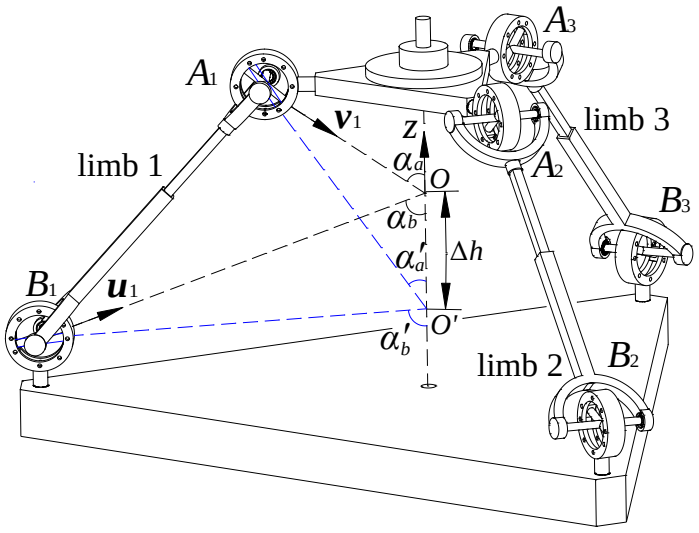

Figure 6-2 The controllable rotation center

After assembling the parallel mechanism, the initial angles α_a and α_b are known, a desired configuration of the 3-(rT)*P*(rT) parallel mechanism can be obtained by calculating Eq. (6.1) when a needed moving distance Δh of rotation center *O* or rT joint angle α'_a or α'_b are given. Thus, by altering the rT joint to change the position of the intersecting point *O* between negative infinite and positive infinite of *z*-axis, the platform can rotate about any point on the *z*-axis. Hence, the rotation center of the 3-(rT)*P*(rT) parallel mechanism can be controlled according to the requirement.

Let $\boldsymbol{a}_i$ and $\boldsymbol{b}_i$ denote the position vectors of the platform rT joint center A_i and the base rT joint center B_i respectively expressed in the global coordinate frame *oxyz*. Let $\boldsymbol{a}'_i$ denote the platform-rT-joint position vectors of center A_i expressed in the platform coordinate frame *ox'y'z'*, d_i and $\boldsymbol{d}_i$ denote the length and limb translation vector from point B_i to A_i in the global coordinate frame *oxyz*. Based on these settings and the geometric structure of the mechanism, the base-rT-joint position vectors can be determined as:

$$\begin{aligned} \boldsymbol{s}_{i1} &= [\cos(3\pi/2 + 2\pi(i-1)/3), \sin(3\pi/2 + 2\pi(i-1)/3), -\cot\alpha_b]^T, \\ \boldsymbol{b}_i &= r_b \boldsymbol{s}_{i1}, \qquad (i = 1,2,3) \end{aligned} \tag{6.2}$$

where $0 < \alpha_b < \pi$, s_{ij} represents the unit vector of the joint axis *j* in limb *i*.

The platform-rT-joint position vectors can be expressed in the platform coordinate frame as

$$\begin{aligned} &\boldsymbol{s}_{i5} = [\cos(3\pi/2 + 2\pi(i-1)/3), \sin(3\pi/2 + 2\pi(i-1)/3), \cot\alpha_a]^T, \\ &\boldsymbol{a}'_i = r_a \boldsymbol{s}_{i5}, \qquad (i = 1, 2, 3) \end{aligned} \tag{6.3}$$

where $0 < \alpha_a < \pi$.

Let **R** be the 3×3 rotational matrix and $\boldsymbol{p}$ be the translation vector of the moving coordinate frame with respect to the global coordinate frame, the closed-loop equation of each limb can be expressed in the global coordinate frame as

$$\boldsymbol{a}_i = \boldsymbol{b}_i + d_i \boldsymbol{s}_{i3} = \boldsymbol{p} + \mathbf{R}.\boldsymbol{a}'_i \quad (i = 1, 2, 3) \tag{6.4}$$

The inverse kinematics is to get input d_i which can be obtained directly from (6.4)

$$\sqrt{(\mathbf{R}\,\boldsymbol{a}'_i + \boldsymbol{p} - \boldsymbol{b}_i)^T (\mathbf{R}\,\boldsymbol{a}'_i + \boldsymbol{p} - \boldsymbol{b}_i)} = d_i \quad (i = 1, 2, 3) \tag{6.5}$$

For the pure rotation phase, there is no translation and $\boldsymbol{p}$ equals to zero in Eq. (6.5). When **R** is known, the limb lengths can be solved from Eq. (6.5). For the pure translation phase, rotation matrix **R** will be the identity matrix. The inverse kinematics can be easily solved from Eq. (6.5) when giving the platform position $\boldsymbol{p}$.

6.3.2 Forward Kinematics

In the forward kinematics analysis, limb length d_i will be known and rotation matrix R in the pure rotation phase or translation vector *p* in the pure translation phase will be solved. For the pure translation case, $\boldsymbol{p}$ can be solved from Eq. (6.4):

$$\boldsymbol{p} = \boldsymbol{b}_i + d_i \boldsymbol{s}_{i3} - \boldsymbol{a}'_i \quad (i = 1, 2, 3) \tag{6.6}$$

The forward kinematics of the pure rotation case is more complex and can be solved in the following way. Setting $\boldsymbol{p}$ equal to zero in Eq. (6.5) and expanding it gives:

$$\begin{aligned} 2(\mathbf{R}\,\boldsymbol{a}_i')^T\boldsymbol{b}_i &= (r_a/\sin\alpha_a)^2+(r_b/\sin\alpha_b)^2-d_i^2 \\ &= 2r_a r_b\cos(\phi_i)/(\sin\alpha_a\sin\alpha_b) \quad (i=1,2,3) \end{aligned} \tag{6.7}$$

which can be described as

$$(\mathbf{R}\,\boldsymbol{s}_{i5})^T\boldsymbol{s}_{i1} = \cos(\phi_i) \quad (i=1,2,3) \tag{6.8}$$

where ϕ_i is the angle between axes s_{i1} and s_{i5}, as in Fig. 6-1.

Using the Cayley formula in Eq. (5.28) and substituting it into Eq. (6.8), simplifying and taking the numerators, gives:

$$f_i(1,c_1,c_2,c_3,c_1c_2,c_1c_3,c_2c_3,c_1^2,c_2^2,c_3^2)=0 \quad (i=1,2,3) \tag{6.9}$$

where $f_i(\cdot)$ is a function of the unknown power products in the bracket, with real constant coefficients depending on the input and mechanism dimension parameters only.

Rewrite Eq. (6.9) as the function of c_1, c_2 by putting the products of power in c_3 into the coefficients:

$$Q_e(c_1,c_2)=\sum_{\substack{i,j=0\\ i+j\le 2}}^{2} G_{e-ij}c_1^i c_2^j = 0 \quad (e = 0,1,2) \tag{6.10}$$

where G_{e-ij} are functions of known parameters and power products of c_3.

Construct the following matrix

$$\Delta(c_1,c_2,t_1,t_2)=\begin{vmatrix} Q_0(c_1,c_2) & Q_1(c_1,c_2) & Q_2(c_1,c_2) \\ Q_0(t_1,c_2) & Q_1(t_1,c_2) & Q_2(t_1,c_2) \\ Q_0(t_1,t_2) & Q_1(t_1,t_2) & Q_2(t_1,t_2) \end{vmatrix} \tag{6.11}$$

where t_1, t_2 are intermediate parameters only. By developing the above equation, $\Delta(c_1, c_2, t_1, t_2)$ is a polynomial of order 2 in c_1, 3 in c_2, 3 in t_1, 2 in t_2. Dixon observed that Δ vanishes when t_1, t_2 substitute for c_1, c_2, implying that $(c_1\text{-}t_1)(c_2\text{-}t_2)$ is a factor of Δ. Therefore, the expression:

$$\delta(c_1,c_2,t_1,t_2)=\frac{\Delta(c_1,c_2,t_1,t_2)}{(c_1-t_1)(c_2-t_2)}=0 \tag{6.12}$$

is a polynomial of order 1 in c_1, 2 in c_2, 2 in t_1, 1 in t_2. δ vanishes when $Q_0(c_1, c_2)$, $Q_1(c_1, c_2)$ and $Q_2(c_1, c_2)$ have common zeros no matter what t_1, t_2 are. The coefficients of each power product $t_1^i t_2^j$ (i=0,1,2; j=0,1) of δ have common zeros which are also the common zeros of equations Q_0, Q_1, Q_2 in Eq. (6.9). This gives five equations in power product of c_1 and c_2, whereas the number of the power product $c_1^i c_2^j$ (i=0,1; j=0,1,2) is also five. Therefore, the coefficients of each power product $c_1^i c_2^j$ in these five equations form a 5×5 matrix **D**. All the above algorithm can be expressed as:

$$\delta(c_1,c_2,t_1,t_2)=\frac{\Delta(c_1,c_2,t_1,t_2)}{(c_1-t_1)(c_2-t_2)}=\boldsymbol{T}\,\mathbf{D}\,\boldsymbol{C}^T=0 \tag{6.13}$$

where $\mathbf{T}=\begin{bmatrix}1 & t_1 & t_1^2 & t_2 & t_1t_2\end{bmatrix}$, $\boldsymbol{C}=\begin{bmatrix}1 & c_2 & c_2^2 & c_1 & c_2c_1\end{bmatrix}$, **D** is a matrix whose elements are polynomials in c_3.

Equations in Eq. (6.10) have common zeros if the determinant of the matrix D equals to 0. Thus an equation in c_3 can be obtained:

$$|\mathbf{D}|=\sum_{i=0}^{+8} h_i c_3^i=0 \tag{6.14}$$

where h_i are real constants depending on input data only.

This implies that an univariate equation in c_3 of order 8 is obtained. Solving Eq. (6.14), all the solutions for c_3 can be obtained. Then substitute c_3 into the following equation:

$$\mathbf{D}\boldsymbol{C}^T = 0 \tag{6.15}$$

According to the Cramer's rule, the solutions of c_1, c_2 can be computed from the above linear system. Substituting all the solutions of c_1, c_2 and c_3 into Eq. (5.28), orientation **R** can be obtained and the forward kinematics is solved.

6.3.3 Jacobian Matrix and 3D Singularity Loci

Taking the derivative of Eq. (6.4), there is

$$\begin{bmatrix} (\boldsymbol{b}_1 \times (\mathbf{R}.\boldsymbol{a}_1'))^T \\ (\boldsymbol{b}_2 \times (\mathbf{R}.\boldsymbol{a}_2'))^T \\ (\boldsymbol{b}_3 \times (\mathbf{R}.\boldsymbol{a}_3'))^T \end{bmatrix} \omega = \begin{bmatrix} \boldsymbol{J}_1 \\ \boldsymbol{J}_2 \\ \boldsymbol{J}_3 \end{bmatrix} \omega = \mathbf{J}\,\omega = \begin{bmatrix} d_1 & & \\ & d_2 & \\ & & d_3 \end{bmatrix} \begin{bmatrix} \dot{d}_1 \\ \dot{d}_2 \\ \dot{d}_3 \end{bmatrix} \tag{6.16}$$

where $\boldsymbol{\omega}$ is the platform orientation velocity, $\dot{d}_i$ is the input velocity of limb i, and $\boldsymbol{J}_i=(\boldsymbol{b}_i\times(\mathbf{R}.\boldsymbol{a}_i))^T$ is the row vector of the Jacobian matrix **J**. Hence Type 2 singularities result when the determinant of **J** equals to zero. Based on the rotation matrix **R** in Eq. (5.28) and the symmetrical structure, the determinant of **J** is given by:

$$\left|\mathbf{J}\right| = f_4(c_1^2c_2, c_2^3, c_3, c_1^2c_3, c_1^3c_3, c_2^2c_3, c_1c_2^2c_3, c_3^3) \tag{6.17}$$

From Eq. (6.17), the determinant of the Jacobian matrix is a quartic polynomial of the three rotation elements (c_1, c_2 and c_3) with coefficients consisting of structure parameters. For a given structure of the 3-(rT)*P*(rT) parallel mechanism, the rotation elements (c_1, c_2 and c_3) can be used to represent the singularity configuration of the platform. By equalling Eq. (6.17) to zero, all the singular points can be found as examples in Fig. 6-3.

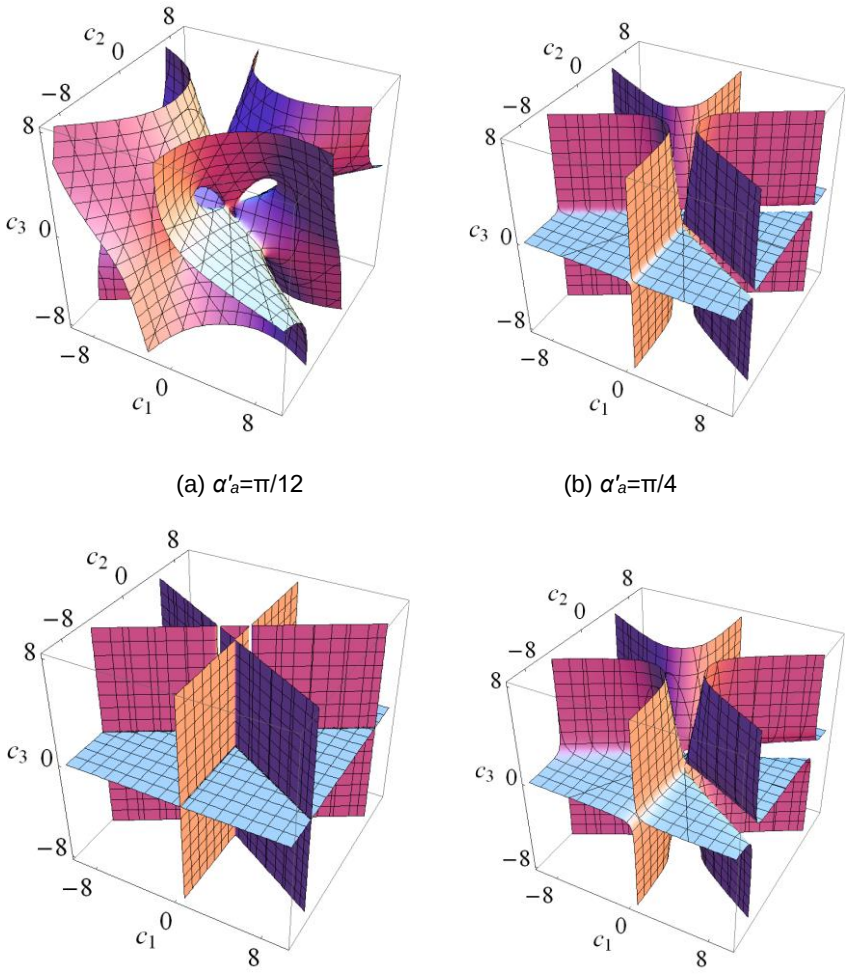

(a) $\alpha'_a=\pi/12$ (b) $\alpha'_a=\pi/4$

(c) $\alpha'_a=\alpha'_b\approx Sin^{-1}(\sqrt{2/3})$ (d) $\alpha'_a=7\pi/18$

Figure 6-3 Singularity Loci

In Fig. 6-3, singularity loci associated with different rotation centers are illustrated. In this example, the parameters used are r_a=1, r_b=2, $\alpha_b=\pi/3$ and $\alpha_a=2\pi/9$. By giving the desired platform angle α'_a representing new rotation center, corresponding base angle α'_b can be calculated from Eq. (6.1) and the determinant polynomial of the Jacobian matrix in Eq. (6.18) is renewed. In general, it can be seen that the singularity loci are symmetrical around the c_3 axis which represents the symmetrical locations of the three limbs between the platform and the base. A special case is the example in Fig. 6-3(c) in which $\alpha'_a=\alpha'_b\approx0.907$ of which the platform and base have the similar shape but different sizes. When α'_a is further from this configuration, the singularity loci are more curved as seen in Fig. 6-3(a) when α'_a is $\pi/12$ while the singularity loci are similar for the cases in Fig. 6-3(b) with $\pi/4$ and Fig. 6-3(d) with $7\pi/18$. For the special case

in Fig. 6-3(c), Eq. (6.18) becomes a polynomial of order 3 in c_1 and order 2 in c_2 with a factor c_3 as:

$$\left|\mathbf{J}\right| = f_5(c_1^3, c_1^2, c_1 c_2^2, c_2^2, 1) * c_3 \tag{6.19}$$

In Eq. (6.19), c_3 is a factor of the determinant, and hence the plane c_3=0 is a part of the singularity loci, and the other parts of the singularity loci depend only on c_1 and c_2. This can be seen from Fig. 6-3(d) in which the singularity loci consists of the c_3=0 plane, and three other scattered parts and a central part on surfaces perpendicular to the c_3=0 plane. The singularity loci surface has clear symmetry on the c_1c_2 plane as a result of the symmetrical limb arrangement and is also symmetrical with respect to the c_2=0 plane, due to the elements of c_2 in the Jacobian matrix determinant being quadratic only.

6.3.4 Limb actuation singularity

Limb actuation singularity [154] defines configurations where the limb cannot be actuated even when the other limb actuation joints are released. In the 3-rT*P*rT metamorphic parallel mechanism, it happens when a limb passes through the rotation center *O*. The following analysis shows a new method to calculate the limb actuation singularity loci.

Based on the Jacobian matrix in Eq. (6.17), limb actuation singularities can be found by making the row vector $\boldsymbol{J}_i = (J_{i1}, J_{i2}, J_{i3}) = 0$. In general, the components J_{ij} are quadratic polynomials of the rotation elements (c_1, c_2, c_3) and $\boldsymbol{J}_i = (J_{i1}, J_{i2}, J_{i3}) = 0$ gives three curved surfaces intersecting at two lines l_{11} and l_{12} which are perpendicular to each other. The physical meaning of lines l_{11} and l_{12} is when the platform rotates to any configuration where OA_1 is collinear with OB_1, in the same direction with $\mathbf{R}\boldsymbol{v}_1 = \boldsymbol{u}_1$, the point ($c_1$, c_2, c_3) is on the line l_{11}. When OA_1 is collinear with OB_1 in the opposite direction, with $\mathbf{R}\boldsymbol{v}_1 = -\boldsymbol{u}_1$, the point ($c_1$, c_2, c_3) is on the line l_{12}. Since the mechanism is symmetrical and the limbs have the same structure, the limb singularities for limb 2 and limb 3 are the same and each of them has two intersection lines (l_{21}, l_{22}, l_{31} and l_{32}) from three curved surfaces based on $\boldsymbol{J}_i = (J_{i1}, J_{i2}, J_{i3}) = 0$.

Their location relative to the mechanism singularity loci is illustrated by combining the limb singularity lines with the singularity loci in Fig. 6-4 in which the rotation center is not changed in the example in Fig. 6-3 with $\alpha'_a = \alpha_a = 2\pi/9$. In Fig. 6-4, lines l_{11}, l_{21} and l_{31} are nearly parallel to c_3=0 plane while the lines l_{12}, l_{22} and l_{32} are nearly perpendicular to the c_3=0 plane. When coming to the special case with $\alpha'_a = \alpha'_b$, the former three lines are in the c_3=0 plane and the latter three are perpendicular to it.

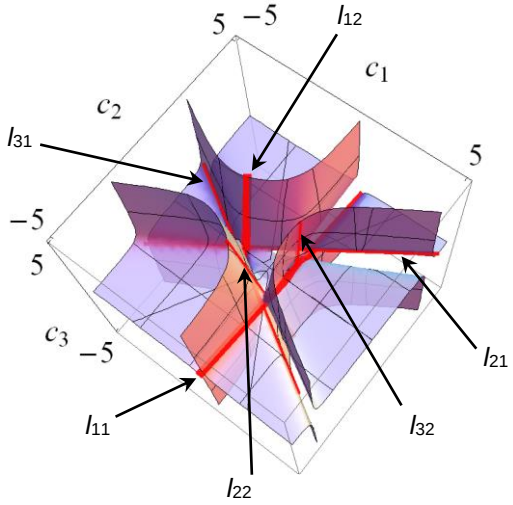

Figure 6-4 Limb actuation singularity loci in the mechanism singularity loci (α'_a=2π/9)

6.3.5 Forward Kinematics Solution Distribution for $\alpha'_a = \alpha'_b = Sin^{-1}(\sqrt{2/3})$ Case

For the special case that $\alpha'_a = \alpha'_b = Sin^{-1}(\sqrt{2/3})$ the forward kinematics solutions have determined distribution and can be uniquely determined. A point C in the (c_1, c_2, c_3) coordinate system as in Fig. 6-5(a), represents an anticlockwise rotation of angle θ about the line OC. When $\theta = \pi$, point C goes to infinity. Similarly, the point C' in the opposite direction of line OC will go to the infinity, when it rotates anticlockwise by angle $\theta = \pi$, about the line OC'. Physically, the two rotations are about the same line but in opposite directions, with rotation angle $\theta = \pi$, indicating that they reach the same configuration. Thus, point C coincides with C' at infinity, indicating that the two ends of any line in the (c_1, c_2, c_3) coordinate system connect to each other. This can be used in dividing the singularity free zones for the mechanism.

As shown in Fig. 6-5(b), the 3D space of (c_1, c_2, c_3) is divided into 14 zones by the four singularity planes. The parts with positive c_3 are numbered from zone z1 to zone z7 as Fig. 6-5(b). Based on the above connectivity analysis, the zone with negative c_3 under zone z1 is

connected to zone z4 with positive c_3 when the lines in these zones go to infinity and the two are considered as one zone, z4. Similarly, the part with negative c_3 under zone z4 is connected to zone z1. This is the same for the other zones, e.g. the part under zone z2 belongs to zone z5. However, zone z7 is different, as zone z7 is connected to its negative part with only one line (c_1=0, c_2=0). Thus, the part under zone z7 is defined as zone z8.

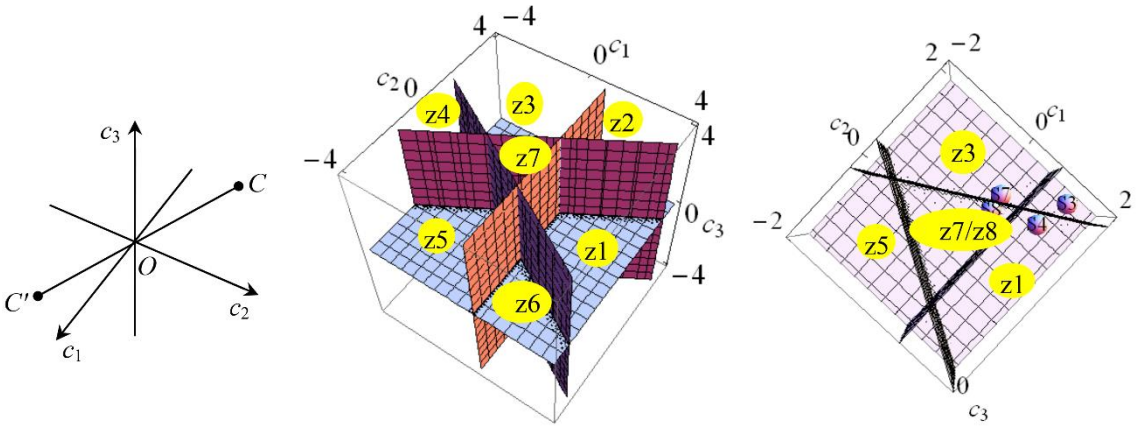

(a) connection at infinity (b) assembly zones (c) FK solution distribution

Figure 6-5 Assembly zones of the 3-rTPrT with orthogonal base and platform

It is shown that the eight forward kinematics solutions represent eight assembly modes and are distributed among eight singularity-free zones [155]. Following this, it is found that the eight forward kinematics solutions are distributed among these eight zones z1 to z8, as illustrated by an example in Fig. 6-5(c), and the eight solutions are listed in Table 6-1. In Fig. 6-5(c), only the solutions with positive c_3 are shown as the other four are directly under them with negative c_3. It is seen that the solutions are distributed as follows: solution S4 in zone z1, S3 in z2, S7 in z3 and S8 in z7. Correspondingly, solution S2 having negative c_3 with solution S4 is in zone z4, S1 with negative c_3 to S3 in z5, S5 with negative c_3 to S7 in z6 and S6 with negative c_3 to S8 in z8. This is also shown in Table 6-1. Based on this, the eight zones correspond to eight assembly modes of the 3-rTPrT with $\alpha'_a = \alpha'_b = Sin^{-1}(\sqrt{2/3})$. Once the mechanism is assembled in one mode, the mechanism will keep in that mode unless it reaches a singularity configuration, and then change to another mode. Thus, the current forward kinematics solution can be uniquely found within the corresponding assembly zone as shown in Fig. 6-5(b).

Table 6-2 FK solutions and zones

	c_1	c_2	c_3	zone
S4/S2	1.22382	1.25615	+/−0.253845	z1/z4
S3/S1	1.36781	1.9475	+/−0.324583	z2/z5
S7/S5	0.3	1.2	+/−0.2	z3/z6
S8/S6	0.359659	0.844666	+/−0.170691	z7/z8

6.3.6 Analytical Singularity-Free Workspace

6.3.6.1 Analytical Description of the Workspace Boundaries

In Section 6.2.3, the rotation elements (c_1, c_2 and c_3) are used to illustrate the singularity loci by using a 3D coordinate system, O-$c_1c_2c_3$. This can be extended to represent the rotation workspace using the same coordinate system with c_1, c_2 and c_3 in three perpendicular directions. According to the physical meaning of the Rodriguez-Hamilton parameters, a point $C(c_1, c_2, c_3) = \tan(\theta/2)*(kx, ky, kz)$ corresponds to a platform rotation by angle θ about an axis $\boldsymbol{k}(kx, ky, kz)$ in the mechanism base coordinate system. Thus, the workspace coordinate system, O-$c_1c_2c_3$, is parallel with the mechanism base coordinate system O-xyz with coincident center O. This property shows that the O-$c_1c_2c_3$ coordinate system has intuitive physical meaning in representing the rotation workspace.

In the 3-rT*P*rT metamorphic parallel mechanism, each limb length has two limits (lower and upper) which constrain the actuation range and determines the rotation workspace of the platform. Based on Eq. (6.7), the limb length limits will result in lower and upper limits of angle ϕ_i between the platform and base vectors $\boldsymbol{v}_i$ and $\boldsymbol{u}_i$ in each limb. Thus, the platform rotation workspace boundaries can be expressed by the two limits $\phi_{i\max/\min}$, by calculating the triangle relation, using Eq. (6.8) as:

$$(\mathbf{R}.\boldsymbol{v}_i)^T.\boldsymbol{u}_i = \cos(\phi_{i\max/\min}) \quad (i = 1, 2, 3) \tag{6.20}$$

For limb 1, it can be expanded as:

$$k_0 + k_1 c_1 + k_2 c_1^2 + k_3 c_2^2 + k_4 c_2 c_3 + k_5 c_3^2 - \Delta\cos(\phi_{i\max/\min}) = 0 \tag{6.21}$$

where $\Delta = 1 + c_1^2 + c_2^2 + c_3^2$, k_i are coefficients depending on the mechanism structure parameters only.

Eq. (6.21) shows the advantage of the (c_1, c_2, c_3) coordinate system, since the coefficients of c_1 and its square consist of mechanism structure parameters only, c_1 can be easily expressed using c_2 and c_3 with coefficients including the angle limits. This makes it possible to have analytical expressions to describe the 3D rotation workspace using the three rotation elements. From Eq. (6.21), c_1 can be solved as:

$$c_1 = \frac{-k_1 \pm \sqrt{k_1^2 - 4k_a k_c}}{2k_a} \tag{6.22}$$

where

$$k_a = k_2 - \cos(\phi_{i\max/\min})$$
$$k_c = k_0 - \cos(\phi_{i\max/\min}) + (k_3 - \cos(\phi_{i\max/\min}))c_2^2 + k_4 c_2 c_3 + (k_5 - \cos(\phi_{i\max/\min}))c_3^2$$

Thus, analytical workspace boundary from limb 1 can be given in the O-$c_1c_2c_3$ coordinate system using Eq. (6.22) with input limits $\phi_{i\max/\min}$. Since the limb arrangement in the 3-rT*P*rT metamorphic parallel mechanism is symmetrical, workspace boundaries corresponding to each of the three legs have a similar shape, but rotated 2π/3 about the c_3 axis. Thus, analytical workspace from limb 2 and limb 3 can be obtained by rotation without extra calculation from Eq. (6.20). The combination of the workspace boundaries of the three limbs will form the whole workspace boundaries of the 3-rT*P*rT metamorphic parallel mechanism.

6.3.6.2 Singularity-Free Workspace with Different Rotation Centers

Following the method in Section 6.2.6.1, some examples are given below to demonstrate the workspace boundaries with different rotation centers. The same example with that in Fig. 6-3 with parameters r_a=1, r_b=2, α_b=π/3 and α_a=2π/9 is used in the following. For the example in Fig. 6-5, the rotation center is changed from the initial configuration to α'_a=π/6. The boundaries of limb 1 (from Eq. (6.22)) are shown in Fig. 6-6(a) where the two surfaces represent the lower and

upper boundaries corresponding to the two limb input limits ($\phi_{i\min}$=0.6, $\phi_{i\max}$=1.85) and the space between the two blue surfaces is the workspace. By rotating the limb one boundaries by 2π/3 about the c_3 axis and taking the intersection of the space between the blue surfaces, the mechanism workspace boundaries can be obtained, Fig. 6-6(b). By combining this workspace with its singularity loci (based on Section 6.2.3), the singularity-free workspace is clearly seen as in Fig. 6-6(c). It can be seen that the mechanism workspace is separated into different parts in different orientation areas. A detailed demonstration is given in Fig. 6-6(c) for the workspace part in the area near the center of point O with (c_1= c_2= c_3=0) in the O-$c_1c_2c_3$ coordinate system. This is the mechanism workspace in general when the mechanism starts from the configuration of which the platform coordinate system is coincident with the base coordinate system.

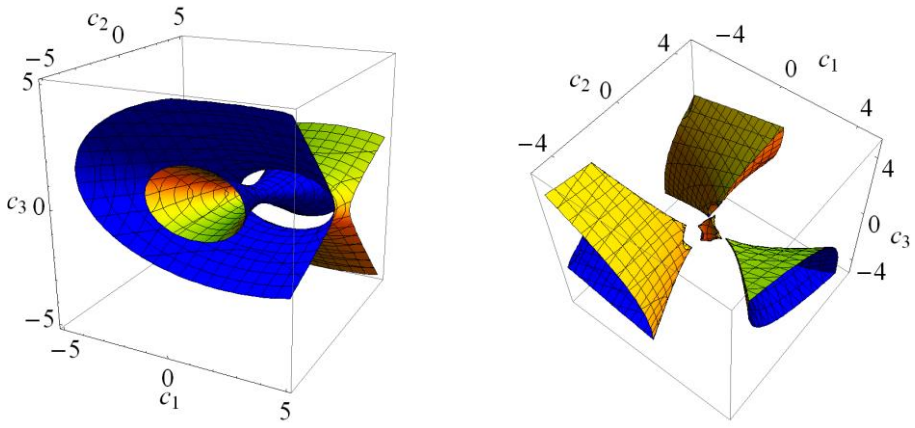

(a) workspace of limb 1 (b) mechanism workspace

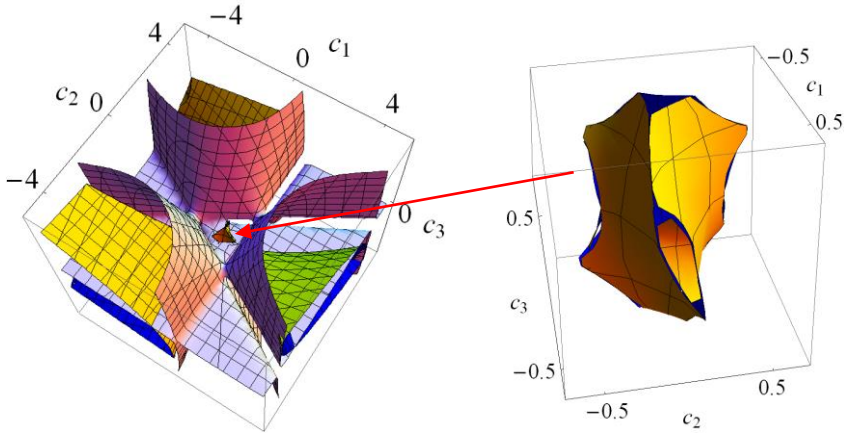

(c) workspace with singularity loci

Figure 6-6 Workspace boundaries (α'_a=π/6)

When changing the rotation centers, based on the same mechanism structure parameters and limb limits, variable singularity-free workspace can be obtained. Some examples are shown in

Fig. 6-7 in which the rotation centers are changed to (a) $\alpha'_a=\pi/12$, (b) $\alpha'_a=\pi/4$, (c) $\alpha'_a=\alpha'_b\approx0.907$ and (d)$\alpha'_a=7\pi/18$. It can be seen that when the rotation center is under the base with $\alpha'_a=\pi/12$ in Fig. 6-7(a) the platform rotation is mainly along the c_3 axis corresponding to z-axis in the mechanism coordinate. The other three cases have similar workspace shape but with different sizes in different areas.

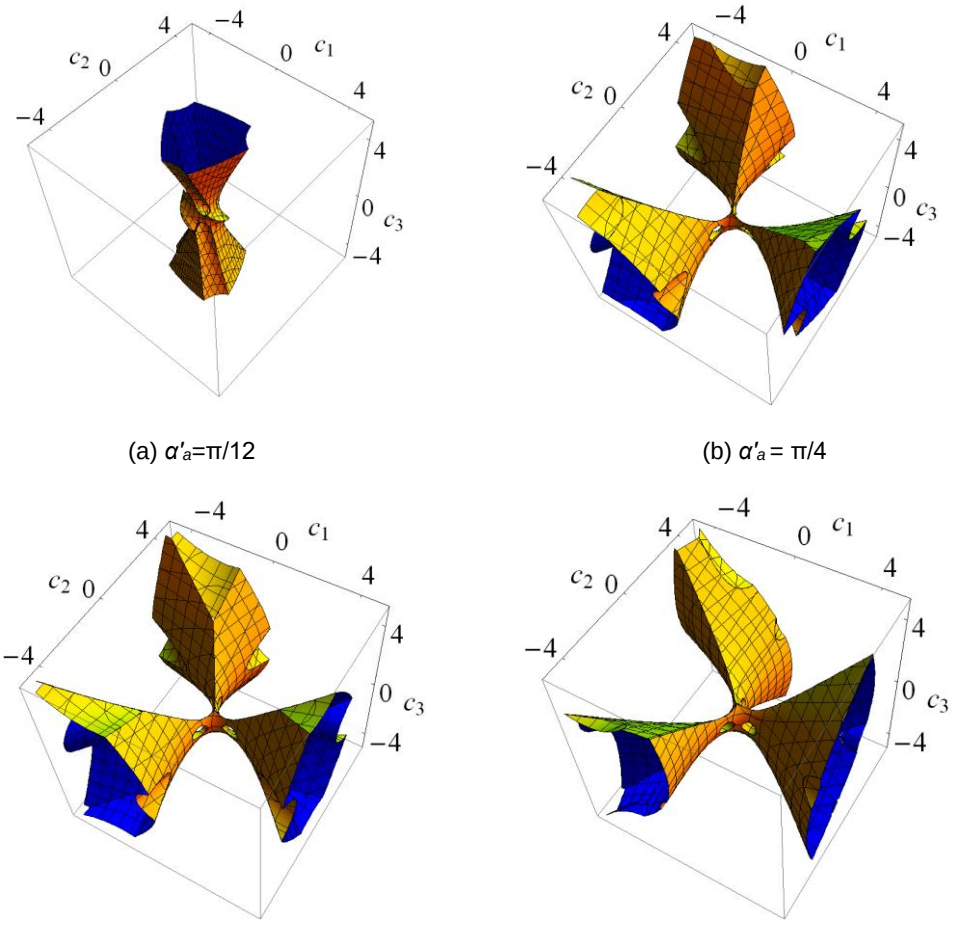

(a) $\alpha'_a=\pi/12$ (b) $\alpha'_a=\pi/4$

(c) $\alpha'_a=\alpha'_b\approx0.907$ (d) $\alpha'_a=7\pi/18$

Figure 6-7 Workspace boundaries with different rotation centers

6.4 Unified Kinematics Modelling of the 3-rTPS

6.4.1 Unified Geometric Constraints

Considering the difference between the two phases of the rT*PS* limb, it can be found that the key part is the rotation about the radial axis which can be represented by angle β as in Fig. 6-8. A limb coordinate system ${}^1o{}^1x{}^1y{}^1z$ is located at the rT joint center with ${}^1x$ axis collinear with the bracket axis and ${}^1y$ axis perpendicular to the bracket surface as in Fig. 6-8.

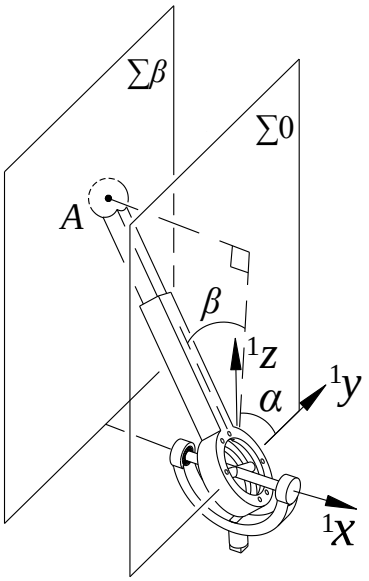

Figure 6-8 Unified modelling of the rTPS limb

It can be taken as that the $(rT)_1PS$ limb has variable angle β while the $(rT)_2PS$ limb has a fixed angle β=0. Geometrically, spherical joint center A is constrained on plane $\sum \beta$ passing through the spherical joint center and perpendicular to the bracket axis for a giving angle β in the $(rT)_1PS$ limb and it is constrained on plane $\sum 0$ passing through the rT joint center and perpendicular to the bracket axis in the $(rT)_2PS$ limb. Based on Fig. 6-8, the spherical joint center A in the limb coordinate system ${}^1o{}^1x{}^1y{}^1z$ can be given as:

$$ {}^1\boldsymbol{a} = l(-\sin\beta, \cos\beta\cos\alpha, \cos\beta\sin\alpha) \begin{cases} \beta & (\mathrm{rT})_1 PS \\ \beta = 0 & (\mathrm{rT})_2 PS \end{cases} \tag{6.23} $$

The rotation about the radial axis of the $(rT)_1PS$ limb can be used as actuation input. Thus, the $(rT)_2PS$ limb can be taken as a special configuration of the $(rT)_1PS$ limb by locking the actuation at β=0. This gives an important method to unify the geometric and kinematics modeling of the 3rT*PS* metamorphic parallel mechanism by covering all its reconfigurable topologies with mobility change. The following is to use the prismatic joint in the $(rT)_2PS$ limb as actuation input and the rotation about the radial axis is added for the second actuation when the limb changes to phase $(rT)_1PS$.

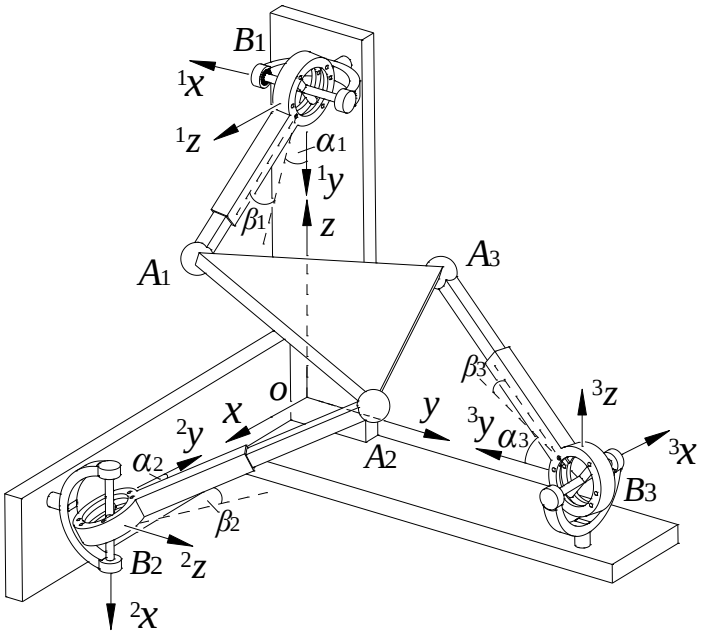

Figure 6-9 Unified kinematics modelling of the 3rT*PS* with perpendicular constraint screws

Based on the above analysis and the coordinate systems of the 3rT*PS* metamorphic parallel mechanism in Fig. 6-9, the geometric constraint of the mechanism can be given as:

$$\begin{cases} \boldsymbol{a}_1 = \boldsymbol{b}_1 + \mathbf{R}(z,-\pi/2)\mathbf{R}(x,-\pi/2)l_1(-\sin\beta_1, \cos\beta_1\cos\alpha_1, \cos\beta_1\sin\alpha_1) \\ \boldsymbol{a}_2 = \boldsymbol{b}_2 + \mathbf{R}(x,-\pi/2)\mathbf{R}(z,\pi/2)l_2(-\sin\beta_2, \cos\beta_2\cos\alpha_2, \cos\beta_2\sin\alpha_2) \\ \boldsymbol{a}_3 = \boldsymbol{b}_3 + \mathbf{R}(z,\pi)l_3(-\sin\beta_3, \cos\beta_3\cos\alpha_3, \cos\beta_3\sin\alpha_3) \end{cases} \quad \begin{cases} \beta_i & (\mathrm{rT})_1 PS \\ \beta_i = 0 & (\mathrm{rT})_2 PS \end{cases} \tag{6.24}$$

where l_i is the limb length, **R**(k, g) represents a rotation about axis k with angle g and is used to translate the vector of the spherical joint center in the limb coordinate systems to the global coordinate system in Fig. 6-9.

6.4.2 Inverse and Forward Kinematics Analysis

6.4.2.1 Inverse Kinematics Analysis

The inverse displacement analysis of the 3rT*PS* metamorphic parallel mechanism is to obtain the actuation parameters (limb length l_i, radial-axis rotation angle β_i) based on the given platform position and orientation. Attach a local coordinate system $o'x'y'z'$ at the centroid of the platform with x' axis passing through spherical joint center A_1 and axis y' parallel to line A_2A_3 as in Fig. 6-10.

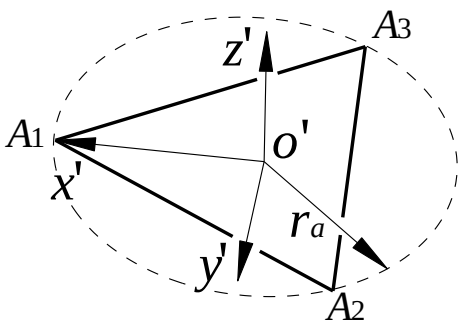

Figure 6-10 The platform coordinate system

When giving the platform position p (p_x, p_y, p_z) and orientation R described in the global coordinate system in Fig.6-9, the position of the spherical joint centers can be obtained as:

$$\begin{cases} \boldsymbol{a}_1 = \boldsymbol{p} + \mathbf{R}.(r_a, 0, 0) \\ \boldsymbol{a}_2 = \boldsymbol{p} + \mathbf{R}.(-r_a/2, \sqrt{3}r_a/2, 0) \\ \boldsymbol{a}_3 = \boldsymbol{p} + \mathbf{R}.(-r_a/2, -\sqrt{3}r_a/2, 0) \end{cases} \tag{6.25}$$

where the spherical joint centers on the platform are symmetrically arranged on a circle with radius r_a.

It should be mentioned that, the platform position should be given based on the mechanism topology as analysed in Section 6.3.1. The basic rule is that when limb 1 is in phase $(\mathrm{rT})_2PS$, position element p_y is constrained by the spherical joint center vector a_1 with its element on y axis a_{1y}=0. This is same for limb 2 with phase $(\mathrm{rT})_2PS$ and p_z is constrained by a_{2z}=0. In limb 3 with phase $(\mathrm{rT})_2PS$, p_x is constrained based on a_{3x}=0. The relation can be concluded as:

$$\begin{cases} p_y = -r_{22}r_a & \text{limb 1 in } (\mathrm{rT})_2PS \\ p_z = r_{31}r_a/2 - \sqrt{3}r_{32}r_a/2 & \text{limb 2 in } (\mathrm{rT})_2PS \\ p_x = r_{11}r_a/2 + \sqrt{3}r_{12}r_a/2 & \text{limb 3 in } (\mathrm{rT})_2PS \end{cases} \tag{6.26}$$

where r_{ij} is the element with the ith row and jth column in the rotation matrix **R**.

By correspondingly equaling Eqs. (6.24) to (6.25), the inverse displacement analysis can be solved:

$$\begin{cases} l_1 = \sqrt{\boldsymbol{c}_1.\boldsymbol{c}_1}, \\ l_2 = \sqrt{\boldsymbol{c}_2.\boldsymbol{c}_2}, \\ l_3 = \sqrt{\boldsymbol{c}_3.\boldsymbol{c}_3}, \end{cases} \quad \begin{cases} \beta_i = -\mathbf{sin}^{-1}(c_{ix}) & (\mathrm{rT})_1 PS \\ \beta_i = 0 & (\mathrm{rT})_2 PS \end{cases} \tag{6.27}$$

where $$\begin{cases} \boldsymbol{c}_1 = \mathbf{R}(x, \pi/2)\mathbf{R}(z, \pi/2)(\boldsymbol{a}_1 - \boldsymbol{b}_1) \\ \boldsymbol{c}_2 = \mathbf{R}(z, -\pi/2)\mathbf{R}(x, \pi/2)(\boldsymbol{a}_2 - \boldsymbol{b}_2) \\ \boldsymbol{c}_3 = \mathbf{R}(z, -\pi)(\boldsymbol{a}_3 - \boldsymbol{b}_3) \end{cases}$$

c_{ix} is the element of vector c_i on the x axis, a_i is expressed in Eqs. (6.25) and b_i is from Eq. (5.1).

6.4.2.2 Forward Kinematics

On the contrary to the inverse displacement analysis, the forward one is to solve the platform position p (p_x, p_y, p_z) and orientation R when giving the corresponding actuation parameters (l_i, β_i) for each topology. Based on this and Fig. 6-10, the geometric constraint of the platform triangle can be described as:

$$\begin{cases} d_{12}^2 = (\boldsymbol{a}_1 - \boldsymbol{a}_2)^2 \\ d_{13}^2 = (\boldsymbol{a}_1 - \boldsymbol{a}_3)^2 \\ d_{23}^2 = (\boldsymbol{a}_2 - \boldsymbol{a}_3)^2 \end{cases} \quad \begin{cases} \beta_i & (\mathrm{rT})_1 PS \\ \beta_i = 0 & (\mathrm{rT})_2 PS \end{cases} \tag{6.28}$$

Substituting Eq. (6.24) into Eq. (6.28) and replacing $\cos\alpha_i = (1-t_i^2)/(1+t_i^2)$, $\sin\alpha_i = 2t_i/(1+t_i^2)$, there is

$$\begin{cases} f_1(1, t_1, t_1^2, t_2^2, t_1 t_2^2, t_1^2 t_2^2) = 0 \\ f_2(1, t_3, t_3^2, t_1^2, t_3 t_1^2, t_3^2 t_1^2) = 0 \\ f_3(1, t_2, t_2^2, t_3^2, t_2 t_3^2, t_2^2 t_3^2) = 0 \end{cases} \tag{6.29}$$

where $f_i(\bullet)$ is a linear function of the power product in the bracket with coefficients depending on known parameters only, t_i is Tan(α_i/2).

By using Sylvester's dialytic elimination method [24,146] for the first two equations in Eq. (6.29), there is

$$f_4(1, t_3, t_2^2, t_3^2, t_2^2 t_3, t_3^3, t_2^4, t_3^4, t_2^2 t_3^2, t_2^2 t_3^3, t_2^4 t_3^1, t_2^2 t_3^4, t_2^4 t_3^2, t_2^4 t_3^3, t_2^4 t_3^4) = 0 \tag{6.30}$$

where $f_4(\bullet)$ is a linear function of the power product in the bracket with coefficients depending on known parameters only.

Then, following the same method for Eq. (6.30) and the third equation in Eq. (6.29), a polynomial with only unknown t_3 can be obtained as:

$$\sum_{i=0}^{+16} h_i t_3^i = 0 \tag{6.31}$$

where coefficient h_i are real constants depending on input data only.

This shows that a univariate equation in t_3 of degree 16 is obtained. Solving Eq. (6.31), sixteen solutions for t_3 can be obtained. Then, t_2 can be solved by substituting each solution of t_3 back to the third equation in Eq. (6.29) and selecting the roots satisfying Eq. (6.30). Following this, t_1 can be solved by substituting each pair of solutions of t_2 and t_3 into the first equation in Eq. (6.29) with proof of the second equation in Eq. (6.29). Based on this, sixteen pair of solutions of t_1, t_2, t_3 are obtained and the spherical joint center A_i can be calculated by substituting α_i=2ArcTan(t_i) into Eq. (6.24). Then, the platform position and orientation can be determined using the three spherical joint centers with Fig. 6-10 as:

$$\begin{cases} \boldsymbol{z}' = (\boldsymbol{a}_2 - \boldsymbol{a}_1) \times (\boldsymbol{a}_3 - \boldsymbol{a}_1) / \left\| (\boldsymbol{a}_2 - \boldsymbol{a}_1) \times (\boldsymbol{a}_3 - \boldsymbol{a}_1) \right\| \\ \boldsymbol{y}' = (\boldsymbol{a}_2 - \boldsymbol{a}_3) / (\sqrt{3} r_a) \\ \boldsymbol{x}' = \boldsymbol{y}' \times \boldsymbol{z}' \\ \mathbf{R} = (\boldsymbol{x}', \boldsymbol{y}', \boldsymbol{z}') \\ \boldsymbol{p} = \boldsymbol{a}_1 - r_a \boldsymbol{x}' \end{cases} \tag{6.32}$$

The real roots correspond to assembly configurations of the 3-rT*PS* parallel mechanism.

6.4.3 Numerical Examples of the Kinematics Analysis

6.4.3.1 Inverse Kinematics Examples

Based on the kinematics analysis in section 6.3.2, inverse kinematics examples for the four topologies of the 3-rT*PS* metamorphic parallel mechanism can be given as in Table 6-2 to demonstrate the unified kinematics modelling. The structure parameters are set as: r_a=10, r_b=2$\sqrt{3}$. In the examples in Table 6-2, the four topologies correspond to the four in Fig. 5-1 to Fig. 5-3, which means that the 2(rT)$_2$*PS*-1(rT)$_1$*PS* is obtained by altering the phase of limb 1 from the topology 3-(rT)$_2$*PS*. Then, the 1(rT)$_2$*PS*-2(rT)$_1$*PS* is obtained by further altering the phase of limb 2. By giving the orientation and position parameters of the platform and using Eq. (6.27), the inverse kinematics can be solved with results in Table 6-2. The input rotation matrix is given as:

$$\mathbf{R}_0 = \begin{bmatrix} 0.0861 & 0.5560 & 0.8267 \\ -0.7223 & -0.5366 & 0.4361 \\ 0.6862 & -0.6347 & 0.3554 \end{bmatrix} \tag{6.33}$$

which is used for all the topologies in Table 6-2.

Table 6-3 Inverse kinematics examples

Topology	DOFs	Input parameters	Output parameters
3(rT)$_2$*PS*	3R	$\mathbf{R}_0$, ($\boldsymbol{p}_0$= (1.817,2.502,3.092))	l_1=5, l_2=7, l_3=6.
2(rT)$_2$*PS*-1(rT)$_1$*PS*	3R1T$_y$	$\mathbf{R}_0$, p_y= p_{0y}+1.4.	l_1=5.19, l_2=7.55, l_3=4.99, β_1=0.273.
1(rT)$_2$*PS*-	3R2T$_{yz}$	$\mathbf{R}_0$, p_y= p_{0y}+1.4, p_z= p_{0z}+1.2.	l_1=4.1865, l_2=7.642, l_3=5.963,

2(rT)$_1$*PS*			β_1=0.341, β_2=0.1577.
3(rT)$_1$*PS*	3R3T	$\mathbf{R}_0$, p_x= p_{0x}-1.3, p_y= p_{0y}+1.4, p_z= p_{0z}+1.2.	l_1=3.7037, l_2=8.7987, l_3=6.103, β_1=0.3876, β_2=0.1368, β_3= −0.2146.

From Table 6-2, $\boldsymbol{p}_0$ is the parasitic position of the 3(rT)$_2$*PS* parallel mechanism when giving the orientation $\mathbf{R}_0$. It can be seen that the number of input parameters increases with the mobility increasing in the topology change. Following this, the number of output parameters also increases with specific rotation angles (β_i) about the radial axes of the (rT)$_1$*PS* limbs instead of value zero in the (rT)$_2$*PS* phase.

6.4.3.2 Forward Kinematics Examples

In order to check the validity of the forward kinematics analysis, the same structure parameters and the output parameters in Table 6-2 in the inverse kinematics examples are used as the input for the forward kinematics examples. Following the procedures in Section 6.3.2.2, the forward kinematics can be solved. As for each topology, there are sixteen solutions for the forward kinematics analysis, only the solutions for topology 3-(rT)$_2$*PS* are listed in Table 6-3 as an example. Real solutions of all the topologies are listed in Table 6-4 with corresponding mechanism assemblies demonstrated in Fig. 6-11.

Table 6-4 Forward kinematics solutions of 3-(rT)$_2$*PS*

	t_1	t_2	t_3
1	-0.0242 + 0.6799*I	0.3989 + 0.4957*I	-1.951 - 0.7218*I
2	-0.0242 - 0.6799*I	0.3989 - 0.4957*I	-1.951 + 0.7218*I
3	0.1929 - 0.4598*I	0.5653 - 0.1*I	-0.1976 - 0.3454*I
4	0.1929 + 0.4598*I	0.5653 + 0.1*I	-0.1976 + 0.3454*I
5	0.3443 - 0.6502*I	-2.3758 - 0.1344*I	0.0042 - 0.6527*I
6	0.3443 + 0.6502*I	-2.3758 + 0.1344*I	0.0042 + 0.6527*I
7	-0.0046	-0.0784	0.046
8	0.4123 - 0.0323*I	-0.0416 - 0.1805*I	0.2592 - 0.2166*I
9	0.4123 + 0.0323*I	-0.0416 + 0.1805*I	0.2592 + 0.2166*I

10	0.2343 - 0.9106*I	0.3278 - 0.8633*I	0.29 - 0.8831*I
11	0.2343 + 0.9106*I	0.3278 + 0.8633*I	0.29 + 0.8831*I
12	-1.6752 + 0.8184*I	-0.0408 - 0.5657*I	0.3571 - 0.5329*I
13	-1.6752 - 0.8184*I	-0.0408 + 0.5657*I	0.3571 + 0.5329*I
14	0.2219	0.1569	0.358
15	-0.0911 - 0.3644*I	0.262 - 0.2656*I	0.5832 - 0.0657*I
16	-0.0911 + 0.3644*I	0.262 + 0.2656*I	0.5832 + 0.0657*I

Table 6-5 Real solutions of forward kinematics

Topology	Real solutions
3(rT)$_2$*PS*	$\mathbf{R}_{11}=\begin{bmatrix}-0.3058 & 0.5142 & 0.8013\\ -0.2824 & -0.8527 & 0.4395\\ 0.9092 & -0.0918 & 0.4059\end{bmatrix}$; $R_{12}=R_0$; p_{11}=(1.0131,0.9782,1.8505); p_{12}= (1.8171, 2.5022,3.0925).
2(rT)$_2$*PS*-1(rT)$_1$*PS*	$\mathbf{R}_{21}=\begin{bmatrix}-0.2888 & 0.4111 & 0.8646\\ -0.1683 & -0.9108 & 0.3768\\ 0.9424 & -0.0366 & 0.3323\end{bmatrix}$; $R_{22}=R_0$; p_{21}= (0.733,1.983,1.7424); p_{22}= (1.8171,3.9022,3.0925).
1(rT)$_2$*PS*-2(rT)$_1$*PS*	$\mathbf{R}_{31}=\begin{bmatrix}-0.1775 & 0.4282 & 0.8861\\ 0.0039 & -0.9001 & 0.4357\\ 0.9841 & 0.0808 & 0.1581\end{bmatrix}$; $\mathbf{R}_{32}=\begin{bmatrix}0.1570 & 0.4216 & 0.8931\\ -0.0437 & -0.9004 & 0.4327\\ 0.9866 & -0.1070 & -0.1229\end{bmatrix}$; $\mathbf{R}_{33}=\begin{bmatrix}0.2859 & 0.4304 & 0.8562\\ -0.4272 & -0.7425 & 0.5158\\ 0.8578 & -0.5132 & -0.0284\end{bmatrix}$; $R_{34}=R_0$; p_{31}= (0.977,1.386,2.662); p_{32}= (1.5367,1.5516,3.23); p_{33}= (1.7862,2.8797,4.2254); p_{34}= (1.8171,3.9022,4.292).
3(rT)$_1$*PS*	$\mathbf{R}_{41}=\begin{bmatrix}0.1286 & 0.4409 & 0.8882\\ -0.0452 & -0.8921 & 0.4495\\ 0.9906 & -0.0979 & -0.0948\end{bmatrix}$; $\mathbf{R}_{42}=\begin{bmatrix}0.2193 & 0.4371 & 0.8723\\ -0.0816 & -0.8827 & 0.4628\\ 0.9722 & -0.1727 & -0.1579\end{bmatrix}$; $\mathbf{R}_{43}=\begin{bmatrix}0.3199 & 0.4307 & 0.8439\\ -0.1962 & -0.8413 & 0.5037\\ 0.9269 & -0.3267 & -0.1846\end{bmatrix}$; $R_{44}=R_0$; p_{41}= (0.2457,1.556,3.2098); p_{42}= (0.391,1.683,3.402); P_{43}= (0.546,2.079,3.786); p_{44}= (0.5171,3.9022,4.292).

In Table 6-4, it can be found that one of the real solutions of the forward kinematics corresponds to the input one of the inverse kinematics examples in Table 6-2, indicating the closure validity of the inverse and forward kinematics analysis. This can be also seen in Fig. 6-11 that the orientation of the platform (green triangle) is the same in Fig. 6-11 (b), (d), (h) and (m), corresponding to the rotation matrix $\mathbf{R}_0$ in Eq. (6.33) which is the input of the inverse kinematics analysis in Table 6-2. In Fig. 6-11, the blue line is the base and the black lines represent the limbs, the platform coordinate system is showed with blue arrow in *x* direction, black arrow in *y* direction and the red arrow in the *z* direction perpendicular to the platform plane.

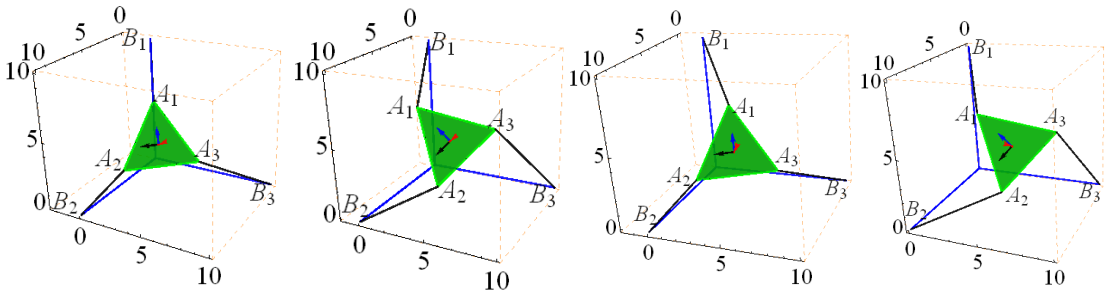

(a) ($\mathbf{R}_{11}$, $\boldsymbol{p}_{11}$) (b) ($\mathbf{R}_{12}$, $\boldsymbol{p}_{12}$) (c) ($\mathbf{R}_{21}$, $\boldsymbol{p}_{21}$) (d) ($\mathbf{R}_{22}$, $\boldsymbol{p}_{22}$)

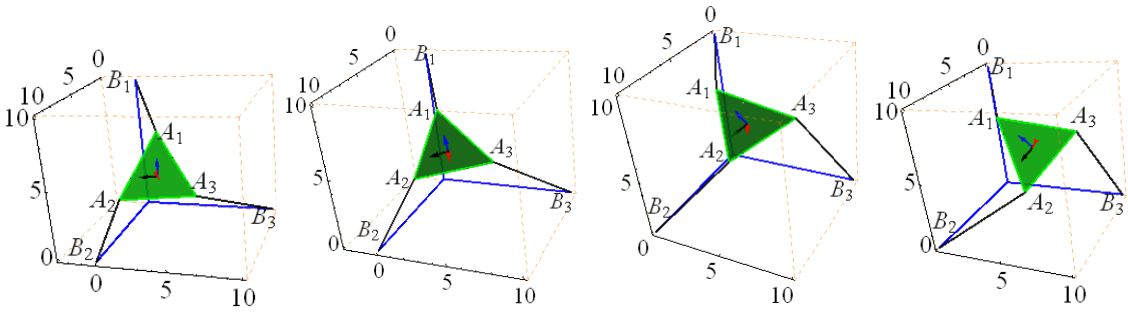

(e) ($\mathbf{R}_{31}$, $\boldsymbol{p}_{31}$) (f) ($\mathbf{R}_{32}$, $\boldsymbol{p}_{32}$) (g) ($\mathbf{R}_{33}$, $\boldsymbol{p}_{33}$) (h) ($\mathbf{R}_{34}$, $\boldsymbol{p}_{34}$)

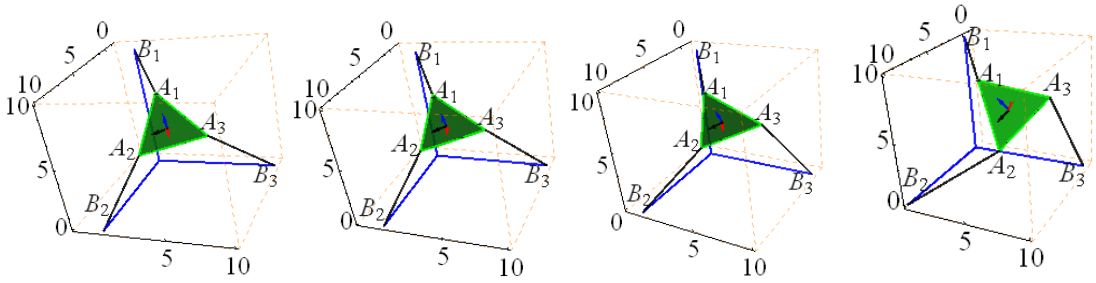

(i) ($\mathbf{R}_{41}$, $\boldsymbol{p}_{41}$) (j) ($\mathbf{R}_{42}$, $\boldsymbol{p}_{42}$) (k) ($\mathbf{R}_{43}$, $\boldsymbol{p}_{43}$) (m) ($\mathbf{R}_{44}$, $\boldsymbol{p}_{44}$)

Figure 6-11 Mechanism assemblies corresponding to the real solutions in Table 4-4

6.5 Unified Kinematics Modelling and Workspace Analysis of the 4-rTPS

In the rT*PS* limb, there are three single DOF joints that can be selected as actuated joints, including the two rotational joints of the rT joint and the prismatic joint. The actuation scheme requires that the selected actuations can determine the platform position and orientation with finite forward kinematics solutions. Based on these, it can be found that any actuation selection from the three single-DOF joints in the four limbs of the 4-rT*PS* metamorphic parallel mechanism as in Fig. 6-12 can satisfy the actuation scheme requirement except the case of 4-$(rT)_2PS$ with bifurcation which requires that the inputs should be from two adjacent limbs. Considering the simplicity of kinematics analysis and that prismatic joints give better force transmission than revolute joints, the four prismatic joints in the mechanism and the two radial rotational joints in limb 1 and limb 2 are selected as the actuated joints corresponding to variable topologies. For mobility n ($2 \leqslant n \leqslant 4$), n prismatic joints will be active while 4-n prismatic joints and the two radial joints are passive. When the mechanism is in mobility 5, the four prismatic joints with one of the two radial joints will be active. All the six joints are active when coming to mobility 6.

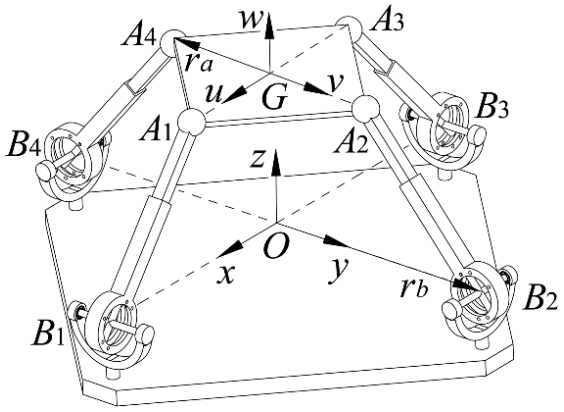

Figure 6-12 The 4-rT*PS* MPM

6.5.1 Unified Limb Kinematics Modelling

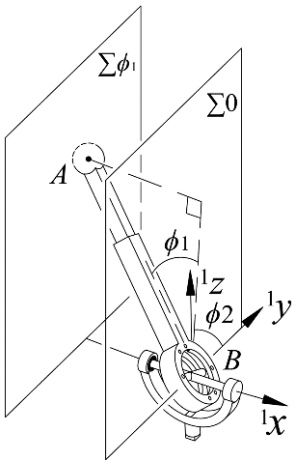

Figure 6-13 Unified limb modelling

For limb 1 and limb 2, when they are in the phase (rT)$_2$*PS*, their prismatic joints are chosen as the actuations. When they are altered into phase (rT)$_1$*PS*, by further selecting the radial axis rotation as the input, a unified kinematics model can be obtained. This is due to the difference between the two phases of the rT*PS* limb as in Fig. 6-13. It can be taken as that the (rT)$_1$*PS* limb has variable radial axis angle ϕ_1 while the (rT)$_2$*PS* limb has a fixed angle ϕ_1=0. Geometrically, spherical joint center *A* is constrained on plane $\sum\phi_1$ passing through the spherical joint center and perpendicular to the bracket axis for a giving angle ϕ_1 in the (rT)$_1$*PS* limb and it is constrained on plane $\sum$0 passing through the rT joint center and perpendicular to the bracket axis in the (rT)$_2$*PS* limb as in Fig. 6-13.

Based on the above analysis and the coordinate systems of the 3-rT*PS* metamorphic parallel mechanism in Fig. 6-12, the geometric constraint of the mechanism relating to limb 1 and limb 2 can be expressed in the fixed coordinate system *Oxyz* by covering their two phases as:

$$\begin{cases} \boldsymbol{a}_1 = \boldsymbol{b}_1 + \mathbf{R}(z,\pi/2)l_1(-\sin\phi_{11}, \cos\phi_{11}\cos\phi_{12}, \cos\phi_{11}\sin\phi_{12}) \\ \boldsymbol{a}_2 = \boldsymbol{b}_2 + \mathbf{R}(z,\pi)l_2(-\sin\phi_{21}, \cos\phi_{21}\cos\phi_{22}, \cos\phi_{21}\sin\phi_{22}) \end{cases} \tag{6.34}$$

where l_i and ϕ_{i1} are the length and radial rotation angle of limb *i* separately, ϕ_{i1}=0 for (rT)$_2$*PS* and it is an unknown for (rT)$_1$*PS*. **R**(*k*, *g*) represents a rotation about axis *k* with angle *g* and is used to translate the vector of the spherical joint center in the limb coordinate systems to the global coordinate system.

For limb 3 and limb 4, when they are in the phase $(\mathrm{rT})_2PS$, no actuation is selected from them. When they are altered into phase $(\mathrm{rT})_1PS$, their prismatic joints will be the actuated joints. Thus, the kinematics modelling is:

$$\begin{cases} (\boldsymbol{a}_3-\boldsymbol{b}_3).(\boldsymbol{a}_3-\boldsymbol{b}_3)=l_3^2;(\boldsymbol{a}_4-\boldsymbol{b}_4).(\boldsymbol{a}_4-\boldsymbol{b}_4)=l_4^2 & (\mathrm{rT})_1PS \\ \boldsymbol{a}_3.(0,1,0)^{\mathrm{T}}=0;\boldsymbol{a}_4.(1,0,0)^{\mathrm{T}}=0 & (\mathrm{rT})_2PS \end{cases} \tag{6.35}$$

where $\boldsymbol{a}_3=(x_3,y_3,z_3)^{\mathrm{T}}$, $\boldsymbol{a}_4=\boldsymbol{a}_1+\boldsymbol{a}_3-\boldsymbol{a}_2$.

By combining the above limb models in different phases, all the kinematics modelling of the reconfigurable topologies of the 4-rT*PS* metamorphic parallel mechanism can be obtained. They can be solved inversely and forwardly in the following way.

6.5.2 Inverse and Forward Kinematics Analysis

6.5.2.1 Inverse Kinematics Analysis

The inverse displacement analysis of the 4-rT*PS* metamorphic parallel mechanism is to obtain the actuation parameters (limb length l_i, radial-axis rotation angle ϕ_{i1}) based on the given platform position and orientation. Based on Eq. (6.34) and Eq. (6.35), the inverse kinematics can be solved directly as

$$\begin{cases} l_i=\left|\mathbf{R}\,\boldsymbol{a}_i'+\boldsymbol{p}-\boldsymbol{b}_i\right| & (i=1,2,3,4) \\ \phi_{11}=\sin^{-1}(\mathbf{R}(z,-\pi/2).(\mathbf{R}\,\boldsymbol{a}_1'+\boldsymbol{p}-\boldsymbol{b}_1).(1,0,0)^{\mathrm{T}}) \\ \phi_{21}=\sin^{-1}(\mathbf{R}(z,-\pi).(\mathbf{R}\,\boldsymbol{a}_2'+\boldsymbol{p}-\boldsymbol{b}_2).(1,0,0)^{\mathrm{T}}) \end{cases} \tag{6.36}$$

These solutions of the inverse kinematics cover all the configurations and can be used directly corresponding to the topology requirements of the actuation.

6.5.2.2 Forward Kinematics

On the contrary to the inverse displacement analysis, the forward one is to solve the platform position $\boldsymbol{p}$ and orientation $\mathbf{R}$ when giving the corresponding actuation parameters (l_i, ϕ_{i1}) for each topology. Based on Eq. (6.34), limb 1 and limb 2 are unified in the kinematics modelling

with consideration of two phases. Then, the forward kinematics can be divided into three cases by considering the limb phases of limb 3 and limb 4.

Case 1: limb 3 and limb 4 both in phase $(rT)_2PS$

Based on the geometric structure of the platform, there are:

$$\begin{cases} (\sqrt{2}r_a)^2 = (\boldsymbol{a}_1 - \boldsymbol{a}_2)^2 \\ (2r_a)^2 = (\boldsymbol{a}_1 - \boldsymbol{a}_3)^2 \\ 2\sqrt{2}r_a^2\cos(\pi/4) = (\boldsymbol{a}_2 - \boldsymbol{a}_1).(\boldsymbol{a}_3 - \boldsymbol{a}_1) \\ \boldsymbol{a}_3.(0,1,0)^{\mathrm{T}} = 0 \\ (\boldsymbol{a}_1 + \boldsymbol{a}_3 - \boldsymbol{a}_2).(1,0,0)^{\mathrm{T}} = 0 \end{cases} \quad \begin{cases} \phi_{i1} & (\mathrm{rT})_1 PS \\ \phi_{i1} = 0 & (\mathrm{rT})_2 PS \end{cases} \tag{6.37}$$

where the first two represent the distances from spherical joint A_1 to A_2 and A_3, the third one describes the angle $\angle A_2A_1A_3=\pi/4$, the fourth and the fifth are from Eq. (6.25) for the spherical joint centers of limb 3 and limb 4 constrained on their own planes.

Substituting Eq. (6.24) and Eq. (6.25) into Eq. (6.27) there is

$$\begin{cases} f_1(\phi_{12}, \phi_{22}) = 0 \\ f_2(\phi_{12}, 1, x_3, y_3, z_3, x_3^2, y_3^2, z_3^2) = 0 \\ f_3(\phi_{12}, \phi_{22}, x_3, y_3, z_3) = 0 \\ f_4(y_3) = y_3 = 0 \\ f_5(\phi_{12}, \phi_{22}, x_3, y_3, z_3) = 0 \end{cases} \tag{6.38}$$

where $f_i(\bullet)$ is a function of the power products in the bracket.

The last three equations in Eq. (6.38) are linear functions of (x_3, y_3, z_3), thus they can be linearly solved. Substituting the results into f_2 and replacing $\cos\phi_{i2} = (1-t_i^2)/(1+t_i^2)$, $\sin\phi_{i2} = 2t_i/(1+t_i^2)$ in f_1 and f_2, there is

$$\begin{cases} f_6(1, t_1^2, t_2^2, t_1 t_2, t_1^2 t_2^2) = 0 \\ f_7(1, t_1^2, t_1^4, t_1^6, t_1^i t_2^j, \ldots, t_1^6 t_2^4) = 0 \ \ (j \neq 0) \end{cases} \tag{6.39}$$

where f_6 and f_7 are linear functions of the power products in the bracket with their coefficients depending on the input parameters only. t_i is Tan(ϕ_{i2}/2).

By using Sylvester's dialytic elimination method [146] for the two equations in Eq. (6.39), a polynomial with only unknown t_1 can be obtained as:

$$\sum_{i=0}^{+10} h_{1i} t_1^{2i} = 0 \tag{6.40}$$

where coefficient h_{1i} are real constants depending on input data only.

This shows that a univariate equation in t_1 of degree 20 is obtained. Solving Eq. (6.40), 20 solutions for t_1 can be obtained. Then, t_2 can be solved by substituting each solution of t_1 back to the equations in Eq. (6.39) and solving the common roots. Following this, (x_3, y_3, z_3) can be linearly solved by substituting each pair of solutions of t_1, t_2 and t_3 into the last three equations in Eq. (6.38). Based on this, 20 sets of solutions of t_1, t_2, t_3 and (x_3, y_3, z_3) are obtained and the spherical joint center A_i can be calculated by substituting ϕ_{i2}=2ArcTan(t_i) into Eq. (6.34) and Eq. (6.35). Then, the platform position and orientation can be determined using the three spherical joint centers as:

$$\begin{cases} \boldsymbol{u} = (\boldsymbol{a}_1 - \boldsymbol{a}_2) / \left|(\boldsymbol{a}_1 - \boldsymbol{a}_2)\right| \\ \boldsymbol{v} = (2\boldsymbol{a}_3 - \boldsymbol{a}_1 - \boldsymbol{a}_2) / \left|(2\boldsymbol{a}_3 - \boldsymbol{a}_1 - \boldsymbol{a}_2)\right| \\ \boldsymbol{w} = \boldsymbol{u} \times \boldsymbol{v}, \mathbf{R} = (\boldsymbol{u}, \boldsymbol{v}, \boldsymbol{w}), \ \ \boldsymbol{p} = \boldsymbol{a}_1 - r_a \boldsymbol{u} \end{cases} \tag{6.41}$$

The real roots correspond to assembly configurations of the 3-rT*PS* parallel mechanism.

Case 2: one of limb 3 and limb 4 is in phase $(rT)_1PS$

Based on the above analysis, when limb 3 (or limb 4) is in phase (rT)$_1$*PS*, the geometric constraints is the same with Eq. (6.37) by replacing the fourth (or fifth equation) with $(\boldsymbol{a}_3-\boldsymbol{b}_3).(\boldsymbol{a}_3-\boldsymbol{b}_3)=l_3^2$ (or $(\boldsymbol{a}_4-\boldsymbol{b}_4).(\boldsymbol{a}_4-\boldsymbol{b}_4)=l_4^2$). For both case there is

$$f_8'(1, x_3, y_3, z_3, x_3^2, y_3^2, z_3^2)=0 \tag{6.42}$$

It is found that f_2 and f_8' are linear functions of (x_3^2, y_3^2, z_3^2) with their coefficients 1. Then a new equation can be obtained from these two by reducing (x_3^2, y_3^2, z_3^2) as

$$f_{82}'(\phi_{12}, 1, x_3, y_3, z_3)=0 \tag{6.43}$$

Thus, (x_3, y_3, z_3) can be linearly solved from f_3, f_5 in Eq. (6.38) and f_{82}' in (18). Following the same procedure for Eq. (6.39), there is

$$\begin{cases} f_6(1, t_1^2, t_2^2, t_1t_2, t_1^2t_2^2)=0 \\ f_7'(1, t_1^2, t_1^4, t_1^6, t_1^8, t_1^it_2^j, \ldots, t_1^8t_2^4)=0 \ \ (j\neq 0) \end{cases} \tag{6.44}$$

It can be seen that f_7' is two order higher than f_7 in terms of t_1. This is because the order change of the geometric constraints of limb 3 (or limb 4) from 1 with the angle constraint in phase (rT)$_2$*PS* to 2 with limb length constraint in phase (rT)$_1$*PS*.

Similarly, using Sylvester's dialytic elimination method [146] for the two equations in Eq. (6.44), a polynomial with only unknown t_1 can be obtained as:

$$\sum_{i=0}^{+12} h_{2i}t_1^{2i}=0 \tag{6.45}$$

where coefficient h_{2i} are real constants depending on input data only.

This shows a univariate equation in t_1 of degree 24 is obtained which is four order higher than Eq. (6.40) due to the phase change of limb 3 (or limb 4). The other procedures can follow those in Case 1.

Case 3: limb 3 and limb 4 are both in phase (rT)$_1$PS

Based on the above analysis, when limb 3 and limb 4 are both in phase (rT)$_1$*PS*, the geometric constraints is the same with Eq. (6.37) by replacing the fourth and the fifth equations with $(\boldsymbol{a}_3-\boldsymbol{b}_3).(\boldsymbol{a}_3-\boldsymbol{b}_3)=l_3^2$ and $(\boldsymbol{a}_4-\boldsymbol{b}_4).(\boldsymbol{a}_4-\boldsymbol{b}_4)=l_4^2$ respectively. There are

$$\begin{cases} f_4'(1, x_3, y_3, z_3, x_3^2, y_3^2, z_3^2)=0 \\ f_5'(1, x_3, y_3, z_3, x_3^2, y_3^2, z_3^2)=0 \end{cases} \tag{6.46}$$

As f_2, f_4' and f_5' are linear functions of (x_3^2, y_3^2, z_3^2) with their coefficients 1. Then two new equations can be obtained from these two by reducing (x_3^2, y_3^2, z_3^2) as

$$\begin{cases} f_{42}'(\phi_{12}, 1, x_3, y_3, z_3)=0 \\ f_{52}'(\phi_{12}, 1, x_3, y_3, z_3)=0 \end{cases} \tag{6.47}$$

Thus, (x_3, y_3, z_3) can be linearly solved from f_3 in Eq. (6.38) and f_{42}', f_{52}' in Eq. (6.47). Following the same procedure for Eq. (6.39), there is

$$\begin{cases} f_6(1, t_1^2, t_2^2, t_1t_2, t_1^2t_2^2)=0 \\ f_9(1, t_1^2, t_1^4, t_1^6, t_1^8, t_1^it_2^j, \ldots, t_1^8t_2^8)=0 \ \ (j\neq 0) \end{cases} \tag{6.48}$$

It can be seen that f_9 is two order higher in terms of t_1 and four order higher in terms of t_2 than f_7. This is because the order change of the geometric constraints of both limb 3 and limb 4 from 1 with the angle constraint in phase (rT)$_2$*PS* to 2 with limb length constraint in phase (rT)$_1$*PS*.

Following Sylvester's dialytic elimination method [146] for the two equations in Eq. (6.48), a polynomial with only unknown t_1 can be obtained as:

$$\sum_{i=0}^{+16} h_{3i} t_1^{2i} = 0 \tag{6.49}$$

where coefficient h_{3i} are real constants depending on input data only.

This shows a univariate equation in t_1 of degree 32 is obtained which is 12 order higher than Eq. (6.40) and 8 order higher than Eq. (6.45) due to the phase change of limb 3 and limb 4. The other procedures can follow those in Case 1.

The above procedures solve forward kinematics of all the topologies of the 4-rT*PS* metamorphic parallel mechanism. It can be seen that with the mobility increasing due to topology change, the forward kinematics polynomials have higher order in terms of the unknowns.

6.5.3 Unified Singularity Modeling with Workspace Analysis

6.5.3.1 Unified Singularity Modeling

The infinitesimal twist of the moving platform of the 4-rT*PS* parallel mechanism can be written as the linear combination of instantaneous twists of each limb:

$$\boldsymbol{S}_G = \dot{\phi}_{i1}\boldsymbol{S}_{i1} + \dot{\phi}_{i2}\boldsymbol{S}_{i2} + \dot{l}_i\boldsymbol{S}_{i3} + \dot{\phi}_{i4}\boldsymbol{S}_{i4} + \dot{\phi}_{i5}\boldsymbol{S}_{i5} + \dot{\phi}_{i6}\boldsymbol{S}_{i6} \quad (i = 1, 2, 3, 4) \tag{6.50}$$

where $\boldsymbol{S}_G$ represents the infinitesimal twist of the moving platform, $\boldsymbol{S}_{ij}$ (j=1,2,3,4,5,6) denotes the unit screw of the jth 1-DOF joint in limb i, $\dot{l}_i$ is the distance rate of the prismatic joint in limb i, $\dot{\phi}_{ij}$ (j=1,2,4,5,6) represent angular rates of the rT joint and spherical joint in limb i.

Based on the kinematics analysis in Section 6.4.2, the translation of the prismatic joint is chosen as the input for limb 1 and limb 2 in the phase $(rT)_2PS$ and the rotation about the radial axis is taken as the second actuation when the limb changes to phase $(rT)_1PS$. There is no actuation

input from limb 3 and limb 4 when they are in phase $(\mathrm{rT})_2PS$ and their prismatic joints are actuated in the phase $(\mathrm{rT})_1PS$. Thus by locking the active joints in the limbs temporarily and taking the reciprocal product on both sides of Eq. (6.50), for limb 1 and limb 2 there is

$$\begin{bmatrix} \boldsymbol{S}_{i1}^r & \boldsymbol{S}_{i2}^r \end{bmatrix}^T \circ \boldsymbol{S}_G = \begin{cases} \begin{bmatrix} 0 & \dot{l}_i \end{bmatrix}^T & (\mathrm{rT})_2 PS \text{ limb} \\ \begin{bmatrix} \dot{\phi}_{i1} & \dot{l}_i \end{bmatrix}^T & (\mathrm{rT})_1 PS \text{ limb} \end{cases} \quad (i = 1, 2) \tag{6.51}$$

where $\boldsymbol{S}_{i1}^r$ is the reciprocal screws of geometric constraint to all motion screws in limb *i* in phase $(\mathrm{rT})_2PS$ and it passes through the spherical joint center with the direction parallel to the bracket axis of the rT joint [10]. $\boldsymbol{S}_{i1}^r$ becomes the actuation screw reciprocal to all the motion screws in Eq. (6.50) except the actuation joint $\boldsymbol{S}_{i1}$ in phase $(\mathrm{rT})_1PS$ and it passes through the spherical joint center with direction perpendicular to both the limb and the radial axis of the rT joint. $\boldsymbol{S}_{i2}^r$ is the actuation screw reciprocal to all in Eq. (6.50) except the prismatic joint screw $\boldsymbol{S}_{i3}$ in both limb phases and it is collinear with the limb.

For limb 3 and limb 4 there is

$$\boldsymbol{S}_{j1}^r \circ \boldsymbol{S}_G = \begin{cases} 0 & (\mathrm{rT})_2 PS \text{ limb} \\ \dot{l}_j & (\mathrm{rT})_1 PS \text{ limb} \end{cases} \quad (j = 3, 4) \tag{6.52}$$

where $\boldsymbol{S}_{j1}^r$ is the reciprocal screws of geometric constraint to all motion screws in limb *j* in phase $(\mathrm{rT})_2PS$ and it has the direction parallel to the bracket axis of the rT joint and passing through the spherical joint center. $\boldsymbol{S}_{j1}^r$ becomes the actuation screw reciprocal to all the motions screws in Eq. (6.50) except the actuated prismatic joint $\boldsymbol{S}_{i3}$ in phase $(\mathrm{rT})_1PS$ and with direction collinear with the limb.

Equations in Eq. (6.51) and Eq. (6.52) for the four limbs can be rewritten in matrix form as:

$$\begin{bmatrix} \boldsymbol{S}_{11}^r \\ \boldsymbol{S}_{12}^r \\ \boldsymbol{S}_{21}^r \\ \boldsymbol{S}_{22}^r \\ \boldsymbol{S}_{31}^r \\ \boldsymbol{S}_{41}^r \end{bmatrix} \circ \boldsymbol{S}_G = \mathbf{J}\,\boldsymbol{S}_G = \begin{bmatrix} \boldsymbol{M}_1 \\ \boldsymbol{b}_1 \times \boldsymbol{u}_1 \quad \boldsymbol{u}_1 \\ \boldsymbol{M}_2 \\ \boldsymbol{b}_2 \times \boldsymbol{u}_2 \quad \boldsymbol{u}_2 \\ \boldsymbol{M}_3 \\ \boldsymbol{M}_4 \end{bmatrix} \boldsymbol{S}_G = \begin{bmatrix} g_1 \\ \dot{l}_1 \\ g_2 \\ \dot{l}_2 \\ g_3 \\ g_4 \end{bmatrix} \tag{6.53}$$

where

$$\text{for } (\text{rT})_2PS: \begin{cases} \boldsymbol{M}_i = \begin{bmatrix} \boldsymbol{a}_i \times \boldsymbol{y} & \boldsymbol{y} \end{bmatrix}, g_i = 0; \\ \boldsymbol{M}_j = \begin{bmatrix} \boldsymbol{a}_j \times \boldsymbol{x} & \boldsymbol{x} \end{bmatrix}, g_j = 0; , \\ (i = 1,3;\ j = 2,4) \end{cases}$$

$$\text{for } (\text{rT})_1PS: \begin{cases} \boldsymbol{M}_i = \begin{bmatrix} \boldsymbol{a}_i \times (\boldsymbol{u}_i \times \boldsymbol{u}_{ir}) & \boldsymbol{u}_i \times \boldsymbol{u}_{ir} \end{bmatrix}, g_i = \dot{\phi}_{i1}; \\ \boldsymbol{M}_j = \begin{bmatrix} \boldsymbol{b}_j \times \boldsymbol{u}_j & \boldsymbol{u}_j \end{bmatrix}, g_j = \dot{l}_j; \\ (i = 1,2;\ j = 3,4) \end{cases}$$

where $\boldsymbol{x}=[1,0,0]^T$, $\boldsymbol{y}=[0,1,0]^T$, $\boldsymbol{u}_i$ is the unit vector of the limb direction, $\boldsymbol{u}_{ir}$ is the unit vector of the radial axis.

Thus **J** is the 6 by 6 Jacobian matrix. In general, the Jacobian matrix maps the velocities between the manipulator and the actuation input. Once the manipulator meets the singular configuration, this mapping loses its function and the rank of the Jacobian matrix decreases to be less than 6. This can be also interpreted that the six constraint forces in **J** are linearly dependent. Inversely, identifying the dependent conditions for the constraint forces in the workspace will reveal the singular configurations of the manipulator. In order to demonstrate this, some numerical parameters with physical constraints are given as: the platform radius r_a=10 cm, base radius r_b=20 cm, spherical joint rotation angle ≤ π/4 radian, bracket-axis rotation angle $\phi_{i1} \le 7\pi/18$ radian, radial axis rotation angle $\phi_{i2} \le \pi/2$ radian, limb length 11 cm ≤ l_i ≤ 22 cm.

6.5.3.2 Workspace and Singularity Analysis of the 4-(rT)$_2$PS (2DOF)

The 4-(rT)$_2$*PS* parallel mechanism has two bifurcated rotations about *x* and *y* axes with an independent translation along *z*-axis. Based on the given physical parameters above, the workspace of this mechanism is demonstrated in Fig. 6-14(a), in which the blue parts represent the singularities identified using the Jacobian matrix in Eq. (6.53) consisting of two actuation

forces and four geometric constraint forces. There are three kinds of singular configurations with one that there is no rotation shown in the center blue in Fig. 6-14(a). This is the home position in which the platform is parallel to the base and the four geometric constraint forces from the four limbs lie in the same plane as in Fig. 6-14(b), resulting in one redundant and constraint singularity [76, 156] in the home position. Once the platform rotates, it involves into one rotation branch. As in Fig. 6-14(c), when the platform rotates about the *x*-axis clockwise, a singularity occurs when the actuation force from limb 2 passing through the spherical joint center A_4 in limb 4. In this case, the two geometric constraint forces in limb 2 and limb 4 are parallel to the line A_1A_3 and all the other four constraint forces intersect the line A_1A_3, resulting in an instantaneous free rotation about the line A_1A_3 with the singular Jacobian of rank five. This is similar when the platform rotates about the *y*-axis as shown in Fig. 6-14(d).

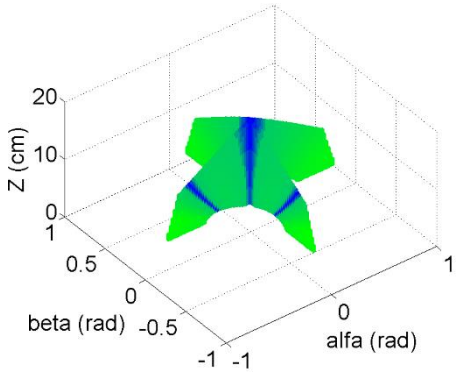

(a) workspace with singularity distribution

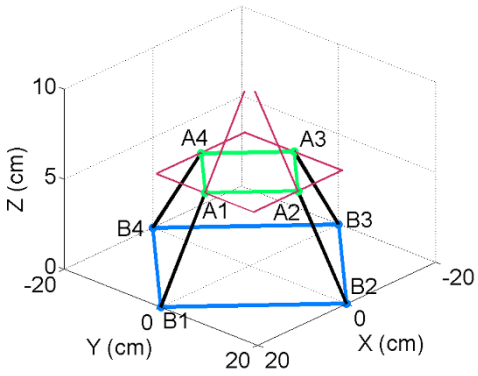

(b) singularity 1

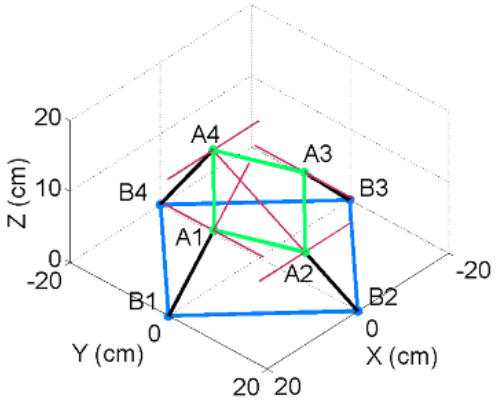

(c) singularity 2

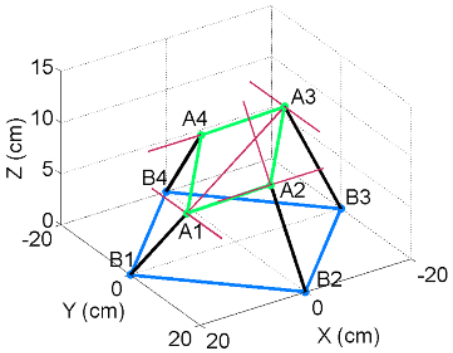

(d) singularity 3

Figure 6-14 Workspace and singular configurations of 4-(rT)$_2$*PS*

6.5.3.3 Workspace and Singularity Analysis of the 3(rT)$_2$PS-1(rT)$_1$PS (3DOF)

When altering the limb 1 from phase 2 to phase 1, the parallel mechanism changes to the 3(rT)$_2$*PS*-1(rT)$_1$*PS* with two rotational and one translational DOFs. The geometric constraint force in limb 1 becomes the actuation constraint force as in Eq. (6.53). Based on these, the workspace with singularities are shown in Fig. 6-15(a) and Fig. 6-15(b) in 3D view and top view respectively. The blue singularity points are clearly located in the workspace and a more detailed singularity locus is shown in Fig. 6-15(c). By investigating the singularity configurations, it can be found that the 3(rT)$_2$*PS*-1(rT)$_1$*PS* has all the singular configurations of the 4-(rT)$_2$*PS* in Fig. 6-14 with one more singular configuration existing as in Fig. 6-15(d). This singularity is the general complex singularity (Type 5a in [157]) in which there are six skew constraint forces with one redundant leading to the Jacobian matrix of rank 5.

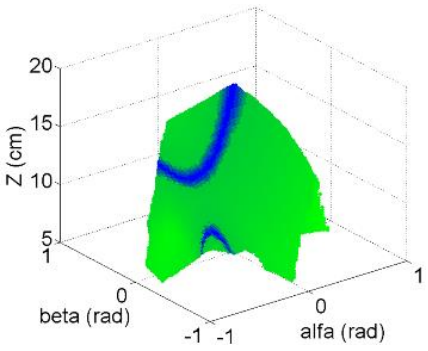

(a) workspace with singularities

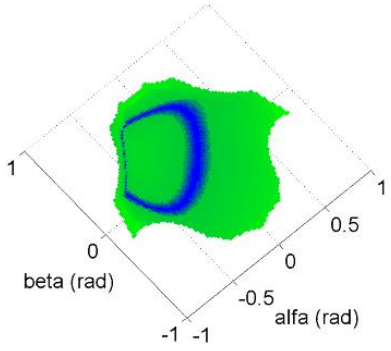

(b) top view

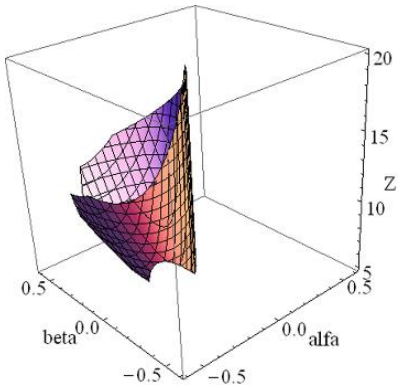

(c) singularity locus

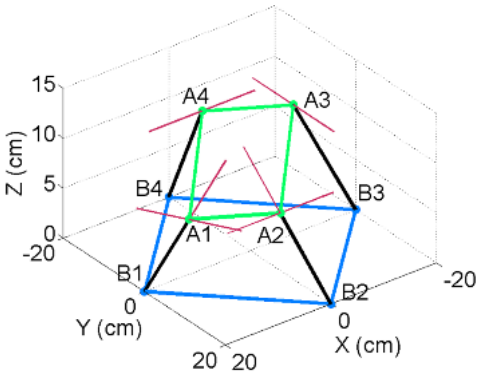

(d) singularity 4

Figure 6-15 Workspace and singularity locus of the 3(rT)$_2$*PS*-1(rT)$_1$*PS*

6.5.3.4 Workspace and Singularity Analysis of the 2(rT)$_2$PS-2(rT)$_1$PS (4DOF)

After further changing limb 2 from phase 2 to phase 1, the mechanism becomes the 4DOF 2(rT)$_2$*PS*-2(rT)$_1$*PS* with three rotational and one translational DOFs. In this case, the six constraint forces in the Jacobian matrix come from two geometric constraint forces in limb 3 and limb 4 with two actuation forces in each of limb 1 and limb 2 as in Eq. (6.53). By investigating the workspace with different rotations about the *z*-axis, singularities in the workspace are shown in Table 6-5 in the Appendix with the same coordinates in Fig. 6-14 and Fig. 6-15. When there is no rotation about *z*-axis, the workspace with singularities is the same with that in Fig. 6-15(a) and (b). When the platform rotates clockwise or anticlockwise about *z*-axis, the workspace becomes smaller with singularity distribution rotates as in Table 6-5. When rotating the platform about z-axis from 0.2 to 0.3, the workspace also becomes smaller with less singularity as shown the singularity loci in the third column in Table 4-5. Comparing with the 3-DOF case in Section 6.4.3.2, all the singular configurations are in the configurations of singularity 1 and singularity 4 while singularity 2 and singularity 3 are avoided when rotating the platform about *z*-axis.

6.5.3.5 Workspace and Singularity Analysis of the 1(rT)$_2$PS-3(rT)$_1$PS (5-DOF)

Based on the 4-DOF 2(rT)$_2$*PS*-2(rT)$_1$*PS* in section 6.2.3.3, by altering limb 3 from phase 2 to phase 1, the mechanism becomes the 5-DOF 1(rT)$_2$*PS*-3(rT)$_1$*PS* with three rotational and two translational DOFs. The geometric constraint force parallel to the *y*-axis in limb 3 becomes the actuation force along the limb. This eliminates singularity 1 at the home position and singularity 3 as in Fig. 6-14. The workspace with singularity distribution is shown in Table 6-6 in terms of different rotations about *z*-axis and different translations along *y*-axis. Due to the constraint force change in limb 3, the singularity distribution changes a lot while the workspace becomes a little different comparing with the 3-DOF 3(rT)$_2$*PS*-1(rT)$_1$*PS* in Fig. 6-15. When the platform translates along the *y*-axis to the negative side (p_y=−3 in Table 6-6) without rotating about the *z*-axis, the rotational workspace about the *x*-axis (α) in clockwise becomes smaller while the singularity keeps similar in the remaining part as shown in Table 6-6. When there is rotation about *z*-axis, the workspace becomes smaller with singularity changes as in Table 6-6.

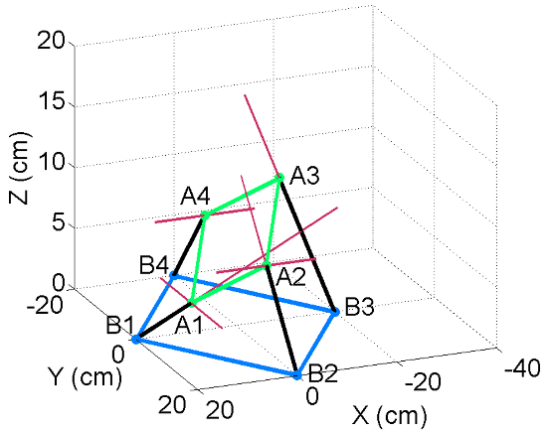

Figure 6-16 Singularity 5

In the workspace of the 5DOF 1(rT)$_2$*PS*-3(rT)$_1$*PS* parallel mechanism, most singularities occur at the configurations similar to singularity 4 in Fig. 6-15(d) with six skew constraint forces and some in the configurations similar to singularity 2 in Fig. 6-15(c). Furthermore, one more singular configuration is found as in Fig. 6-16 (Type 3b.2 in [158]). In this case, the plane formed by the parallel constraint forces from limb 2 and limb 4 passes through the intersecting point of the two prismatic-joint-actuation forces in limb 1 and limb 3. One of these four forces is redundant and the Jacobian matrix has rank 5. It occurs when there are anticlockwise pure rotations about the *y*-axis.

6.5.3.6 Workspace and Singularity Analysis of the 4-(rT)$_1$PS (6-DOF)

After changing all the limb phases from 2 to 1, the mechanism becomes the 4-(rT)$_1$*PS* parallel mechanism with all the six DOFs and the six constraint forces in the Jacobian in Eq. (6.53) are all actuation forces from the four limbs. In order to show and compare the workspace, three samples are listed in Table IV in the Appendix with 3D view workspace and detailed singularity loci. When p_x=0, p_y=0, and θ =0, the 4-(rT)$_1$*PS* has similar workspace with the 5-DOF 1(rT)$_2$*PS*-3(rT)$_1$*PS* in section 6.4.3.4 but with much different singularity distribution. Due to the change from geometric constraint parallel to *x*-axis to actuation force along the limb in limb 4, the singularities mainly happen when the platform rotates anticlockwise about *x*-axis and clockwise about *y*-axis as seen from the top-view workspace in the first row in Table 6-7. By investigating the singularities, it is found that most singular configurations come from the singularity 4 case in Fig. 6-15(d) with six skew forces and one redundant. Another singular configuration has all the

six constraint forces intersecting the A_1A_2 line, which is similar to singularity 2 and singularity 3 in Fig. 6-14 and the platform has an instantaneous rotation about the A_1A_2 line. One more case as singularity 6 in Fig. 6-17(a) is found at the home position when the platform is parallel to the base with only translation along z-axis and the four actuation forces along the four limbs intersecting at one point, resulting one redundant.

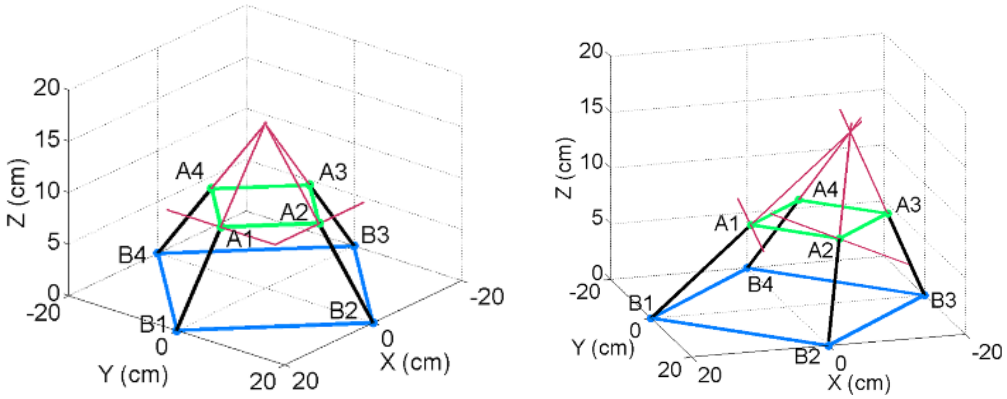

(a) home position (b) configuration (p_x=-4, p_y=2, p_z =8)

Figure 6-17 Singularity 6 in two different configurations

When setting p_x=0, p_y=0, and p_z =10, the workspace with three rotations and singularity distribution is shown in the second row in Table 6-7. Similarly, the singularities mainly locate at the side when the platform rotates anticlockwise about x-axis and clockwise about y-axis. Singular configurations are also similar with the first case in Table 6-7.

When setting all the rotations zero, the platform will experience pure translations. However, the four actuation forces along the four limbs always intersect at one point in this case as singularity 6 in Fig. 6-17(b). After rotating the platform about z-axis, the configurations are still under singularity due to the fact that the four forces lie on the same regulus [157] with one redundant. The rotation about x or y axes can help avoid this singular problem as shown in the third row in Table IV with a rotation (α=0.2) about x-axis. Most part of the workspace is singularity free while some singularities exist when the platform translates to the positive side of x-axis which causes singularity with six skew forces. The situation is similar when the platform rotates about y-axis.

The workspace and singularity analysis shows all the singularities in the workspace which can be used to reduce singularities in the design of the 4-rT*PS* mechanism and free-singularity

workspace can be used in the application motion plan. Take the 2-DOF bifurcated motion for example, singularities are found when the platform is parallel to the base and when the platform rotates to the positive sides of *x*-axis and *y*-axis as shown in Fig. 6-14(a). One more actuator can be used to solve the constraint singularity when the platform is parallel to the base while the motion plan can focus on the negative sides of *x*-axis and *y*-axis to avoid all the singularities. This is the same for all the other topologies as shown in Fig. 6 and Tables 6-5, 6-6 and 6-7. Thus, these singularities of the 4-rT*PS* mechanism can be avoided in the applications.

Table 6-6 Workspace and singularity loci of the $2(rT)_2PS$-$2(rT)_1PS$

	workspace with singularities (3D view)	workspace with singularities (top view)	singularity loci
$\theta = 0.2$	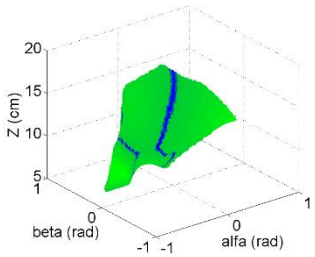	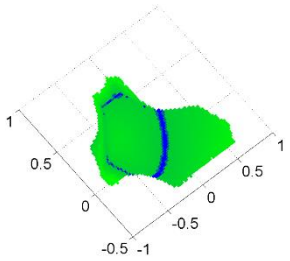	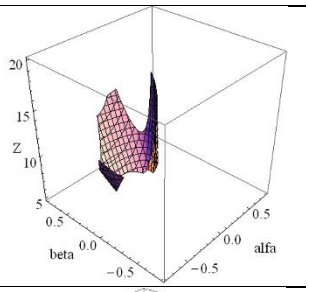
$\theta = -0.2$	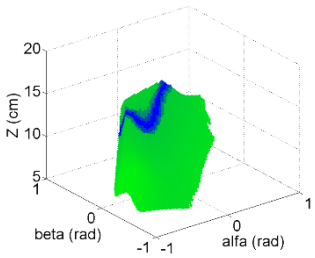	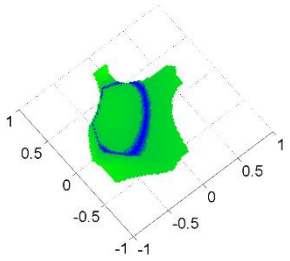	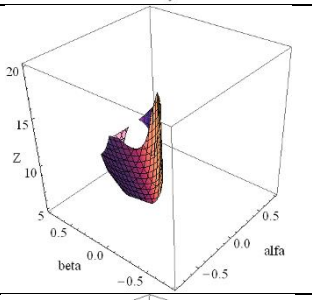
$\theta = 0.3$	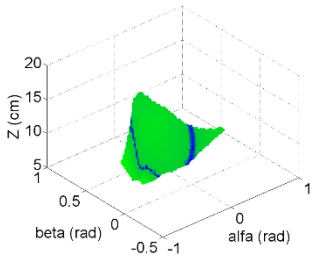	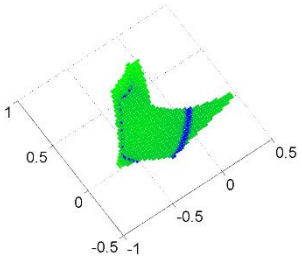	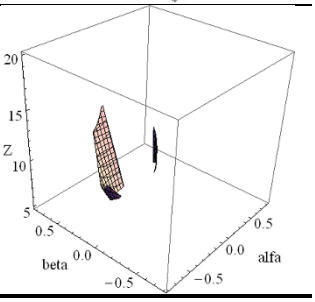

Table 6-7 Workspace and singularity loci of the 1(rT)$_2$*PS*-3(rT)$_1$*PS*

	workspace with singularities (3D view)	workspace with singularities (top view)	singularity loci
p_y=0, $\theta = 0$	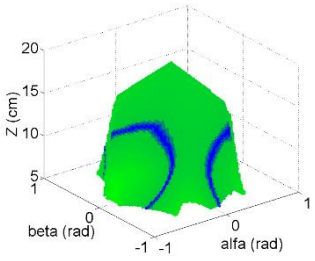	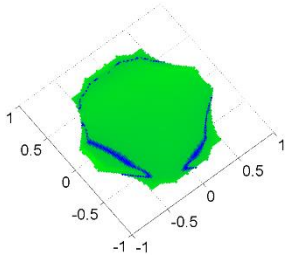	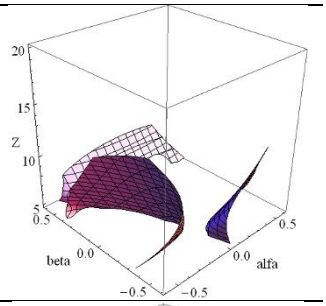
p_y =-3, $\theta = 0$	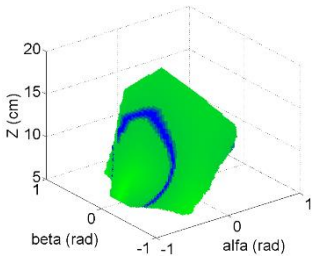	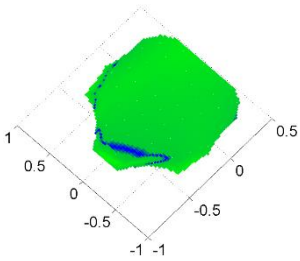	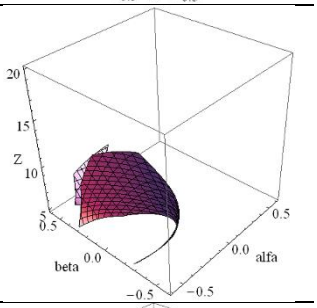
p_y =1, $\theta = 0.2$	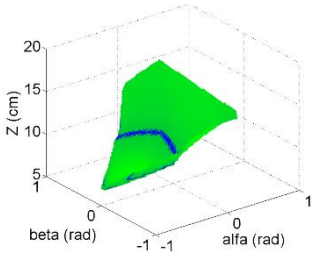	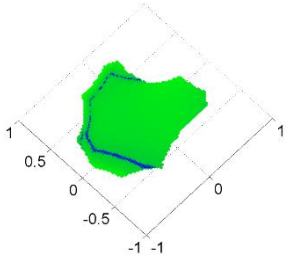	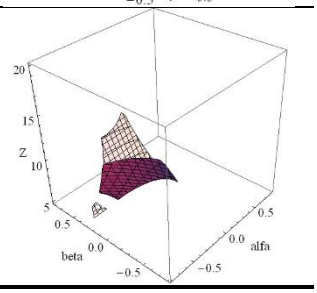

Table 6-8 Workspace and singularity loci of the 4(rT)$_1$*PS*

	workspace with singularities (3D view)	workspace with singularities (top view)	singularity loci
p_x =0, p_y =0, θ =0,	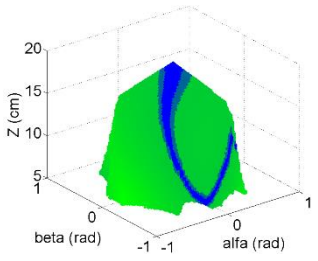	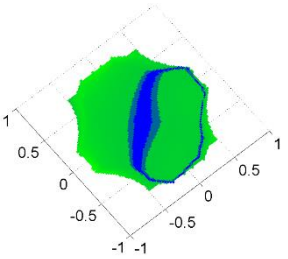	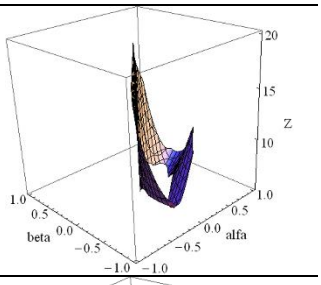
p_x =0, p_y =0, p_z =10,	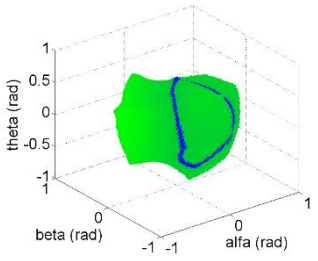	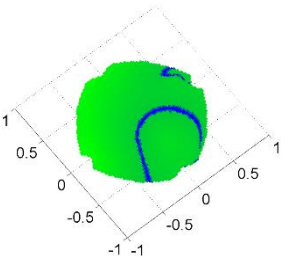	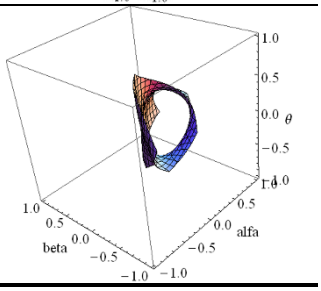

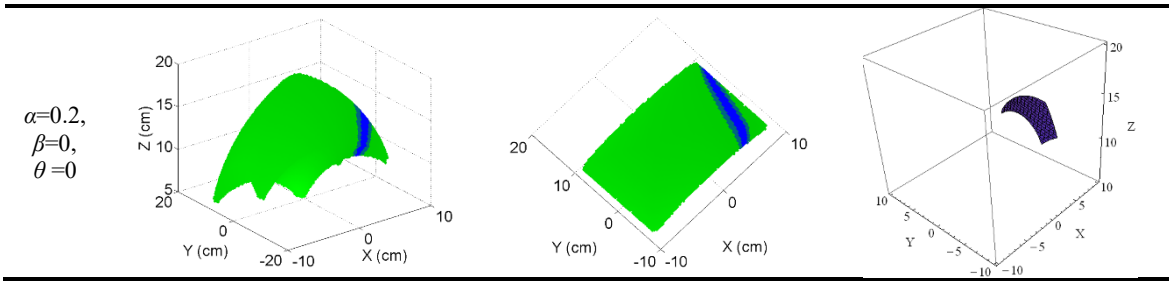

6.6 Unified Kinematics Modelling and Workspace Analysis of the 3-rRPS

6.6.1 Unified Kinematics Modelling

The inverse displacement analysis of the 3-rR*PS* metamorphic parallel mechanism is to obtain the actuation parameters (limb length l_i) based on the given platform position and orientation. When giving the platform position $\boldsymbol{p}$ (p_x, p_y, p_z) and orientation **R** described in the global coordinate system in Fig. 6-18, the actuation inputs which are the limb lengths can be calculated directly from Eq. (5.25):

$$l_i = \sqrt{(\mathbf{R}\,\boldsymbol{a}_i' + \boldsymbol{p} - \boldsymbol{b}_i)^2} \quad (i = 1, 2, 3) \tag{6.54}$$

This is the same for all the topologies with different mobility but it should be mentioned that, the platform position and orientation parameters cannot be given freely. They should follow the geometric constraint relations analysed in Section 6.6.4 that the translations are calculated by given orientation for 3R motion case and two rotations and one translation can be given arbitrarily for the 1T2R motion case.

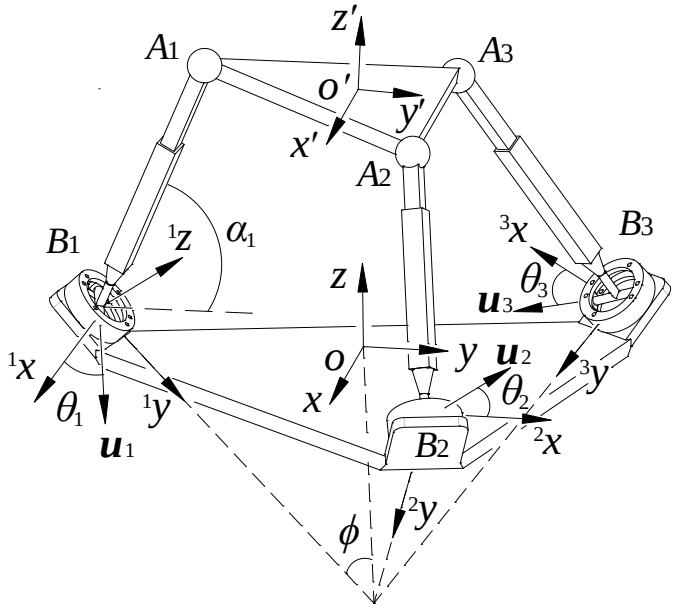

Figure 6-18 Unified kinematics modelling of the 3-rT*PS* with perpendicular constraint screws

On contrary to the inverse one, forward displacement analysis is to solve the platform position $\boldsymbol{p}$ (p_x, p_y, p_z) and orientation **R** when giving the corresponding actuation parameters (l_i) for each topology. The strategy for the 3-rR*PS* metamorphic parallel mechanism is to use the limb parameters to express the spherical joint center vector $\boldsymbol{a}_i$ to form the constraint equations based on the platform geometry. To do this, a limb coordinate system ${}^io{}^ix{}^iy{}^iz$ is attached to each rR joint as in Fig. 6-18, where ${}^iz$ axis is along the normal $\boldsymbol{n}$ of the base plane of the rR joint and ${}^iy$ axis intersects the z axis. The following solving procedure gives a unified forward kinematics analysis valid for all topologies of the 3-rR*PS* MPM with different mobility.

Based on the above analysis and the coordinate systems of the 3-rR*PS* MPM in Fig. 6-18, geometric constraints of the mechanism can be given as:

$$\begin{cases} \boldsymbol{b}_1 = (0, -r_b, 0)^T, \boldsymbol{b}_2 = r_b(\sin\pi/3, \cos\pi/3, 0)^T, \boldsymbol{b}_3 = r_b(-\sin\pi/3, \cos\pi/3, 0)^T \\ \boldsymbol{a}_1 = \boldsymbol{b}_1 + \mathbf{R}_z(0)\mathbf{R}_x(\phi - \pi/2)\mathbf{R}_z(\theta_1)l_1(0, \cos\alpha_1, \sin\alpha_1) \\ \boldsymbol{a}_2 = \boldsymbol{b}_2 + \mathbf{R}_z(2\pi/3)\mathbf{R}_x(\phi - \pi/2)\mathbf{R}_z(\theta_2)l_2(0, \cos\alpha_2, \sin\alpha_2) \\ \boldsymbol{a}_3 = \boldsymbol{b}_3 + \mathbf{R}_z(4\pi/3)\mathbf{R}_x(\phi - \pi/2)\mathbf{R}_z(\theta_3)l_3(0, \cos\alpha_3, \sin\alpha_3) \end{cases} \tag{6.55}$$

where l_i is the length of limb i, $\mathbf{R}_k(g)$ represents a rotation about axis k with angle g and is used to translate the vector of the spherical joint center in the limb coordinate system to the global

coordinate system in Fig. 6-18. θ_i describes the direction of the rR joint rotation axis $\boldsymbol{u}_i$ and α_i is the angle between the limb and its projection on the ${}^{i}x{}^{i}o{}^{i}y$ plane (plane Σ) in limb i.

Based on this, the triangle of the platform geometry can be described as:

$$\begin{cases} (\sqrt{3}r_a)^2 = (\boldsymbol{a}_1 - \boldsymbol{a}_2)^2 \\ (\sqrt{3}r_a)^2 = (\boldsymbol{a}_1 - \boldsymbol{a}_3)^2 \\ (\sqrt{3}r_a)^2 = (\boldsymbol{a}_2 - \boldsymbol{a}_3)^2 \end{cases} \tag{6.56}$$

Substituting Eq. (6.55) into Eq. (6.56) and applying $\cos\alpha_i = (1-t_i^2)/(1+t_i^2)$, $\sin\alpha_i = 2t_i/(1+t_i^2)$, there is

$$\begin{cases} f_1(1, t_1, t_1^2, t_2^2, t_1t_2^2, t_1^2t_2^2) = 0 \\ f_2(1, t_3, t_3^2, t_1^2, t_3t_1^2, t_3^2t_1^2) = 0 \\ f_3(1, t_2, t_2^2, t_3^2, t_2t_3^2, t_2^2t_3^2) = 0 \end{cases} \tag{6.57}$$

where $f_i(\bullet)$ is a linear function of the power products in the bracket with coefficients depending on known parameters only, t_i represents $\mathrm{Tan}(\alpha_i/2)$.

By using Sylvester's dialytic elimination method [146] for the first two equations in Eq. (6.57), there is

$$f_4(1, t_3, t_2^2, t_3^2, t_2^2t_3, t_3^3, t_2^4, t_3^4, t_2^2t_3^2, t_2^2t_3^3, t_2^4t_3^1, t_2^2t_3^4, t_2^4t_3^2, t_2^4t_3^3, t_2^4t_3^4) = 0 \tag{6.58}$$

where $f_4(\bullet)$ is a linear function of the power product in the bracket with coefficients depending on known parameters only.

Then, following the same method for Eq. (6.58) and the third equation in Eq. (6.57), a polynomial with only unknown t_3 can be obtained as:

$$\sum_{i=0}^{+16} h_i t_3^i = 0 \tag{6.59}$$

where coefficient h_i are real constants depending on input data only.

This shows that a univariate equation in t_3 of degree 16 is obtained. Solving Eq. (6.59), sixteen solutions of t_3 can be obtained. Then, t_2 can be solved by substituting each solution of t_3 into the third equation in Eq. (6.57) and selecting the roots satisfying Eq. (6.58). Following this, t_1 can be solved by substituting each pair of solutions of t_2 and t_3 into the first equation in Eq. (6.57) with proof of the second equation in Eq. (6.57). Based on this, sixteen pair of solutions of t_1, t_2, t_3 are obtained and the spherical joint center A_i can be calculated by substituting α_i=2ArcTan(t_i) into Eq. (6.55). Then, the platform position and orientation can be determined using the three spherical joint centers with Fig. 6-18 as:

$$\begin{cases} \boldsymbol{z}' = (\boldsymbol{a}_2 - \boldsymbol{a}_1) \times (\boldsymbol{a}_3 - \boldsymbol{a}_1) / \left\| (\boldsymbol{a}_2 - \boldsymbol{a}_1) \times (\boldsymbol{a}_3 - \boldsymbol{a}_1) \right\| \\ x' = (\boldsymbol{a}_2 - \boldsymbol{a}_3) / (\sqrt{3} r_a) \\ \boldsymbol{y}' = \boldsymbol{z}' \times \boldsymbol{x}' \\ \mathbf{R} = (\boldsymbol{x}', \boldsymbol{y}', \boldsymbol{z}') \\ \boldsymbol{p} = \boldsymbol{a}_1 + r_a \boldsymbol{y}' \end{cases} \tag{6.60}$$

This shows the unified forward kinematics solution of the 3rR*PS* metamorphic parallel mechanism for both the 3R motion and the 1T2R motion.

6.6.2 Singularity Loci

The infinitesimal twist [159] of the moving platform of the 3-rR*PS* MPM can be written as the linear combination of instantaneous twists of each limb:

$$\boldsymbol{S}_G = \dot{\phi}_{i1} \boldsymbol{S}_{i1} + \dot{l}_i \boldsymbol{S}_{i2} + \dot{\phi}_{i3} \boldsymbol{S}_{i3} + \dot{\phi}_{i4} \boldsymbol{S}_{i4} + \dot{\phi}_{i5} \boldsymbol{S}_{i5} \qquad (i = 1, 2, 3) \tag{6.61}$$

where $\boldsymbol{S}_G$ represents the infinitesimal twist of the moving platform, $\boldsymbol{S}_{ij}$ (j=1,2,3,4,5) denotes the unit screw of the jth 1-DOF joint in limb i, $\dot{l}_i$ is the distance rate of the prismatic joint in limb i, $\dot{\phi}_{ij}$ (j=1,3,4,5) represent angular rates of the rR joint and spherical joint in limb i.

By locking the active joints in the limbs temporarily and taking reciprocal product on both sides of Eq. (6.61), there is

$$\begin{bmatrix} \boldsymbol{S}_{i1}^r & \boldsymbol{S}_{i2}^r \end{bmatrix}^T \circ \boldsymbol{S}_G = \begin{bmatrix} 0 & \dot{l}_i \end{bmatrix}^T \quad (i = 1,2,3) \tag{6.62}$$

where $\boldsymbol{S}_{i1}^r$ is the reciprocal screw of geometric constraint to all motion screws in limb i and it passes through the spherical joint center with direction parallel to rotation axis $\boldsymbol{u}_i$ of the rR joint. $\boldsymbol{S}_{i2}^r$ is the actuation screw reciprocal to all motion screws in Eq. (6.61) except the prismatic joint screw $\boldsymbol{S}_{i2}$ and it is collinear with the limb.

Equations in Eq. (6.62) for the three limbs can be rewritten in matrix form as:

$$\begin{bmatrix} \boldsymbol{S}_{11}^r \\ \boldsymbol{S}_{21}^r \\ \boldsymbol{S}_{31}^r \\ \boldsymbol{S}_{12}^r \\ \boldsymbol{S}_{22}^r \\ \boldsymbol{S}_{32}^r \end{bmatrix} \circ \boldsymbol{S}_G = \mathbf{J}\,\boldsymbol{S}_G = \begin{bmatrix} \boldsymbol{a}_1 \times \boldsymbol{u}_1 & \boldsymbol{u}_1 \\ \boldsymbol{a}_2 \times \boldsymbol{u}_2 & \boldsymbol{u}_2 \\ \boldsymbol{a}_3 \times \boldsymbol{u}_3 & \boldsymbol{u}_3 \\ \boldsymbol{b}_1 \times \boldsymbol{s}_1 & \boldsymbol{s}_1 \\ \boldsymbol{b}_2 \times \boldsymbol{s}_2 & \boldsymbol{s}_2 \\ \boldsymbol{b}_3 \times \boldsymbol{s}_3 & \boldsymbol{s}_3 \end{bmatrix} \boldsymbol{S}_G = \begin{bmatrix} 0 \\ 0 \\ 0 \\ \dot{l}_1 \\ \dot{l}_2 \\ \dot{l}_3 \end{bmatrix}, \tag{6.63}$$

In Eq. (6.63), **J** is the 6 by 6 Jacobian matrix which maps velocities between the manipulator and the actuation input. Once the manipulator meets singular configurations, this mapping loses its function and the rank of the Jacobian matrix decreases to be less than 6. This can be also interpreted that the six constraint forces in **J** are linearly dependent. Inversely, identifying the dependent conditions for the constraint forces in the workspace will reveal the singular configurations of the manipulator. In order to demonstrate this, some dimensionless parameters with physical constraints are given as: the platform radius r_a=1, base radius r_b=2, ϕ=

π/2−ArcSin($\sqrt{3}$/3) representing that the three normal vectors of the three rR joints are perpendicular to each other.

Type 2 singularities appear when the determinant of **J** equals to zero. Based on the rotation matrix **R** of Cayley formula in Eq. (5.28) and mobility analysis in Section 3.6.4, the determinant of **J** is given by:

$$|\mathbf{J}| = \begin{cases} f_5(c_1, c_2, c_3, \ldots) & 3\text{R } motion \\ f_6(c_1, c_2, p_z, \ldots) & 1\text{T2R } motion \end{cases} \tag{6.64}$$

where f_5 is a function of c_1, c_2 and c_3 with their products up to 10th order for the topologies with 3R motion and f_6 is a function of c_1, c_2 and p_z with their products up to 11th order for the topologies with 1T2R motion. Those parameters are used respectively to represent the singularity points of the platform. By equalling Eq. (6.64) to zero, all singular points can be found and some examples are illustrated in Fig. 6-19 and Fig. 6-20.

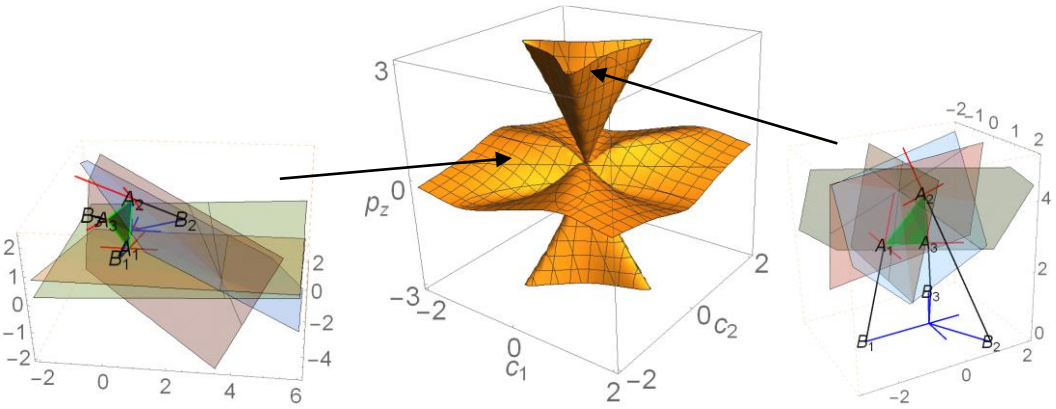

(c_1=0.5, c_2=−0.5, p_z=0.3) (c_1=0.2, c_2=−0.79, p_z=3)

Figure 6-19 Singularity loci and two singular configurations of the 1T2R case (θ_1= θ_2= θ_3=0)

In Fig. 6-19, the singularity loci of the 3-rR*PS* MPM with 1T2R motion (θ_1= θ_2= θ_3=0) is shown. It can be seen that the loci is symmetrical due to the symmetrical limb arrangement. Two singular configurations and their corresponding points on the singularity loci are shown on Fig. 6-19. It agrees with the conclusion [160] that in singularity configurations the four planes, the platform plane and a plane from each limb formed by the actuation force and constraint force in the limb,

intersect at one point which makes the rank of the Jacobian matrix 5. It can be also found that when p_z is close to zero which is that the platform is close to the base, there are more possibilities to meet singularity configurations. However, in real applications, the platform will work with positive p_z much bigger than zero for which the singularity loci is quite uniform and represented by the tetrahedron shaped surface with an open side along the z direction and a vertex at the zero point with c_1=c_2=p_z=0 as in Fig. 6-19.

As analysed in Section 6.6.4, there are various topologies of the 3rR*PS* MPM with 3R motion by changing the rR joint rotation axes to different directions. The following shows singularity loci of four cases in Fig. 6-20. It can be seen that when θ_1= θ_2= θ_3 the singularity loci are symmetrical due to the symmetrical limb arrangement. The case with θ_1= θ_2= θ_3=π/2 gives similar spherical parallel mechanism to the pyramid parallel mechanism [139]. When the three rR joint axes do not have the same angle θ, the loci is not symmetrical as shown in Fig. 6-20(b). Generally, the space close to the center (c_1=c_2= c_3=0) is separated into upper and lower part by the loci which are the main singularities in the mechanism workspace as shown in the following section.

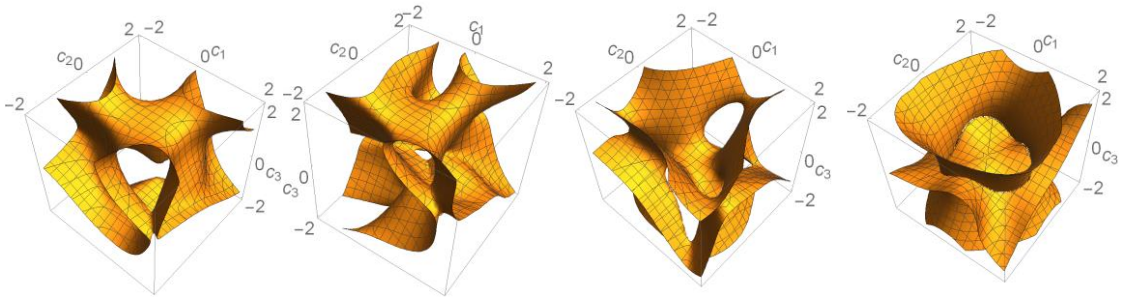

(a) θ_1= θ_2= θ_3= π/6 (b) θ_1=0, θ_2= π/6, θ_3=π/4 (c) θ_1= θ_2= θ_3=π/3 (d) θ_1= θ_2= θ_3=π/2

Figure 6-20 Singularity loci of topologies with 3R motion

6.6.3 Singularity-Free Workspace

In the 3-rR*PS* MPM, each limb length has two limits (lower and upper) which constrain the actuation range and determine the workspace of the platform. Thus, the platform workspace boundaries can be expressed by the two limits $l_{i\max/\min}$ following the geometric constraints in Eq. (5.25):

$$(\mathbf{R}\boldsymbol{a}_i' + \boldsymbol{p} - \boldsymbol{b}_i)^2 = l_{i\max/\min}^2 \quad (i = 1,2,3) \tag{6.65}$$

Similar to the singularity representation, the independent parameters are used to illustrate the boundary with (c_1, c_2, c_3) for the 3R motion and (c_1, c_2, p_z) for the 1T2R motion. Two examples are shown in Fig. 6-21 (a) and (b) in which the following parameters are used: spherical joint rotation angle ≤ π/3 radian, rR joint rotation angle ≤ π/3 radian, limb length $1.6 \le l_i \le 2.88$.

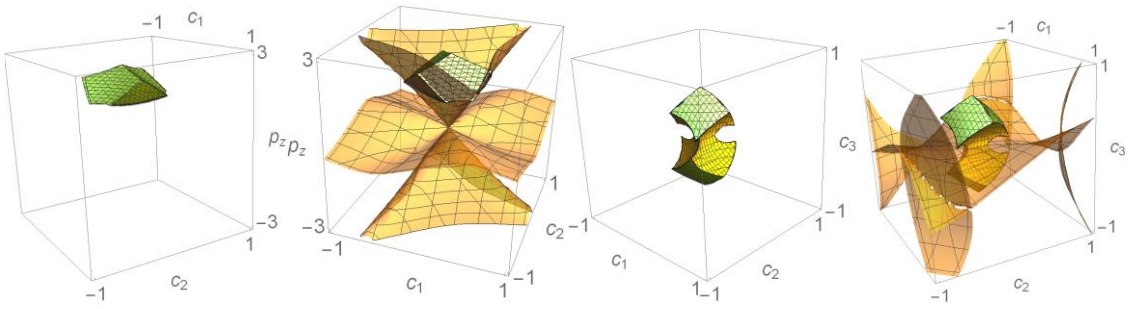

(a) 1T2R motion (θ_1= θ_2= θ_3=0) (b) 3R motion (θ_1= θ_2= θ_3=π/3)

Figure 6-21 Workspace of different topologies

Fig. 6-21(a) shows that workspace of the 1T2R case only exists in the area with p_z between 1 and 3 based on the geometric parameters and constraints given. Most of the part is singularity-free as seen in the combination figure with the singularity loci in Fig. 6-21(a). Differently, workspace of the 3R case has symmetrical parts with respect to the plane c_3=0 as in Fig. 6-21(b) and they are corresponding to positive and negative rotations about z axis. Comparing with the singularity loci, the workspace is separated into two singularity-free parts. To avoid singularities, the mechanism needs to work with positive or negative z-axis rotation only. The way to define singularity-free workspace in this section will be used as in the optimal design in Chapter 7.

6.6.4 Parameter Effect on Maximum Singularity-Free Workspace

Singularity-free workspace can be taken as the primary performance index for a parallel mechanism and is an important topic in mechanism design. This section aims at exploring effect of some key parameters of the 3-rR*PS* MPM on its singularity-free workspace. Each topology of the 3-rR*PS* MPM is a parallel mechanism and to show the effect by covering all working topologies with different motion types is a challenge. In the following, the two main topologies with 1T2R motion (θ_1= θ_2= θ_3=0) and 3R motion (θ_1= θ_2= θ_3=π/2) will be considered together.

Based on the kinematics model shown in Fig. 6-18, key parameters of the 3-rR*PS* MPM are the base and platform sizes (r_b and r_a), rR joint base location angle ϕ and the limb length range ($l_{min} \le l_i \le l_{max}$) which is the same for all three limbs. Mechanical constraints including maximum passive joint angles and limb interference should also be considered in the calculation. In the following, passive joint angles are limited in the range as $-\psi_{max} \le \psi_i \le \psi_{max}$, where ψ_i denotes rotation angle from its home position of any revolute joint, and spherical joint along three orthogonal directions one of which is along the limb at the home position. ψ_{max} is given $\pi/3$ in this paper. The minimum distance between any two limbs is limited to be 0.01 to avoid limb interference.

In the following, effect of the key parameters (r_a, r_b, ϕ, l_i) on maximum singularity-free workspace V will be illustrated for the two topologies with 1T2R motion ($\theta_1 = \theta_2 = \theta_3 = 0$) and 3R motion ($\theta_1 = \theta_2 = \theta_3 = \pi/2$). V is calculated as the volume inside of the workspace boundaries and the singularity surface as demonstrated in Section 6.5.3.

6.6.4.1 Effect of Limb Length Range ($l_{min} \le l_i \le l_{max}$)

Based on the kinematics, it can be imagined that limb length range limits the translation along z axis of the 1T2R motion and both of them can be as large as infinite. But this is different for the 3R motion with parasitic translation motion with which the limb length has minimum and maximum values even if there is no other constraint. This is the reason that limb length range is selected as one of the parameters for optimization as an arbitrarily selected limb length range may not cover the effective workspace of the 3R motion. By using dimensionless values $r_a=1$, $r_b=2$, $l_{max}=1.8l_{min}$, workspace volume V with respect to different l_{min} (from 1.3 to 4) under different rR joint base location angle ϕ for the two topologies are shown in Fig. 6-22. In Fig. 6-22(a), it can be seen that the workspace volume of the 3R motion has a peak value for each angle ϕ while the minimum limb length l_{min} corresponding to the peak value increases when ϕ increases from 50° to 80°. The peak value is bigger when the angle ϕ is larger indicating that a larger rR joint base location angle ϕ can help increase the workspace of the 3R motion when a corresponding limb length l_{min} is provided. An example of the peak workspace volume V of the 3R motion is shown in Fig. 6-22(b) which shows the boundary is symmetrical due to the symmetrical limb arrangement. The maximum rotation about z axis is around ±68° ($c_3 = \pm 0.675$), around ±58° ($c_1 = c_2 = \pm 0.56$) about x axis and y axis.

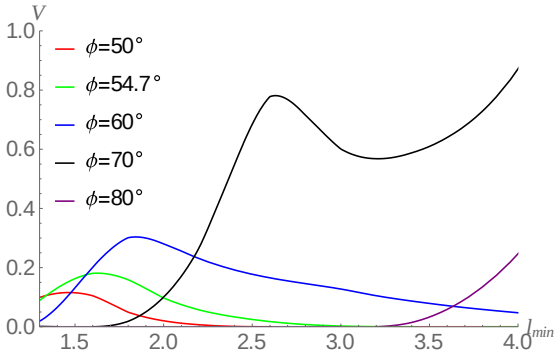

(a) 3R motion V vs l_{min}

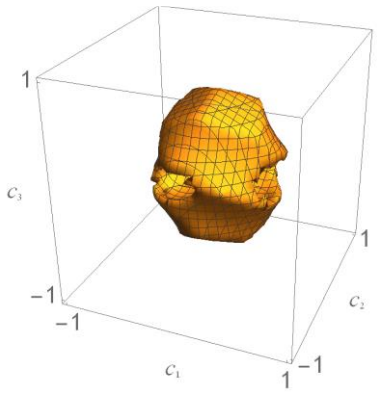

(b) 3R with ϕ=70° and l_{min}=2.8

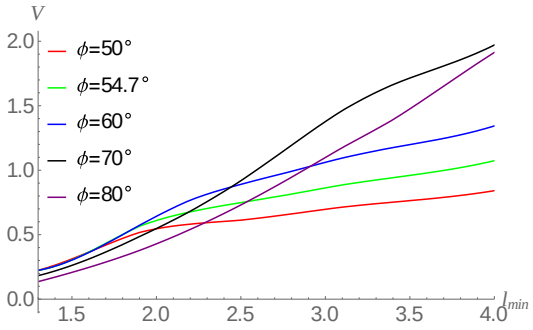

(c) 1T2R motion V vs l_{min}

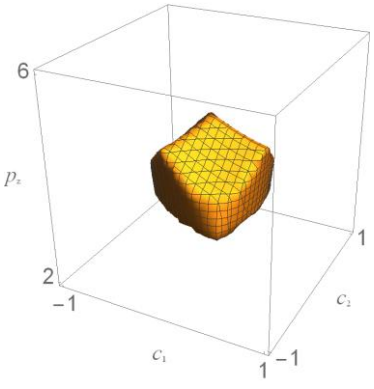

(d) 1T2R with ϕ=70° and l_{min}=2.8

Figure 6-22 Maximum singularity-free workspace volume and the limb length range

Fig. 6-22(c) shows the workspace volume of the 3-rR*PS* MPM with 1T2R motion with respect to the same limb length range (l_{min} from 1.3 to 4) and variable rR joint base location angle ϕ. There is a clear trend that the workspace volume increases when the minimum limb length l_{min} increases. A bigger angle ϕ provides larger V when ϕ is less than 70° and l_{min} is over 2.5 while the workspace volume decreases when ϕ is 80° (purple line). Thus to have a good workspace volume, a longer l_{min} and an angle ϕ close to 70° will be good design values. An example of the workspace volume V of the 1T2R motion is shown in Fig. 6-22(d) which shows the boundary is also symmetrical. The maximum translation along z axis is around 2.1(2.72≤ p_z ≤4.82), with rotation angle −60.6° to 52.7° (−0.585≤ c_1≤ 0.496) about x axis and ±58° (c_2=±0.53) about y axis.

Thus, considering the two topologies and the workspace volume curves in Fig. 6-22, a longer l_{min} and a larger angle ϕ close to 70° are good design values.

6.6.4.2 Effect of the Base Radius r_b

By using r_a=1, l_{max}=1.8l_{min}, l_{min}=3.1, the maximum singularity-free workspace volumes with respect to different base radius r_b (from 0.7 to 4.5) and different rR joint base location angle ϕ are shown in Fig. 6-23 for the 3R and 1T2R motion. The general trend is similar for both cases that the peak value of the workspace volume is around the same value for different ϕ and it requires smaller base size r_b when angle ϕ is bigger to reach the peak volume V. It can be also seen that a similar base size r_b can make both topologies reach the maximum singularity-free workspace volume for a given angle ϕ. For example, r_b≈2.9 gives the maximum V ≈ 0.85 for the 3R motion with ϕ =60° (blue curve) in Fig. 6-23(a) while r_b≈3 gives the maximum V ≈ 1.6 for the 1T2R motion with same ϕ =60° (blue curve) in Fig. 6-23(b). This makes it easy to select base size r_b by giving rR joint base location angle ϕ or inversely.

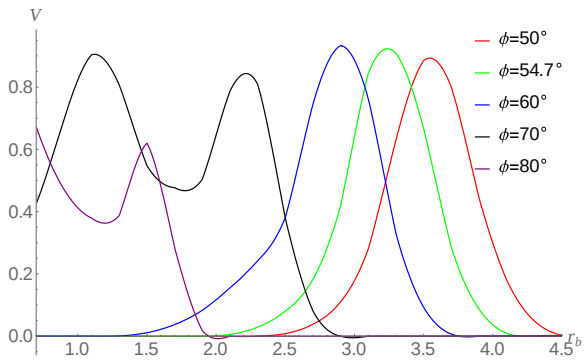

(a) 3R motion V vs r_b

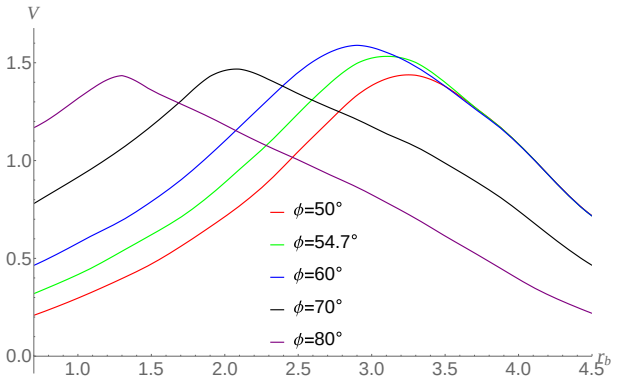

(b) 1T2R motion V vs r_b

Figure 6-23 Maximum singularity-free workspace volume and the base radius r_b

6.6.4.3 Effect of the Platform Radius r_a

By selecting r_b=2, l_{max}=1.8l_{min}, l_{min}=3.1, the maximum singularity-free workspace volume with respect to different base radius r_a (from 0.3 to 4.1) and different rR joint base location angle ϕ

are shown in Fig. 6-24 for the 3R and 1T2R motion. Generally, a smaller platform size r_b will provide larger workspace volume V for both cases. The increase of angle ϕ will increase the volume V a lot in 3R motion when ϕ is less than 70° as in Fig. 6-24(a) and it drops a lot for ϕ =80° while V is almost zero when ϕ =50°. The trend is similar for the 1T2R motion in Fig. 6-24(b) but angle ϕ does not affect the workspace volume V as much as that in the 3R case. Thus, a smaller platform size r_a and a larger angle ϕ close to 70° are preferable.

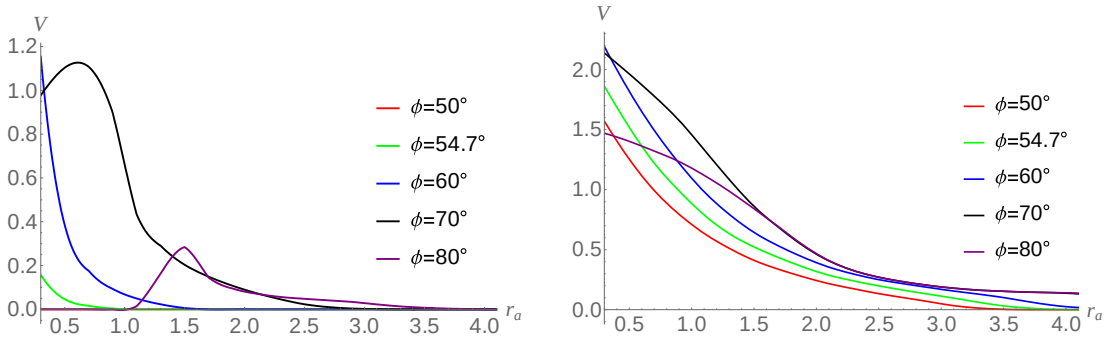

(a) 3R motion V vs r_a (b) 1T2R motion V vs r_a

Figure 6-24 Maximum singularity-free workspace volume and the base radius r_a

The above gives a general idea of the effect of those key parameters on the maximum singularity-free workspace of both 3R and 1T2R motion of the 3-rR*PS* MPM. This provides references at the initial stage of the mechanism design.

6.7 Conclusions

This chapter contributed to proposing a unfied kinematics solving method for metamorphic parallel mechanisms based on reconfigurable joints. Every topology of a metamorphic parallel mechanism is equivalent to a traditional parallel mechanism. The proposed strategy solved the kinematics analysis of all the topologies (equivalently a series of parallel mechanisms) in a unified manner by creatively modelling the mechanisms from their limbs and taking one phase of the reconfigurable joint as special case of another. Based on this, the kinematics analysis of four metamorphic parallel mechanisms was solved analytically. Moreover, the unified kinematics model also revealed some novel properties of the metamorphic parallel mechanisms. For example, the 3-rTPrT not only has reconfigurable rotation and translation mobility but also can

reconfigure inside each motion type. The rotation center of the pure rotation phase can be reconfigured along the z-axis while the pure translation motion can have different range resulted from the reconfigurable joint tuning. Similarlly the 3-rRPS has infinite number of rotation phases with pure rotation motion but different workspace and kinematics performance.

Another import finding is the introduction of Cayley parameters to the singularity and workspace analysis and representation. The Cayley parameter based 3D coordinate system shows intuitive physical meaning of the rotation motion and gives clear singularity loci demonstration and singularity-free workspace representation. This model also enabled the analytical description of the workspace of the 3-rTPrT metamorphic parallel mechanism and showed forward kinematics solution zones for general spherical parallel mechanisms. The latter also provided unique forward kinematics solution mapping for the pyramid symmetrical spherical parallel mechanism phase of the 3-rTPrT.

The strategy and method in this chapter can be also applied to traditional parallel mechanism analysis and extended to other metamorphic parallel mechanisms and reconfigurable parallel mechanisms.

Chapter 7 Unified Kinematics Performance Representation and Optimal Design of MPMs Considering Variable Working Phases

7.1 Optimal Design Methods of Parallel Mechanisms

Parallel mechanism design starts from application requirements on basic functional mobility and performance which can include workspace, accuracy, stiffness, payload, speed/acceleration and others with constraints on actuation, sensing, footprint and size [161]. Optimal design of parallel mechanisms are normally for dimension parameter design and most of the time focuses on kinematics performance optimization after the selection of a parallel mechanism structure. Among all performance indices, workspace is the most important and primary one considered in almost all optimal design work of parallel mechanisms [162] while kinematics performance can be represented by Jacobian condition number [23], dexterity [163], manipulability [23], motion/force transmissibility [164-166], etc. Those variable parameters lead to the optimal design a multi-criteria and challenge problem. Different methods have been proposed to solve this multi-objective process including atlas method [167-168], exact design method [169-170], cost function approach [171-172], and others. Atlas and exact design methods showed good applications but are limited to a small number of design parameters due to their representation principles. By combining different performance indices with weighted objective functions, the cost function approach was developed to manage multi-criteria in a single formula. This method has a few drawbacks while one of them is the physical meaning of the final function that combines different parameter units by the weights. It also showed concerns on finding optimal solutions and satisfying all constraints but it was effective in some simple mechanism designs [173].

In this work, the cost function method is applied mainly considering the following. The main idea of this chapter is not to make progress on developing new optimal design method but to investigate the way to unify the optimal design process on metamorphic parallel mechanisms covering all mobility phases. Since each phase of a metamorphic parallel mechanism is equivalent to a traditional parallel mechanism, the optimal design is actually to consider a few parallel mechanisms which share the same structure parameters at one time. Weighted cost

function method in this case shows the advantage in demonstrating how the workspace and other kinematics indices can be considered in a combined way for multi-parallel-mechanism phases. In this study, it actually works a lot on parameter effect on each performance index, for example, the workspace. The cost-fuction approach is only used after this effect map is obtained to demonstrate how possibly a method is to unify the whole design by combining the workspace of phase 1, phase 2, etc with their kinematics performance in every phase. So all the above mentioned optimal design methods can be explored based on this but will be future work.

In the following optimal design, workspace and kinematics performance are selected for the objectives. In literature, two kinds of workspace objective methods were presented. One is to achieve the workspace to contain a prescribed workspace, for example, a rectangular shap in 2D or a ball in 3D [170, 174]. The other is to maximize the workspace by designing proper parameters. In this work, the latter is applied since we do not have a specific task but working on general optimal design of metamorphic parallel mechanisms. On the other hand, kinematics performance is commonly represented by the condition number of the Jacobian matrix but it has coordinate inhomogeneity and defectiveness in some parallel mechanisms [175]. Homogeneous Jacobian matrix is built in this work to solve the above issue of the condition number method. However, the motion/force transmissibility [175-176] is believed to be a more effective unified way to represent the kinematics performance for all mobility phases having both translational and rotational motion from the reconfiguration of a metamorphic parallel mechanism. This is partial of the findings of this work on the exploration of a unified optimal design method and process for metamorphic parallel mechanisms with multi-phases and variable mobility.

7.2 Unified Kinematics Performance Representation

Performance representation provides the basic input to the optimal design of parallel mechanisms. Since the MPMs can have variable mobility phases, a unified performance representation covering all phases is preferred. Motion/force transmission shows work of a wrench on a twist and gives a systematic method to describe the kinematics performance of MPMs in different phases. Three different transmission types with corresponding indices were

introduced in literature including input transmission, output transmission and constraint transmission [164], which will be applied in the following.

7.2.1 Motion/Force Transmissibility of the 3-rTPrT

For the rT*P*rT limb in the 3-rTPrT MPM as in Section 5.3, the input transmission, defined as reciprocal product of the input twist screw of the actuator and its transmission wrench screw in a limb, is constant as the actuation wrench is in the same line with the actuation twist which is along the prismatic joint. Their reciprocal product gives 1 and it is not considered further. Here transmission wrench screw represents a wrench by which motion/force from the actuator is transmitted to the moving platform. The other two transmission indices will be investigated for the pure translation and pure rotation topologies which have different transmission formats [177].

7.2.1.1 The 3-rTPrT with Pure Translation

In the pure translation case, all limbs are in the parallel phase as in Fig. 5-8. Based on the five twist screws associated to the five 1-DOF joint axes, the transmission wrench screw can be obtained by locking the actuated joint and taking the reciprocal screw to all other twist screws except the locked one as:

$$\boldsymbol{S}_{Ti} = \begin{bmatrix} \boldsymbol{s}_{i3}^T & \boldsymbol{a}_i^T \times \boldsymbol{s}_{i3}^T \end{bmatrix} \quad (i = 1, 2, 3) \tag{7.1}$$

which is a force along the prismatic joint and passing by the platform rT joint center ($\boldsymbol{a}_i$) that represents the actuation input.

By taking the reciprocal screw to all the five twist screws in Fig. 5-8, the constraint wrench screw in each limb can be obtained:

$$\boldsymbol{S}_{ci} = \begin{bmatrix} \boldsymbol{0} & \boldsymbol{s}_{i45}^T \end{bmatrix} \quad (i = 1, 2, 3) \tag{7.2}$$

which is a moment in the direction perpendicular to the two rotation axes ($\boldsymbol{s}_{i4}$ and $\boldsymbol{s}_{i5}$) of the platform rT joint in limb *i*, where **0** is the zero vector [0,0,0], $\boldsymbol{s}_{i45} = \boldsymbol{s}_{i4} \times \boldsymbol{s}_{i5} / \left| \boldsymbol{s}_{i4} \times \boldsymbol{s}_{i5} \right|$.

Thus, the screw based overall Jacobian matrix can be directly obtained and its determinant equals to:

$$\left|\mathbf{J}\right| = \left\| \begin{bmatrix} \boldsymbol{S}_{T1} \\ \boldsymbol{S}_{T2} \\ \boldsymbol{S}_{T3} \\ \boldsymbol{S}_{c1} \\ \boldsymbol{S}_{c2} \\ \boldsymbol{S}_{c3} \end{bmatrix} \right\| = \left\| \begin{bmatrix} \boldsymbol{s}_{13}^T & \boldsymbol{a}_1^T \times \boldsymbol{s}_{13}^T \\ \boldsymbol{s}_{23}^T & \boldsymbol{a}_2^T \times \boldsymbol{s}_{23}^T \\ \boldsymbol{s}_{33}^T & \boldsymbol{a}_3^T \times \boldsymbol{s}_{33}^T \\ \mathbf{0} & \boldsymbol{s}_{145}^T \\ \mathbf{0} & \boldsymbol{s}_{245}^T \\ \mathbf{0} & \boldsymbol{s}_{345}^T \end{bmatrix} \right\| = \left\| \begin{bmatrix} \boldsymbol{s}_{13}^T \\ \boldsymbol{s}_{23}^T \\ \boldsymbol{s}_{33}^T \end{bmatrix} \right\| * \left\| \begin{bmatrix} \boldsymbol{s}_{145}^T \\ \boldsymbol{s}_{245}^T \\ \boldsymbol{s}_{345}^T \end{bmatrix} \right\| \tag{7.3}$$

which represents the singularity configurations of the parallel mechanism when it equals to zero. Later analysis will show the direct relation between the motion/force transmission and this determinant.

7.2.1.1.1 Output Transmission

It is defined as reciprocal product of the output motion twist screw of the platform and the transmission wrench screw of a limb actuator. By locking two limbs except the *i*th limb, the platform will have a 1-DOF motion. It's twist screw $\boldsymbol{S}_{Oi}$ is called the output twist screw and can be obtained by taking reciprocal screw to the other five wrench screws in the Jacobian matrix in Eq. (7.3) except the *i*th transmission wrench $\boldsymbol{S}_{Ti}$:

$$\boldsymbol{S}_{Oi} = \left[\mathbf{0} \quad \boldsymbol{s}_{j3}^T \times \boldsymbol{s}_{k3}^T / \left| \boldsymbol{s}_{j3} \times \boldsymbol{s}_{k3} \right| \right] \quad (i, j, k = 1, 2, 3; i \neq j \neq k) \tag{7.4}$$

which is a pure translation along the line that is perpendicular to both limb *j* and limb *k*.

Then the output transmission virtual coefficient [165] is represented by the reciprocal product

$$\boldsymbol{S}_{Ti} \circ \boldsymbol{S}_{Oi} = \boldsymbol{s}_{i3} \cdot \boldsymbol{s}_{j3} \times \boldsymbol{s}_{k3} / \left| \boldsymbol{s}_{j3} \times \boldsymbol{s}_{k3} \right| \tag{7.5}$$

which shows the work of the actuation input of limb *i* on the 1-DOF translation motion of the platform when the other two limbs are locked. Based on this, the power coefficient is defined as:

$$\lambda_{Ti} = \frac{\left| \boldsymbol{S}_{Ti} \circ \boldsymbol{S}_{Oi} \right|}{\left| \boldsymbol{S}_{Ti} \circ \boldsymbol{S}_{Oi} \right|_{\max}} = \frac{\cos\theta_i}{1} \tag{7.6}$$

where θ_i is the angle between limb *i* ($\boldsymbol{s}_{i3}$) and the line ($\boldsymbol{s}_{j3} \times \boldsymbol{s}_{k3}$) which is perpendicular to both the other two limbs.

Thus there are three power coefficients for the three limbs and they depend on the limb directions. The minimum power coefficient is taken as the output transmission index (OTI):

$$\gamma_O = \min\{\lambda_{T1}, \lambda_{T2}, \lambda_{T3}\} = \min\{\cos\theta_1, \cos\theta_2, \cos\theta_3\} \tag{7.7}$$

which can be used to represent the output transmission performance at the given mechanism configuration.

The output transmission represents the contribution of the limb to the platform motion. When any θ_i is π/2, the virtual coefficient becomes zero indicating that limb *i* cannot transmit any power to the platform along its motion. This represents singular configuration of the parallel mechanism. It can be also noted that

$$\boldsymbol{s}_{13} \cdot \boldsymbol{s}_{23} \times \boldsymbol{s}_{33} = \boldsymbol{s}_{23} \cdot \boldsymbol{s}_{13} \times \boldsymbol{s}_{33} = \boldsymbol{s}_{33} \cdot \boldsymbol{s}_{13} \times \boldsymbol{s}_{23} = \left\| \begin{bmatrix} \boldsymbol{s}_{13}^T \\ \boldsymbol{s}_{23}^T \\ \boldsymbol{s}_{33}^T \end{bmatrix} \right\| = 0 \tag{7.8}$$

which means the three limb power coefficients represent the same singularity configurations and it also equals to the first factor of the Jacobian matrix determinant in Eq. (7.3).

7.2.1.1.2 Constraint Transmission

Similar to the output transmission, constraint transmission is the reciprocal product of the virtual output motion twist screw of the platform and the constraint wrench screw of a limb and can be obtained in the following way. Locking all the limb actuation and releasing the constraint ($\boldsymbol{S}_{Ci}$) from limb *i*, the platform can virtually have a 1-DOF twist motion $\boldsymbol{S}_{OCi}$ which can be obtained by taking the reciprocal screw to the other five wrench screws in the Jacobian matrix in Eq. (7.3) except the *i*th constraint wrench $\boldsymbol{S}_{Ci}$:

$$\boldsymbol{S}_{OCi} = \begin{bmatrix} \boldsymbol{s}_{OCi}^T & r_{oci}^T \times \boldsymbol{s}_{OCi}^T \end{bmatrix} \tag{7.9}$$

which is a pure rotation motion along the line that is perpendicular to both $\boldsymbol{s}_{j45}$ in limb *j* and $\boldsymbol{s}_{k45}$ in limb *k*, where $\boldsymbol{s}_{OCi} = \boldsymbol{s}_{j45} \times \boldsymbol{s}_{k45} / \left| \boldsymbol{s}_{j45} \times \boldsymbol{s}_{k45} \right|, (i, j, k = 1,2,3; i \neq j \neq k)$, $\boldsymbol{r}_{oci}$ represents a point on the line $\boldsymbol{s}_{OCi}$.

Then the constraint transmission virtual coefficient is obtained by the reciprocal product

$$\boldsymbol{S}_{Ci} \circ \boldsymbol{S}_{OCi} = \boldsymbol{s}_{i45} \cdot \boldsymbol{s}_{OCi} = \cos\theta_{Ci} \tag{7.10}$$

which shows the work of the constraint wrench $\boldsymbol{S}_{Ci}$ on the virtual 1-DOF motion of the platform. θ_{ci} is the angle between $\boldsymbol{s}_{i45}$ and $\boldsymbol{s}_{OCi}$.

Following this, the power coefficient is defined as:

$$\lambda_{Ci} = \frac{\left| \boldsymbol{S}_{Ci} \circ \boldsymbol{S}_{OCi} \right|}{\left| \boldsymbol{S}_{Ci} \circ \boldsymbol{S}_{OCi} \right|_{\max}} = \frac{\cos\theta_{Ci}}{1} \tag{7.11}$$

and the minimum one is taken as the constraint transmission index (CTI):

$$\gamma_{OC} = \min\{\lambda_{C1}, \lambda_{C2}, \lambda_{C3}\} = \min\{\cos\theta_{C1}, \cos\theta_{C2}, \cos\theta_{C3}\} \tag{7.12}$$

which can be used to represent the closeness to constraint singularity.

When Eq. (7.10) equals to zero, the constraint wrench cannot provide any constraint to the defined motion of the platform which will gain extra mobility. Thus the mechanism meets constraint singularities which can be expressed as:

$$\boldsymbol{s}_{145} \cdot \boldsymbol{s}_{245} \times \boldsymbol{s}_{345} = \boldsymbol{s}_{245} \cdot \boldsymbol{s}_{145} \times \boldsymbol{s}_{345} = \boldsymbol{s}_{345} \cdot \boldsymbol{s}_{145} \times \boldsymbol{s}_{245} = \left\| \begin{bmatrix} \boldsymbol{s}_{145}^T \\ \boldsymbol{s}_{245}^T \\ \boldsymbol{s}_{345}^T \end{bmatrix} \right\| = 0 \tag{7.13}$$

which shows that the three constraint power coefficients represent the same constraint singularity configurations of the platform and it equals to the second factor of the Jacobian matrix determinant in Eq. (7.3).

Thus, by taking the Jacobian matrix determinant in Eq. (7.3) equal to zero, all the output transmission singularities and constraint singularities of the 3-rT*P*rT MPM with pure translation motion can be expressed.

7.2.1.2 The 3-rTPrT with Pure Rotation

In the pure rotation case, all the limbs are in the intersecting phase as in Fig.5-7. The transmission wrench screw comes from the prismatic joint in each limb and it's the same with that in Eq. (7.1) that is a force along the prismatic joint. The constraint wrench can be obtained in the same way for Eq. (7.2) but it becomes a constraint force in this pure rotation case:

$$\boldsymbol{S}_{cir} = \begin{bmatrix} \boldsymbol{s}_{i2}^T & \boldsymbol{0} \end{bmatrix} \quad (i = 1, 2, 3) \tag{7.14}$$

which is a force parallel to the bracket axis ($\boldsymbol{s}_{i2}$) of the rT joint and passing by the rotation center *o*.

Similarly, the screw based overall Jacobian matrix **J** can be directly obtained and its determinant equals to:

$$\left|\mathbf{J}\right| = \left\| \begin{bmatrix} \boldsymbol{S}_{T1} \\ \boldsymbol{S}_{T2} \\ \boldsymbol{S}_{T3} \\ \boldsymbol{S}_{c1r} \\ \boldsymbol{S}_{c2r} \\ \boldsymbol{S}_{c3r} \end{bmatrix} \right\| = \left\| \begin{bmatrix} \boldsymbol{s}_{13}^T & \boldsymbol{a}_1^T \times \boldsymbol{s}_{13}^T \\ \boldsymbol{s}_{23}^T & \boldsymbol{a}_2^T \times \boldsymbol{s}_{23}^T \\ \boldsymbol{s}_{33}^T & \boldsymbol{a}_3^T \times \boldsymbol{s}_{33}^T \\ \boldsymbol{s}_{12}^T & \mathbf{0} \\ \boldsymbol{s}_{22}^T & \mathbf{0} \\ \boldsymbol{s}_{32}^T & \mathbf{0} \end{bmatrix} \right\| = \left\| \begin{bmatrix} \boldsymbol{s}_{13}^T & m_1\boldsymbol{s}_{12}^T \\ \boldsymbol{s}_{23}^T & m_2\boldsymbol{s}_{22}^T \\ \boldsymbol{s}_{33}^T & m_3\boldsymbol{s}_{32}^T \\ \boldsymbol{s}_{12}^T & \mathbf{0} \\ \boldsymbol{s}_{22}^T & \mathbf{0} \\ \boldsymbol{s}_{32}^T & \mathbf{0} \end{bmatrix} \right\| = m_1 m_2 m_3 \left\| \begin{bmatrix} \boldsymbol{s}_{12}^T \\ \boldsymbol{s}_{22}^T \\ \boldsymbol{s}_{32}^T \end{bmatrix} \right\|^2 \tag{7.15}$$

where m_i is the magnitude of $\boldsymbol{a}_i \times \boldsymbol{s}_{i3}$. Eq. (7.15) represents singularity configurations of the 3-rT*P*rT MPM with pure rotation motion when it equals to zero. It can be seen that it fully depends on the relation among bracket axes ($\boldsymbol{s}_{12}$, $\boldsymbol{s}_{22}$, $\boldsymbol{s}_{32}$) of the rT joints in the three limbs.

7.2.1.2.1 Output Transmission

Similarly by locking two limbs except the *i*th limb, the platform will have a 1-DOF motion. The output twist screw $\boldsymbol{S}_{Oi}$ is obtained by taking reciprocal screw to the other five wrench screws in the Jacobian matrix in Eq. (7.15) except the *i*th transmission wrench $\boldsymbol{S}_{Ti}$:

$$\boldsymbol{S}_{Oi} = \left[\boldsymbol{s}_{j2}^T \times \boldsymbol{s}_{k2}^T / \left| \boldsymbol{s}_{j2} \times \boldsymbol{s}_{k2} \right| \quad \mathbf{0} \right] \quad (i, j, k = 1, 2, 3; i \neq j \neq k) \tag{7.16}$$

which is a pure rotation along the line passing by the rotation center *o* and perpendicular to both bracket axes in limb *j* and limb *k*.

Then the output transmission virtual coefficient is expressed by the reciprocal product

$$\boldsymbol{S}_{Ti} \circ \boldsymbol{S}_{Oi} = m_i \boldsymbol{s}_{i2} \cdot \boldsymbol{s}_{j2} \times \boldsymbol{s}_{k2} / \left| \boldsymbol{s}_{j2} \times \boldsymbol{s}_{k2} \right| \tag{7.17}$$

which shows the work of the actuation input of limb *i* on the 1-DOF rotation motion of the platform when the other two limbs are locked.

Based on this, the power coefficient is defined as:

$$\lambda_{Tir} = \frac{\left|\boldsymbol{S}_{Ti} \circ \boldsymbol{S}_{Oi}\right|}{\left|\boldsymbol{S}_{Ti} \circ \boldsymbol{S}_{Oi}\right|_{\max}} = \frac{m_i \cos\beta_i}{m_i * 1} = \cos\beta_i \tag{7.18}$$

where β_i is the angle between the bracket axis ($\boldsymbol{s}_{i2}$) in limb *i* and the line ($\boldsymbol{s}_{j2} \times \boldsymbol{s}_{k2}$) which is perpendicular to both bracket axes of the other two limbs.

Thus output transmission index of the pure rotation case is:

$$\gamma_{Or} = \min\{\lambda_{T1r}, \lambda_{T2r}, \lambda_{T3r}\} = \min\{\cos\beta_1, \cos\beta_2, \cos\beta_3\} \tag{7.19}$$

which is used to describe the closeness to the output transmission singularity. When any of them equals to zero, the mechanism meets singularity and the limb cannot transmit power to the platform. It is also noted that

$$\boldsymbol{s}_{12} \cdot \boldsymbol{s}_{22} \times \boldsymbol{s}_{32} = \boldsymbol{s}_{22} \cdot \boldsymbol{s}_{12} \times \boldsymbol{s}_{32} = \boldsymbol{s}_{32} \cdot \boldsymbol{s}_{12} \times \boldsymbol{s}_{22} = \left\| \begin{bmatrix} \boldsymbol{s}_{12}^T \\ \boldsymbol{s}_{22}^T \\ \boldsymbol{s}_{32}^T \end{bmatrix} \right\| = \left|\mathbf{J}\right| = 0 \tag{7.20}$$

which shows zero output transmission power coefficients are equal to each other and also equal to the zero Jacobian matrix determinant. They represent the same singularity configurations of the 3-(rT)*P*(rT) MPM with pure rotation motion.

7.2.1.2.2 Constraint Transmission

Using similar way with the pure translation case, by locking all the limb actuation and releasing the constraint ($\boldsymbol{S}_{Cir}$) from limb *i*, a 1-DOF platform twist motion $\boldsymbol{S}_{OCir}$ can be obtained by taking reciprocal screw to the other five wrench screws in the Jacobian matrix in Eq. (7.15) except the *i*th constraint wrench $\boldsymbol{S}_{Cir}$:

$$\boldsymbol{S}_{OCir} = \begin{bmatrix} \boldsymbol{s}_{OCir}^T & r_{ocir}^T \times \boldsymbol{s}_{OCir}^T \end{bmatrix} = \begin{bmatrix} \boldsymbol{s}_{OCir}^T & m_{jk} \boldsymbol{s}_{j2} \times \boldsymbol{s}_{k2} \end{bmatrix} \tag{7.21}$$

which is a pure rotation motion along the line $\boldsymbol{s}_{OCir}$ and passing by a point $\boldsymbol{r}_{ocir}$. Since it is reciprocal to the other two constraint forces which pass by the origin *o*, the second part of this twist $\boldsymbol{S}_{OCir}$ should have $\boldsymbol{r}_{ocir}\times\boldsymbol{s}_{OCir}= m_{jk}\boldsymbol{s}_{j2}\times\boldsymbol{s}_{k2}$ which is perpendicular to both the other two constraint forces represented by bracket axes of the other two limbs. m_{jk} denotes the magnitude.

Following this, the constraint transmission virtual coefficient is calculated by the reciprocal product

$$\boldsymbol{S}_{Cir}\circ\boldsymbol{S}_{OCir}=m_{jk}\boldsymbol{s}_{i2}\cdot\boldsymbol{s}_{j2}\times\boldsymbol{s}_{k2}=m_{jk}\cos\beta_i \tag{7.22}$$

which shows the constraint work of the constraint wrench $\boldsymbol{S}_{Cir}$ on the virtual 1-DOF motion of the platform. In general the platform motion is constrained when Eq. (7.22) is not zero and the mechanism meets constraint singularity if it becomes zero.

Following this, the constraint power coefficient is:

$$\lambda_{Cir}=\frac{\left|\boldsymbol{S}_{Cir}\circ\boldsymbol{S}_{OCir}\right|}{\left|\boldsymbol{S}_{Cir}\circ\boldsymbol{S}_{OCir}\right|_{\max}}=\frac{m_{jk}\cos\beta_i}{m_{jk}*1}=\cos\beta_i=\lambda_{Tir} \tag{7.23}$$

which is the same with the output transmission power coefficient in Eq. (7.18). Thus, the constraint transmissibility is the same with the output transmissibility of the 3-(rT)*P*(rT) MPM with pure rotation motion. This can be also seen from the Jacobian matrix determinant in Eq. (7.15) which has square of the same factor of virtual coefficient of the output transmission and the constraint transmission. Then the constraint transmission index is the same with the output transmission index in Eq. (7.19).

Based on the above it can be concluded that the factors of the Jacobian matrix determinant of the 3-(rT)*P*(rT) MPM represent its output transmissibility and constraint transmissibility. While in the pure translation case the two are different as in Eq. (7.3), they are the same in the pure

rotation case as in Eq. (7.15). When the Jacobian determinant equals to zero, output transmission and constraint singularities can be found.

7.2.1.3 Variable Motion/Force Transmissibility and Singularity Loci

As explained in Section 7.2.1, by tuning the radial axes of the rT joints in all limbs, the rotation center of the pure rotation motion can be controlled and the workspace of the pure translation motion can be also controllable. At the same time, their transmissibility and singularity loci will be variable. To demonstrate this, four different configurations are selected as in Fig. 7-1 and represented by angle α_{ai} which is the angle between the radial axis of the platform rT joint and the z-axis. At those four configurations, the radial axis of the platform rT joint intersects with the z-axis at point P_i (i=1,2, 3, 4). As in Fig. 7-1, P_1 is above the platform, P_2 is on the platform, P_3 is in the middle while P_4 is under the base. Correspondingly, $\alpha_{a1} = 2\pi/3$, $\alpha_{a2} = \pi/2$, $\alpha_{a3} = \sin^{-1}(\sqrt{2/3})$, and $\alpha_{a4} = \pi/6$. In the following examples, the platform and base sizes are set r_a=1 and r_b=2.

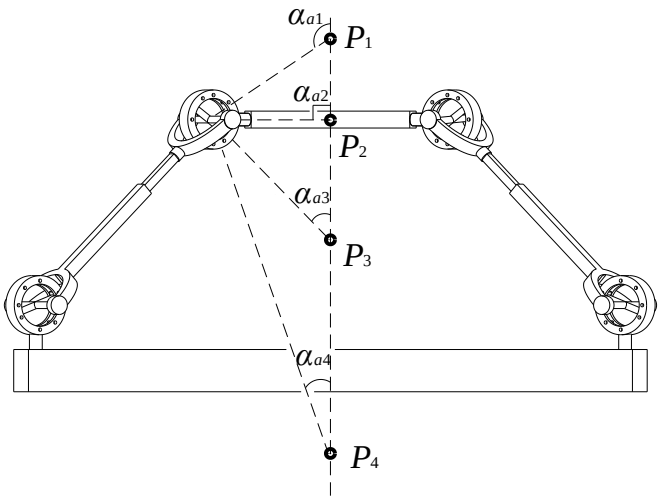

Figure 7-1 Four different rotation centers

7.2.1.3.1 3-rTPrT with Pure Translation

Variable transmission indices and singularity loci of the 3-rT*P*rT MPM with pure translation are illustrated in Fig. 7-2 corresponding to the four different radial axis setup of the rT joint in Fig. 7-1. Based on Eqs. (7.5)-(7.7), the output transmission index depends only on the directions of

the three limbs and is the same as in Fig. 7-2(e) for all the four cases. When the output transmission index equals to zero, output transmission singularity occurs for the 3-rT*P*rT MPM which are represented by the same yellow plane (z=0) in all the four cases in Fig. 7-2(a) to (d). This shows that the tuning of the radial axes of the rT joints will not affect the output transmission index and singularity in the pure translation motion. Differently, the radial axes change will bring different constraint transmission indices (right: blue curves) and constraint singularity loci (left: blue surfaces) as shown Fig. 7-2(a) to (d). In general, the transmission index values are high when the platform is close to the z-axis (x=y=0) and it decrease when the platform moves away. A special case is that when the radial axes are set to be perpendicular to the z-axis with α_{a2} = π/2 as in Fig. 7-2(b), the constraint transmission singularity loci coincide with the output transmission singularity loci which are the plane z=0. This means that all the areas above or below this plane are singularity-free workspaces. However, the constraint transmission index (right: blue curves) shows that the transmissibility decreases and it is close to constraint singularity when the platform moves close to the z-axis. While generally the singularity loci are curved surfaces as in Fig. 7-2(a) and (d), they become three planes for α_{a3}=$\sin^{-1}(\sqrt{2/3})$ in Fig. 7-2(c). At this configuration, the three radial axes of the platform rT joints are orthogonal to each other. Comparing the constraint transmission indices for the four cases, it can be seen that workspace close to z-axis with high index values is larger when the radial axes of the platform rT joints have smaller angle with the z-axis. A big area with CTI=0.9 has been shown in Fig. 7-2(d) and it is close to the output transmission performance in Fig. 7-2(e).

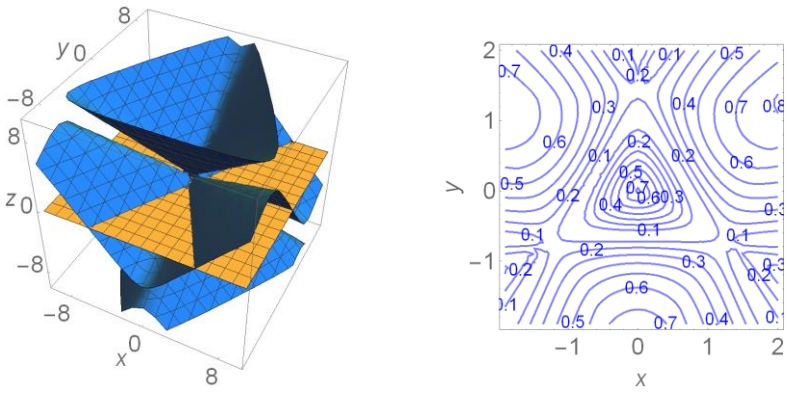

(a) α_{a1}=2π/3 (left: singularity loci, right: CTI at z=1.5)

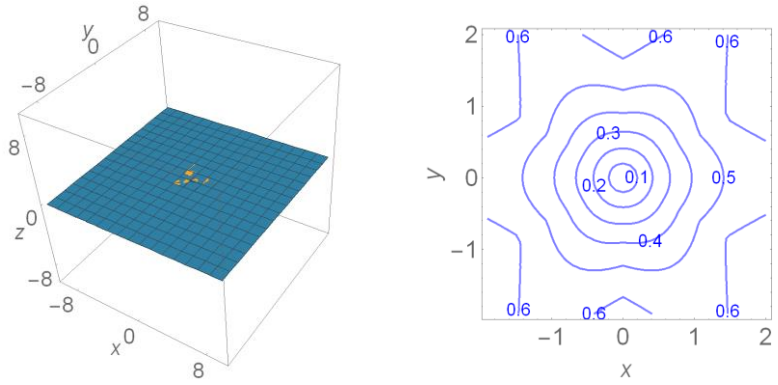

(b) α_{a2}= π/2 (left: singularity loci, right: CTI at z=1.5)

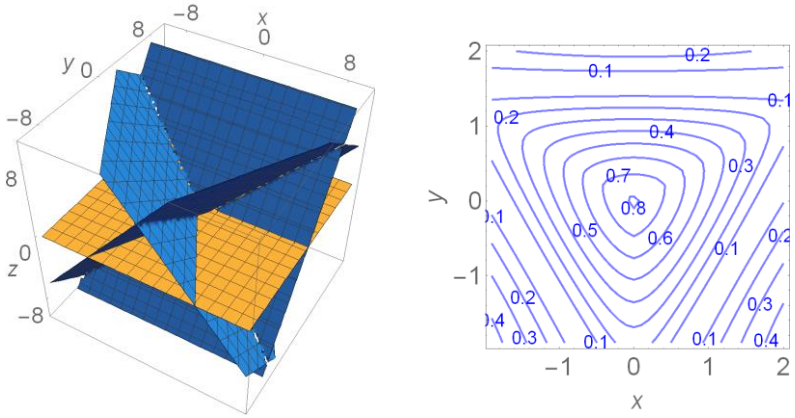

(c) α_{a3}=$\sin^{-1}(\sqrt{2/3})$ (left: singularity loci, right: CTI at z=1.5)

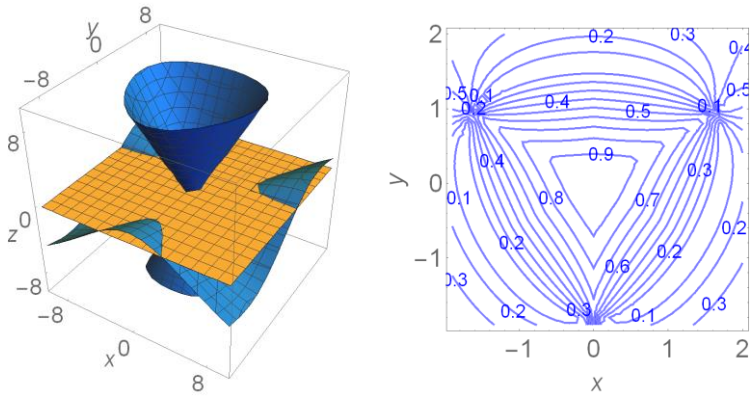

(d) α_{a4}=π/6 (left: singularity loci, right: CTI at z=1.5)

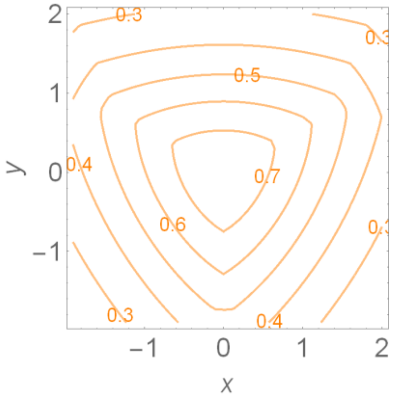

(e) Output transmission index at z=1.5

Figure 7-2 Variable transmission indices and singularity loci of the pure translation motion

7.2.1.3.2 3-rTPrT with Pure Rotation

For the 3-rT*P*rT MPM with pure rotation, points P_i (i=1,2, 3, 4) in Fig. 7-1 represent four different rotation centers of the platform and corresponding angle (α_b) between the radial axes of the base rT joints and the z-axis can be calculated based on Fig. 6-2 and Eq. (6.1). From Section 7.1.1.2, it's found that the output transmissibility and constraint transmissibility are the same for the pure rotation case. Thus there will be only one type of singularity loci and transmission index as shown in Fig. 7-3 for the four different configurations. Generally, the singularity loci are symmetrical and curved surfaces due to the symmetrical limb arrangement of the 3-rT*P*rT MPM. On the right side, output or constraint transmission indices are shown for each case on the plane with c_3=0.5 which means a rotation of about 2π/3 about z-axis is used. The rotated and symmetrical index curves also show this rotation on the c_1-c_2 plane. Similar to the pure translation case in Section 7.1.1.3.1, workspace close to c_3-axis (c_1=c_2=0) with high index values is larger when the rotation center is close to the negative side of the z-axis. A big area with CTI/OTI over 0.8 is shown in Fig. 7-3(d) for the case that the rotation center is below the base represented by point P_4 in Fig. 7-1.

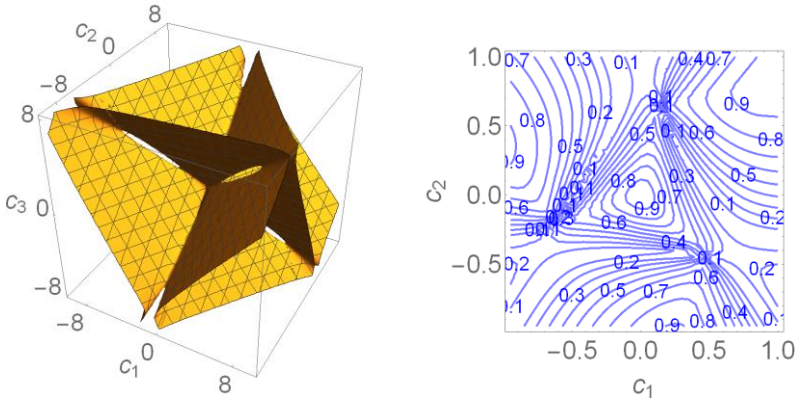

(a) α_{a1}=2π/3 (left: singularity loci, right: CTI/OTI at c_3=0.5)

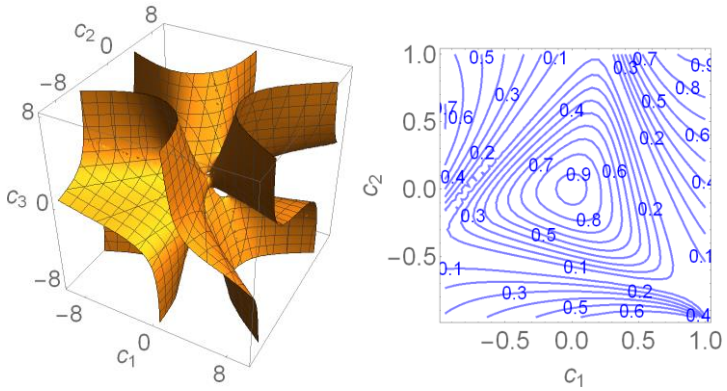

(b) α_{a2}= π/2 (left: singularity loci, right: CTI/OTI at c_3=0.5)

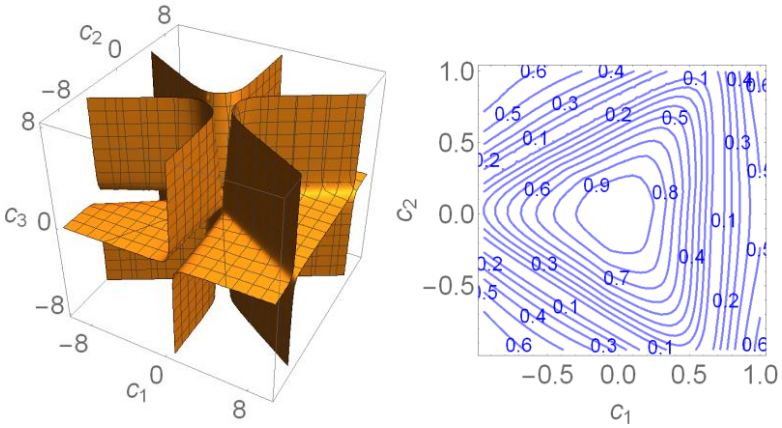

(c) α_{a3}=sin^{-1}($\sqrt{2/3}$)(left: singularity loci, right: CTI/OTI at c_3=0.5)

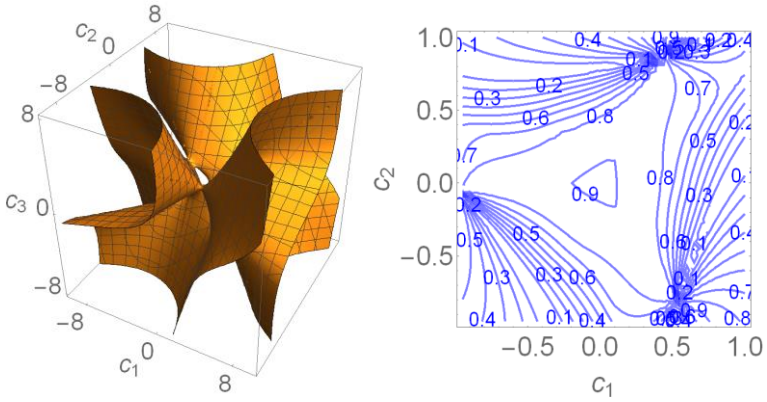

(d) α_{a4}=π/6 (left: singularity loci, right: CTI/OTI at c_3=0.5)

Figure 7-3 Variable transmission indices and singularity loci of the pure rotation motion

7.2.2 Motion/Force Transmissibility of the 3-rRPS

For the rR*PS* limb, the input transmission is constant as the actuation wrench is in the same line with the actuation twist which is along the prismatic joint. Their reciprocal product gives 1 and it is not considered further. The other two transmission indices will be investigated and they have

the same format for the 1T2R and 3R motion, representing a unified kinematics performance representation.

7.2.2.1 Output Transmission

By locking two limbs except the *i*th limb, the platform will have a 1-DOF motion. It's twist screw $\boldsymbol{S}_{Oi}$ is called the output twist screw and can be obtained by taking reciprocal screw to the other five wrench screws in the Jacobian matrix in Eq. (6.63) except the *i*th transmission wrench $\boldsymbol{S}_{Ti}$:

$$\boldsymbol{S}_{Oi} = \begin{bmatrix} \boldsymbol{s}_{Oi}^T & \boldsymbol{r}_{Oi}^T \times \boldsymbol{s}_{Oi}^T + h_{Oi}\boldsymbol{s}_{Oi}^T \end{bmatrix} \quad (i = 1,2,3) \tag{7.24}$$

which is a screw motion along the line represented by unit vector $\boldsymbol{s}_{Oi}$ with pitch h_{oi} and passing by a point $\boldsymbol{r}_{Oi}$.

Then the output transmission virtual coefficient [165] is represented by the reciprocal product

$$\boldsymbol{S}_{Ti} \circ \boldsymbol{S}_{Oi} = \boldsymbol{s}_i \cdot (\boldsymbol{r}_{Oi}^T \times \boldsymbol{s}_{Oi}^T + h_{Oi}\boldsymbol{s}_{Oi}^T) + \boldsymbol{a}_i^T \times \boldsymbol{s}_i^T \cdot \boldsymbol{s}_{Oi}^T \tag{7.25}$$

which shows the work of the actuation input of limb *i* on the 1-DOF translation motion of the platform when the other two limbs are locked. Based on this, the power coefficient is defined as:

$$\lambda_{Ti} = \frac{\left|\boldsymbol{S}_{Ti} \circ \boldsymbol{S}_{Oi}\right|}{\left|\boldsymbol{S}_{Ti} \circ \boldsymbol{S}_{Oi}\right|_{\max}} = \frac{\left|h_{Oi}\cos\theta_{Oi} - d_{Oi}\sin\theta_{Oi}\right|}{\sqrt{h_{Oi}^2 + d_{Oi\max}^2}} \tag{7.26}$$

where θo_i is the angle between limb *i* ($\boldsymbol{s}_i$) and the output motion screw ($\boldsymbol{s}_{Oi}$) and d_{Oi} is the distance between these two lines, $d_{Oi\max}$ is the maximum distance between the two lines and can be calculated from

$$d_{Oi\max} = \left|(\boldsymbol{a}_i - \boldsymbol{r}_{Oi}) \times \boldsymbol{s}_{Oi}\right| \tag{7.27}$$

Thus there are three power coefficients for the three limbs and they depend on the limb directions. The minimum power coefficient is taken as the output transmission index (OTI):

$$\gamma_O = \min\{\lambda_{T1}, \lambda_{T2}, \lambda_{T3}\} \tag{7.28}$$

which can be used to represent the output transmission performance at the given mechanism configuration.

The output transmission represents the contribution of the limb to the platform motion. When any λ_{Ti} is zero it indicates that limb *i* cannot transmit any power to the platform along its motion. This represents singular configuration of the parallel mechanism.

7.2.2.2 Constraint Transmission

Similar to the output transmission, the constraint transmission can be obtained in the following way. Locking all the limb actuation and releasing the constraint ($\boldsymbol{S}_{Ci}$) from limb *i*, the platform can virtually have a 1-DOF twist motion $\boldsymbol{S}_{OCi}$ which can be obtained by taking reciprocal screw to the other five wrench screws in the Jacobian matrix in Eq. (6.63) except the *i*th constraint wrench $\boldsymbol{S}_{Ci}$:

$$\boldsymbol{S}_{OCi} = \begin{bmatrix} \boldsymbol{s}_{OCi}^T & \boldsymbol{r}_{OCi}^T \times \boldsymbol{s}_{OCi}^T + h_{OCi}\boldsymbol{s}_{OCi}^T \end{bmatrix} \quad (i = 1, 2, 3) \tag{7.29}$$

which is a screw motion along the line represented by unit vector $\boldsymbol{s}_{OCi}$ with pitch h_{OCi} and passing by a point $\boldsymbol{r}_{OCi}$.

Then the constraint transmission virtual coefficient is obtained by the reciprocal product

$$\boldsymbol{S}_{Ci} \circ \boldsymbol{S}_{OCi} = \boldsymbol{u}_i \cdot (\boldsymbol{r}_{OCi}^T \times \boldsymbol{s}_{OCi}^T + h_{OCi}\boldsymbol{s}_{OCi}^T) + \boldsymbol{a}_i^T \times \boldsymbol{u}_i^T \cdot \boldsymbol{s}_{OCi}^T \tag{7.30}$$

which shows the constraint work of the constraint wrench $\boldsymbol{S}_{Ci}$ on the virtual 1-DOF motion of the platform.

Following this, the power coefficient is defined as:

$$\lambda_{Ci} = \frac{\left|\boldsymbol{S}_{Ci} \circ \boldsymbol{S}_{OCi}\right|}{\left|\boldsymbol{S}_{Ci} \circ \boldsymbol{S}_{OCi}\right|_{\max}} = \frac{\left|h_{OCi}\cos\theta_{OCi} - d_{OCi}\sin\theta_{OCi}\right|}{\sqrt{h_{OCi}^2 + d_{OCi\max}^2}} \tag{7.31}$$

where θoc_i is the angle between constraint screw ($\boldsymbol{S}_{Ci}$) and the virtual output motion screw ($\boldsymbol{S}_{OCi}$) and d_{OCi} is the distance between these two lines, $d_{OCi\max}$ is the maximum distance between them and can be calculated from

$$d_{OCi\max} = \left|(\boldsymbol{a}_i - \boldsymbol{r}_{OCi}) \times \boldsymbol{s}_{OCi}\right| \tag{7.32}$$

The minimum power coefficient is taken as the constraint transmission index (CTI):

$$\gamma_{OC} = \min\{\lambda_{C1}, \lambda_{C2}, \lambda_{C3}\} \tag{7.33}$$

which can be used to represent the closeness to constraint singularity.

When Eq. (7.31) equals to zero, the constraint wrench cannot provide any constraint to the defined motion of the platform which will gain extra mobility. Thus the mechanism meets constraint singularities.

7.2.2.3 Variable Motion/Force Transmissibility and Singularity Loci

As explained in Section 5.4, by tuning the rR joint axes in all limbs, the 3-rR*PS* MPM can have infinite number of phases with 3R motion and four cases with 1T2R motion. In this case, the workspace associated with different phases will be different and at the same time, their transmissibility and singularity loci will be variable. To demonstrate this, four different phases are selected and represented by the rR joint angles (θ_1, θ_2, θ_3) of the three limbs. Their singularity loci, output transmission index and constraint transmission index are calculated as in Fig. 7-4. In the examples, the platform and base sizes are set r_a=1 and r_b=2, the rR joint base location angle ϕ=π/2−ArcSin($\sqrt{3}$/3) representing that the normal vectors of the three rR joints are perpendicular to each other.

Fig. 7-4(a) shows the case with $\theta_1= \theta_2= \theta_3=0$ which has 1T2R motion. Its singularity loci is illustrated on the left by the curved surfaces in the 3D space constructed by the three parameters representing the translation (p_z) along z-axis and two rotations (c_1 and c_2, which are Rodriguez-Hamilton parameters [146]) about x-axis and y-axis. It can be seen that the loci is symmetrical due to the symmetrical limb arrangement. The loci consists of two tetrahedron shaped surfaces and a curved close-to-plane surface which are all intersecting at the origin with $c_1=c_2=p_z=0$. The space between them represents the singularity-free workspace of the 3rR*PS* MPM with $\theta_1= \theta_2= \theta_3=0$. The middle and right figures of Fig. 7-4(a) tell the output transmission index and constraint transmission index on the c_1-c_2 plane with p_z =1.5. While the blue curved lines show the transmission index, the red curve represents the singularity loci on the selected plan with p_z =1.5. It can be seen that the singularity loci describe the mechanism configurations with zero output transmission or constraint transmission indices. The index numbers are higher when it is close to the center ($c_1=c_2= 0$) or far away from the singularity loci.

Fig. 7-4(b)-(d) show the singularity loci, OTI and CTI of the 3rR*PS* MPM with 3R motion at three cases when $\theta_1= \theta_2= \theta_3=$ π/6, π/3, and π/2. The 3D singularity loci are illustrated along the three rotation directions expressed by the Rodriguez-Hamilton parameters c_1, c_2, and c_3. In general, the singularity loci of the three cases are all symmetrical but different between each other. In the $\theta_1= \theta_2= \theta_3=$ π/6 case, there is a big singularity free workspace around the origin of ($c_1=c_2=c_3=0$) but it will meet singularity when there is a pure rotation about the z-axis. This is different when $\theta_1= \theta_2= \theta_3$ increases as for the π/3 and π/2 cases that the mechanism meets singularity at the origin ($c_1=c_2=c_3=0$) but has singularity-free workspace below and above this point. The OTI and CTI are all shown on the plane with c_3=0.5. Similar with the 1T2R case in Fig. 7-4(a), both OTI and CTI have higher values when it is far from the singularity loci (red curve) and reach zero on the singularity curve. A larger area with CTI=0.9 than OTI=0.9 has been shown in π/6 and π/3 cases in Fig. 7-4(b) and (c) and it is opposite for the π/2 case as in Fig. 5-4(d). It seems the OTI has been improved when increasing the rR joint angles ($\theta_1= \theta_2= \theta_3$) on the selected rotation plane (c_3=0.5) while the CTI decreases.

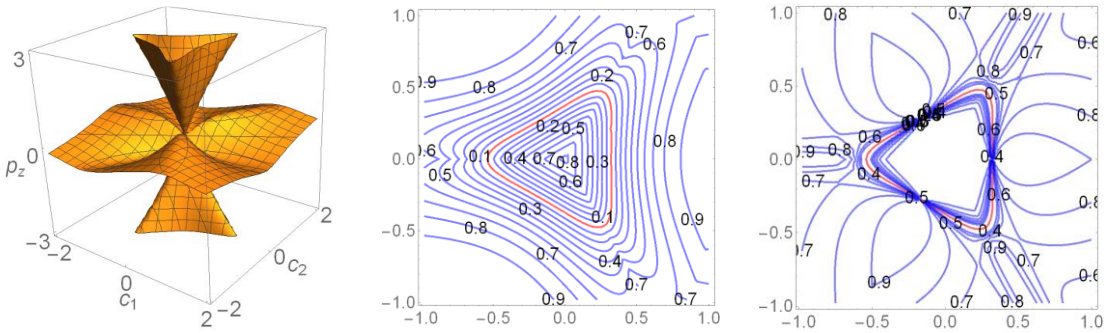

(a) θ_1= θ_2= θ_3=0 with 1T2R motion (left: singularity loci, middle: OTI at p_z=1.5, right: CTI at p_z =1.5)

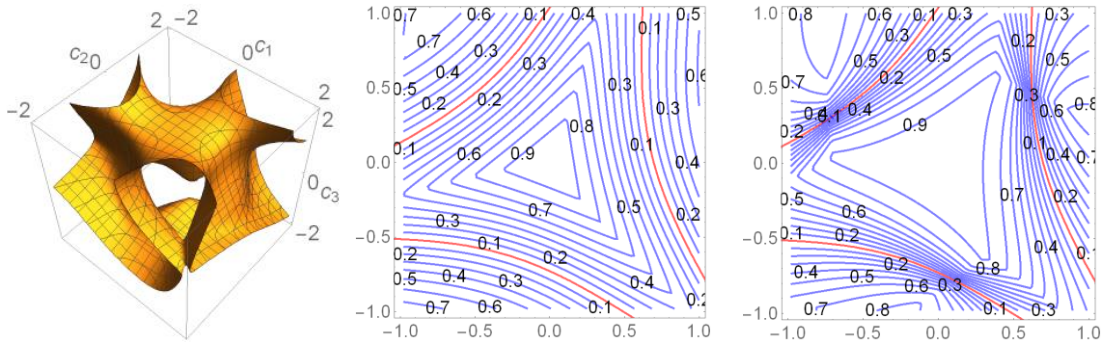

(b) θ_1= θ_2= θ_3= π/6 with 3R motion (left: singularity loci, middle: OTI at c_3=0.5, right: CTI at c_3=0.5)

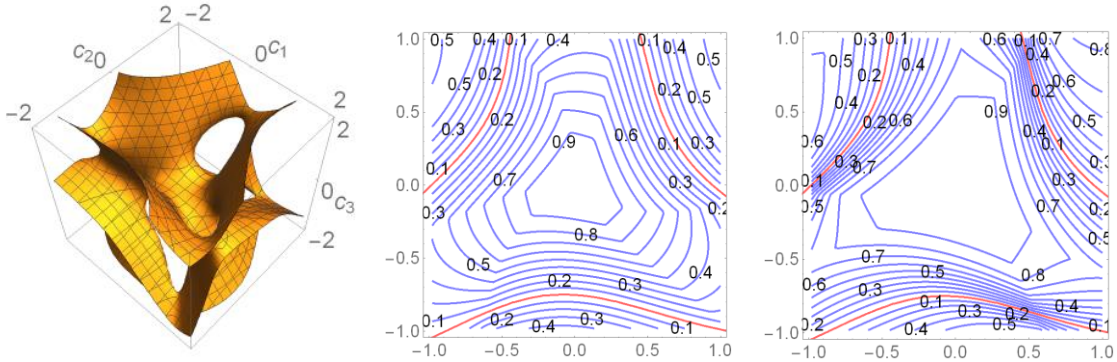

(c) θ_1= θ_2= θ_3= π/3 with 3R motion (left: singularity loci, middle: OTI at c_3=0.5, right: CTI at c_3=0.5)

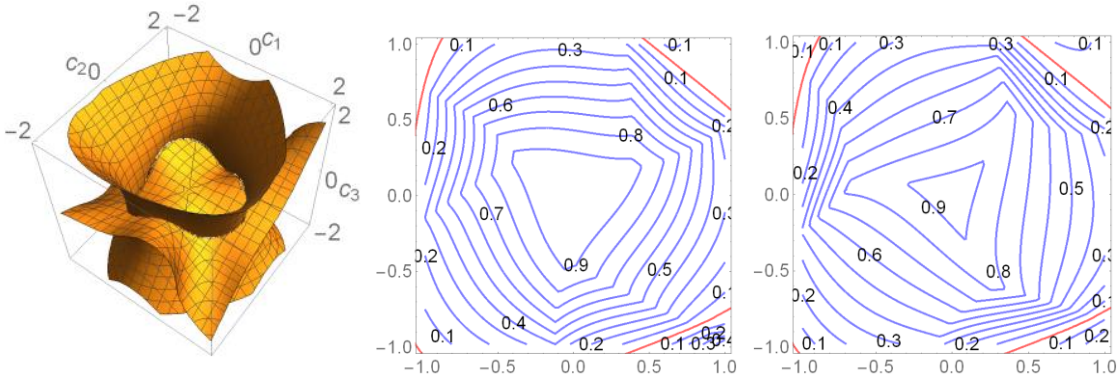

(d) θ_1= θ_2= θ_3= π/2 with 3R motion (left: singularity loci, middle: OTI at c_3=0.5, right: CTI at c_3=0.5)

Figure 7-4 Variable Transmission Indices and Singularity Loci

7.3 Unified Optimal Design of the 3-rRPS Based on Motion/Force Transmissibility

Each phase of the 3-rR*PS* MPM is a parallel mechanism and there is an optimal design based on selected design criteria. To have an optimal design of the metamorphic parallel mechanism to cover all working phases with different motion types is a challenge task. However, since all phases share the same physical structure and actuation parameters, there is a rule to design parameters in an optimal way. In this section, the four phases (θ_1= θ_2= θ_3=0 for 1T2R motion and θ_1= θ_2= θ_3= π/6, π/3, and π/2 for 3R motion) will be investigated in the optimal design aims at giving the best combined performance.

7.3.1 Design Variables and Performance Indices

The key parameters of the 3-rR*PS* MPM in the optimization are the base and platform sizes (r_b and r_a), rR joint base location angle ϕ and the limb length range ($l_{min} \le l_i \le l_{max}$). Considering practical mechanical limb strokes, it is commonly l_{max}=1.8l_{min} which means the stroke of the limb can be eighty percent of its minimum length. Then l_{min} will be taken as one of the key parameters in the design and the rR joint base location angle is set at ϕ=π/2−ArcSin($\sqrt{3}$/3) for the design that the normal vectors of the three rR joints are perpendicular to each other. To have a relative relation, the length parameters are normalized by the base size r_b as $\lambda_a = r_a/r_b$, $\lambda_{lmin} = l_{min}/r_b$. Thus, λ_a represents the ratio between the platform and base sizes and λ_{lmin} shows the ratio of the minimum limb length over the base size. Mechanical constraints including maximum passive joint angles and limb interference should also be considered in the calculation. In the following, passive joint angles are limited in the range as $-\psi_{max} \le \psi_i \le \psi_{max}$, where ψ_i denotes rotation angle from its home position of any revolute joint, and spherical joint along three orthogonal directions one of which is along the limb at the home position. ψ_{max} is given π/3 in this paper. The minimum distance between any two limbs is limited to be 0.01 to avoid limb interference.

Optimal design of the 3-rR*PS* MPM in this work is to find the best parameter set to have maximum singularity-free workspace with good kinematics performance represented by the motion/force transmissibility. Thus, the optimal design objective function is given as:

$$\begin{cases} \text{maximize} & V \\ \text{maximize} & k \end{cases}, \qquad k = \frac{\int_V k_i dV}{V}, \quad k_i = \mathbf{min}\{\gamma_O, \gamma_{OC}\} \tag{7.34}$$

Subject to: $-\pi/3 \le \psi_i \le \pi/3$,

$0.2 \le \lambda_a \le 1.2$,

$0.5 \le \lambda_{lmin} \le 1.6$,

distance between two limbs ≥0.01.

where V is the maximum singularity-free workspace volume, k is the average motion/force transmissibility in the workspace V and is represented locally by the minimum of the OTI and the CTI. k will be between 0 and 1. The best kinematics performance corresponds to the value 1 which gives the best transmissibility.

7.3.2 Optimal Design

Based on the optimal design objective function in Eq. (7.34), the combined effect of the key parameters on the maximum singularity-free workspace and transmission performance has been calculated and the results are illustrated in Fig. 5-5 for the four phases. In general, a larger singularity-free workspace corresponds to a worse average transmission performance. In Fig. 7-5(a), a smaller platform size (λ_a) gives a larger singularity-free workspace (blue surface) for the 1T2R motion but the transmission performance decreases when increasing λ_a. In general, both workspace and transmissibility increase when getting longer limbs (λ_{lmin}). This can be understood based on the singularity loci in Fig. 7-4(a) which shows that the increase of the limb length (λ_{lmin}) will directly increase the singularity-free workspace along the p_z direction and there will be more space far from the singularities inside the vertical tetrahedron giving better transmissibility.

For the other three phases with 3R motion, it is similar that there is a larger workspace with a smaller platform size (λ_a) but either too large or too small minimum limb length (λ_{lmin}) will give small workspace and there is an optimal point to have the peak workspace volume on the green workspace surfaces as in Fig. 7-5(b)-(d). It can be also seen that there is an area with zero workspace volume and the area becomes larger when $\theta_1 = \theta_2 = \theta_3$ increases from π/6, to π/3, and to π/2. This is also reflected by the transmission performance represented by the blue

surfaces with zero-value areas. To compare those three cases, the three workspace surfaces are illustrated together in Fig. 7-5(e) and the transmission performance is in Fig. 7-5(f). The workspace surfaces intersect at one point around λ_{lmin}=1.2 and λ_a=0.2. In general, when λ_{lmin}<1.2, small rR joint angles give larger workspace volume as shown by the order π/6 (green surface), π/3 (blue), and π/2 (red). This is opposite for λ_{lmin}>1.2 and it means that a longer leg length is needed when increasing the rR joint angles to have a large workspace volume. Generally the transmission performance is close to each other for the three cases as in Fig. 7-5(f) and the average is very close to 0.9. In detailed comparison, larger rR joint angles can give better performance. They all decrease when λ_{lmin} increases or λ_a decreases which is opposite to the workspace results.

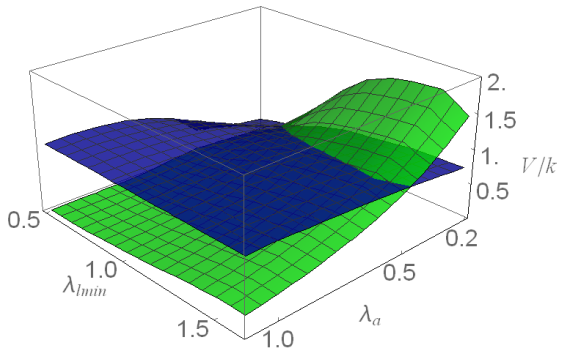

(a) θ_1= θ_2= θ_3=0 with 1T2R motion (green: workspace, blue: transmission)

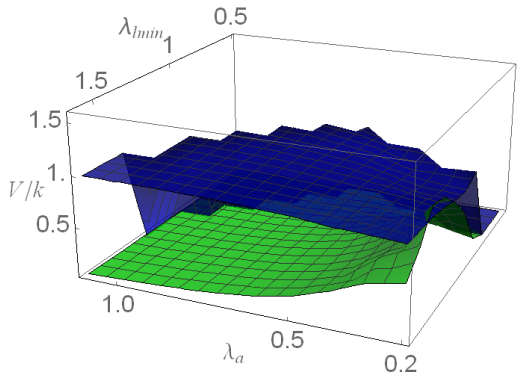

(b) θ_1= θ_2= θ_3= π/6 with 1T2R motion (green: workspace, blue: transmission)

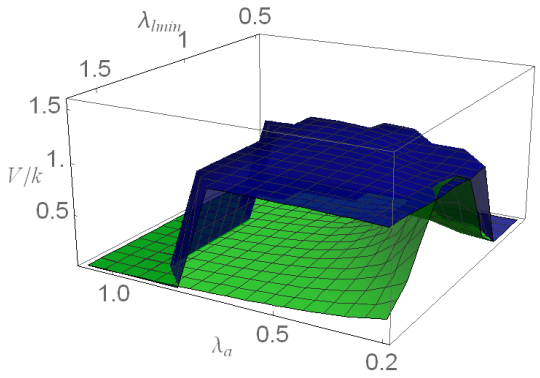

(c) θ_1= θ_2= θ_3= π/3 with 1T2R motion (green: workspace, blue: transmission)

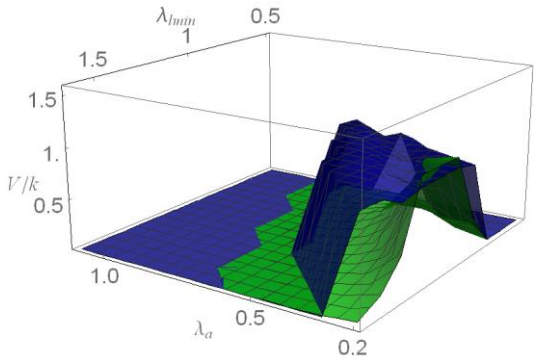

(d) $\theta_1 = \theta_2 = \theta_3 = \pi/2$ with 1T2R motion (green: workspace, blue: transmission)

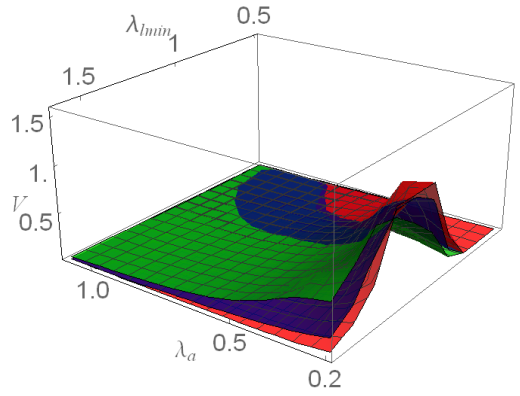

(e) Workspace comparison (green: π/6, blue: π/3, red: π/2)

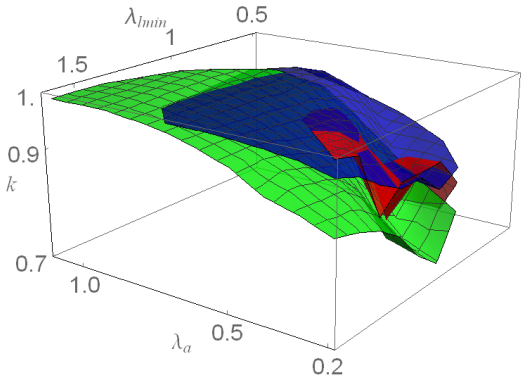

(f) Transmissibility comparison (green: π/6, blue: π/3, red: π/2)

Figure 7-5 Optimal Design Results

7.3.3 An Optimal Design Example

In specific applications, a larger singularity-free workspace has more priority. So based on the above analysis, a smaller platform size is preferred, for example λ_a=0.4. Then the minimum limb length should be selected properly to have the best workspace and transmission performance considering the 1T2R and 3R phases. This is shown in Fig. 7-6 in which singularity-free

workspace (solid curves) and transmission performance (dashed curves) of $\theta_1 = \theta_2 = \theta_3 = 0$ with 1T2R motion and $\theta_1 = \theta_2 = \theta_3 = \pi/6$, $\pi/3$, and $\pi/2$ with 3R motion are illustrated. It can be seen that the 1T2R phase has the largest workspace volume and worst transmissibility among the four cases while the three 3R phases have similar performance. Workspace volume of the 1T2R phase increases continuously to reach the peak point at $\lambda_{lmin}=1.5$ and starts to drop but its transmissibility increases when λ_{lmin} increases. However, when $\lambda_{lmin}<0.8$ the 3R phases have zero workspace and when $\lambda_{lmin}>1.5$ the workspace is very small. To cover all the four phases, the best minimum limb length is around $\lambda_{lmin}=1.3$. If only the 1T2R and one of the 3R phases are considered, for example $\theta_i = \pi/2$ (purple), $\lambda_{lmin}=1.25$ (vertical dashed black line) gives the best combination of the performance. A more accurate way is to give weight to the workspace volume and transmissibility and also to each phase to calculate the final performance in a quantitative way as in the following section.

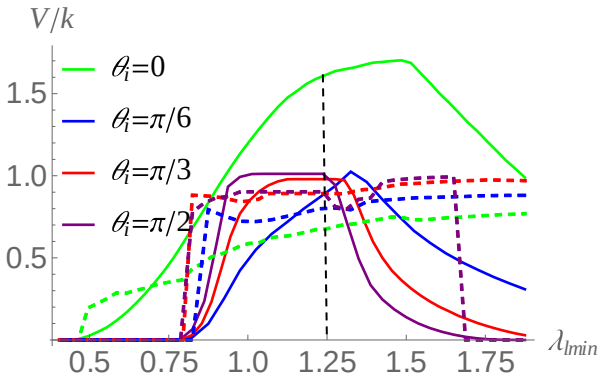

(a) the optimal design

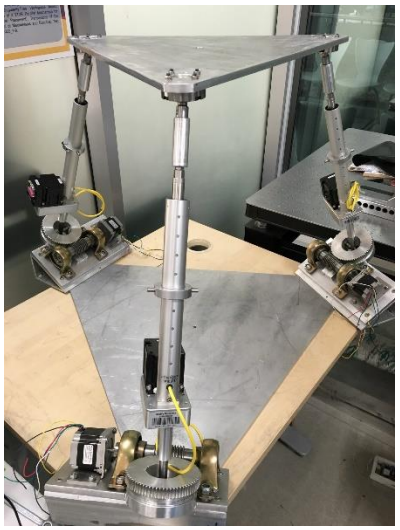

(b) the built prototype with $\lambda_{lmin}=1.25$

Figure 7-6 An example with $\lambda_a=0.4$ (solid for workspace, dashed for transmission, green: 0, blue: π/6, red: π/3, purple: π/2)

7.4 Unified Optimal Design of the 3-rRPS Based on Jacobian Condition Number

Motion/force transimissiblity gives a systematic way to optimally design the 3-rRPS as shown above. In this section, the commonly used Jacobian condition number will be applied as a bench mark or comparison solution. A weighted method is also proposed to consider the importance of each phase and also the detailed performance in each phase.

7.4.1 Design Variables and Performance indices

Design variables are the same with that in Section 7.2.1. In addition to the maximum singularity-free workspace, the kinematics performance is represented by the condition number $k_i=\sigma_{max}/\sigma_{min}$, ($\sigma_{max}$ and σ_{min} are the maximum and minimum singular values of the Jacobian matrix) is a widely used parameter in parallel mechanism design and optimization [178]. For the 3R topology, the Jacobian matrix has unified unit of rotation angles. However, the 1T2R topology has coupled translation and rotation due to which the Jacobian matrix has mixed units which causes inconsistent condition numbers in representing kinematics performance. In the following, the condition number is calculated using the dimensional homogeneous Jacobian matrix [179] which is derived as below.

Since the 1T2R topology has one translation and two rotation motions, the actuation Jacobian involves both linear and angular velocity mappings. Thus, its singular values are not in the same unit and its condition number cannot be used directly for kinematics performance evaluation. Following this, the approach of mapping the platform velocity to linear velocities in some directions at selected points on the platform representing the platform mobility [179] is used. This mapping provides a uniform unit between the linear platform point velocities and linear actuation limb inputs. To present the motion of the platform, linear velocities along $\boldsymbol{n}=(0,0,1)^T$ at the three spherical joint centers A_1, A_2 and A_3 are selected. Then these linear velocities can be expressed by the platform velocity in the platform coordinate frame as:

$$\boldsymbol{v}_p = \begin{bmatrix} v_1 & v_2 & v_3 \end{bmatrix}^T = \mathbf{J}_p \mathbf{M}^T \boldsymbol{S}_G \tag{7.35}$$

where v_i is the linear velocity along $\boldsymbol{n}$ at the selected point, $\mathbf{J}_p = \begin{bmatrix} \boldsymbol{S}_{n1} & \boldsymbol{S}_{n2} & \boldsymbol{S}_{n3} \end{bmatrix}^T$, $\mathbf{M} = \begin{bmatrix} \mathbf{R} & \mathbf{0} \\ \mathbf{0} & \mathbf{R} \end{bmatrix}$, $\boldsymbol{S}_{ni} = \begin{bmatrix} \boldsymbol{n} & \boldsymbol{a}_i' \times \boldsymbol{n} \end{bmatrix}^T, (i = 1,2,3)$, $\boldsymbol{a}_i'$ is the vector of point A_i at which linear velocities are selected.

From the overall Jacobian maxtrix in Eq. (6.63), there is

$$\mathbf{J}\,\boldsymbol{S}_G = \begin{bmatrix} \mathbf{J}_a \\ \mathbf{J}_c \end{bmatrix} \boldsymbol{S}_G = \begin{bmatrix} 0 \\ 0 \\ 0 \\ \dot{l}_1 \\ \dot{l}_2 \\ \dot{l}_3 \end{bmatrix} = \begin{bmatrix} \mathbf{0} \\ \dot{\boldsymbol{l}}_a \end{bmatrix} \tag{7.36}$$

Then

$$\boldsymbol{S}_G = (\mathbf{J}^T\,\mathbf{J})^{-1}\,\mathbf{J}_a^T\,\dot{\boldsymbol{l}}_a \tag{7.37}$$

Combining Eqs. (7.35) and (7.37), the selected linear velocities can be obtained directly from the linear actuation input velocities:

$$\boldsymbol{v}_p = \mathbf{J}_p\,\mathbf{M}^T(\mathbf{J}^T\,\mathbf{J})^{-1}\,\mathbf{J}_a^T\,\dot{\boldsymbol{l}}_a = \mathbf{J}_D^{-1}\,\dot{\boldsymbol{l}}_a \tag{7.38}$$

where $\mathbf{J}_D = (\mathbf{J}_p\,\mathbf{M}^T(\mathbf{J}^T\,\mathbf{J})^{-1}\,\mathbf{J}_a^T)^{-1}$ is the 3×3 dimensional homogeneous Jacobian matrix with unified unit.

For the 3R topology, the unit of the Jacobian matrix is unified so it can be directly obtained from the overall Jacobian matrix in Eq. (6.63) as:

$$\mathbf{J}_{a3R} = \begin{bmatrix} \boldsymbol{b}_1 \times \boldsymbol{s}_1 & \boldsymbol{s}_1 \\ \boldsymbol{b}_2 \times \boldsymbol{s}_2 & \boldsymbol{s}_2 \\ \boldsymbol{b}_3 \times \boldsymbol{s}_3 & \boldsymbol{s}_3 \end{bmatrix} \tag{7.39}$$

The condition numbers of $\mathbf{J}_D$ and $\mathbf{J}_{a3R}$ are used in the optimal design.

The optimal design of the 3-rR*PS* MPM in this section is to find the best parameter set to have maximum singularity-free workspace with good kinematics performance covering the two topologies of 1T2R motion ($\theta_1 = \theta_2 = \theta_3 = 0$) and 3R motion ($\theta_1 = \theta_2 = \theta_3 = \pi/2$). Thus, the optimal design cost function can be given as:

$$\begin{cases}\text{maximize} & V \\ \text{maximize} & k\end{cases}, \qquad k = \frac{V}{\int_V k_i dV} \tag{7.40}$$

Subject to: $-\pi/3 \leqslant \psi_i \leqslant \pi/3$,

$0.3 \leqslant \lambda_a \leqslant 1$,

$0.5 \leqslant \lambda_{lmin} \leqslant 1.6$,

$40° \leqslant \phi \leqslant 80°$,

limb distance $\leqslant 0.01$,

where V is the maximum singularity-free workspace volume, k is the inverse average condition number in the workspace V and is between 0 and 1. The best kinematics performance corresponds to the value 1 when the velocity mapping is isotropic.

7.4.2 Optimal Design

Based on the optimal design function in Eq. (7.40), the combined effect of the key parameters on the maximum singularity-free workspace and kinematics performance has been calculated and the results are illustrated in Fig. 7-7 for both 3R and 1T2R topologies. In general, a larger singularity-free workspace corresponds to a worse average kinematics performance. A smaller platform size (λ_a) gives a larger singularity-free workspace for both topologies as shown in Fig. 7-7(a) and (c) in which the blue one (λ_a=0.3) shows the best and the red one (λ_a=1) is the worst. This is directly opposite to the kinematics performance as in Fig. 7-7(b) and (d) in which the red ones provide higher numbers while the blue ones are at the bottom.

For the 3R topology, an approximate ratio λ_{lmin}/ϕ = 1 between the minimum leg length and rR joint base location angle ϕ will give a large workspace for a given platform size as shown by the bump parts of each colour in Fig. 7-7(a). The maximum singularity-free workspace increases when λ_{lmin} and ϕ increase at the same time. The largest workspace is represented by the point on the blue surface (λ_a=0.3) with λ_{lmin} = 1.6, ϕ = 64°. For each platform size, it can be also found that when the limb length is not enough, the workspace is zero. This happens for a small ϕ with a large λ_{lmin} or a big ϕ with a small λ_{lmin}. As mentioned above, the kinematics performance has an opposite trend with workspace as in Fig. 7-7(b). For a fixed platform size, the average

condition number increases when both λ_{lmin} and ϕ decrease at the same time. The best kinematics performance is represented by the peak point on the yellow surface (λ_a=0.8) with λ_{lmin} = 0.8, ϕ = 60°.

For the 1T2R topology, surfaces of both workspace and kinematics performance are smoother than the 3R case as in Fig. 7-7(c) and (d). The trend is also clear that when the minimum leg length λ_{lmin} increases, the maximum singularity-free workspace increases while the average condition number decreases. A smaller rR joint base location angle ϕ is preferable considering the kinematics performance while a specific value (around ϕ = 70°) provides the largest singularity-free workspace for a fixed platform size (λ_a).

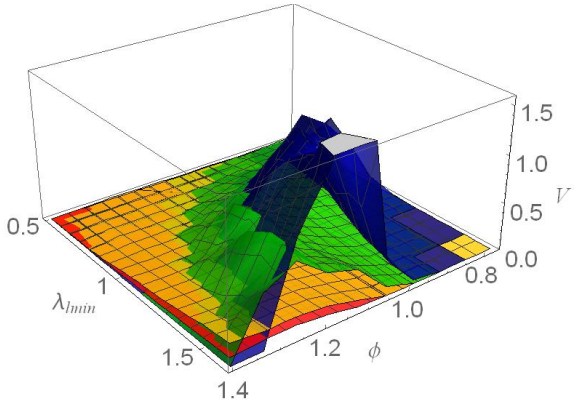

(a) 3R workspace

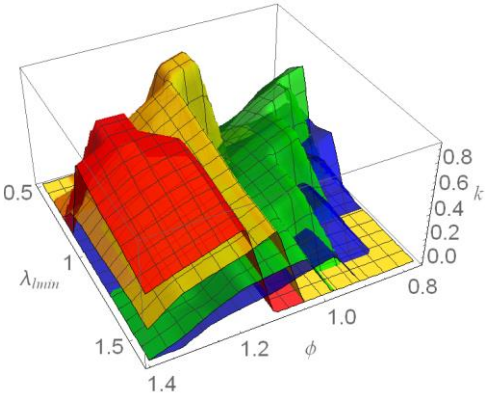

(b) 3R kinematics performance

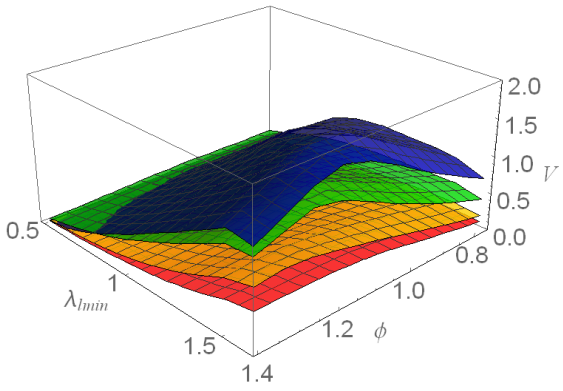

(c) 1T2R workspace

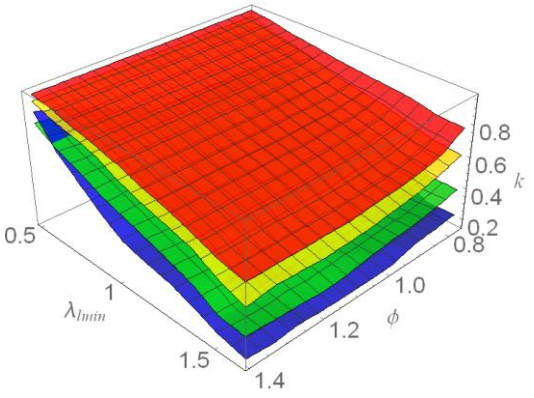

(d) 1T2R kinematics performance

Figure 7-7 Optimal design of the 3-rR*PS* MPM (blue for λ_a=0.3, green for λ_a=0.5, yellow for λ_a=0.8, red for λ_a=1)

To conclude above optimal design results, a larger angle ϕ close to 70°, a bigger minimum limb length l_{min}, a smaller platform size r_a will provide the best set of parameters to have a maximum singularity-free workspace for both 3R and 1T2R motion of the 3-rR*PS* MPM. However, the kinematics performance represented by the average condition number of the Jacobian matrix has an opposite trend. A smaller ϕ, smaller minimum limb length l_{min}, and a bigger platform size r_a will provide better average kinematics performance. A trade-off needs to be made between the two performance objectives and also between the two topologies which share the same mechanical parameters. A combined criterion can be given as

$$\text{maximize} \quad C = w_1(w_{11}V_{3R} + w_{12}k_{3R}) + w_2(w_{21}V_{1T2R} + w_{22}k_{1T2R}) \tag{7.41}$$

where w_1 and w_2 are the weights of the 3R topology and the 1T2R topology in the objective function with $w_1 + w_2 = 1$, $0 \leqslant w_1, w_2 \leqslant 1$, w_{i1} and w_{i2} (i=1 for 3R, i=2 for 1T2R) are the weights for maximum singularity-free workspace and kinematics performance of each topology with $w_{i1} + w_{i2} = 1$, $0 \leqslant w_{i1}, w_{i2} \leqslant 1$. V_{3R} and V_{1T2R} are normalized workspace and $0 \leqslant V_{3R}, V_{1T2R} \leqslant 1$. As mentioned above, the inverse averaged condition numbers k_{3R} and k_{1T2R} follow $0 \leqslant k_{3R}, k_{1T2R} \leqslant 1$.

An example can be given as w_1=0.4, w_2 =0.6, w_{11}=0.5, w_{12} =0.5, w_{21}=0.7, w_{22} =0.3, which means the performance of the 3R topology weighs forty percent and the 1T2R topology contributes sixty percent to the overall objective. For the 3R topology, workspace and kinematics performance have equal weight while workspace shows more important with seventy percent in the 1T2R topology optimization. Based on those, the best performance is found at C=0.637, with λ_a=0.3, λ_{lmin} = 1.6, and ϕ = 64°, which is on the blue surface in Fig. 7-7. This shows that the workspace dominates the result. If changing weights of the workspace to be w_{11}=0.3, w_{12} =0.7, w_{21}=0.5, w_{22} =0.5, the result will be C=0.534, with λ_a=0.8, λ_{lmin} = 0.6, and ϕ = 60°, which corresponds to a point on the yellow surface in Fig. 7-7. Thus, priorities represented by the function weights can be given to the topologies and their workspace or kinematics performance in the optimization. Then Eq. (7.41) will give the optimal result with the best combined performance.

7.5 Prototype Design and Challenges

Based on the above concept design, kinematics and optimal design analysis, prototypes of two selected metamorphic parallel mechanisms were built. The original goal was not targeting any application but for proof of concept of this kind reconfigurable parallel mechanisms. Some important lessons have been learned based on the prototyping process and one of the main issue is to meet the critical geometric constraints to achieve the desired mobility. The poor quality of the fabricated components and purchased actuators made the first prototype of the 3-rTPrT metamorphic parallel mechanism completely failed to realize neither the pure rotation motion or the pure translation motion. But the worm gear based design of the rT joint is believed a good solution for this concept. Following that, the rR joint was also designed based on the same worm gear solution and the 3-rRPS prototype showed improved quality with a better linear actuator. One of the reasons to select the 3-rRPS for the prototype is that its pure rotation phase does not need very critical geometric constraints, for example, all axes intersecting at one point, although the 2R1T motion phase has the one plane constraint which can be possibly realized in the design. Detailed work is presented in the following.

7.5.1 Prototyp Design of the 3-rTPrT

The main reason to select the 3-rTPrT metamorphic parallel mechanism is its reconfiguration to pure translation or pure rotation mobility, which is very novel comparing with traditional parallel mechanisms since those are two complete different motion types. This reconfiguration comes from the key component, the rT joint. There can be different solutions to realize the rT joint concept, like gear chains, belt system, and others. But considering the requirement to have the radial axis tuned and fixed on the selected position in the groove, the worm gear solution is selected since it can lock the worm ring by itself as in Fig. 7-8. The radial axis bar is attached with the worm wheel which can be rotated with respect to the housing ring by the worm, which realizes the alteration of the rT joint reconfiguration and the radial axis can be fixed by the self-locking of the worm gear system. The bracket axis bar is connected to the U-shape bracket which will be connected to the limbs. A small motor attached to the worm shaft can automatically tune the radial axis to the desired direction which will also make the parallel mechanism reconfiguration automatic.

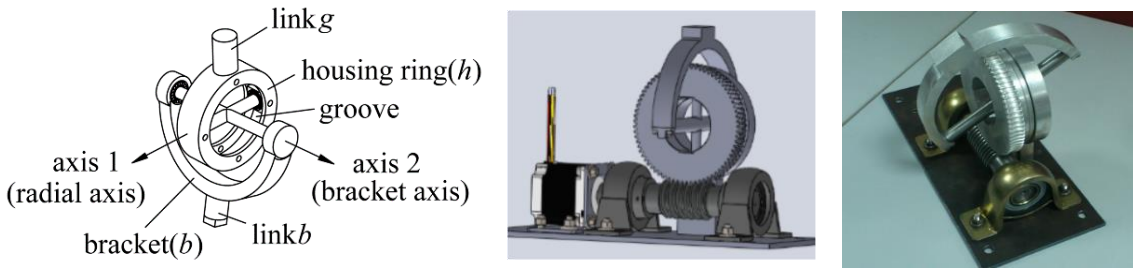

(a) the rT joint concept (b) CAD model (c) prototype

Figure 7-8 Prototye design of the rT joint

Six of those rT joints were built with aluminium structure and steel shafts while each weighs 1.9kg. The design could be smaller and lighter but it's limited by the capability of the available workshop. Three linear actuators (FA-PO-150-12-xx, 12VDC, stroke 12", load 150lbs) were purchased to be the prismatic joints in the three limbs of the 3-rTPrT prototype as in Fig. 7-9 while the platform and base were made from aluminium plate in the triangular shap. Six NEMA23 step motors (3V, 2A/phase, 90Ncm output torque, 1.8 deg step angle) were installed for the six worm shafts of the rT joints assembled on the platform and base.

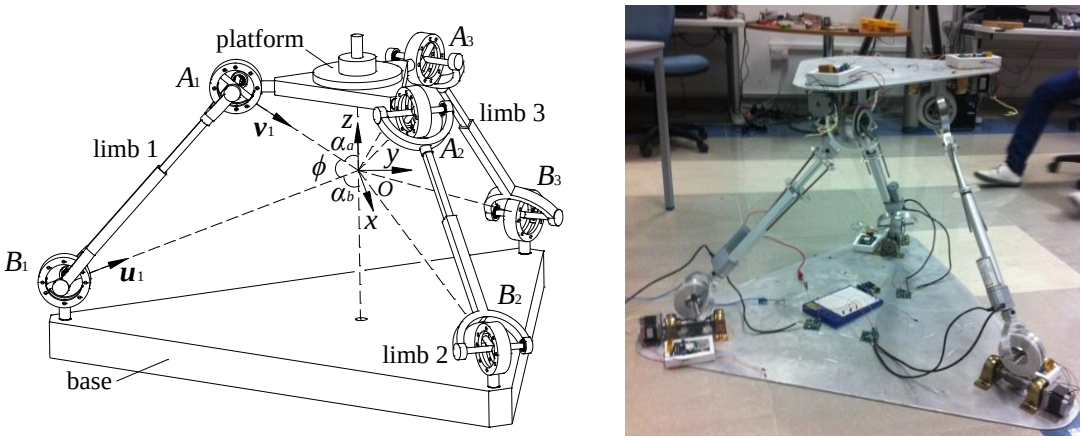

Figure 7-9 Prototype of the 3-rTPrT

The system was assembled as in Fig. 7-9 but the designed configuration was not achieved due to a few reasons. The first one is the selected linear actuator could not support the torque load along its shaft which gave an extra rotation degree of freedom along the limb that theoretically made the platform to be a 6-DOF system. The second issue is the connection between the linear actuator and the rT joint which could not constrain the extra motion from the heavy load of the platform. All those actually are also related to the heavy worm-gear rT joints and the heavy platform. The intersecting or parallel goemtric relation between the rT joint axes was found also a challenge requirement in the realization due to the rough accuracy of all the components and

assembly. At the end, the prototy did not allow the rT joint axis alinement for the pure rotation or pure translation phases but it could not be improved at that time due to limited resources.

7.5.2 Prototyp Design of the 3-rRPS

All the above lessons had been learned and applied when coming to the 3-rRPS prototyping. The reason it was selected came from that the spherical joints on the platform could be light and small, the rotation along the limb or linear actuator will not affect the platform motion, and the axes alinement requirement is more realizable since the three rR joints are all on the base.

Reconfiguration of the 3-rR*PS* metamorphic parallel mechanism comes from reconfiguration of its rR joint. Thus the rR joint tuning is a key step in the configuration change between the 3R and 2R1T motion. Following the rT joint solution, the worm gear system is also used for the rR joint tuning as in Fig. 7-10 in which the rotation bar is attached with the worm wheel which can be rotated with respect to the base ring by the worm which realizes the alteration of the rR joint axis ***u*** and the axis can be fixed by the self-locking of the worm gear system. Similar to the rT joint, a small motor can be attached to the worm in each rR joint to tune the rR joint axis automatically.

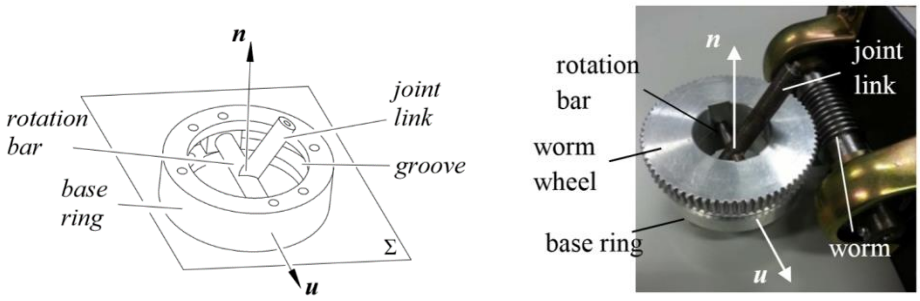

Figure 7-10 Prototype of the rR joint

The 3-rR*PS* prototype in Fig. 7-11 was built by fixing three rR joints on the base and three spherical joints (Hephaist SRJ-012C, 72kg payload, 0.18kg weight, 40deg swing angle) on the platform connected by three linear actuators (Ultramotion, series B3 type linear actuator, 8 inch stroke, 100kg payload, with SM23165D smart motor, acme nut/lead screw- 0.083" self-locking pitch).

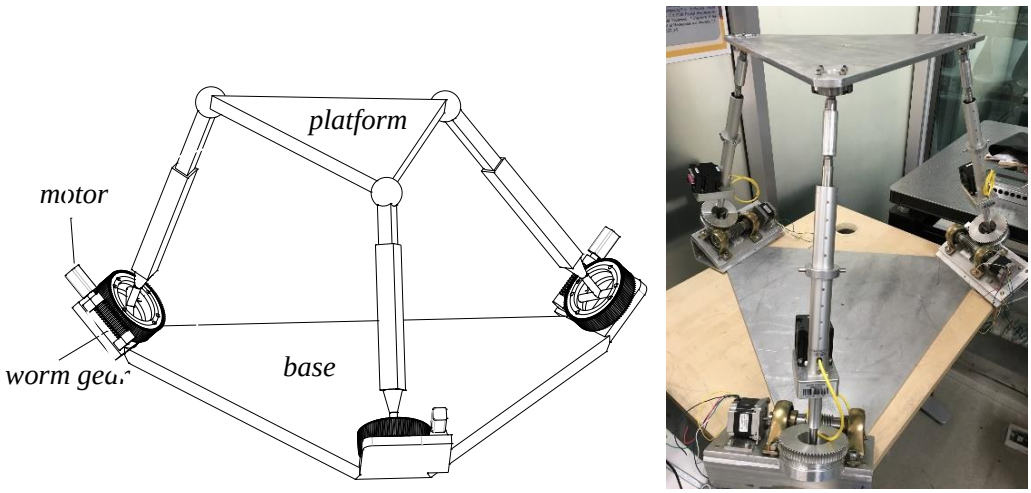

Figure 7-11 Prototype of the 3-rRPS metamorphic parallel mechanism

The system shows good quality comparing with the previous 3-rTPrT prototype but still has some obvious errors due to the joint clearance. This existence of manufacturing errors and joint clearances will allow for infinitesimal rotations or movements of mechanism limbs, leading to extra degrees of freedom of the moving platform [180]. Thus, kinematic sensitivity [181] of parallel mechanisms with respect to different errors has become an important issue for mechanism design and analysis. The limb can have different angles with the base plane, which can be described by adding virtual revolute joints [182] between the limb and base. In this work, a preliminary study has been conducted on inspecting the joint clearance and measuring the platform output free motion after locking all the actuators. The main clearance from the fabricated worm-gear rT joint is the 2mm free motion between the worm and the support surface as shown in Fig. 7-12. This is similar for all the three rT joints of the 3-rRPS prototype. By attaching three markers to the platform in the Optitrack system which has accuracy around 0.1mm and by locking all the inputs, the linear actuators along the limbs, the platform free motion can be measured as the setup in Fig. 7-12.

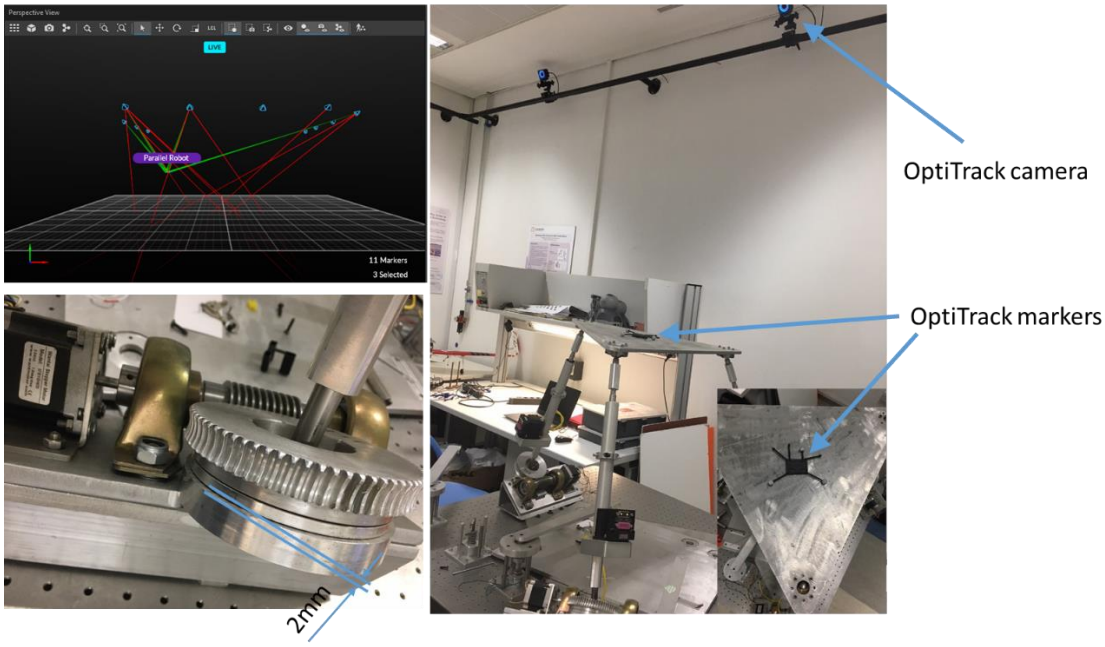

Figure 7-12 Joint clearance and motion tracking setup

The experiment was done by starting the system recording and moving the platform manually for possible free motion with about 20 seconds. Based on the marker positon data analysis, the platform free motion can be described by the position and rotation errors as in Fig. 7-13. It can be seen that the platform has very small position error within 1mm along the Z-axis but big X-axis error upto 15mm. The maximum position error along the Y-axis is about 7mm. Associated with the free translation, there is also free rotation represented by the XYZ Euler angle errors as in Fig. 7-13(b). The free rotation error is a combination of mainly the X and Z Euler angles with both upto 15deg. Thus, the clearance of the prototype rT joints bring a big platform motion error which should be further investigated, reduced and compensated by modifying the rT joints and improving the assembly. The control of the platform will be a future focus to explore the control requirements fo metamorphic parallel mechanisms with multi-phases sbased on the kinematics and dynamics modelling, and more calibration work.

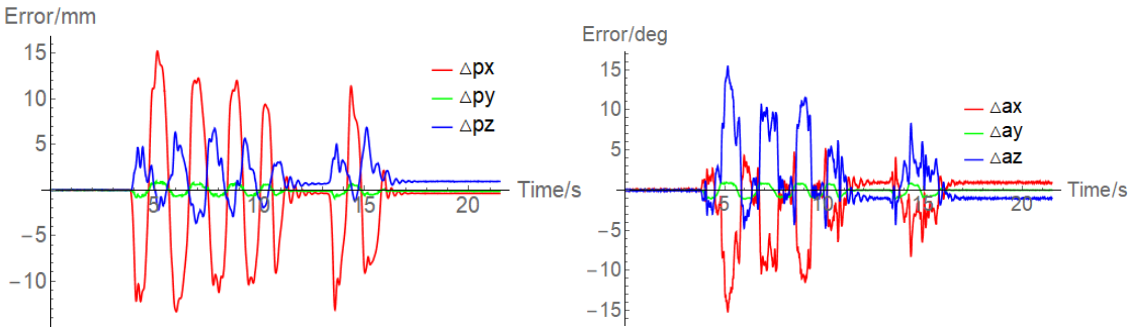

(a) platform position error (b) platform Euler angle error

Figure 7-13 Platform motion error after locking all the three actuators

Another design solution to the 3-rRPS is proposed as in Fig. 7-14 and the rR joint reconfiguration relies on a bevel gear system. Similar to the worm gear solution, the rotation bar of the rR joint is attached to a bevel gear which can be altered by another bevel gear. In the 3-rRPS MPM, a main bevel gear on the base is used as the input with a motor input and it controls the bevel gear of the rR joint in each limb through an intermediate bevel gear as in Fig. 7-14.

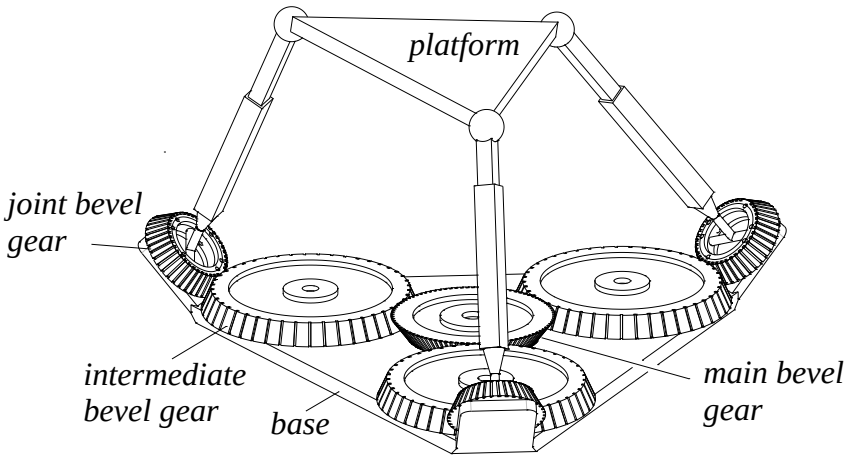

Figure 7-14 Bevel gear based synchronized rR joint solution

It can be seen that the worm gear solution gives flexibility of controlling each rR joint independently while the bevel gear solution tunes all three limbs in a synchronized way. The former needs three small motors and the latter needs only one motor input. The bevel system will provide symmetrical rR joint axes in the 3-rR*PS* MPM when the initial configuration are symmetrical. This might be preferred as generally symmetrical workspace and kinematics performance are used in applications. The worm gear system can be selected if non-symmetrical configurations are needed.

7.6 Conclusions

This chapter contributed to the unified optimal design process for metamorphic parallel mechanisms by covering all their configuration phases with variable mobility. The key challenge solved was to find a way to represent the kinematics performance of all the MPM phases each of which is equivalent to a traditional parallel mechanism. Motion/force transimissibility was

found to be a good way by calculating the input and output efficiency between force and motion and avoiding the mixed unit issue in inhomogeneity Jacobean matrix. By setting up the objective function including maximize the singularity-free workspace and the kinematics performance, the optimal design of the 3-rRPS MPM was conducted by covering the 2R1T phase and three 3R phases with different performance. The proposed method could effectively show the trend of the performance with resepct to the design parameter change and the tradeoff between the workspace and the kinematics performance could result in the optimal parameter design. While this was the main contribution and objective of this chapter, the other investigation was actually to explore the performance relation among the phases since they share the same design parameters. A weighted method was applied to set up weights between different phases and also the workspace and the kinematics performance objectives. This is not an ideal optimal design way since the mixed parameter units do not provide clear physical meaning of the obtained optimal results. But it's a good demonstration of the relation between the phases and that they are strongly coupled based on the same mechanism structure parameters.

Based on the optimal design, prototypes were also targeted to show the reconfiguration functions and performance of metamorphic parallel mechanisms. A big lesson was learnt that very high accuracy was required in manufacturing to satisfying the critical geometric constraints in the 3-rTPrT MPM and the prototype was not successfully made functional. Following that, the 3-rRPS showed a good design with less critical geometric constraints and good reconfigurable phases. The built prototype still had joint errors with 2mm and caused the platform a free motion of translation upto 15mm for one direction and rotation upto 15deg Euler angles. Lots of future work will be conducted to reduce the joint clearance and the effect to the platform motion.

Chapter 8 Unified Inverse Dynamic Modelling of MPMs Covering All Phases

8.1 Overview of the Strategy and Method

Similar to the unified kinematics modelling, the strategy of unifying the dynamics is also to model the MPMs through their limbs considering their fixed limb structures and input methods while the platforms have different output motion resulted from the reconfigurable joint tuning.

Before going to the detailed dynamic models, it has to be clarified that the following models are based on the assumption that all parameters are ideal and known, which can be different from the real designed prototypes as in chapter 7. A more detailed applicability review of those dynamic models in this chapter will be discussed in section 8.4.

8.2 Unified Dynamic Modelling of the 3-rTPrT [183]

8.2.1 Two Phases and Coordinates of the 3-rTPrT

The 3-rT*P*rT MPM has been introduced in Section 5.3 and it has three different phases with different mobility including pure rotation phase, pure translation phase and 3T1R phase. In this section, the dynamic model covering the pure rotation and pure translation phases will be presented. The unified kinematics analysis has been explained in Section 6.2 and the parameters will be continually used. The coordinates of the two phases are reviewed in Fig. 8-1 and Fig. 8-2.

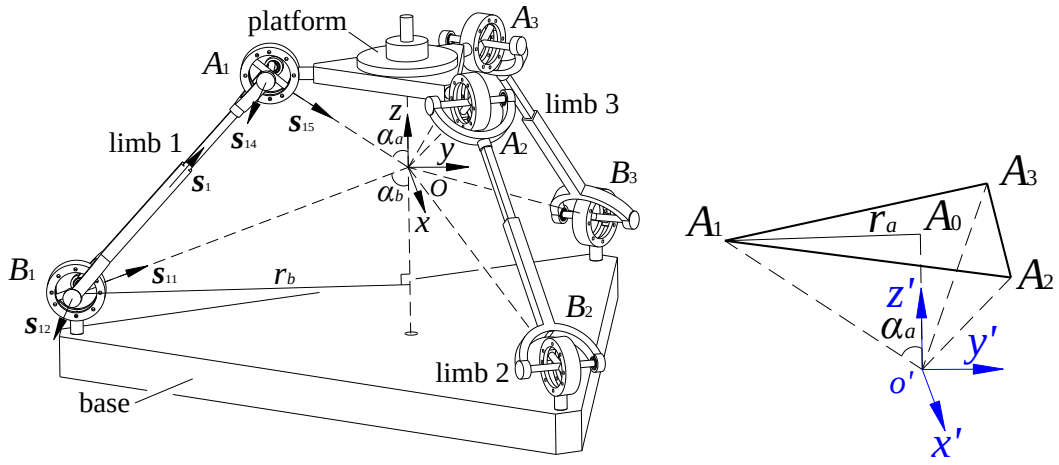

(a) The pure rotation phase (b) The platform coordinate frame

Figure 8-1 The pure rotation phase of the 3-rT*P*rT and its coordinate frames

In both phases, the setting of the coordinate frames follows the same but the center of the platform coordinate frame *o′* is able to move away from point *o* in the translation motion. This coordinate frame setting can keep the geometric parameters in a unified format as shown below for the unified kinematics and dynamics modelling.

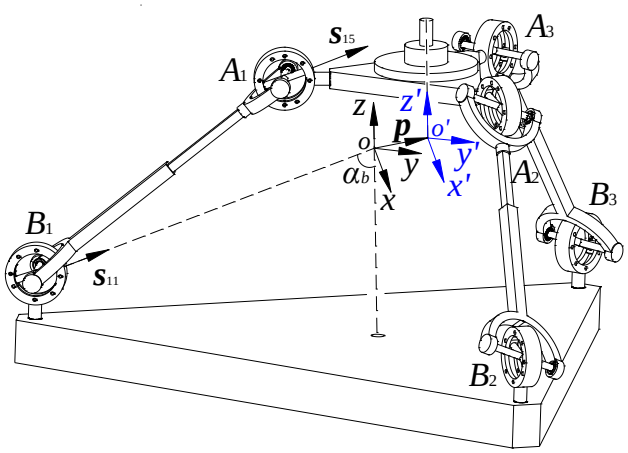

Figure 8-2 The pure translation phase of the 3-rT*P*rT

In the following, a unified dynamics model will be set up to cover both pure rotation and pure translation phases of the 3-rT*P*rT metamorphic parallel mechanism. The general procedure is to start from the pure rotation phase and then cover the pure translation phase by tuning corresponding parameters and geometric constraints.

As in Eq. (6.4), the closed-loop equation of each limb can be expressed in the global coordinate frame as

$$\boldsymbol{a}_i = \boldsymbol{b}_i + d_i \boldsymbol{s}_i = \boldsymbol{p} + \mathbf{R}.\boldsymbol{a}'_i \quad (i = 1, 2, 3) \tag{8.1}$$

For the pure rotation phase, there is no translation and $\boldsymbol{p}$ will be eliminated in Eq. (8.1). When **R** is known, the inverse kinematics is to get the input d_i which can be obtained directly from Eq. (8.1). For the pure translation phase, rotation matrix **R** will be the identity matrix. The inverse kinematics can be easily solved from Eq. (8.1) when giving the platform position $\boldsymbol{p}$. The detailed inverse and forward kinematics are shown in Section 6.2.

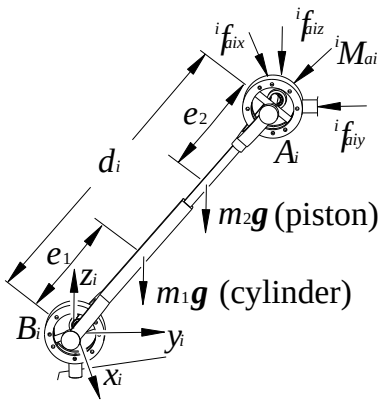

Figure 8-3 Limb coordinate frame and parameters

To simplify dynamics analysis by forming Newton equations in local coordinate systems of the limbs, a limb coordinate frame $B_ix_iy_iz_i$ is attached to the center B_i of the base rT joint in limb $i$as shown in Fig. 8-3. The rotation transformation from $B_ix_iy_iz_i$ to the base coordinate frame can be described by a rotation matrix $\mathbf{R}_i$. As in Fig. 8-3, each limb consists of a cylinder and a piston. e_1 is the distance between base rT joint center B_i and the center of mass of the ith limb cylinder and e_2 is the distance between platform rT joint center A_i and the center of mass of the ith limb piston. Then the position vectors of the centers of mass of the ith cylinder and piston can be given as

$$\begin{cases} r_{1i} = \boldsymbol{b}_i + e_1 \boldsymbol{s}_i \\ r_{2i} = \boldsymbol{b}_i + (d_i - e_2)\boldsymbol{s}_i \end{cases} \tag{8.2}$$

8.2.2 Velocity and Acceleration Analysis

The velocities and accelerations of the limbs can be calculated inversely from the velocity of the platform. By taking the derivative of Eq. (8.1), the velocity of the platform rT joint center A_i can be obtained:

$$\boldsymbol{v}_{ai} = \boldsymbol{v}_p + \boldsymbol{\omega}_p \times \mathbf{R}.\boldsymbol{a}_i' \quad (i = 1,2,3) \tag{8.3}$$

which can be transformed into the limb coordinate frame in which the velocity of the platform rT joint center A_i can be described as:

$$^i\boldsymbol{v}_{ai} = \mathbf{R}_i^T \boldsymbol{v}_{ai} = d_i\, ^i\boldsymbol{\omega}_i \times {}^i\boldsymbol{s}_i + \dot{d}_i\, ^i\boldsymbol{s}_i \quad (i = 1,2,3) \tag{8.4}$$

where the lead superscript *i* indicates the vector is expressed in the *i*th limb coordinate frame, ${}^{i}\boldsymbol{\omega}_i$ is the *i*th limb angular velocity and $\dot{d}_i$ is its linear velocity along the limb, ${}^{i}\boldsymbol{s}_i$ is the unit vector of the limb in its own coordinate frame.

By Dot-multiplying and Cross-multiplying both sides of Eq. (8.4) by ${}^{i}\boldsymbol{s}_i$ respectively, the linear and angular velocities of the limb can be obtained:

$$\begin{cases} \dot{d}_i = {}^{i}\boldsymbol{v}_{ai} \cdot {}^{i}\boldsymbol{s}_i \\ {}^{i}\boldsymbol{\omega}_i = ({}^{i}\boldsymbol{s}_i \times {}^{i}\boldsymbol{v}_{ai}) / d_i \end{cases} \tag{8.5}$$

Then, the velocities of the centers of mass of the cylinder and piston, ${}^{i}\boldsymbol{v}_{1i}$ and ${}^{i}\boldsymbol{v}_{2i}$, can be calculated by differentiating Eq. (8.2) and using Eqs. (8.4)-(8.5) as:

$$\begin{cases} {}^{i}\boldsymbol{v}_{1i} = e_1 {}^{i}\boldsymbol{\omega}_i \times {}^{i}\boldsymbol{s}_i \\ {}^{i}\boldsymbol{v}_{2i} = (d_i - e_2) {}^{i}\boldsymbol{\omega}_i \times {}^{i}\boldsymbol{s}_i + \dot{d}_i {}^{i}\boldsymbol{s}_i \end{cases} \tag{8.6}$$

By further differentiating Eq. (8.3) and Eq. (8.4), the acceleration of the platform rT joint center A_i can be expressed in the base frame and the limb frame as:

$$\begin{cases} \dot{\boldsymbol{v}}_{ai} = \dot{\boldsymbol{v}}_p + \dot{\boldsymbol{\omega}}_p \times \mathbf{R} \cdot \boldsymbol{a}_i' + \boldsymbol{\omega}_p \times (\boldsymbol{\omega}_p \times \mathbf{R} \cdot \boldsymbol{a}_i') \\ {}^{i}\dot{\boldsymbol{v}}_{ai} = \mathbf{R}_i^T \cdot \dot{\boldsymbol{v}}_{ai} = 2\dot{d}_i {}^{i}\boldsymbol{\omega}_i \times {}^{i}\boldsymbol{s}_i + d_i {}^{i}\dot{\boldsymbol{\omega}}_i \times {}^{i}\boldsymbol{s}_i + \\ \qquad\qquad d_i {}^{i}\boldsymbol{\omega}_i \times ({}^{i}\boldsymbol{\omega}_i \times {}^{i}\boldsymbol{s}_i) + \ddot{d}_i {}^{i}\boldsymbol{s}_i \end{cases} \tag{8.7}$$

Similar to the velocity analysis for Eq. (8.5), by Dot-multiplying and Cross-multiplying both sides of Eq. (8.7) with ${}^{i}\boldsymbol{s}_i$ respectively, the linear and angular accelerations of the limb can be obtained:

$$\begin{cases} \ddot{d}_i = {}^{i}\dot{\boldsymbol{v}}_{ai} \cdot {}^{i}\boldsymbol{s}_i + d_i {}^{i}\boldsymbol{\omega}_i \cdot {}^{i}\boldsymbol{\omega}_i \\ {}^{i}\dot{\boldsymbol{\omega}}_i = ({}^{i}\boldsymbol{s}_i \times {}^{i}\dot{\boldsymbol{v}}_{ai} - 2\dot{d}_i {}^{i}\boldsymbol{\omega}_i) / d_i \end{cases} \tag{8.8}$$

Then, accelerations of centers of mass of the cylinder and piston, ${}^i\dot{\boldsymbol{v}}_{1i}$ and ${}^i\dot{\boldsymbol{v}}_{2i}$, can be obtained by the derivative of Eq. (8.6):

$$\begin{cases} {}^i\dot{\boldsymbol{v}}_{1i} = e_1\,{}^i\dot{\boldsymbol{\omega}}_i \times {}^i\boldsymbol{s}_i + e_1\,{}^i\boldsymbol{\omega}_i \times ({}^i\boldsymbol{\omega}_i \times {}^i\boldsymbol{s}_i) \\ {}^i\dot{\boldsymbol{v}}_{2i} = 2d_i\,{}^i\boldsymbol{\omega}_i \times {}^i\boldsymbol{s}_i + (d_i - e_2)\,{}^i\dot{\boldsymbol{\omega}}_i \times {}^i\boldsymbol{s}_i + \\ \qquad (d_i - e_2)\,{}^i\boldsymbol{\omega}_i \times ({}^i\boldsymbol{\omega}_i \times {}^i\boldsymbol{s}_i) + \ddot{d}_i\,{}^i\boldsymbol{s}_i \end{cases} \tag{8.9}$$

8.2.3 Inverse Dynamic Analysis of the 3-(rT)*P*(rT) metamorphic parallel mechanism

Based on the above velocity and acceleration analysis, the limb and platform dynamic equations can be set up. In the limb coordinate frame, Euler's equation of motion about the base rT joint center B_i can be written as:

$${}^i\boldsymbol{n}_i^B = \frac{d({}^i\boldsymbol{h}_i^B)}{dt} \tag{8.10}$$

where ${}^i\boldsymbol{n}_i^B$ is the resultant moment exerted on the ith limb about the center B_i and ${}^i\boldsymbol{h}_i^B$ is the combined angular momentum of the ith limb about the same point B_i, there are

$${}^i\boldsymbol{h}_i^B = m_1 e_1({}^i\boldsymbol{s}_i \times {}^i\boldsymbol{v}_{1i}) + m_2(d_i - e_2)({}^i\boldsymbol{s}_i \times {}^i\boldsymbol{v}_{2i}) + {}^i\mathbf{I}_{1i}\,{}^i\boldsymbol{\omega}_i + {}^i\mathbf{I}_{2i}\,{}^i\boldsymbol{\omega}_i \tag{8.11}$$

$${}^i\boldsymbol{n}_i^B = d_i\,{}^i\boldsymbol{s}_i \times (-{}^i\boldsymbol{f}_{ai}) + (m_1 e_1 + m_2(d_i - e_2))({}^i\boldsymbol{s}_i \times \mathbf{R}_i^T\,.\boldsymbol{g}) - {}^i\boldsymbol{M}_{ai} + {}^i\boldsymbol{M}_{bi} \tag{8.12}$$

where m_1 and m_2 are the masses of the cylinder and piston of the limbs, ${}^i\mathbf{I}_{1i}$ and ${}^i\mathbf{I}_{2i}$ are the inertias of the cylinder and piston expressed in the limb coordinate frame, $\boldsymbol{g}$=(0,0,-g)^T is the acceleration of gravity in the base coordinate system, ${}^i\boldsymbol{f}_{ai} = ({}^i f_{aix}, {}^i f_{aiy}, {}^i f_{aiz})^T$ is the joint force at the platform rT joint center A_i exerted on the platform by the limb i as shown in Fig.4, ${}^i\boldsymbol{M}_{ai} = M_{ai}\,{}^i\boldsymbol{n}_{ai}$ is the joint moment at the platform rT joint center A_i with magnitude M_{ai} and direction ${}^i\boldsymbol{n}_{ai}$ which is perpendicular to both the two rotation axes of the platform rT joint, this is similar for the base rT joint B_i with reaction moment ${}^i\boldsymbol{M}_{bi} = M_{bi}\,{}^i\boldsymbol{n}_{bi}$. It can be noted that for the

pure translation phase, ${}^{i}\boldsymbol{n}_{ai} = {}^{i}\boldsymbol{n}_{bi}$ as the platform rT joint and the base rT joint have parallel rotation axes.

Based on Newton's law of motion of the moving platform, the translation motion can be expressed in the base coordinate frame as:

$$\sum_{i=1}^{6} \mathbf{R}_i \,.\, {}^{i}\boldsymbol{f}_{ai} + m_p \boldsymbol{g} = m_p (\dot{\boldsymbol{v}}_p + \dot{\boldsymbol{\omega}}_p \times \boldsymbol{r}_c + \boldsymbol{\omega}_p \times (\boldsymbol{\omega}_p \times \boldsymbol{r}_c)) \tag{8.13}$$

where m_p is the mass of the platform.

The angular motion and moment of the platform have the following relation in the base coordinate frame:

$$\begin{aligned} \boldsymbol{n}_p &= \mathbf{I}_p \,\dot{\boldsymbol{\omega}}_p + \boldsymbol{\omega}_p \times (\mathbf{I}_p \,\boldsymbol{\omega}_p) + m_p \boldsymbol{r}_c \times (\dot{\boldsymbol{v}}_p + \dot{\boldsymbol{\omega}}_p \times \boldsymbol{r}_c + \boldsymbol{\omega}_p \times (\boldsymbol{\omega}_p \times \boldsymbol{r}_c)) \\ &= \sum_{i=1}^{6} (\boldsymbol{a}_i \times (\mathbf{R}_i \,.\, {}^{i}\boldsymbol{f}_{ai}) + \mathbf{R}_i \,.\, {}^{i}\boldsymbol{M}_{ai}) + m_p \boldsymbol{r}_c \times \boldsymbol{g} \end{aligned} \tag{8.14}$$

where **I***p*= **R**.**I***pc*.**R**$^{\mathrm{T}}$, **I***pc* is the inertia matrix of the platform expressed in its principal coordinate frame at the center of mass, $\boldsymbol{r}_c$ is the vector of the center of mass of the platform in the base coordinate frame.

In general, the inverse dynamics analysis is to solve the actuation forces by giving the platform motion including position, velocity and acceleration. This can be solved by combining the equations in Eqs. (8.11-8.14) which have fifteen equations with fifteen unknowns (${}^{i}f_{aix}$, ${}^{i}f_{aiy}$, ${}^{i}f_{aiz}$, M_{ai}, M_{bi}, i=1,2,3) resulting in a coupled 15×15 matrix for the final solution. Following this, the actuation force f_{acti} from the prismatic joint in limb i can be given as:

$$f_{acti} = {}^{i}f_{aiz} - m_2 g * \cos(\phi_i - \alpha_b) + m_2 \, {}^{i}\dot{\boldsymbol{v}}_{2i} \,.\, {}^{i}\boldsymbol{s}_i \tag{8.15}$$

where $\phi_i = \mathrm{Arccos}(\boldsymbol{s}_i \,.\, \boldsymbol{s}_{i1})$ is the angle between the limb and the line OB_i.

Reaction forces ${}^{i}\boldsymbol{f}_{bi}$ at the base rT joint center B_i can be further solved from the following:

$$ {}^{i}\boldsymbol{f}_{bi} = {}^{i}\boldsymbol{f}_{ai} - (m_1 + m_2)\mathbf{R}_i^T \boldsymbol{.g} + m_1 {}^{i}\dot{\boldsymbol{v}}_{1i} + m_2 {}^{i}\dot{\boldsymbol{v}}_{2i} \tag{8.16} $$

The above gives the unified dynamics model of the 3-rT*P*rT metamorphic parallel mechanism covering both pure rotation and pure translation phases. In the pure rotation phase, the platform linear velocity $\boldsymbol{v}_p$ and linear acceleration $\dot{\boldsymbol{v}}_p$ will be zero while the angular velocity $\boldsymbol{\omega}_p$ and angular acceleration $\dot{\boldsymbol{\omega}}_p$ are the input of the inverse dynamics. In the pure translation phase, the platform angular velocity $\boldsymbol{\omega}_p$ and angular acceleration $\dot{\boldsymbol{\omega}}_p$ are zero while the platform linear velocity $\boldsymbol{v}_p$ and linear acceleration $\dot{\boldsymbol{v}}_p$ are the input for the inverse dynamics analysis.

8.2.4 Joint Force Decomposition for Decoupled Inverse Dynamics Analysis

Section 3 gives the inverse dynamics solution by solving the 15×15 matrix. Actually, the inverse dynamics analysis can be simplified by decoupling the platform and limb equations by applying proper joint force decomposition. From Eq. (8.12), by Dot-multiplying both sides by ${}^{i}\boldsymbol{s}_i$ there is:

$$ {}^{i}\boldsymbol{s}_i \boldsymbol{.}\, {}^{i}\boldsymbol{n}_{bi} \boldsymbol{*} M_{bi} = {}^{i}\boldsymbol{s}_i \boldsymbol{.}\, {}^{i}\boldsymbol{n}_{ai} \boldsymbol{*} M_{ai} \tag{8.17} $$

which shows that the joint moments at the base and platform rT joints are dependent without evolving any joint forces. This gives the magnitude of the base rT joint moment by the platform rT joint moment. In the pure translation phase, $\boldsymbol{n}_{ai} = \boldsymbol{n}_{bi}$, indicating that $M_{bi}=M_{ai}$. Thus, the joint moment acted on the platform by the platform rT joint is directly from the moment at the base rT joint provided by the base to the limb in the pure translation mechanism phase.

By Dot-multiplying both sides of Eq. (8.12) by the unit vector ${}^{i}\boldsymbol{s}_{i2}$ along the bracket axis of the rT joint there will be:

$$ {}^{i}\boldsymbol{f}_{ai} \boldsymbol{.}\, {}^{i}\boldsymbol{s}_{i2} \times {}^{i}\boldsymbol{s}_i = {}^{i}\boldsymbol{s}_{i2} \boldsymbol{.} ((m_1 e_1 + m_2 (d_i - e_2))({}^{i}\boldsymbol{s}_i \times \mathbf{R}_i^T \boldsymbol{.g}) - {}^{i}\boldsymbol{n}_i^B) / d_i \tag{8.18} $$

which indicates that the projection of the joint force ${}^{i}\boldsymbol{f}_{ai}$ on the direction perpendicular to both ${}^{i}\boldsymbol{s}_{i2}$ and ${}^{i}\boldsymbol{s}_{i}$ is only related to the limb motion and thus can be directly calculated in the inverse dynamics analysis.

By taking ${}^{i}\boldsymbol{s}_{i6} = {}^{i}\boldsymbol{s}_{i} \times {}^{i}\boldsymbol{s}_{i2}$ and Dot-multiplying both sides of Eq. (8.12) by ${}^{i}\boldsymbol{s}_{i6}$, there is

$$\begin{aligned} {}^{i}\boldsymbol{f}_{ai}.{}^{i}\boldsymbol{s}_{i2} = {}^{i}\boldsymbol{s}_{i6}.((m_1 e_1 + m_2(d_i - e_2))({}^{i}\boldsymbol{s}_{i} \times \mathbf{R}_i^T.\boldsymbol{g}) - \\ \boldsymbol{M}_{ai} + \boldsymbol{M}_{bi} - {}^{i}\boldsymbol{n}_i^B)/d_i \end{aligned} \tag{8.19}$$

Thus, the projection of the joint force ${}^{i}\boldsymbol{f}_{ai}$ on the direction ${}^{i}\boldsymbol{s}_{i2}$ can be expressed by the joint moments and the limb motion.

Based on those, if the limb coordinate frame $B_i x_i y_i z_i$ is set with the z_i axis along the limb (${}^{i}\boldsymbol{s}_{i}$), x_i axis in line with the bracket axis (${}^{i}\boldsymbol{s}_{i2}$) of the rT joint and then y_i axis will be along the direction ${}^{i}\boldsymbol{s}_{i6} = {}^{i}\boldsymbol{s}_{i} \times {}^{i}\boldsymbol{s}_{i2}$. Following this, there is

$$\begin{cases} {}^{i}f_{aix} = \boldsymbol{f}_{ai}.{}^{i}\boldsymbol{s}_{i2} \\ {}^{i}f_{aiy} = -{}^{i}\boldsymbol{f}_{ai}.{}^{i}\boldsymbol{s}_{i2} \times {}^{i}\boldsymbol{s}_{i} \end{cases} \tag{8.20}$$

which can be solved directly by Eq. (8.18) and Eq. (8.19).

Thus, nigh unknowns (${}^{i}f_{aix}$, ${}^{i}f_{aiy}$, M_{bi}, i=1,2,3) can be expressed by other six unknowns from Eq. (8.17) through Eq. (8.20). Substituting these into the platform dynamics equations Eq. (8.13) and Eq. (8.14), six equations with six unknowns (${}^{i}f_{aiz}$, M_{ai}, i=1,2,3) will be obtained. Thus the inverse dynamics analysis is simplified with the limb and platform dynamics decoupled.

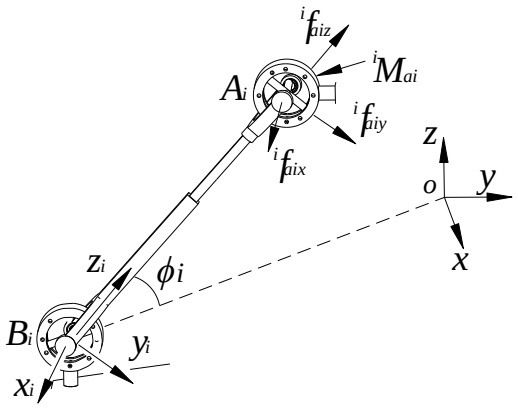

Figure 8-4 A limb coordinate frame to simplify the joint force decomposition

Following the above, the limb coordinate frame is shown in Fig. 6-4. In this case, the transformation from the local coordinate frame to the global coordinate frame can be expressed as:

$$\mathbf{R}_i = \mathbf{R}_z(\frac{2\pi}{3}(i-1))\mathbf{R}_x(\frac{\pi}{2}-\alpha_b)\mathbf{R}_y(\theta_i)\mathbf{R}_x(\phi_i-\frac{\pi}{2}) \tag{8.21}$$

where $\theta_i = \text{Arccos}((\boldsymbol{s}_i \times \boldsymbol{u}_i).(\mathbf{R}_z(\frac{2\pi}{3}(i-1)).(1,0,0)^T))$.

Eq. (8.21) is in the same form for both pure rotation and pure translation phases of the 3-rT*P*rT metamorphic parallel mechanism.

Thus, the general procedures to solve the inverse dynamics of the 3-rT*P*rT metamorphic parallel mechanism with pure rotation and pure translation phases can be concluded. Firstly, based on Eqs. (8.13), (8.14) and (8.20) the six unknowns ($^{i}f_{aiz}$, M_{ai}, *i*=1,2,3) including three joint forces along the z_i axis in the limb coordinate frame and the three moments at the platform rT joint centres can be solved. Then joint forces on the other two directions can be calculated from Eq. (8.20). After that, the actuation forces can be directly obtained from Eq. (8.15) and the corresponding reaction forces and moments at the base rT joints can be solved from Eq. (8.16) and Eq. (8.17) respectively.

8.2.5 Numerical Example and Analysis

In this section, numerical examples are provided based on the proposed dynamic model to analyse the dynamic behaviour of the 3-(rT)*P*(rT) metamorphic parallel mechanism with pure rotation and pure translation phases. Actuation forces and joint forces are calculated for both phases and comparison is made to understand the dynamic requirements in the joints which will be useful for optimal design and control of this metamorphic parallel mechanism.

Table 8-1 Numerical example parameters

Items	m_p	m_1	m_2	r_a	r_b	$\mathbf{I}_{pc}$
Value	5	1	1	0.3	0.5	Diag[0.1125, 0.1125, 0.225]
Items	α_a	α_b	e_1	e_2	r_p	$\mathbf{I}_1=\mathbf{I}_2$
Value	π/4	π/3	0.2	0.2	0.4	Diag[0.0533, 0.0533, 0.0001]

In the simulation, the mechanism parameters are given in Table 8-1 in which the length is in meter and the mass is in kg. To compare the two phases, the platform motion is planned to move the center of mass of the platform along a circular trajectory on the $z=r_a*\cos(\pi/12)/\sin(\alpha_a)$ plane with radius $r_a*\sin(\pi/12)/\sin(\alpha_a)$ at the center $(0,0,r_a*\cos(\pi/12)/\sin(\alpha_a))^T$. The angular velocity of the circular trajectory is 2π/5 rad/s which means the platform will move one circle in 5 seconds. The simulation results for the pure rotation phase are illustrated in Fig. 8-5. It can be seen in Fig. 8-5(a)-(c) that the joint force components on limb x_i axis ($^i f_{aix}$, red line) and y_i axis ($^i f_{aiy}$, green line) are very small as the motion of the limbs and the platform is mainly supported by the force along the limb direction ($^i f_{aiz}$, blue line). Following these and from Eq. (8.15), the actuation force of each limb can be calculated and is shown in Fig. 8-5(d). In addition to the main part from $^i f_{aiz}$, the gravity force of the piston is another main contribution to the actuation force and the part from the acceleration of the piston is very small based on the given platform motion. The total magnitudes of the platform rT joint forces are also shown in Fig. 8-5(e) and those of the base rT joint forces are illustrated in Fig. 8-5(f). It is clear that the gravity force and the inertia force of the cylinder in each limb make the base rT joint force much larger than the platform rT joint force while the gravity force is the main part. Considering joint moments, they are both small at the platform rT joint and base rT joint in each limb as shown in Fig. 8-5(g) and (h).

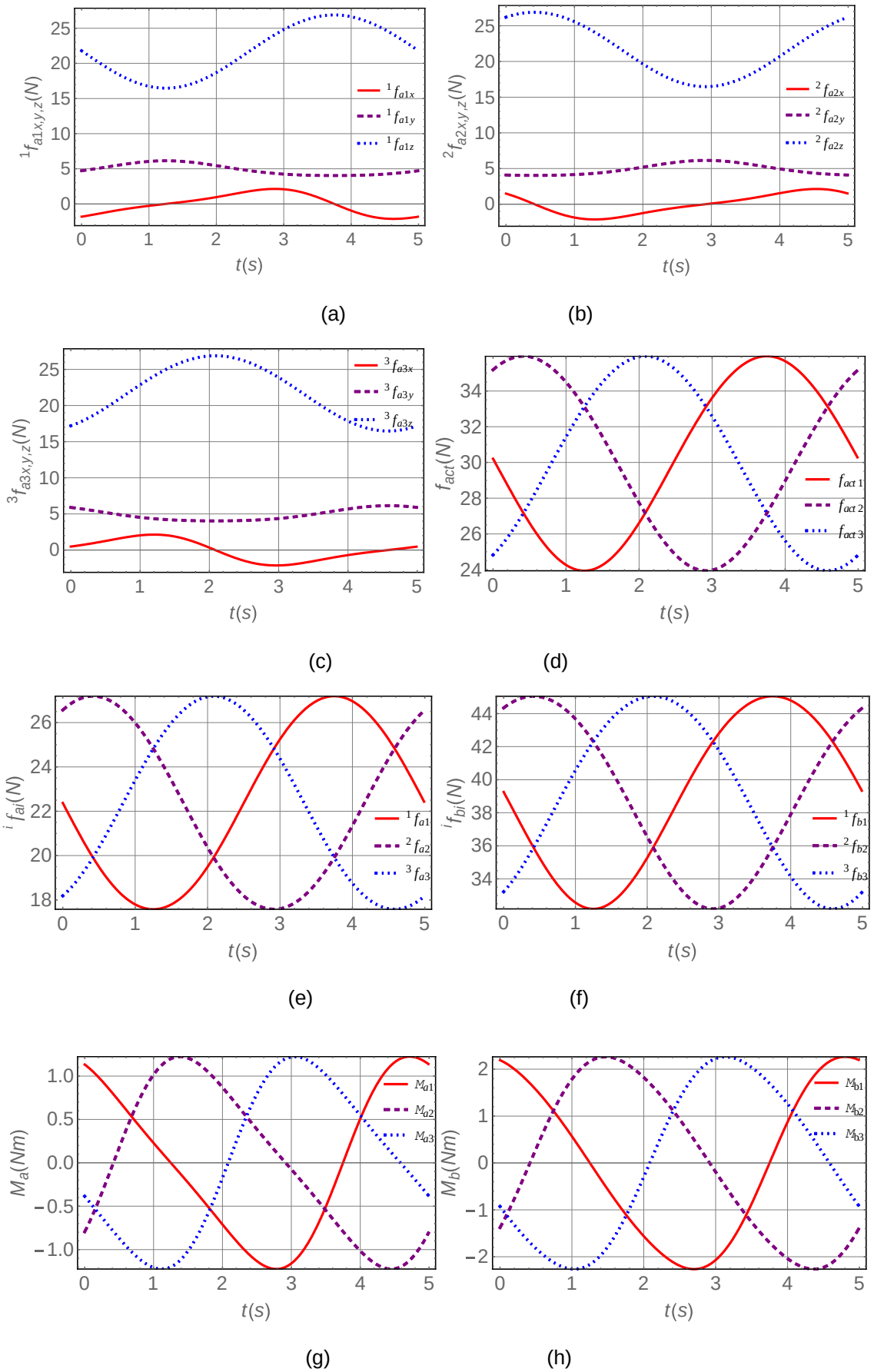

Figure 8-5 Simulation results for the pure rotation phase

By tuning the rT joint in each limb to make the radial axis of the platform rT joint to be parallel to the base rT joint, the 3-(rT)*P*(rT) metamorphic parallel mechanism is changed into the pure translation phase. Following the same circular trajectory by moving the center of mass of the platform along the circle on the $z=r_a*\cos(\pi/12)/\sin(\alpha_a)$ plane with radius $r_a*\sin(\pi/12)/\sin(\alpha_a)$ at the center $(0, 0, r_a*\cos(\pi/12)/\sin(\alpha_a))^T$ and the same speed of 2π/5 rad/s. This motion will be realized by pure translation motion of the platform.

The simulation results are recorded in Fig. 8-6. Similar to the pure rotation phase, in each limb the main force of the platform rT joint is the one along limb direction ($^i f_{aiz}$) while the other two components ($^i f_{aix}$, $^i f_{aiz}$) are very small as in Fig. 8-6(a)-(c). Differently, this limb direction force $^i f_{aiz}$ is larger than that in the pure rotation phase. This also results in that the actuation force in each limb is larger than that in the pure rotation phase as seen in Fig. 8-6(d). Another difference is that the range of the limb direction force $^i f_{aiz}$ in the pure translation phase (6~38N) is larger than that in the pure rotation phase (16~27N). This is because that the limbs do not need a large motion to rotate the platform to follow the trajectory while limbs in the pure translation phase need to move in a larger space to support the translation motion of the platform. Consequently, the reaction forces at the base rT joints in the pure translation phase are larger than those in the pure rotation phase as in Fig. 8-6(f). The joint moments are shown in Fig. 8-6(g) and (h) from which it's clear that the platform rT joint and the base rT joint have the same moment with opposite directions as calculated from Eq. (8.17). It is noted that joint moments in the pure translation phase (-10~10Nm) are much larger than those in the pure rotation phase (-2~2Nm). This is due to the fact that in the pure rotation phase, each limb provides a constraint force to constrain the platform translation while the rotation is free. But in the pure translation phase, each limb needs to give a constraint moment to realize the pure translation motion of the platform.

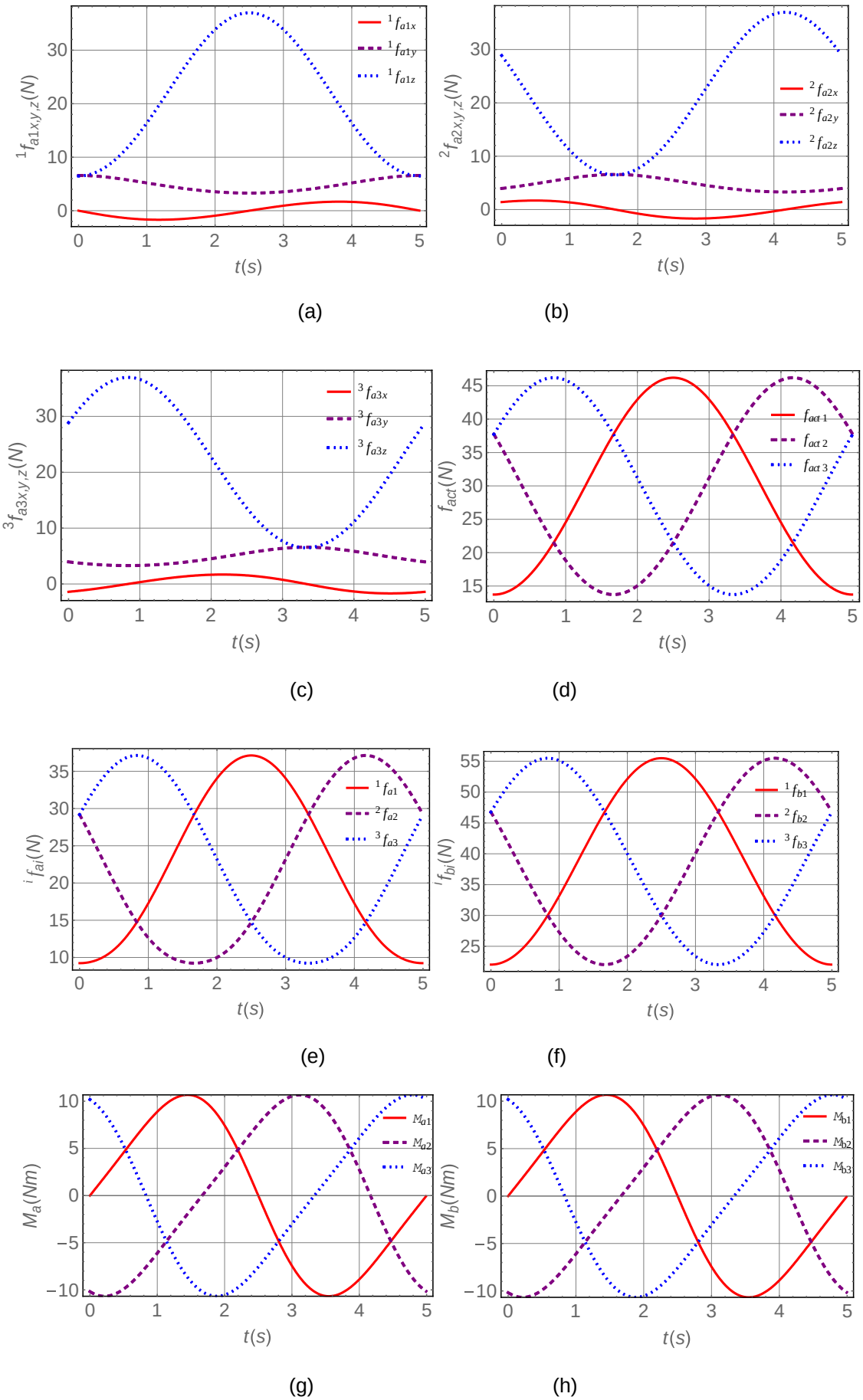

Figure 8-6 Simulation results for the pure translation phase

8.3 Unified Dynamic Modelling of a 3-rTPS

This section presents the topology variation of a 3-rT*PS* metamorphic parallel mechanism which can change its mobility from 3 to 6. The reconfiguration stems from a reconfigurable rT*PS* limb of which the two phases can be unified by taking one as a special case of the other. Based on this, unified inverse kinematics is solved and a unified dynamics modelling is built using screw theory which naturally represents the geometric constraint and actuation forces in the same manner. The obtained modelling covers all the topologies of the parallel mechanism. A numerical example demonstrates the theoretical results which provide basis for this metamorphic parallel robot with applications in reconfiguration-required environment.

8.3.1 The 3-rTPS and Its Reconfiguration

The under analysed 3-rT*PS* metamorphic parallel mechanism consists of three reconfigurable rT*PS* limbs as in Fig. 8-7. In the limb, there is a reconfigurable Hooke rT joint, a prismatic joint and a spherical joint. The reconfigurability of this limb stems from the configuration change of the rT joint which allows the radial rotation axis change with respect to the limb, resulting in two typical phases of the rT*PS* limb as in Fig. 8-7. While in Fig. 8-7(a), the radial axis is perpendicular to the limb (prismatic joint) denoted as $(rT)_1PS$, it is collinear with the limb (prismatic joint) passing through the spherical joint center in Fig. 8-7(b) and the limb phase is $(rT)_2PS$. In Fig. 8-7, β is the angle between the limb and its projection on the plane passing through rT joint center and perpendicular to the bracket axis, β =0 in the $(rT)_2PS$. α is the angle between that projection and the line passing through rT joint center and perpendicular to the bracket surface.

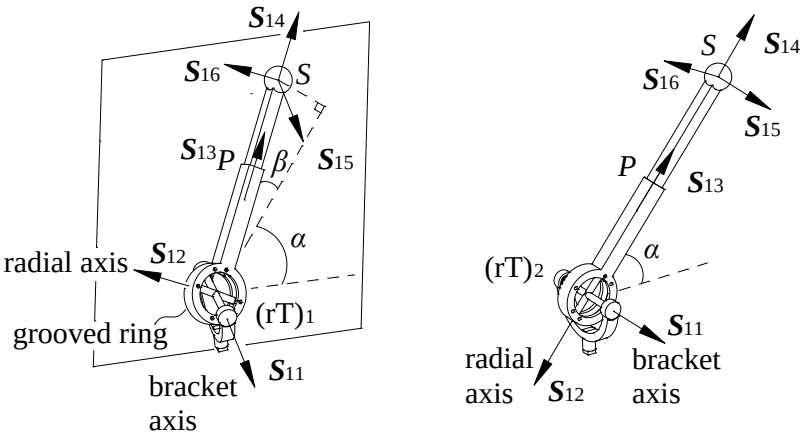

(a) (rT)$_1$*PS* (b) (rT)$_2$*PS*

Figure 8-7 Two phases of the rT*PS* limb

Three reconfigurable rT*PS* limbs are symmetrically arranged in the 3-rT*PS* metamorphic parallel mechanism by connecting the platform and the base as in Fig. 8-8 with 3-(rT)$_2$*PS* topology. Based on the screw systems in Fig. 8-7, the (rT)$_1$*PS* limb has six DOFs with no constraint to the platform and the (rT)$_2$*PS* limb has five DOFs with a constraint force passing through the spherical joint centre and parallel to the bracket axis of the rT joint. By altering the limb phase between these two, the 3-rT*PS* metamorphic parallel mechanism has variable topologies with different mobility.

Start from the 3-(rT)$_2$*PS* topology as in Fig. 8-8 and let points A_i and B_i denote the spherical joint center and the rT joint center in limb i (i=1,2,3) respectively. Locate a global coordinate system *Oxyz* at the base center *O* with *x*-axis passing through the rT joint center of limb 1 and *z*-axis perpendicular to base plane. Attach a platform coordinate system *o*'*x*'*y*'*z*' at the centroid of the platform with *x*' axis passing through spherical joint center A_1 and axis *z*' perpendicular to the platform plane. Let $\boldsymbol{a}_i$ and $\boldsymbol{b}_i$ denote the vectors of points A_i and B_i in the coordinate system *Oxyz*, d_i be the distance between the spherical joint center A_i and the rT joint center B_i.

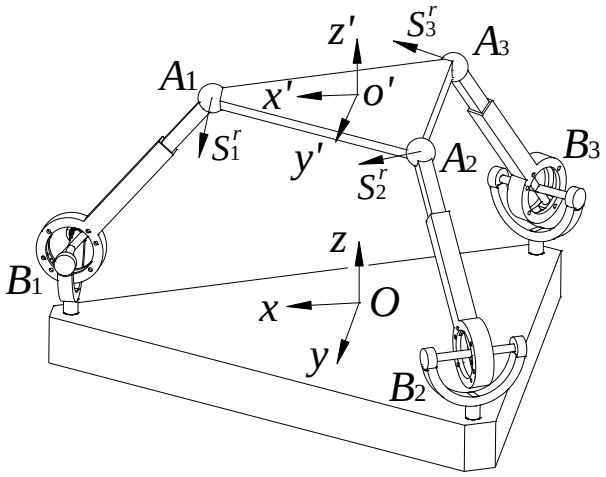

Figure 8-8 The 3-(rT)$_2$*PS* metamorphic parallel mechanism

The constraint screw system of the 3-(rT)$_2$*PS* parallel mechanism in Fig. 8-8 can be given as:

$$\left\{\boldsymbol{S}^r\right\}=\left\{\begin{array}{l}\boldsymbol{S}_1^r=\left[\boldsymbol{n}_1 \quad \boldsymbol{a}_1\times\boldsymbol{n}_1\right]\\ \boldsymbol{S}_2^r=\left[\boldsymbol{n}_2 \quad \boldsymbol{a}_2\times\boldsymbol{n}_2\right]\\ \boldsymbol{S}_3^r=\left[\boldsymbol{n}_3 \quad \boldsymbol{a}_3\times\boldsymbol{n}_3\right]\end{array}\right\} \tag{8.22}$$

where $\boldsymbol{n}_i$ is unit vector of the bracket axis in limb *i*.

The three constraint forces in Eq. (8.22) constrain two translations along *x*-axis and *y*-axis with one rotation about *z*-axis. Thus, the 3(rT)$_2$*PS* parallel mechanism with parallel constraint screws has three DOFs with two rotations about *x*-axis and *y*-axis with one translation along *z*-axis (2R1T).

Altering the (rT)$_2$*PS* limbs in the previous 3-(rT)$_2$*PS* parallel mechanisms into the phase (rT)$_1$*PS* will result in various new mechanism topologies with increased mobility. After changing the phase of one limb, the 3-(rT)$_2$*PS* parallel mechanisms become the topology 2(rT)$_2$*PS*-1(rT)$_1$*PS* in Fig. 8-9(a) that has two parallel constraint screws following Eq. (8.22). One constraint less makes the 2(rT)$_2$*PS*-1(rT)$_1$*PS* one more DOF than the 3-(rT)$_2$*PS*. Based on the constraint screw analysis, the 2(rT)$_2$*PS*-1(rT)$_1$*PS* parallel mechanism has four DOFs with three rotations and one translation along *z*-axis (3R1T).

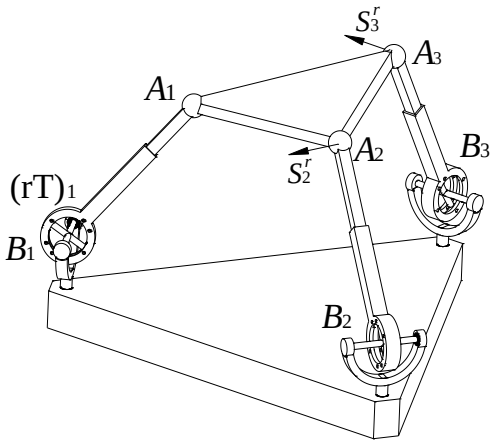

(a) 2$(rT)_2$*PS*-1$(rT)_1$*PS* (4DOFs-3R1T)

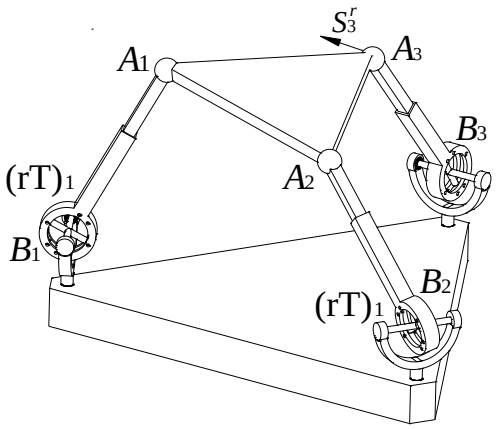

(b) 1$(rT)_2$*PS*-2$(rT)_1$*PS* (5DOFs-3R2T)

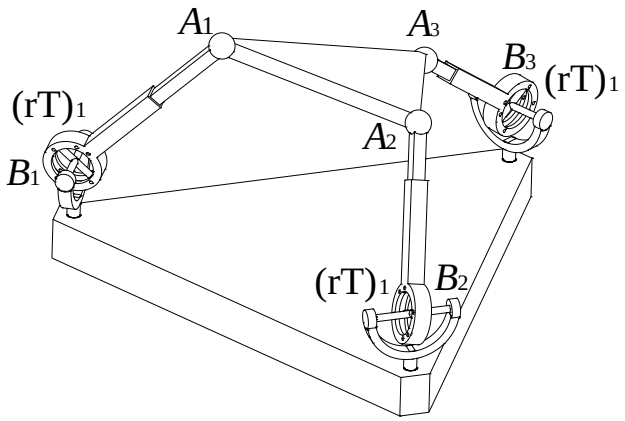

(c) 3$(rT)_1$*PS* (6DOFs-3R3T)

Figure 8-9 Variable topologies of the 3-(rT)*PS*

When further changing one more limb phases, the mechanism changes to the topology 1$(rT)_2$*PS*-2$(rT)_1$*PS* as in Fig. 8-9(b), which has only one constraint screw that limited the translation along $\boldsymbol{s}_3^r$ parallel to the bracket axis in limb 3. This mechanism has five DOFs with three rotations and two translations perpendicular to $\boldsymbol{s}_3^r$, (3R2T). When changing the third limb to phase $(rT)_1$*PS*, the mechanism becomes another topology 3$(rT)_1$*PS* as in Fig. 8-9(c) that does not have any constraint screw with full mobility 6.

The above shows one way of changing the limb phases in the order from limb 1 to limb 3 one by one. Actually, when changing the phases in different order or by different number, the mechanism can vary its topology from any one to another with mobility change among 3, 4, 5 and 6.

8.3.2 Unified Kinematics Analysis

Since the 3-rT*PS* metamorphic parallel mechanism has variable topologies with different mobility each of which is an independent parallel mechanism, how to model those mechanisms in a unified form for applications becomes a challenge. The following sections solve this problem.

8.3.2.1 Unified Inverse Displacement Analysis

Considering difference between the two phases of the rT*PS* limb, it can be found that the key part is the rotation about the radial axis which can be represented by angle β as in Fig. 8-7. It can be taken as that the $(rT)_1PS$ limb has variable angle β while the $(rT)_2PS$ limb has a fixed angle β=0. Thus, the $(rT)_2PS$ limb can be taken as a special configuration of the $(rT)_1PS$ limb by locking the actuation at β=0. This gives an important method to unify the geometric and kinematics modeling of the 3-rT*PS* metamorphic parallel mechanism by covering all its reconfigurable topologies with mobility change. The following is to use the prismatic joint in the $(rT)_2PS$ limb as actuation input and the rotation about the radial axis is added for the second actuation when the limb changes to phase $(rT)_1PS$.

Based on the above analysis and the coordinate systems of the 3rT*PS* metamorphic parallel mechanism in Fig. 8-8, the spherical joint center vector $\boldsymbol{a}_i$ in the global coordinate system *Oxyz* is:

$$\begin{cases} \boldsymbol{a}_1 = \boldsymbol{b}_1 + \mathbf{R}(z,\pi/2)d_1(-\mathbf{s}\beta_1, \mathbf{c}\beta_1\mathbf{c}\alpha_1, \mathbf{c}\beta_1\mathbf{s}\alpha_1) \\ \boldsymbol{a}_2 = \boldsymbol{b}_2 + \mathbf{R}(z,7\pi/6)d_2(-\mathbf{s}\beta_2, \mathbf{c}\beta_2\mathbf{c}\alpha_2, \mathbf{c}\beta_2\mathbf{s}\alpha_2) \\ \boldsymbol{a}_3 = \boldsymbol{b}_3 + \mathbf{R}(z,-\pi/6)d_3(-\mathbf{s}\beta_3, \mathbf{c}\beta_3\mathbf{s}\alpha_3, \mathbf{c}\beta_3\mathbf{s}\alpha_3) \end{cases} \tag{8.23}$$

where d_i is the limb length, $\mathbf{R}(z, h)$ represents a rotation about axis z with angle h.

The inverse displacement analysis of the 3rT*PS* metamorphic parallel mechanism is to obtain the actuation parameters (limb length d_i, radial-axis rotation angle β_i) based on the given platform position and orientation. When giving the platform position $\boldsymbol{p}$ (p_x, p_y, p_z) and orientation $\mathbf{R}$ described in the global coordinate system in Fig. 8-8, the position of the spherical joint centers can be obtained as:

$$\begin{cases} \boldsymbol{a}_1 = \boldsymbol{p} + \mathbf{R}.(r_a, 0, 0) \\ \boldsymbol{a}_2 = \boldsymbol{p} + \mathbf{R}.(-r_a/2, \sqrt{3}r_a/2, 0) \\ \boldsymbol{a}_3 = \boldsymbol{p} + \mathbf{R}.(-r_a/2, -\sqrt{3}r_a/2, 0) \end{cases} \tag{8.24}$$

where the spherical joint centers on the platform are symmetrically arranged on a circle with radius r_a.

By correspondingly equalling Eq. (8.24) to Eq. (8.23), the inverse displacement analysis can be solved:

$$\begin{cases} d_i = \sqrt{\boldsymbol{c}_i.\boldsymbol{c}_i} \\ \beta_i = -\sin^{-1}(c_{ix}/d_i) \end{cases} \tag{8.25}$$

where $\begin{cases} \boldsymbol{c}_1 = \mathbf{R}(z, -\pi/2)(\boldsymbol{a}_1 - \boldsymbol{b}_1) \\ \boldsymbol{c}_2 = \mathbf{R}(z, -7\pi/6)(\boldsymbol{a}_2 - \boldsymbol{b}_2) \\ \boldsymbol{c}_3 = \mathbf{R}(z, \pi/6)(\boldsymbol{a}_3 - \boldsymbol{b}_3) \end{cases}$, c_{ix} is the *x*-axis component of vector $\boldsymbol{c}_i$. It should be noted that β_i naturally equals to zero when the limb is in phase (rT)$_2$*PS*, which is in the unified form for all the topologies.

8.3.2.2 Unified Velocity/Acceleration Analysis

The velocity twist of the moving platform of the 3(rT)*PS* parallel mechanism can be written as the linear combination of instantaneous twists in each limb:

$$\boldsymbol{S}_{VO} = \dot{\alpha}_i \boldsymbol{S}_{i1} + \dot{\beta}_i \boldsymbol{S}_{i2} + \dot{d}_i \boldsymbol{S}_{i3} + \dot{\phi}_{i4} \boldsymbol{S}_{i4} + \dot{\phi}_{i5} \boldsymbol{S}_{i5} + \dot{\phi}_{i6} \boldsymbol{S}_{i6} \quad (i = 1, 2, 3) \tag{8.26}$$

where $\boldsymbol{S}_{VO} = [\boldsymbol{\omega}_o \ \ \boldsymbol{v}_o]$, $\boldsymbol{\omega}_o$ is the angular velocity of the platform, $\boldsymbol{v}_o$ represents the translational velocity of the point on the moving platform and coincides with *O*, $\boldsymbol{S}_{ij}$ (*j*=1,2,3,4,5,6) denotes the unit screw of the *j*th 1-DOF joint in limb *i*, $\dot{d}_i$ is the translation rate of the prismatic joint in limb *i*, $\dot{\alpha}_i$, $\dot{\beta}_i$ and $\dot{\phi}_{ij}$ (*j*=3,4,5) represent angular rates of the rT joint and spherical joint in limb *i* respectively.

Eq. (8.26) can be written in the matrix form as

$$(\mathbf{J}_i)^{-1}\boldsymbol{S}_{VO} = \begin{bmatrix} \dot{\alpha}_i & \dot{\beta}_i & \dot{d}_i & \dot{\phi}_{i4} & \dot{\phi}_{i5} & \dot{\phi}_{i6} \end{bmatrix}^T, \qquad (i = 1, 2, 3) \tag{8.27}$$

where $\mathbf{J}_i = \begin{bmatrix} \boldsymbol{S}_{i1}{}^T & \boldsymbol{S}_{i2}{}^T & \boldsymbol{S}_{i3}{}^T & \boldsymbol{S}_{i4}{}^T & \boldsymbol{S}_{i5}{}^T & \boldsymbol{S}_{i6}{}^T \end{bmatrix}$ is the *i*th limb Jacobian. Eq. (8.27) can be used to obtain the joint velocities in the limb based on the given platform velocity and the results will be applied to the Lie screw calculation in the acceleration analysis.

Based mechanism constraint analysis, the translation of the prismatic joint is chosen as the input for the $(\mathrm{rT})_2PS$ limb and the rotation about the bracket axis is taken as the second actuation when the limb changes to phase $(\mathrm{rT})_1PS$. Thus by locking the active joints in the limbs temporarily, and taking the reciprocal product (represented by *o*) on both sides of Eq. (8.26), for each limb there is

$$\begin{bmatrix} \boldsymbol{S}_{i2}^r & \boldsymbol{S}_{i3}^r \end{bmatrix}^T \circ \boldsymbol{S}_{VO} = \begin{bmatrix} \dot{\beta}_i & \dot{d}_i \end{bmatrix}^T, \quad \begin{cases} \dot{\beta}_i = 0 & (\mathrm{rT})_2 PS \text{ limb} \\ \dot{\beta}_i & (\mathrm{rT})_1 PS \text{ limb} \end{cases} \tag{8.28}$$

where $\begin{cases} \boldsymbol{S}_{i2}^r = \begin{bmatrix} \boldsymbol{s}_{i2} \times \boldsymbol{u}_i & \boldsymbol{a}_i \times (\boldsymbol{s}_{i2} \times \boldsymbol{u}_i) \end{bmatrix} / d_i \\ \boldsymbol{S}_{i3}^r = \begin{bmatrix} \boldsymbol{u}_i & \boldsymbol{b}_i \times \boldsymbol{u}_i \end{bmatrix} \end{cases}$.

Equations in Eq. (8.28) for the three limbs can be rewritten in matrix form as:

$$\begin{bmatrix} \boldsymbol{S}_{12}^r \\ \boldsymbol{S}_{13}^r \\ \boldsymbol{S}_{22}^r \\ \boldsymbol{S}_{23}^r \\ \boldsymbol{S}_{32}^r \\ \boldsymbol{S}_{33}^r \end{bmatrix} \circ \boldsymbol{S}_{VO} = \mathbf{J} \circ \boldsymbol{S}_{VO} = \begin{bmatrix} \dot{\beta}_1 \\ \dot{d}_1 \\ \dot{\beta}_2 \\ \dot{d}_2 \\ \dot{\beta}_3 \\ \dot{d}_3 \end{bmatrix} \tag{8.29}$$

Thus **J** is the Jacobian matrix and the joint rates can be obtained from Eq. (8.29) when the platform velocity is given. This solves the inverse velocity analysis based on the unified kinematics modeling by covering all the topologies of the metamorphic parallel mechanism.

Similar to the velocity relation, the reduced acceleration state or accelerator [184] of the moving platform can be also written as the linear combination of instantaneous acceleration screws of all the joints in each limb as:

$$\boldsymbol{S}_{aO} = \ddot{\alpha}_i \boldsymbol{S}_{i1} + \ddot{\beta}_i \boldsymbol{S}_{i2} + \ddot{d}_i \boldsymbol{S}_{i3} + \ddot{\phi}_{i4} \boldsymbol{S}_{i4} + \ddot{\phi}_{i5} \boldsymbol{S}_{i5} + \ddot{\phi}_{i6} \boldsymbol{S}_{i6} + \boldsymbol{S}_{Lie-i} \quad (i = 1,2,3) \tag{8.30}$$

where $\boldsymbol{S}_{aO} = [\dot{\boldsymbol{\omega}}_o \quad \dot{\boldsymbol{v}}_o - \boldsymbol{\omega}_o \times \boldsymbol{v}_o]$ is the accelerator, $\dot{\boldsymbol{\omega}}_o$ is the angular acceleration of the platform, $\dot{\boldsymbol{v}}_o$ represents the translational acceleration of the point on the moving platform and coincides with *O*, $\boldsymbol{S}_{ij}$ is the same as in Eq. (8.26), $\ddot{d}_i$ is the translation acceleration of the prismatic joint in limb *i*, $\ddot{\alpha}_i$, $\ddot{\beta}_i$ and $\ddot{\phi}_{ij}$ (*j*=3,4,5) are the angular accelerations of the rT joint and spherical joint in limb *i* respectively. $\boldsymbol{S}_{Lie\text{-}i}$ is the *Lie screw* in the *i*th limb as:

$$\begin{aligned}
\boldsymbol{S}_{Lie-i} = & \left[\dot{\alpha}_i \boldsymbol{S}_{i1} \quad \dot{\beta}_i \boldsymbol{S}_{i2} + \dot{d}_i \boldsymbol{S}_{i3} + \dot{\phi}_{i4} \boldsymbol{S}_{i4} + \dot{\phi}_{i5} \boldsymbol{S}_{i5} + \dot{\phi}_{i6} \boldsymbol{S}_{i6} \right] \\
& + \left[\dot{\beta}_i \boldsymbol{S}_{i2} \quad \dot{d}_i \boldsymbol{S}_{i3} + \dot{\phi}_{i4} \boldsymbol{S}_{i4} + \dot{\phi}_{i5} \boldsymbol{S}_{i5} + \dot{\phi}_{i6} \boldsymbol{S}_{i6} \right] \\
& + \left[\dot{d}_i \boldsymbol{S}_{i3} \quad \dot{\phi}_{i4} \boldsymbol{S}_{i4} + \dot{\phi}_{i5} \boldsymbol{S}_{i5} + \dot{\phi}_{i6} \boldsymbol{S}_{i6} \right] \\
& + \left[\dot{\phi}_{i4} \boldsymbol{S}_{i4} \quad \dot{\phi}_{i5} \boldsymbol{S}_{i5} + \dot{\phi}_{i6} \boldsymbol{S}_{i6} \right] \\
& + \left[\dot{\phi}_{i5} \boldsymbol{S}_{i5} \quad \dot{\phi}_{i6} \boldsymbol{S}_{i6} \right] \qquad (i = 1,2,3)
\end{aligned}$$

where [* *] represents the Lie product [184].

Thus, the limb joint accelerations can be obtained:

$$(\mathbf{J}_i)^{-1}(\boldsymbol{S}_{aO} - \boldsymbol{S}_{Lie-i}) = \left[\ddot{\alpha}_i \quad \ddot{\beta}_i \quad \ddot{d}_i \quad \ddot{\phi}_{i4} \quad \ddot{\phi}_{i5} \quad \ddot{\phi}_{i6} \right]^T \qquad (i = 1,2,3) \tag{8.31}$$

Similar to the velocity analysis, the actuator accelerations can be inversely solved by giving the platform acceleration as:

$$\mathbf{J}\circ \boldsymbol{S}_{aO} - \begin{bmatrix} \boldsymbol{S}_{12}^{r}\circ \boldsymbol{S}_{Lie-1} \\ \boldsymbol{S}_{13}^{r}\circ \boldsymbol{S}_{Lie-1} \\ \boldsymbol{S}_{22}^{r}\circ \boldsymbol{S}_{Lie-2} \\ \boldsymbol{S}_{23}^{r}\circ \boldsymbol{S}_{Lie-2} \\ \boldsymbol{S}_{32}^{r}\circ \boldsymbol{S}_{Lie-3} \\ \boldsymbol{S}_{33}^{r}\circ \boldsymbol{S}_{Lie-3} \end{bmatrix} = \begin{bmatrix} \ddot{\beta}_1 \\ \ddot{d}_1 \\ \ddot{\beta}_2 \\ \ddot{d}_2 \\ \ddot{\beta}_3 \\ \ddot{d}_3 \end{bmatrix} \tag{8.32}$$

8.3.3 Unified Inverse Dynamics Based Virtual Work Principle

8.3.3.1 Velocities and Accelerations of the Centers of Mass

In order to describe the virtual work of the parallel mechanism system, the velocities and accelerations representing the centers of mass of the platform, lower limb and upper limb in each limb should be calculated based on the given platform motion parameters. From Eq. (8.27) and Eq. (8.29), there is

$$\begin{bmatrix} \dot{\alpha}_i \\ \dot{\beta}_i \\ \dot{d}_i \\ \dot{\phi}_{i4} \\ \dot{\phi}_{i5} \\ \dot{\phi}_{i6} \end{bmatrix} = ((\mathbf{J}\circ)\,\mathbf{J}_i)^{-1} \begin{bmatrix} \dot{\beta}_1 \\ \dot{d}_1 \\ \dot{\beta}_2 \\ \dot{d}_2 \\ \dot{\beta}_3 \\ \dot{d}_3 \end{bmatrix}, \quad (i = 1,2,3) \tag{8.33}$$

Following this and Eq. (8.29), the velocity screws of platform, the lower and upper parts in the limb in terms of the actuation input velocities can be obtained by

$$\begin{cases} \boldsymbol{S}_{VO} = \dot{\beta}_1 \boldsymbol{S}_{Po}^{1} + \dot{d}_1 \boldsymbol{S}_{Po}^{2} + \dot{\beta}_2 \boldsymbol{S}_{Po}^{3} + \dot{d}_2 \boldsymbol{S}_{Po}^{4} + \dot{\beta}_3 \boldsymbol{S}_{Po}^{5} + \dot{d}_3 \boldsymbol{S}_{Po}^{6} \\ \boldsymbol{S}_{VlO-i} = \dot{\alpha}_i \boldsymbol{S}_{i1} + \dot{\beta}_i \boldsymbol{S}_{i2} = \dot{\beta}_1 \boldsymbol{S}_{loi}^{1} + \dot{d}_1 \boldsymbol{S}_{loi}^{2} + \dot{\beta}_2 \boldsymbol{S}_{loi}^{3} + \dot{d}_2 \boldsymbol{S}_{loi}^{4} \\ \qquad\qquad + \dot{\beta}_3 \boldsymbol{S}_{loi}^{5} + \dot{d}_3 \boldsymbol{S}_{loi}^{6} \\ \boldsymbol{S}_{VuO-i} = \dot{\alpha}_i \boldsymbol{S}_{i1} + \dot{\beta}_i \boldsymbol{S}_{i2} + \dot{d}_i \boldsymbol{S}_{i3} = \dot{\beta}_1 \boldsymbol{S}_{uoi}^{1} + \dot{d}_1 \boldsymbol{S}_{uoi}^{2} + \dot{\beta}_2 \boldsymbol{S}_{uoi}^{3} \\ \qquad\qquad + \dot{d}_2 \boldsymbol{S}_{uoi}^{4} + \dot{\beta}_3 \boldsymbol{S}_{uoi}^{5} + \dot{d}_3 \boldsymbol{S}_{uoi}^{6} \end{cases} \tag{8.34}$$

Then the velocity screw $\boldsymbol{S}_{VlO\text{-}i}=[\boldsymbol{\omega}_l \quad \boldsymbol{v}_{lo}]$ in Eq. (8.34) with presentation point *O* can be changed to $\boldsymbol{S}_{Vlcm\text{-}i}=[\boldsymbol{\omega}_l \quad \boldsymbol{v}_{lcm}]$ with presentation point of the center of mass of the lower limb by changing all the screws in Eq. (8.34) as

$$\begin{gathered}\boldsymbol{S}_{lcmi}^{j}=\left[\mathrm{P}(\boldsymbol{S}_{loi}^{j}) \quad D(\boldsymbol{S}_{loi}^{j})+\mathrm{P}(\boldsymbol{S}_{loi}^{j})\times\boldsymbol{r}_{li}\right] \\ (i=1,2,3;\ j=1,2,...,6)\end{gathered} \tag{8.35}$$

where $\mathrm{P}(*)$ and $\mathrm{D}(*)$ give the primary part and dual part of the screw, $\boldsymbol{r}_{li}$ is the vector from the point *O* to the center of mass of the lower limb. The velocity screws of the platform and the upper limb can be changed similarly.

Based on the acceleration equations in Eq. (8.30) and Eq. (8.31), the accelerations of the lower limb and upper limb with presentation point *O* can be obtained as

$$\begin{cases}\boldsymbol{S}_{alO-i}=\left[\dot{\boldsymbol{\omega}}_{li} \quad \boldsymbol{a}_{loi}\right]=\ddot{\alpha}_i\boldsymbol{S}_{i1}+\ddot{\beta}_i\boldsymbol{S}_{i2}+\boldsymbol{S}_{Lie-li} \\ \boldsymbol{S}_{auO-i}=\left[\dot{\boldsymbol{\omega}}_{ui} \quad \boldsymbol{a}_{uoi}\right]=\ddot{\alpha}_i\boldsymbol{S}_{i1}+\ddot{\beta}_i\boldsymbol{S}_{i2}+\ddot{d}_i\boldsymbol{S}_{i3}+\boldsymbol{S}_{Lie-ui}\end{cases} \tag{8.36}$$

where $\boldsymbol{S}_{Lie\text{-}li}$ and $\boldsymbol{S}_{Lie\text{-}ui}$ are the *Lie screws* as in Eq. (8.30).

Then, the accelerations of the centers of mass of the lower limb can be obtained as

$$\boldsymbol{S}_{alcm-i}=\left[\dot{\boldsymbol{\omega}}_{li} \quad \boldsymbol{a}_{lcmi}\right]=\left[\dot{\boldsymbol{\omega}}_{li} \quad \boldsymbol{a}_{loi}+\dot{\boldsymbol{\omega}}_{li}\times\boldsymbol{r}_{li}+\boldsymbol{\omega}_{li}\times(\boldsymbol{\omega}_{li}\times\boldsymbol{r}_{li})\right] \tag{8.37}$$

The acceleration screws of the upper limb can be obtained similarly.

8.3.3.2 Virtual Work Based Inverse Dynamics

Generally, the wrench on the moving platform of the 3-rT*PS* metamorphic parallel mechanism can be described as

$$\boldsymbol{S}_{FPcm}=\left[m_P(\boldsymbol{g}-\boldsymbol{a}_{Pcm})+\boldsymbol{f}_P \quad \boldsymbol{\tau}_P-\mathbf{I}_P\dot{\boldsymbol{\omega}}_P-\boldsymbol{\omega}_P\times\mathbf{I}_P\boldsymbol{\omega}_P\right] \tag{8.38}$$

where $\boldsymbol{a}_{Pcm}$ is the translational acceleration of the center of mass of the platform, $\boldsymbol{f}_P$ and $\boldsymbol{\tau}_P$ are the external force and torque applied to the center of mass of the platform, $\mathbf{I}_P$ is the inertia matrix of the platform.

Similarly, the wrenches on the lower limb and upper limb can be given as below by considering that there is no external forces and torques on the limbs.

$$\begin{cases} \boldsymbol{S}_{Flcmi} = \left[m_{li}(\boldsymbol{g} - \boldsymbol{a}_{lcmi}) \quad -\mathbf{I}_{li}\,\dot{\boldsymbol{\omega}}_{li} - \boldsymbol{\omega}_{li} \times \mathbf{I}_{li}\,\boldsymbol{\omega}_{li} \right] \\ \boldsymbol{S}_{Fucmi} = \left[m_{ui}(\boldsymbol{g} - \boldsymbol{a}_{ucmi}) \quad -\mathbf{I}_{ui}\,\dot{\boldsymbol{\omega}}_{ui} - \boldsymbol{\omega}_{ui} \times \mathbf{I}_{ui}\,\boldsymbol{\omega}_{ui} \right] \end{cases} \tag{8.39}$$

where $\mathbf{I}_{li}$ and $\mathbf{I}_{ui}$ are the inertia matrices of the lower limb and upper limb in limb *i*.

Based on the above analysis, the total power *W* performed by the mechanism system forces is:

$$\begin{aligned} W &= \boldsymbol{S}_{FPcm} \circ \boldsymbol{S}_{Vcm} \\ &+ \sum_{i=1}^{3} (\boldsymbol{S}_{Flcmi} \circ \boldsymbol{S}_{Vlcm-i} + \boldsymbol{S}_{Fucmi} \circ \boldsymbol{S}_{Vucm-i} + \tau_{i2}\dot{\beta}_{i2} + F_{i3}\dot{d}_{i3}) \end{aligned} \tag{8.40}$$

Using the principle of virtual work [185], the below exists by expanding Eq. (8.40)

$$\begin{aligned} \delta W = &[\boldsymbol{S}_{FPcm} \circ \boldsymbol{S}^1_{Pcm} + \sum_{i=1}^{3} (\boldsymbol{S}_{Flcmi} \circ \boldsymbol{S}^1_{lcmi} + \boldsymbol{S}_{Fucmi} \circ \boldsymbol{S}^1_{ucmi}) + \tau_{12}]\delta\dot{\beta}_{12} \\ +&[\boldsymbol{S}_{FPcm} \circ \boldsymbol{S}^2_{Pcm} + \sum_{i=1}^{3} (\boldsymbol{S}_{Flcmi} \circ \boldsymbol{S}^2_{lcmi} + \boldsymbol{S}_{Fucmi} \circ \boldsymbol{S}^2_{ucmi}) + F_{13}]\delta\dot{d}_{12} + \cdots \\ +&[\boldsymbol{S}_{FPcm} \circ \boldsymbol{S}^6_{Pcm} + \sum_{i=1}^{3} (\boldsymbol{S}_{Flcmi} \circ \boldsymbol{S}^6_{lcmi} + \boldsymbol{S}_{Fucmi} \circ \boldsymbol{S}^6_{ucmi}) + F_{33}]\delta\dot{d}_{32} \end{aligned} \tag{8.41}$$

Then there is

$$\begin{cases} \boldsymbol{S}_{FPcm} \circ \boldsymbol{S}_{Pcm}^{1} + \sum_{i=1}^{3} (\boldsymbol{S}_{Flcmi} \circ \boldsymbol{S}_{lcmi}^{1} + \boldsymbol{S}_{Fucmi} \circ \boldsymbol{S}_{ucmi}^{1}) + \tau_{12} = 0 \\ \boldsymbol{S}_{FPcm} \circ \boldsymbol{S}_{Pcm}^{2} + \sum_{i=1}^{3} (\boldsymbol{S}_{Flcmi} \circ \boldsymbol{S}_{lcmi}^{2} + \boldsymbol{S}_{Fucmi} \circ \boldsymbol{S}_{ucmi}^{2}) + F_{13} = 0 \\ \quad \vdots \\ \boldsymbol{S}_{FPcm} \circ \boldsymbol{S}_{Pcm}^{6} + \sum_{i=1}^{3} (\boldsymbol{S}_{Flcmi} \circ \boldsymbol{S}_{lcmi}^{6} + \boldsymbol{S}_{Fucmi} \circ \boldsymbol{S}_{ucmi}^{6}) + F_{33} = 0 \end{cases} \tag{8.42}$$

Thus, the actuation input (τ_{i2}, F_{i3}) (i=1,2,3) can be solved inversely when giving the platform acceleration and velocity. It should be noted that there is one actuation input F_{i3} when limb i is in phase (rT)$_2$*PS* and there are two (τ_{i2}, F_{i3}) when it is changed to phase (rT)$_1$*PS*. For the inverse dynamics analysis of a topology of the 3(rT)*PS* metamorphic parallel mechanism, corresponding equations in Eq. (8.42) should be selected considering the phase of each limb. Take the 2(rT)$_1$*PS*-1(rT)$_2$*PS* in which limb 2 is in phase (rT)$_2$*PS* as an example, the actuation input (τ_{12}, F_{13}, F_{23}, τ_{32}, F_{33}) can be solved in Eq. (8.42).

8.3.4 Numerical Example

Based on the above dynamic modeling, this section uses a numerical example to demonstrate the theoretical procedures. The mechanism parameters are listed in Table 8-2, in which e_l is the distance from center of mass of the lower limb to the rT joint center and e_u is the distance from center of mass of the upper limb to the spherical joint center.

Table 8-2 Parameters of the 3-(rT)PS

Items	**Mass(kg)**	**Inertia (kgm^2)**	**Size (m)**
Platform	2	Diag[0.6, 0.8,1.2]	r_a=0.18
Lower limb	0.5	Diag[0.3, 0.3,0.0001]	e_l=0.1
Upper limb	0.5	Diag[0.2, 0.2,0.0001]	e_u=0.15
Base	N/A		r_b=0.35

The inverse dynamic analysis is based on the input of the platform with a translation in the *xOz* plane and a rotation about *x*-axis. The *x* and *z* components, the rotation angle all follow the following periodic function:

$$\begin{cases} \gamma = (0.3/2\pi)^2(-\sin(2\pi t/0.3)) + 0.3t/2\pi \\ \dot{\gamma} = (0.3/2\pi)(1-\cos(2\pi t/0.3)) \\ \ddot{\gamma} = \sin(2\pi t/0.3) \end{cases} \tag{8.43}$$

The platform starts from initial position (0, 0, 0.24) with no initial orientation. The simulation results are listed in Fig. 8-10. It can be seen that the joint velocity and acceleration of the rotation about the radial axis in limb 1 are zero due to the fact that the platform only translates in the *xOz* plane with rotation about *x*-axis. The limb joint velocities and accelerations in limb 2 and limb 3 are also relatively symmetry based on this platform motion.

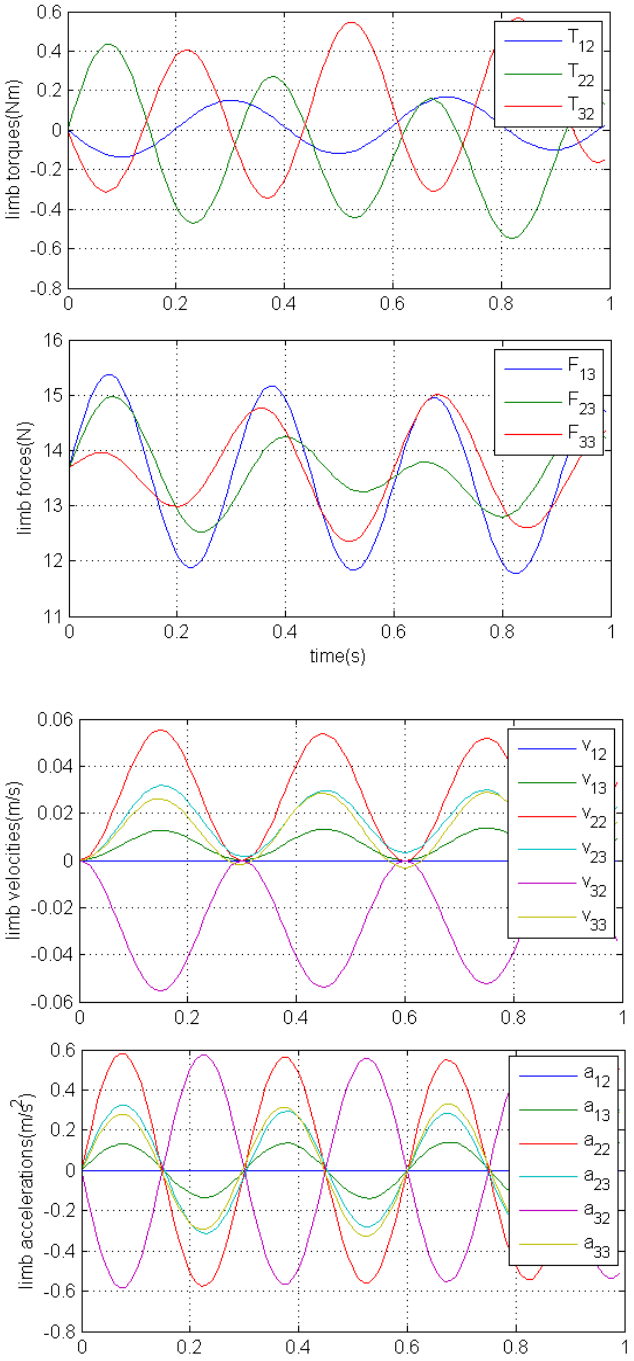

Figure 8-10 Simulation results

The selected platform motion also demonstrates the unified dynamic analysis of the metamorphic parallel mechanism covering 5-DOF topology 1(rT)$_2$*PS*-2(rT)$_1$*PS* (limb 1 in (rT)$_2$*PS*) and 6-DOF topology 3(rT)$_1$*PS*. In the 5-DOF case, the obtained torque of the radial axis (τ_{12}) in limb 1 represents the reaction torque and it represents actuation torque in the 6-DOF topology. Thus, this unified form can give unified dynamics analysis for all topologies.

8.4 Applicability of the Dynamic Models

As mentioned in the beginning of this chapter, the two dynamic models are based on the assumption that all the parameters are ideal and known. This means the model equations are not ready for direct applications and many steps are still ahead before applying them in the realization and control of the parallel mechanisms. Based on chapter 7, joint clearance is common and can affect the platform motion a lot. Thus all the prototyped parameters are not ideal and same with the theoretically designed ones. Both kinematics calibration [186, 187] and dynamic parameter identification are needed when coming to real system modelling and control.

Specifically, the major effect from the parameter uncertainty [186] on the dynamic model of the 3-rTPrT is that the developed simplified dynamic model in section 8.2.4 may not exist. This is due to that the method is based on the ideal joint force decomposition relation at the platform rT joint center. The joint clearance may cause the two rotational joint axes of the rT joint not perpendicular to each other and to the limb axis. In this case, the simplied parameter relations in Eqs. (8.17-8.19) do not exist and the inverse dynamics of the 3-rTPrT can not be solved by the six equations (Eqs. 8.13-8.14) of the platform dynamics directly. But the general formed inverse dynamics in section 8.2.3 is still valid and the 15 unknows can be solved based on the 15 general equations, Eqs. (8.11-8.14).

The main potential issue with the dynamic model of the 3-rTPS due to the parameter uncertainty can be the basic geometric constraint relation in the rT joint phase 2. It requires the radial axis to be inline with the limb axis and passing through the spherical joint center which is very critical to realize the output platform mobility. The unsatisfied condition will introduce errors in the limb dynamics when calculating the limb joint velocities and accelerations which will then

cause inaccurate results in the inverse dynamics. But those errors can be bounded to a small range if very high accurate manufacturing process is applied and calibration [187] can also help compenstate them for the final controlled performance.

Thus, the dynamic models in this chapter are mainly showing a solution to model the dynamics of multi-phases of the metamorphic parallel mechanisms in a unified theoretical manner. They provide the basis and tools at the design stage to have basic knowledge about the possible dynamic performance, actuation requirement, dimensional and dynamic parameter selection, joint force reaction, joint component choosing, and others.

8.5 Conclusions

This chapter made contribution in proposing the unified inverse dynamics modelling for metamorphic parallel mechanisms by covering all the mobility phases through the strategy of modelling the system from the limbs. This was applied on two metamorphic parallel mechanisms, the 3-rTPrT and the 3-rTPS. In both the pure rotation and pure translation phases of the 3-rTPrT metamorphic parallel mechanism, the rTPrT limb have the same geometric constraint relations among all the limb joints. This founding gave the possibility to solve both phases in one way from the velocity, acceleration to the actuation input forces in the inverse dynamics featured by 15 unknowns in 15 equations. By specifically investigating the joint reaction forces at the platform rT joint cente, a special force decomposition was found, leading to a simplified inverse dynamics analysis by expressing 9 unknowns by the other 6. Then only the six platform dynamic equations are needed to solve the six unknowns. A numerical example was also illustrated to compare the joint reaction forces and actuation force requirements of the pure rotation and pure translation phases when realizing the same trajectory of the platform center point. It was found that the pure rotation phase showed less actuation force, joint reaction force and reaction moments than the pure translation phase for the demonstrated trajectory, which provided reference on the design and application plan.

By modelling from the limb and taking one phase of the rT limb as a special case of the other general phase, the inverse dynamics of the 3-rTPS metamorphic parallel mechanism could be

solved in unified force equations based on the virtual work principle to cover all its phases with mobility 3, 4, 5 and 6. Screw theory was used and showed unified format in sovling the joint velocities, accelerations and dynamic forces in the process, which was another factor contributing to the unified dynamics analysis.

This chapter also gave a critical review of the applicability of the proposed dynamics modelling method. It's concluded that the models were based on ideal parameter assumptions and parameter uncertainties from joint clearance and assembly erros can affect seriously the model results. Future work can include more detailed investigation on how the prototype errors which are not avoidable will affect the dynamic model and the reconfiguration of the metamorphic parallel mechanisms.

Chapter 9 Conclusions and Future Work

Metamorphic parallel mechanisms are a new class of reconfigurable parallel mechanisms which have the capability of reconfiguring into different phases with variable mobility and motion types to adapt to different application requirements. MPMs are still in their early stage and worth a systematic research. Thus this work focused on the fundamentals by developing new methods in synthesizing metamorphic parallel mechanisms and modelling their variable topologies in a unified way to provide basis for them in various applications. Detailed results and contributions of this thesis is summarized in the following based on the main body from chapter 2 to chapter 8 and lot of meaningful future work will be planned and continued.

9.1 Conclusions

The state-of-the-art of reconfigurable parallel mechanisms was presented based on the thorough literature review in chapter 2. A general background of parallel mechanism research was introduced from the original application oriented invention to the 6-DOF Stewart platforms and to recent effort on lower DOF parallel mechanisms. Based on this and the society change requirement, motivation of developing reconfigurable parallel mechanisms was revealed for the fact to fulluse the advantages of lower DOF parallel mechanisms for fast application change. The chapter creatively explored the core difference between existing reconfigurable parallel mechanism design principles, which was geometric constraint change to the platform through joint configuration change. This helped classify existing methods into five categories including reassembly based, singularity based, reconfigurable platform based, lockable joint based and metamorphic ways covering reconfigurable joint and link coincidence methods. The first four are not preferred methods due to their extra assembly effort, small workspace, complex model, and less theoretical value while the metamorphic parallel mechanisms show a promising way to develop reconfigurable parallel mechanisms. They have flexibility of local reconfiguration in the limb and possibility of applying existing synthesis/design methods for new development with the modular joint concept and direct joint geometric constraint change. Very few work on systematic synthesis and modelling of metamorphic parallel mechanisms has been done in the literature although some novel applications were proposed. This provides the basic background, justification and motivation of this work to propose a systematic synthesis method and unified

modelling to cover variable configurations of metamorphic parallel mechanisms, an important branch of reconfigurable parallel mechaisms.

Metamorphic parallel mechanisms are a class of new reconfigurable parallel mechanisms with case-by-case designs exist in the literature. To progress on their development, chapter 3 proposed a systematic synthesis strategy for metamorphic parallel mechanisms through designing reconfigurable joints and reconfigurable limbs. From design side, two reconfigurable joints, rT joint and rR joint, have been invented as the reconfiguration source to build twelve reconfigurable units. Following this, possible reconfigurable limbs were obtained by numerating all joint and link combinations classified based on their mobility change. From the synthesis side, the basic condition of mobility change was formulated in screw theory representing their geometric constraint change through the screw rank change before and after the reconfiguration in the limb. This is the same condition when constructing metamorphic parallel mechanisms using the reconfigurable limbs. Based on those two foundations, a general procedure for mobility-change-aimed metamorphic parallel mechanism construction was created and systematically described by introducing the mobility number representation, limb type selection and number calculation.

Using the proposed model and procedure, a family of metamorphic parallel mechanisms, facilitating a range of mobility change between 3 and 6 and a spherical motion when the mobility reaches 3, was synthesized. This was not only a demonstration and validation of the proposed method but also obtained 76 metamorphic parallel mechanisms which are new in the literature. The presented method can be extended to synthsize more metamorphic parallel mechanisms based on the strategy of using reconfigurable joints and limbs. Some obtained ones were summarized as examples and also worth exploring more on their reconfiguration and modelling since they are new in the literature.

Following the general synthesis procedure, chapter 4 proposed a new synthesis method for a specific class of metamorphic parallel mechanisms using the reconfigurable rTPS limb. The reconfiguration capability of the rTPS limb was modelled and explained using the basic geometric constraint equations representing the motion of the spherical joint center in the limb. It was found in one phase, the spherical joint center could move freely in the space, in another

phase it was constrained on a plane. This finding was then used to set up the new synthesis method by considering all possible dependency and 3D arrangement of the constraint planes to construct new parallel mechanism structures. All possible cases have been considered from using two to six rTPS limbs to assemble *n*-$(rT)_2$PS (n=2,3,..,6) parallel mechanisms.

Another important contribution of this chapter was the geometric constraint equation based mechanism mobility analysis. The platform rotation matrix and translation vector were used to reveal the independent relation among their parameters which clealy represented the independent translation and rotation freedom of the platform. This relation also provided the way to explain all the redundant geometric conditions for the *n*-$(rT)_2$PS assemblies. By altering the limbs from $(rT)_2$PS to $(rT)_1$PS, new mechanism phases are obtained with mobility change based on each topology. Generally, an *n*-$(rT)_2$PS (n=2,3,..,6) parallel mechanism has *n*+1 phases with mobility change varied from 6-*n* to 6.

In addition to the new synthesis and modelling method, the main achievement of chapter 4 were the obtained new metamorphic parallel mechanisms which have shown very wide range of mobility change capabilities. For example, the 6-rTPS metamorphic parallel mechanism covers almost all the possible 3D space motion types from a structure with mobility 0 to the full mobility 6. Some novel symmetrical mechanisms have also been found and have potential good performance for real applications, like the 3-rTPS and 4-rTPS metamorphic parallel mechanisms.

Chapter 5 contributed to modelling the geometric constraint change of four novel metamorphic parallel mechanisms, finding their reconfiguration rules and demonstrating their reconfigurable mobilities. As mentioned in the synthesis chapters, the core of metamorphic parallel mechanism reconfiguration is the geometric constraint change from the reconfigurable joints. This is very well described by screws and their dependency is represented by the screw rank change. By associating the motion screws to all joints including the reconfigurable rT joint, their geometric relation is modelled and the corresponding reciprocal screws illustrate their constraint to the platform, which then tells the platform output mobility. This method was applied for the 3-rTPS with perpendicular constraint and it was found to be able to reconfigure into six different phases with mobility change from 3 to 6. Similarly, the constraint screw system also clearly

demonstrated the pure rotation phase, pure translation phase and the 4-DOF 1R3T phase of the 4-rTPS metamorphic parallel mechanism.

Similar to the screw method, this chapter also introduced the basic geometric loop-close equation based constraint modelling and analysis method. Different with the screw method by associating a screw to each joint axis, this method considers the limb structure as a whole and focuses on the output motion capability of the limb end connecting to the platform. By revealing the dependency among all the limb equations, the relation of the translation and rotation parameters is found and that indicates the mobility of the platform. Based on this method, the 4-rTPS metamorphic parallel mechanism shows mobility change between 2 and 6. A special property is also found that it has bifurcated rotation motion at mobility 2 about two perpendicular directions. Similarly, the pure rotation and 1T2R phases of the reconfigurable revolute joint based 3-rRPS MPM was also demonstrated.

Chapter 6 contributed to proposing an unfied kinematics solving method for metamorphic parallel mechanisms based on reconfigurable joints. Every topology of a metamorphic parallel mechanism is equivalent to a traditional parallel mechanism. The proposed strategy solved the kinematics analysis of all the topologies (equivalently a series of parallel mechanisms) in a unified manner by creatively modelling the mechanisms from their limbs and taking one phase of the reconfigurable joint as special case of another. Based on this, the kinematics analysis of four metamorphic parallel mechanisms was solved analytically. Moreover, the unified kinematics model also revealed some novel properties of the metamorphic parallel mechanisms. For example, the 3-rTPrT not only has reconfigurable rotation and translation mobility but also can reconfigure inside each motion type. The rotation center of the pure rotation phase can be reconfigured along the z-axis while the pure translation motion can have different range resulted from the reconfigurable joint tuning. Similarlly the 3-rRPS has infinite number of rotation phases with pure rotation motion but different workspace and kinematics performance.

Another import finding is the introduction of Cayley parameters to the singularity and workspace analysis and representation. The Cayley parameter based 3D coordinate system shows intuitive physical meaning of the rotation motion and gives clear singularity loci demonstration and singularity-free workspace representation. This model also enabled the analytical description of

the workspace of the 3-rTPrT metamorphic parallel mechanism and showed forward kinematics solution zones for general spherical parallel mechanisms. The latter also provided unique forward kinematics solution mapping for the pyramid symmetrical spherical parallel mechanism phase of the 3-rTPrT. The strategy and method in this chapter can be also applied to traditional parallel mechanism analysis and extended to other metamorphic parallel mechanisms and reconfigurable parallel mechanisms.

Chapter 7 made progress on the unified optimal design process for metamorphic parallel mechanisms by covering all their configuration phases with variable mobility. The key challenge solved was to find a way to represent the kinematics performance of all the MPM phases each of which is equivalent to a traditional parallel mechanism. Motion/force transimissibility was found to be a good way by calculating the input and output efficiency between force and motion and avoiding the mixed unit issue in inhomogeneity Jacobean matrix. By setting up the objective function including maximize the singularity-free workspace and the kinematics performance, the optimal design of the 3-rRPS MPM was conducted by covering the 2R1T phase and three 3R phases with different performance. The proposed method could effectively show the trend of the performance with resepct to the design parameter change and the tradeoff between the workspace and the kinematics performance could result in the optimal parameter design. While this was the main contribution and objective of this chapter, the other investigation was actually to explore the performance relation among the phases since they share the same design parameters. A weighted method was applied to set up weights between different phases and also the workspace and the kinematics performance objectives. This is not an ideal optimal design way since the mixed parameter units do not provide clear physical meaning of the obtained optimal results. But it's a good demonstration of the relation between the phases and that they are strongly coupled based on the same mechanism structure parameters.

Based on the optimal design, prototypes were also targeted to show the reconfiguration functions and performance of metamorphic parallel mechanisms. A big lesson was learnt that very high accuracy was required in manufacturing to satisfying the critical geometric constraints in the 3-rTPrT MPM and the prototype was not successfully made functional. Following that, the 3-rRPS showed a good design with less critical geometric constraints and good reconfigurable phases. The built prototype still had joint errors with 2mm and caused the platform a free motion

of translation upto 15mm for one direction and rotation upto 15deg Euler angles. Lots of future work will be conducted to reduce the joint clearance and the effect to the platform motion.

Contribution of chapter 8 was made in proposing the unified inverse dynamics modelling for metamorphic parallel mechanisms by covering all the mobility phases through the strategy of modelling the system from the limbs. This was applied on two metamorphic parallel mechanisms, the 3-rTPrT and the 3-rTPS. In both the pure rotation and pure translation phases of the 3-rTPrT metamorphic parallel mechanism, the rTPrT limb have the same geometric constraint relations among all the limb joints. This founding gave the possibility to solve both phases in one way from the velocity, acceleration to the actuation input forces in the inverse dynamics featured by 15 unknowns in 15 equations. By specifically investigating the joint reaction forces at the platform rT joint cente, a special force decomposition was found, leading to a simplified inverse dynamics analysis by expressing 9 unknowns by the other 6. Then only the six platform dynamic equations are needed to solve the six unknowns. A numerical example was also illustrated to compare the joint reaction forces and actuation force requirements of the pure rotation and pure translation phases when realizing the same trajectory of the platform center point. It was found that the pure rotation phase showed less actuation force, joint reaction force and reaction moments than the pure translation phase for the demonstrated trajectory, which provided reference on the design and application plan.

By modelling from the limb and taking one phase of the rT limb as a special case of the other general phase, the inverse dynamics of the 3-rTPS metamorphic parallel mechanism could be solved in unified force equations based on the virtual work principle to cover all its phases with mobility 3, 4, 5 and 6. Screw theory was used and showed unified format in sovling the joint velocities, accelerations and dynamic forces in the process, which was another factor contributing to the unified dynamics analysis.

This chapter also gave a critical review of the applicability of the proposed dynamics modelling method. It’s concluded that the models were based on ideal parameter assumptions and parameter uncertainties from joint clearance and assembly erros can affect seriously the model results. Future work can include more detailed investigation on how the prototype errors which

are not avoidable will affect the dynamic model and the reconfiguration of the metamorphic parallel mechanisms.

9.2 Future Work

MPMs are still in the early stage. Lot of work should be continued and novel mechanisms and modelling results can be expected. The following topics and directions are suggested:

(1) This study proposed a way to systematically synthesize MPMs and obtained a large number of novel MPMs using the reconfigurable units based on the rT joint and the rR joint. The strategy is mainly based on local limb redundant geometric constraints to change the platform constraint and mobility. Different methods should aslo exist and can be explored to fully utilize the reconfigurable joints to synthesize more MPMs, for example, combined constraint screw change from more than one limbs to the platform.

(2) Unified modelling can be further investigated to provide more intrinsic relation between parameters and the kinematics performance considering the reconfiguration. Since all the phases share the same mechanical structure and parameters, once the design is fixed, the kinematics performance of all the phases are relatively fixed. Thus they are coupled. This phenameno could be further explored and the kinematics coupling relation could be revealed. In this case, one phase might be possible to represent the performance of the other phases and thus represents the metamorphic parallel mechanism. This will be a very useful way to unify the performance representation for further optimal design and applications of the mechanism.

(3) Optimal Design: As discussed in chapter 7, there are several different optimal design methods of parallel mechanisms and this work selected the objective function based one with some common issues. Different methods might be tried and compared with particular consideration of the reconfiguration of the MPMs. A specific task or design for a class of tasks can be considered for the true optimal design to realize a specified workspace and satisfy the minimum performance requirements, like minimum motion/force transimissibility indices, minimum accuracy, minimum force capability, minimum acceleration and velocity values, and at the same time following the application constraints of the dimensions, footprint, power consumption, cost, etc.

(4) The weighted objective function has the obvious issue that it does not have a clear physical meaning and obtained results do not show a understandable performance division. But it showed a good connection and coupling in this work for linking different phases of a metamorphic parallel mechanism. Based on the above point (2), if the coupling relation between phases is found, this weighted method will be associated with clear physical meaning to represent different phases as a whole in the optimal design process. This should be explored and will be useful for optimal design for MPMs and other reconfigurable parallel mechanisms.

(5) Dynamic performance modelling and optimization: Due to the limited time, this work did not go for the dynamic performance analysis and it based optimization which should be necessary work for the applications of the metamorphic parallel mechanisms. Similar to the kinematics performance, a unified way should be explored to represent the dynamics performance of all phases together to optimize the common structure parameters among them. The ratio, scale or performance division between them can be investigated since they are coupled.

(6) Stiffness reconfiguration: another topic that should be explored is the stiffness variation from the reconfiguration. Mechanically, the mechanism is in the same structure but with local joint direction change. This will cause the platform output motion change but also the corresponding stiffness change. The variation should be known for the knowledge in application based design. On the other side, there might be applications requiring variable stiffness change and this reconfiguration can be a solution to change the platform output stiffness once this rule is clearly found.

(7) Based on the experience in the prototyping, clearance and critical geometric constraints are the two main issues affect the final performance of the design. The initial point to solve this is to start from the reconfigurable joint design by improving the current worm gear based solution accuracry and quality. The joint reconfiguration control should be also included in the design cycle since it’s critical in realizing the mechanism reconfiguration and performance after the joint reconfigured. From the accuracy, mechanical positioning might be a solution by introducing mechanical stopper or slots in fixing the rotational joint axes into the desired location and direction. For more general and continuous joint axis reconfiguration, feedback control with high resolute encoder based position sensing should be considered.

(8) Following the above point (7), the final performance of the mechanism platform will be also critically related to the kinematics and dynamics paramters. Their effect on the platform motion should be theoretically analysed and understood. The joint clearance and assembly erros may not only change the performance but also the mobility if the required geometric constraints are bias far from its nominal value. This model will also help in finding strategies to minimize the errors and effect to the final platform motion performance through workspace based trajectory planning and input compensation.

(9) Before all the theoretical kinematics and dyanmics models can be applied to the real platform, system parameter identification should be conducted. For the dynamic parameters including the mass, intertia, first order moment, linear dynamic model can be derived for system identification. But it was also found in the literature that not all of them showed effective contribution to the dynamic performance of the platform and thus could not be idenfitied correctly. From this point of view, an advantage of using multi-phases with different mobility might be found to effectively identify different parameter sets in different phases which in combined manner solves all the parameters.

(10) Based on all the above, a major future work is the experimental reconfiguration validation and performance evaluation for selected metamorphic parallel mechanism prototype, for example, the built 3-rRPS. One of the key component is the control law development which should work for all phases with good robustness and adaptability. Before this, basic PID cotnrollers might be used for each phase with functional output and then a gain scheduling method can be developed based on those tested PID controllers. Model based control might be more attractive considering automatic adaption, for example, adaptive control, which also has the capability in updating the system parameters in real time and adaptive to different phases but detailed control gains and parameters should be investigated.

References

[1] Gough, V.E., 1956, Automobile stability, control, and tyre performance, *Proc. Automobile Division, Inst. Mech. E.*, 171, 392-394.

[2] Huang, T., Li, M., Zhao, X.M., Mei, J.P., Chetwynd, D.G., and Hu, S.J., 2005, Conceptual design and dimensional synthesis of 3-DOF module of the TriVariant—a novel 5-DOF reconfigurable hybrid robot, *IEEE Transactions on Robotics*, 21(3), 449-456.

[3] Huang, T., Wang, J.S., and Whitehouse, D.J., 1999, Closed form solution to the workspace of hexapod-based virtual axis machine tools, *ASME Journal of Mechanical Design*, 121(1), 26-31.

[4] Dai, J.S., and Kerr, D.R., 2000, Six-component contact force measurement device based on the Stewart platform, *Proc. Inst. Mech. Eng., Part C: J. Mech. Eng. Sci.*, 214(5), 687–697.

[5] Girone, M.J., Burdea, G.C., and Bouzit, M., 1999, The Rutgers ankle orthopedic rehabilitation interface. In Proc. of the ASME, Dynamic Systems and Control Division, International Mechanical Engineering Congress and Exposition, 67, 305-312.

[6] Brandt, G., Zimolong, A., Carrat, L., Merloz, P., Staudte, H.W., Lavallee, S., Radermacher, K., and Rau, G., 1999, CRIGOS: a compact robot for image- guided orthopedic surgery, *IEEE Transactions on Information Technology in Biomedicine*, 3(4), 252-260.

[7] Merlet, J.P., 2008, Parallel Robots, 2nd Edition. Springer.

[8] Gan, D.M., Liao, Q.Z., Dai, J.S., and Wei, S.M., 2010, Design and kinematics analysis of a new 3CCC parallel mechanism, *Robotica*, 28(7), 1065-1072.

[9] Chen, I.M., Li, S.H., and Cathala, A., 2003, Mechatronic design and locomotion of Amoebot—a metamorphic underwater vehicle, *Journal of Robotic Systems*, 20(6), 307-314.

[10] Gan, D.M., Dai, J.S., Liao, Q.Z., 2009, Mobility analysis of two types of metamorphic parallel mechanisms, *ASME Journal of Mechanisms and Robotics*, 1**,** 041007_1-9.

[11] Bonev I. The True Origins of Parallel Robots. Newsletter, 2001, http://www.parallemic.org/Reviews/Review007.html

[12] Gwinnett, J.E., Amusement devices, US Patent No. 1,789,680, January 20, 1931.

[13] Pollard, W.L.G., Spray painting machine, US Patent No. 2,213,108, August 26, 1940.

[14] Cappel, K.L., Motion simulator, US Patent No. 3,295,224, January 3, 1967.

[15] Stewart, D., 1965, A platform with six degrees of freedom, *Proceedings of the IMechE*, 180, Pt. 1, No. 15, 371-385,.

[16] Dasgupta, B, Mruthyunjaya, T.S., 2000, The Stewart platform manipulator: a review, *Mechanism and Machine Theory*, 35, 15-40.

[17] Hunt, K. H., 1983, Structural Kinematics of In-Parallel-Actuated Robot-Arms, *ASME J. Mech., Transm., Autom. Des.*, 105, 705-712.

[18] Mohamed, M. G., and Duffy, J., 1985, A Direct Determination of the Instantaneous Kinematics of Fully Parallel Robot Manipulators, *ASME J. Mech., Transm., Autom. Des*., 107, 226-229

[19] Fichter, E. F., 1986, A Stewart Platform-Based Manipulator: General Theory and Practical Construction, *Int. J. Robot. Res*., 5, 157-182.

[20] Faugere, J. C., and Lazard, D., 1995, Combinatorial classes of parallel manipulators, *Mech. Mach. Theory*, 30, no.6, 765-776.

[21] Liao, Q. Z., Senevirantne, L. D., and Earles, S. W. E., 1995, Forward positional analysis for the general 4-6 in-parallel platform, *Journal of Mechanical Engineering Science*, 209, 55-67.

[22] Dafaoui, E. M., Amirat, Y., Pontnau, F., and Francois, C., 1998, Analysis and design of a six-DOF parallel manipulator: Modeling, singular configurations and workspace, *IEEE Trans. Robot. Autom.*, 14, 78-91.

[23] Merlet, J. P., 2006, Jacobian, Manipulability, Condition Number, and Accuracy of Parallel Robots, *ASME J. Mech. Des*., 128, 199-206.

[24] Gan, D. M., Liao, Q. Z., Dai, J. S., Wei S. M., and Seneviratne, L. D., 2009, Forward displacement analysis of the general 6-6 Stewart mechanism using Grobner bases, *Mechanism and Machine Theory*, 44(9), 1640-1647.

[25] Dai, J. S., Sodhi, C., and Kerr, D. R., 1994, Design and Analysis of a New Six-Component Force Transducer Based on the Stewart Platform for Robotic Grasping, *Proceedings of the second Biennial European Joint Conference on Engineering Systems Design and Analysis*, *ASME PD*, Vol. 64, No. 8-3, London, 809-817.

[26] Soh, G.S., and McCarthy, J.M., 2009, Parametric Design of a Spherical Eight-Bar Linkage Based on a Spherical Parallel Manipulator, *Transactions of the ASME: Journal of Mechanisms and Robotics*, 1(2), 011004 (1-8).

[27] Gan, D. M., Dai, J. S., Dias, J., Umer, R., and Seneviratne, L. D. 2015, Singularity-Free Workspace Aimed Optimal Design of a 2T2R Parallel Mechanism for Automated Fiber Placement, *Transactions of the ASME: Journal of Mechanisms and Robotics*, 7(4), 041022_1-9.

[28] Husty, M. L., 1996, An Algorithm for Solving the Direct Kinematics of General Stewart-Gough Platforms, *Mech. Mach. Theory*, 31(4), 365-380.

[29] Gan, D. M., Liao, Q. Z., Dai, J. S., Wei, S. M., and Seneviratne, L. D., 2009, Forward displacement analysis of a new 1CCC-5SPS parallel mechanism using Grobner theory, *Proc. IMechE, Part C: J. Mechanical Engineering Science*, 223(C5), 1233-1241.

[30] Baiges, I. J., and Duffy, J., 1996, Dynamic Modeling of Parallel Manipulators, *Proceedings of the 1996 ASME Design Engineering Technical Conferences*, paper No. 96-DETC/MECH-1136.

[31] Jobin, J.-P., and Gosselin, C., 2009, Discretely Deformable Surface Based on Mechanical Interpolation: Application to the Design of a Dynamically Reconfigurable Theater Stage, *Transactions of the ASME: Journal of Mechanisms and Robotics*, 1(2), 11005 (1-9).

[32] Huang, Z., and Fang, Y. F., 1996, Studying on the Kinematic Characteristics of 3-DOF In-Parallel Actuated Platform Mechanisms, *Mech. Mach. Theory*, 31, 1009-1018.

[33] Di Gregorio, R., and Parenti-Castelli, V., 1998, A translational 3-DOF parallel manipulator, in *Advances in Robot Kinematics: Analysis and Control*, MA: Kluwer, Norwell, 49-58.

[34] Pouliot, N. A., Nahon, M. A., and Gosselin, C. M., 1998, Motion Simulation Capabilities of Three-Degree-Of-Freedom Flight Simulators, *AIAA J. Aircraft,* 35(1), 9-17.

[35] Tsai, L. W., and Joshi, S. A., 2002, Kinematic Analysis of 3 DOF Position Mechanisms for Use in Hybrid Kinematic Machines, *ASME J. Mech. Des*., 124(2), 245-253.

[36] Zhao, T.S., Dai, J.S., and Huang, Z., 2002, Geometric Synthesis of Spatial Parallel Manipulators with Fewer Than Six Degrees of Freedom, *Journal of Mechanical Engineering Science*, 216(12), 1175-1185.

[37] Fang, Y. F., and Tsai, L. W., 2004, Structure Synthesis of a Class of 3-DOF Rotational Parallel Manipulators, *IEEE Trans. Robot. Autom*., 20, 117-121.

[38] Saglia, J.A., Dai, J.S., and Caldwell, D.G., 2008, Geometry and kinematic analysis of a redundantly actuated parallel mechanism that eliminates singularities and improves dexterity, *ASME J. Mech. Des*., 130, 12450_1-5.

[39] Clavel, R., Device for the Movement and Positioning of an Element in Space, US Patent No. 4,976,582, December 11, 1990.

[40] http://www04.abb.com/global/seitp/seitp202.nsf/c71c66c1f02e6575c125711f004660e6/d3900b3c7489746bc12571b700351d6c/$FILE/Data+Sheet+IRB+340HR.pdf

[41] http://www.fanuc.eu/pl/en/robots/robot-filter-page/m1-series/m-1ia-05s

[42] Miller, K., 1995, Modeling of Dynamics and Model-Based Control of DELTA Direct-Drive Parallel Robot, *Journal of Robotics and Mechatronics*, 17(4), 344-352.

[43] Laribi, M.A., Romdhane, L., and Zeghloul, S., 2007, Analysis and dimensional synthesis of the DELTA robot for a prescribed workspace Mechanism and Machine Theory, 42(7), 859–870.

[44] Xie F.G., and Liu, X.J., 2015, Design and development of a high-speed and high-rotation robot with four identical arms and a single platform, *ASME Journal of Mechanisms and Robotics*, 7(4), 041015_1-12,.

[45] Albert Lester Balmaceda-Santamaría, Eduardo Castillo-Castaneda, Jaime Gallardo-Alvarado, 2016, A Novel Reconfiguration Strategy of a Delta-Type Parallel Manipulator, *International Journal of Advanced Robotic Systems*, 13(1), 1-11.

[46] Neumann, K.-E., US patent 4,732,525, Mar. 22, 1988.

[47] Siciliano, B., 1999, The Tricept robot: Inverse kinematics, manipulability analysis and closed-loop direct kinematics algorithm, *Robotica*, 17(4), 437- 445.

[48] Lee, K., Shah, D.K., 1987, Kinematic analysis of a three degrees of freedom in-parallel actuated manipulator, in: *Proceedings of the IEEE International Conference on Robotics and Automation*, 1, 345–350.

[49] Merlet, J.P., 2001, Micro parallel robot MIPS for medical applications, *Proceedings of the 8th International Conference on Emerging Technologies and Factory Automation*, Antibes-Juan les Pins, France, 2001.

[50] Huang, Z., Wang, J., and Fang, Y., 2002, Analysis of instantaneous motions of deficient-rank 3rps parallel manipulators, *Mechanism and Machine Theory*, 37, 229–240.

[51] Liu, C.H., and Cheng, S., 2004, Direct singular positions of 3RPS parallel manipulator, *ASME J. Mech. Des*. 126, 1006–1016.

[52] Fitle, K., Pehlivan, A. U., and O'Malley, M. K., 2015, A robotic exoskeleton for rehabilitation and assessment of the upper limb following incomplete spinal cord injury, *IEEE International Conference on Robotics and Automation (ICRA)*. Seattle, Washington,

2015.

[53] http://www.pkmtricept.com/productos/index.php?id=en&Nproduct=1240238156

[54] Gosselin, C., St-Pierre, E., and Gagné, M., 1996, On the Development of the Agile Eye: Mechanical Design, Control Issues and Experimentation, *IEEE Rob. Autom. Mag.*, 3(4), 29–37.

[55] Gogu, G., 2012, Parallel Wrists with Three Degrees of Freedom, Structural Synthesis of Parallel Robots, *Solid Mechanics and Its Applications*, 183, 483-552.

[56] Innocenti, C., and Parenti-Castelli, V., 1993, Echelon form solution of direct kinematics for the general fully-parallel spherical wrist, *Mechanism and Machine Theory*, 28(4), 553-561.

[57] Kong, X.-W., 1998, Forward Displacement Analysis of Three New Classes of Analytic Spherical Parallel Manipulators, *Proceedings of 1998 ASME Design Engineering Technical Conferences*, DETC98/MECH-5953, USA, September 13-16, 1998.

[58] Gan, D. M., Seneviratne, L. D., and Dias, J., 2012, Design and Analytical Kinematics of a Robot Wrist Based on a Parallel Mechanism, *Proceedings of the 14th International Symposium on Robotics and Applications*, Puerto Vallarta, Mexico, June 24-28, 2012.

[59] Karouia, M., and Hervé, J. M., 2000, A Three-dof Tripod for Generating Spherical Rotation". in: J. Lenarcic,M.M. Stanisic (Eds.), *Advances in Robot Kinematics*, Kluwer Academic Publishers, Netherlands, 395–402.

[60] Tsai, L. W., and Sameer, J., 2000, Kinematics and Optimization of a Spatial 3-UPU Parallel Manipulator, *ASME J. Mech. Des*., 122, 439–446.

[61] Di Gregorio, R., 2003, Kinematics of the 3-UPU Wrist, *Mechanism and Machine Theory*, 28, 253-263.

[62] Gosselin, C., and Angeles, J., 1989, The Optimum Kinematic Design of a Spherical Three-Degree-of-Freedom Parallel Manipulator, *ASME J. Mech., Transm. Autom. Des.*, 111(2), 202–207.

[63] Vischer, P., and Clavel, R., 2000, Argos: A Novel 3-dof Parallel Wrist Mechanism, *Int. J. Robot. Res.*, 19(1), 5–11.

[64] Gregorio, R. D., 2001, A New Parallel Wrist Using Only Revolute Pairs: the 3-RUU Wrist, *Robotica*, 19(3), 305–309.

[65] Cox, D., and Tesar, D., 1989, The Dynamic Model of A Three-Degree-of-Freedom Parallel Robotic Shoulder Module, presented at 4th Int. Conf. Adv. Robot., Columbus,

OH.

[66] Hofschulte, J., Seebode, M., and Gerth, W., 2004, Parallel Manipulator Hip Joint for a Bipedal Robot, *Climbing and Walking Robots*, Springer, New York, 601–609.

[67] Cui, L., and Dai, J. S., 2012, Reciprocity-Based Singular Value Decomposition for Inverse Kinematic Analysis of the Metamorphic Multifingered Hand, *ASME Journal of Mechanisms and Robotics*, 4(3), 034502.

[68] Cui, L., and Dai, J. S., 2011, Posture, workspace, and manipulability of the metamorphic multifingered hand with an articulated palm, *ASME Journal of Mechanisms and Robotics*, 3(2), 021001.

[69] Li, T., and Payandeh, S., 2002, Design of Spherical Parallel Mechanisms for Application to Laparoscopic Surgery, *Robotica*, 20(2), 133–138.

[70] Kuo, C.-H., and Dai, J. S., 2012, Kinematics of a Fully-Decoupled Remote Center-of-Motion Parallel Manipulator for Minimally Invasive Surgery, *ASME J. Med. Devices*, 6(2), 021008.

[71] Dai, J., Zhao, T., and Nester, C., 2004, Sprained Ankle Physiotherapy Based Mechanism Synthesis and Stiffness Analysis of Rehabilitation Robotic Devices, Special Issue Rehabil. Robot., *Auton. Robot.*, 16(2), 207–218.

[72] https://cra.org/crn/2017/02/2016-robotics-roadmap-national-robotics-initiative-2-0/

[73] Dash, A. K., Chen, I.-M., Yeo, S. H., and Yang, G., 2005, Task-oriented configuration design for reconfigurable parallel manipulator systems, *Int J Com-Int Manuf*, 18, 615-634.

[74] Finistauri, A. D., Xi, F., and Petz, B., 2008, Architecture design and optimization of an on-thefly reconfigurable parallel robot, in *Parallel Manipulators, towards New Applications*, H. Wu, Ed., 1st ed Vienna: I-Tech Education and Publishing, 379-404.

[75] Bi, Z. M., and Wang, L., 2009, Optimal design of reconfigurable parallel machining systems, *Robot Com-Int Manf*, 25, 951-961.

[76] Zlatanov, D., Bonev, I.A., and Gosselin, C.M., 2002, Constraint singularities of parallel mechanisms, in: Proc. IEEE Int. Conf. Robot. Autom., Washington, D.C., 496–502.

[77] Wohlhart, K., 1996, Kinematotropic linkages, In: Lenarcic J. Parenti-Castelli V., *Advances in Robot Kinematics*, Kluwer, Dordrecht, 1996, 359-368.

[78] Fanghella, P., Galletti, C., and Giannotti, E., 2006, Parallel robots that change their group of motion, In: Lenarčič J. Parenti-Castelli V., *Advances in Robot Kinematics: Mechanisms and Motion*, Springer, Dordrecht, 2006, 49-56.

[79] Kong, X.W., Gosselin, C.M., and Richard, P.L., 2007, Type synthesis of parallel mechanisms with multiple operation modes, *ASME J. Mech. Des*., 129(6), 595–601.

[80] Kong, X.W., 2013, Type Synthesis of 3-DOF parallel manipulators with both a planar operation mode and a spatial translational operation mode1, *J. Mechanisms Robotics*, 5(4), 041015.

[81] Walter, D.R., Husty, M.L., and Pfurner, M., 2008, The SNU 3-UPU parallel robot from a theoretical viewpoint, Proceedings of the Second International Workshop on Fundamental Issues and Future Research Directions for Parallel Mechanisms and Manipulators, Montpellier, France, Sept. 21-22, 2008, 151-158.

[82] Walter, D.R., Husty, M.L., and Pfurner, M., 2009, A complete kinematic analysis of the SNU 3-UPU parallel robot. In D.J. Bates, G.-M. Besana, S. Di Rocco, and C.W. Wampler, editors, *Interactions of Classical and NumericalAlgebraic Geometry*, volume Contemporary Mathematics 496, 2009, 331-346.

[83] Zeng, Q., Ehmann, K. F., and Cao, J., 2016, Design of general kinematatropic mechanisms, *Robot Com-Int Manf*, 38, 67-81.

[84] Refaat, S., Hervé, J.M., Nahavandi, S., and Trinh, H., 2007, Two-mode over-constrained three-Dofs rotational-translational linear-motor-based parallel-kinematics mechanism for machine tool applications, *Robotica*, 25(4), 461–466.

[85] Li, Q., and Hervé, J.M., 2009, Parallel mechanisms with bifurcation of Schoenflies motion, *IEEE Transactions on Robotics*, 25(1), 158-164.

[86] Chen, Q.H., Li, Q.C., Wu, C.Y., Hu, X.D., and Huang, Z., 2009, Mobility analysis of 4-RPRPR and 4-RRRPR parallel mechanisms with bifurcation of Schoenflies motion by screw theory, *ASME/IFToMM International Conference on Reconfigurable Mechanisms and Robotics*, London, June 22-24, 2009, 279-284.

[87] Gogu, G., 2011, Maximally regular T2R1-type parallel manipulators with bifurcated spatial motion, *ASME J. Mech. Rob.*, 3(1), 011010_1-8.

[88] Gogu, G. 2011, Bifurcation in constraint singularities and structural parameters of parallel mechanisms, *Meccanica*, 46, 65-74.

[89] Gan, D.M., Dai, J.S., and Liao, Q.Z., 2010, Constraint analysis on mobility change of a novel metamorphic parallel mechanism, *Mechanism and Machine Theory*, 45(12), 1864-1876.

[90] Zhang, K.T., Dai, J.S., and Fang, Y.F., 2010, Topology and constraint analysis of phase

change in the metamorphic chain and its evolved mechanism. *ASME J. Mech. Des.*, 132(12), 121001_1-11.

[91] Gan, D. M., and Dai, J. S., 2013, Geometry Constraint and Branch Motion Evolution of 3-*PUP* Parallel Mechanisms with Bifurcated Motion, *Mechanism and Machine Theory*, 61, 168-183.

[92] Bonev, I.A., Briot, S., Wenger, P., and Chablat, D., 2008, Changing assembly modes without passing parallel singularities in non-cuspidal 3-RPR planar parallel robots, *Second International Workshop on Fundamental Issues and Future Research Directions for Parallel Mechanisms and Manipulators*, Montpellier, France, September 21–22, 2008.

[93] Pagis, G., Bouton, N., Briot, S., and Martinet, P., 2015, Enlarging parallel robot workspace through type-2 singularity crossing, *Control Engineering Practice*, 39, 1-11.

[94] Nurahmi, L., Caro, S., and Wenger, P., 2015, Operation Modes and Singularity analysis of 3-PRS Parallel Manipulators with different arrangements of P-joints, *Proceedings of the ASME 2015 International Design Engineering Technical Conference and Computers and Information in Engineering Conference*, Boston, USA, August 2-5, 2015.

[95] Wenger, P., 2007, Cuspidal and noncuspidal robot manipulators, *Special issue of Robotica on Geometry in Robotics and Sensing*, 25(6), 677-690.

[96] Arakelian, V., Briot, S., and Glazunov, V., 2008, Increase of singularity-free zones in the workspace of parallel manipulators using mechanisms of variable structure, *Mech Mach Theory*, 43(9), 1129–1140.

[97] Caro, S., Chablat, D., and Hu, Y., 2014, Algorithm for the Actuation Mode Selection of the Parallel Manipulator NAVARO, *ASME International Design Engineering Technical Conferences and Computers and Information in Engineering Conference*, Volume 5B: 38th Mechanisms and Robotics Conference, Buffalo, New York, USA, August 17–20, 2014.

[98] Zeng, Q., and Ehmann, K. F., 2014, Design of parallel hybrid-loop manipulators with kinematotropic property and deployability, *Mechanism and Machine Theory*, 71, 1-26.

[99] Kronig, L., 2010, Overview of Biomimetics and Artiomemetics in Robotics, Final Year Undergraduate Project Report, Heriot-Watt University, Edinburgh, UK.

[100] Kong, X.W., and Jin, Y., 2016, Type Synthesis of 3-DOF multi-mode translational/spherical parallel mechanisms with lockable joints, *Mechanism and Machine Theory*, 96, 323-333.

[101] Dai, J.S., Rees, J.J., 1999, Mobility in metamorphic mechanisms of foldable/erectable kinds, *ASME J. Mech. Des*., 121(3), 375–382.

[102] Dai, J.S., and Wang, D., 2007, Geometric analysis and synthesis of the metamorphic robotic hand, *ASME J. Mech. Des.*, 129(11), 1191-1197.

[103] Leonesio, M., Bianchi, G., and Manara, P., 2007, A general approach for self-locking analysis in closed kinematic chains, Proceedings of the 12th World Congress in Mechanism and Machine Theory, Besancon, France, Jun., 2007, 141–147.

[104] Winder, B.G., Magleby, S.P., and Howell, L.L., 2009, Kinematic representations of pop-up paper mechanisms, *ASME J. Mech. Rob*., 1(2), 021009.

[105] Ye, W., Fang, Y., Zhang, K., and Guo, S., 2014, A new family of reconfigurable parallel mechanisms with diamond kinematotropic chain, *Mechanism and Machine Theory*, 74, 1-9.

[106] Kuo, C.H., and Yan, H.S., 2007, On the mobility and configuration singularity of mechanisms with variable topologies, *ASME J. Mech. Des.*, 129, 617-624.

[107] Gan, D.M., Dai, J.S., and Caldwell, D.G., 2011, Constraint-based limb synthesis and mobility-change aimed mechanism construction, *ASME J. Mech. Des.*, 133(5), 051001_1-9.

[108] Zhang, K.T., Dai, J.S., and Fang, Y.F., 2012, Geometric constraint and mobility variation of Two 3SvPSv metamorphic parallel mechanisms, *ASME Journal of Mechanical Design*, 135(1), 11001.

[109] Ye, W., Fang, Y., Zhang, K., and Guo, S., 2016, Mobility variation of a family of metamorphic parallel mechanisms with reconfigurable hybrid limbs, *Robot Com-Int Manf*, 41, 145-162.

[110] Gan, D. M., Dias, J., and Seneviratne, L. D., 2016, Unified Kinematics and Optimal Design of a 3-rRPS Metamorphic Parallel Mechanism with a Reconfigurable Revolute Joint, *Mechanism and Machine Theory*, 96(part 2), 239-254.

[111] Grosch, P., Di Gregorio, R., López, J., and Thomas, F., 2010, Motion planning for a novel reconfigurable parallel manipulator with lockable revolute joints, *Proceedings on 2010 IEEE International Conference on Robotics and Automation*, 3–7 May, 2010, Anchorage, AK, 4697–4702.

[112] Coppola, G., Zhang, D., and Liu, K.F., 2014, A 6-DOF reconfigurable hybrid parallel manipulator, *Robot Com-Int Manf*, 30, 99-106.

[113] Tian, Y.B., Zhang, D., Yao, Y.A., Kong, X.W., and Li, Y.Z., 2017, A reconfigurable multi-mode mobile parallel robot, *Mechanism and Machine Theory*, 111, 39-65.

[114] Li, D., Li, C., Zhang, Z., and Kong, X., 2014, Block adjacency matrix method for analyzing the configuration transformations of metamorphic parallel mechanisms, *Proceedings of the ASME Design Engineering Technical Conferences & Computers and Information in Engineering Conference*, DETC2014- 34850, August 17–20, 2014, Buffalo, USA.

[115] Carbonari, L., Callegari, M., Palmieri, G., and Palpacelli, M.-C., 2014, A new class of reconfigurable parallel kinematic machines, *Mechanism and Machine Theory*, 79, 173-183.

[116] Hervé, J. M., and Sparacino, F., 1991, Structural Synthesis of Parallel Robots Generating Spatial Translation, In Proceedings of the Fifth International Conference on Advanced Robotics, Pisa, Italy, 1, 808–813.

[117] Carricato, M., and Parenti-Castelli, V., 2003, A Family of 3-DOF Translational Parallel Manipulators, *ASME J. Mech. Des*., 125(2), 302–307.

[118] Jin, Q., and Yang, T.-L., 2004, Theory for Topology Synthesis of Parallel Manipulators and Its Application to Three-Dimension-Translation Parallel Manipulators, *ASME J. Mech. Des*., 126(4), 625–639.

[119] Yang, T. L., Liu, A. X, Jin Q., Luo, Y. F., Shen, H. P., Hang, L.B., 2009, Position and Orientation Characteristic Equation for Topological Design of Robot Mechanisms, *ASME Journal of Mechanical Design*, 131(2), 021001-(1-17).

[120] Frisoli, A., Checcacci, D., Salsedo, F., and Bergamasco, M., 2000, Synthesis by Screw Algebra of Translating In-Parallel Actuated Mechanisms, *Advances in Robot Kinematics*, J. Lenarčič and M. M. Stanišič, eds., Kluwer Academic, Dordrecht, pp. 433–440.

[121] Huang, Z., and Li, Q. C., 2002, General Methodology for the Type Synthesis of Lower-Mobility Symmetrical Parallel Manipulators and Several Novel Manipulators, *Int. J. Robot. Res*., 21(2), 131–145.

[122] Kim, D., and Chung, W. K., 2003, Kinematic Condition Analysis of Three-DOF Pure Translational Parallel Manipulators, *ASME J. Mech. Des*., 125(2), 323–331.

[123] Kong, X., and Gosselin, C. M., 2004, Type Synthesis of 3-DOF Spherical Parallel Manipulators Based on Screw Theory, *ASME J. Mech. Des*., 126(1), 101–108.

[124] Dai, J.S., Huang, Z., and Lipkin, H., 2006, Mobility of Overconstrained Parallel

Mechanisms, Special Supplement on Spatial Mechanisms and Robot Manipulators, *ASME J. Mech. Des*., 128(1), 220-229.

[125] Maraje S., Nurahmi, L., and Caro, S., 2016, Operation Modes comparison of a reconfigurable 3-PRS Parallel Manipulator based on kinematics performance, Proceedings of the ASME International Design Engineering Technical Conference and Computers and Information in Engineering Conference, Charlotte, North Carolina, USA, August 21-24, 2016.

[126] Palpacelli, M.-C., Carbonari, L., Palmieri, G., and Callegari, M., 2015, Analysis and Design of a Reconfigurable 3-DoF Parallel Manipulator for Multimodal Tasks, *IEEE/ASME Transactions on Mechatronics*, 20(4), 1975-1985.

[127] Ye, W., Fang, Y., and Guo, S.. 2017, Design and analysis of a reconfigurable parallel mechanism for multidirectional additive manufacturing, *Mechanism and Machine Theory*, 112, 307-326.

[128] Dai, J.S., Wang, D.L, and Cui, L., 2009, Orientation and Workspace Analysis of the Multifingered Metamorphic Hand — Metahand, *IEEE Transactions on Robotics*, 25(4), 942-947.

[129] Wei, G.W., Dai, J.S., Wang, S.X., and Luo, H.F., 2011, Kinematic analysis and prototype of a metamorphic anthropomorphic hand with a reconfigurable palm, *Int. J. Hum. Robot*., 8, 459-479.

[130] Wei, G.W., Stephan, F., Aminzadeh, V., Würdemann, H., Walker, R., Dai, J.S., and Gogu, G., 2014, DEXDEB--Application of DEXtrous robotic hands for DEBoning operation, in F. Rohrbein et al. (eds), in *Gearing Up and Accelerating Cross-Fertilization between Academic and Industrial Robotics Research in Europe*, Springer Tracts in Advanced Robotics, 94, 217-235.

[131] Zhang, K.T., Fang, Y.F., and Fang, H.R., 2007, Design and analysis of a rovermechanism based on the metamorphic principle, *Journal of Beijing University of Aeronautics and Astronautics*, 33, 838-841.

[132] Ding, X.L., and Xu, K., 2009, Design and analysis of a novel metamorphic wheel-legged rover mechanism, *J. Cent. South. Univ*. *T*., 40, 91-101.

[133] Zhang, W.X., Ding, X.L., and Dai, J.S., 2009, Design and stability of operating mechanism for a spacecraft hatch, *Chinese. J. Aeronaut*. 22, 453-458.

[134] Li, S.J., Wang, H.G., Meng, Q.L., and Dai, J. S., 2016, Task-based structure synthesis of

source metamorphic mechanisms and constrained forms of metamorphic joints, *Mechanism and Machine Theory*, 96, 334-345.

[135] Waldron, K. J., Kinzel, G. L., 1998, Kinematics, Dynamics, and Design of Machinery, *John Wiley & Sons Inc.*

[136] Dai, J. S., and Rees, J. J., 2001, Interrelationship Between Screw Systems and Corresponding Reciprocal Systems and Applications, *Mech. Mach. Theory*, 36, 633-651.

[137] Dai, J.S. and Rees Jones, J., 2002, Null Space Construction Using Cofactors from a Screw Algebra Context, *Proc. Royal Society, Lond. A: Mathematical, Physical and Engineering Sciences*, 458(2024), 1845-1866.

[138] Dai, J. S., 2006, An Historical Review of the Theoretical Development of Rigid Body Displacements from Rodrigues Parameters to the Finite Twist, *Mechanism and Machine Theory*, 41(1), 41-52.

[139] Huang Z., and Fang, Y.F., 1996, Kinematic characteristics analysis of 3-DOF in-parallel actuated pyramid mechanisms, *Mech. Mach. Theory*, 31(8), 1009-1018.

[140] Gan, D. M., Dai, J. S., Dias, J., and Seneviratne, L. D., 2014, Constraint-plane-based synthesis and topology variation of a class of metamorphic parallel mechanisms, *Journal of Mechanical Science and Technology*, 28(10), 4179-4191.

[141] Kong, X., and Gosselin, C., 2000, Classification of 6-SPS parallel manipulators according to their components, *Proc. of ASME Design Engineering Technical Conferences*, Baltimore, Mariland, USA (2000) DETC2000/MECH–14105.

[142] Zhang, C., and Song, S., 1991, Forward kinematics of a class of parallel (Stewart) platforms with closed-form solutions, *IEEE International Conference on Robotics and Automation*, Sacramento, CA , USA, 2676–2681.

[143] Gan, D. M., Dai, J. S., Dias, J., and Seneviratne, L. D., 2013, Reconfigurability and unified kinematics modeling of a 3rTPS metamorphic parallel mechanism with perpendicular constraint screws, *Robotics and Computer Integrated Manufacturing*, 29(4), 121-128.

[144] Gan, D. M., Dai, J. S., Dias, J., and Seneviratne, L. D., 2013, Unified kinematics and singularity analysis of a metamorphic parallel mechanism with bifurcated motion, *Transactions of the ASME: Journal of Mechanisms and Robotics*, 5(3), 041104_1-11.

[145] Dai, J. S., Holland, N., and Kerr, D. R., 1995, Finite Twist Mapping and Its Application to Planar Serial Manipulators with Revolute Joints, *J. Mech. Eng. Sci*., 209, 263-272.

[146] Bottema, O., and Roth, B., Theoretical Kinematics, North-Holland, New York, 1979.

[147] Gan, D. M., Dai, J. S., Dias, J., and Seneviratne, L. D., 2015, Forward Kinematics Solution Distribution and Analytic Singularity-Free Workspace of Linear-Actuated Symmetrical Spherical Parallel Manipulators, ASME: Journal of Mechanisms and Robotics, 7(4), 041007_1-8.

[148] Husty, M.L., 1996, An Algorithm for Solving the Direct Kinematics of General Stewart–Gough Platform, *Mech. Mach. Theory*, 31, 365–380.

[149] Bai, S. P., Hansen, M. R., and Angeles, J., 2009, A Robust Forward-Displacement Analysis of Spherical Parallel Robots, *Mech. Mach. Theory*, 44, 2204–2216.

[150] Huang, Z., and Yao, Y. L., 1999, A New Closed-Form Kinematics of the Generalized 3-dof Spherical Parallel Manipulator, *Robotica*, 17(5), 475–485.

[151] Innocenti, C., 1995, Direct Kinematics in Analytical Form of the 6-4 Fully-Parallel Mechanism, *ASME Journal of Mechanical Design*, 117, 89-95.

[152] Lu, Y., Zhang, M., Shi, Y., and Yu, J., 2009, Kinematics and Statics Analysis of a Novel 4-dof 2SPS+2SPR Parallel Manipulator and Solving Its Workspace, *Robotica*, 27(5), 771-778.

[153] Sokolov, A., and Xirouchakis, P., 2005, Kinematics of a 3-DOF Parallel Manipulator with an R-P-S Joint Structure, *Robotica*, 23(2), 207-217.

[154] Kong, X., Gosselin, C. M., and Ritchie, J. M., 2011, Forward Displacement Analysis of a Linearly Actuated Quadratic Spherical Parallel Manipulator, *ASME Journal of Mechanisms and Robotics*, 3, 011007_1-6.

[155] Bonev, I. A., Chablat, D., and Wenger, P., 2006, Working and Assembly Modes of the Agile Eye, Proceedings of the 2006 IEEE International Conference on Robotics and Automation, Orlando, FL, May 15–19, 2317–2322.

[156] Zlatanov, D., Bonev, I.A., and Gosselin, C.M., 2002, Constraint Singularities as C-Space Singularities, In: Lenarcic J. Thomas F., *Advances in Robot Kinematics*, Kluwer, Dordrecht, 183-192.

[157] Merlet, J.P., 1989, Singular Configurations of Parallel Manipulators and Grassmann Geometry, *Int. J. Robot. Res.*, 8(5), 45-56.

[158] Hao, F., and McCarthy, J.M., 1998, Conditions for Line-Based Singularities in Spatial Platform Manipulators, *J. Robot. Syst.*, 15(1), 43–55.

[159] Dai, J.S., 2012, Finite displacement screw operators with embedded Chasles' motion,

ASME Journal of Mechanisms and Robotics, 4(4), 041002_1-9.

[160] Kong, X.W., and Gosselin, C.M., 2001, Uncertainty singularity analysis of parallel manipulators based on the instability analysis of structures, *International Journal of Robotics Research*, 20(1), 847–856.

[161] Merlet, J. P., and Daney, D., 2008, Appropriate Design of Parallel Manipulators, *Smart Devices and Machines for Advanced Manufacturing*, Springer, London, 1-25, doi: 10.1007/978-1-84800-147-3_1.

[162] Lou, Y., Liu, G., and Li, Z., 2008, Randomized Optimal Design of Parallel Manipulators, *IEEE Transactions on Automation Science and Engineering*, 5(2), 223-233.

[163] Gosselin, C., 1988, Kinematic Analysis Optimization and Programming of Parallel Robotic Manipulators, PhD Thesis, McGill University, Montréal, Canada.

[164] Liu, X.J., Wu, C., and Wang, J.S., 2012, A New Approach for Singularity Analysis and Closeness Measurement to Singularities of Parallel Manipulators, *ASME J. Mech. Robot*. 4(4), 041001(1-10).

[165] Chen, C., and Angeles, J., 2007, Generalized Transmission Index and Transmission Quality for Spatial Linkages, *Mech. Mach. Theory*, 42(9), 1225–1237.

[166] Liu, H.T., Huang, T., Kecskemethy, A., and Chetwynd, D.G., 2014, A Generalized Approach for Computing the Transmission Index of Parallel Mechanisms, *Mechanism and Machine Theory*, 74, 245-256.

[167] Clavel, R., 1991, Conception d'un Robot Parallèle Rapide à 4 Degrés de Liberté, PhD Thesis, EPFL, Lausanne, Switzerland, nq 925.

[168] Badescu, M., and Mavroidis, C., 2004, Workspace Optimization of 3-legged UPU and UPS Parallel Platforms with Joint Constraints, *ASME Journal of Mechanical Design*, 126(2), 291–300.

[169] Chablat, D., and Wenger, P., 2003, Architecture Optimization of a 3-dof Translational Parallel Mechanism for Machining Applications, the Orthoglide, *IEEE Transactions on Robotics and Automation*, 19(3), 403–410.

[170] Merlet, J-P., 1997, Designing a Parallel Manipulator for a Specific Workspace, *International Journal of Robotics Research*, 16(4), 545–556.

[171] Du Plessis, L.J., and Snyman, J.A., 2006, Determination of Optimum Geometries for a Planar Reconfigurable Machining Platform Using the LFOPC Optimization Algorithm, *Mechanism and Machine Theory*, 41(3), 307–333.

[172] Huang, T., Li, M., Li, Z., Chetwynd, D.G., and Whitehouse, D.J., 2004, Optimal Kinematic Design of 2-dof Parallel Manipulators with Well-Shaped Workspace Bounded by a Specific Conditioning Index, *IEEE Transactions on Robotics and Automation*, 20(3), 538–543.

[173] Das, I., and Dennis, J.E., 1997, A Closer Look at Drawbacks of Minimizing Weighted Sums of Objectives for Pareto Set Generation in Multicriteria Optimization Problem, *Structural Optimization*, 14, 63–69.

[174] Guillot, M., and Gosselin, C. M., 1991, The Synthesis of Manipulators with Prescribed Workspace, *ASME J. Mech. Des*., 113(3), 451–455.

[175] Wang, J., Wu, C., and Liu, X.-J., 2010, Performance Evaluation of Parallel Robots: Motion/Force Transmissibility and Its Index, *Mech. Mach. Theory*, 45(10), 1462–1476.

[176] Huang, T., Wang, M.X., Yang, S.F., Sun, T., Chetwynd, D.G., and Xie, F.G., 2014, Force/Motion Transmissibility Analysis of Six Degree of Freedom Parallel Mechanisms, *ASME J. Mech. Robot.*, 6, 031010_1-5.

[177] Gan, D. M., Dai, J. S., Dias, J., and Seneviratne, L. D., 2016, Variable motion/force transmissibility of a metamorphic parallel mechanism with reconfigurable 3T and 3R motion, *Transactions of the ASME: Journal of Mechanisms and Robotics*, 8(5), 051001_1-9.

[178] Sun, T., Song, Y., Li, Y., and Zhang, J., 2010, Workspace Decomposition Based Dimensional Synthesis of a Novel Hybrid Reconfigurable Robot, *ASME Journal of Mechanisms and Robotics*, 2, 031009_1-8.

[179] Liu, H., Huang, T., and Chetwynd, D.G., 2011, A Method to Formulate a Dimensionally Homogeneous Jacobian of Parallel Manipulators, *IEEE Transactions on Robotics*, 27(1), 150-156.

[180] Han, C., Kim, J., Kim, J., and Park, F., 2002, Kinematic Sensitivity Analysis of the 3-UPU Parallel Mechanism, *Mech. Mach. Theory*, 37, 787–798.

[181] Meng, J., Zhang, D.J., and Li, Z.X., 2009, Accuracy Analysis of Parallel Manipulators with Joint Clearance, *ASME J. Mech. Des.*, 131(1), 011013_1-9.

[182] Huda, S., Takeda, Y., and Hanagasaki, S., 2011, Kinematic Design of 3-URU Pure Rotational Parallel Mechanism to Perform Precise Motion with a Large Workspace, *Meccanica*, 46(1), 89-100.

[183] Gan, D. M., Dai, J. S., Dias, J., and Seneviratne, L. D., 2016, Joint force decomposition

and variation in unified inverse dynamics analysis of a metamorphic parallel mechanism, *Meccanica*, 51(7), 1583-1593.

[184] Rico, J. M., Gallardo, J., and Duffy, J., 1999, Screw Theory and Higher Order Analysis of Open Serial and Closed Chains, *Mechanism and Machine Theory*, 34(4), 559-586.

[185] Tsai, L.W., 1999, Robot Analysis: The Mechanics of Serial and Parallel Manipulators, Wiley, New York.

[186] Olarra, A., Axinte, D., and Kortaberria, G., 2018, Geometrical Calibration and Uncertainty Estimation Methodology for a Novel Self-Propelled Miniature Robotic Machine Tool, *Robotics and Computer-Integrated Manufacturing*, 49, 204-214.

[187] Olarra, A., Axinte, D., Uriarte, L., and Bueno, R., 2017, Machining with the WalkingHex: A Walking Parallel Kinematic Machine Tool for in Situ Operations, *CIRP Annals - Manufacturing Technology*, 66, 361–364.